Current Awareness Bulletin

of

SCHOLARLY ARTICLES PUBLISHED BY

Faculty, Students and Alumni

~ October 2012 ~

DELHI TECHNOLOGICAL UNIVERSITY CENTRAL LIBRARY
(formerly Delhi College of Engineering, Bawana Road, DELHI)

PREFACE

This is the first Current Awareness Bulletin Service started by Delhi Technological University Library. The aim of the bulletin is to compile, preserve and disseminate information published by the Faculty, Students and Alumni for mutual benefits. The bulletin also aims to propagate the intellectual contribution of DTU as a whole to the academia. It contains information resources available in the internet in the form of articles, reports, presentation published in international journals, websites, etc. by the faculty and students of Delhi Technological University in the field of science and technology. The publication of Faculty and Students which are not covered in this bulletin may be because of the reason that either the full text was not accessible or could not be searched by the search engine used by the library for this purpose. To make the bulletin more comprehensive, the learned faculty and Students may provide their uncovered publication to the library either through email or in CD, etc.

This issue contains the information published during October 2012. The arrangement of the contents is alphabetical wise starting from A-Z. The Full text of the article which is either subscribed by the University or available in the web has been provided in this Bulletin.

CONTENTS

13. *Multidimensional role of CD34 Protein in Hematopoietic Stem cell Biology by* ****Vimal Kishor Singh****, Kohichiro Tsuji,* ****PB Sharma*** *and Ramesh Chandra.*

14. Patch Antenna Array Fault Modeling and Its Monitoring by ***@Umesh Kumar*** and ****Rajiv Kapoor***.

15. Performance and Emission Studies of a Compression Ignition Engine on blends of Calophyllum Oil and Diesel by ***@Chinmay Mishra, @Naveen Kumar, @Sidharth and @B. S. Chauhan.***

16. Phase Control of Nanostructured Iron Oxide for Application to Biosensor by ****Rachna Sharma****, Ved Varun Agrawal1, A. K. Srivastava, Govind, Lata Nain, Imran Chaudhar, Soumya Ranjan Kabi, R. K. Sinha and* ****Bansi D. Malhotra***.

17. Some Exact Solutions of Magnetized viscous model in String Cosmology by ****C.P. Singh and *Vijay Singh.***

18. String Cosmology with Magnetic field in Anisotropic Space-time by ****C.P. Singh and *Vijay Singh.***

***** **Faculty**
@ **Students/Research Scholars**
# **Alumni**

A New Mobility Model for Multimedia Networks

Munish Kumar
School of IT
CDAC, Noida, 201307, INDIA

Z. A. Jaffery
Department of Electrical Engineering
Jamia Milia Islamia, New Delhi, INDIA

Moinuddin
Department of Electrical Engineering
Jamia Milia Islamia, New Delhi, INDIA

***Abstract*—**Mobile IP is the current standard proposed by IETF for mobility management in IP networks. Its importance increases if network is supporting multimedia applications. Mobile node communicates with a static Correspondent Node. The main consideration is when Mobile Node and Correspondent Node both are visiting beyond their home networks and changing their network. For real time applications it needs faster reestablishment of a broken connection due to change of network. The proposed model works after changing the address of a node due to change of network. It differentiates between the initial establishment and intermediate reestablishment of communication between mobile node and correspondent node in lesser steps than 3RP[1,2]. The proposed model will be efficient if nodes are changing their networks frequently due to high mobility of the nodes and will cause less loss of packet and faster handoff. This model will also help in better utilization of available bandwidth which is a sensitive parameter in mobile multimedia networks.
Key words: *Mobility, Correspondent node, 3RP*

1. INTRODUCTION

Real time applications on internet now require new effecient ways of utilization of network resources reliably. On internet, each node needs unique identity-as IP address in the network. A node with a static IP address cannot change the point of attachment during network access but it is highly required to change the address to support the mobility of nodes. This is adaptive nature of IP address which provides true mobility[3].

Internet Engineering Task Force (IETF) standardized Mobile IP for mobility protocol for internet. Mobile IP allows a Mobile Node (MN) to change its point of access. Mobile IP has two different versions based on IPv4 and IPv6. Mobile IPv4 uses separate UDP based protocol for registration. The IPv4 header had limitations in mobility because of its header length and scalability[4,5]. So IPv4 based networks could not grow as per the current need of today. It has another limitation that needs triangular routing between MN and CN both nodes which requires extra attention[6].

Limitations of mobile IPv4 enforces for better solution. Mobile IPv6 has overcome the limitations of mobile IPv4. It can grow up to 2^{128}-1 nodes and provides unique identity to each node. It is integrated as header extension which means it is divided into different headers- Mobility Header, Authentication Header and Security Header etc. All these headers have defined functionalities and are part of mobile IPv6 main header[7,8].

The possible scenarios of MN and CN are when-

(i) MN and CN both remains in their home networks.
(ii) MN is mobile and CN is stationary.
(iii) MN is stationary and CN is mobile.
(iv) MN and CN both are mobile.

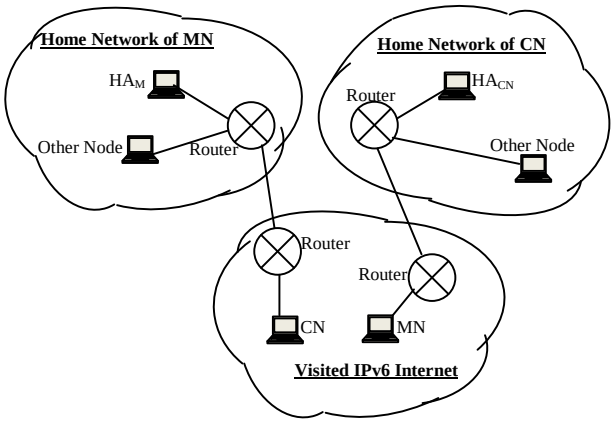

Figure 1: An Example of Mobility

The first case is common and easy to handle because no node is mobile there. This is based on static IP address. Whereas second and third cases are similar having one node movable and another is not allowed to change its network. The last case shows true mobility where both communicating nodes, MN & CN both, are allowed to change their network. As in Figure 1, MN and CN both have left their home networks and moved to a foreign network (FN).

As in fourth case, when MN leaves its home network, Home Agent, (HA_{MN}) and enters the foreign network (FN), it links down from HA_{MN} and links up to FN. FN router identifies the new foreign nodes (here MN) and now FN uses Dynamic Host Configuration Protocol (DHCP) to provide its network access to foreign nodes with new Care-of-Address (CoA). Through Foreign network Agent (FA), MN sends its CoA to HA_{MN} and gets bound with its home HA_{MN}. After getting an acknowledgement from HA_{MN} now MN is ready to re-establish the broken communication

Manuscript received September 5, 2012
Manuscript revised September 20, 2012

with CN. There are two ways to re-establish the communication being in foreign network.

(i). Get request(s) through HA_{MN}.

(ii). Initiate a new communication message.

MN has list of CNs and sends message to them with new CoA after proper authentication and security to identify the actual correspondent nodes. MN also gets new request through HA_{MN}. MN and CN now identify to each other and ensure a reliable communication. There is an existing model known as Reverse Return Routability Procedure (3RP). It takes six steps for fresh registration as well as reestablishment of communication after link break-up due to change of access point/network by a mobile node. It consumes good amount of time and affects the performance particularly when link is reestablished after a link break up. The proposed model may reduce this time by reducing the number of steps for registration. In the present work we have proposed a new mobility model which exchanges lesser messages during fresh and after link break-up registration to establish the communication link.

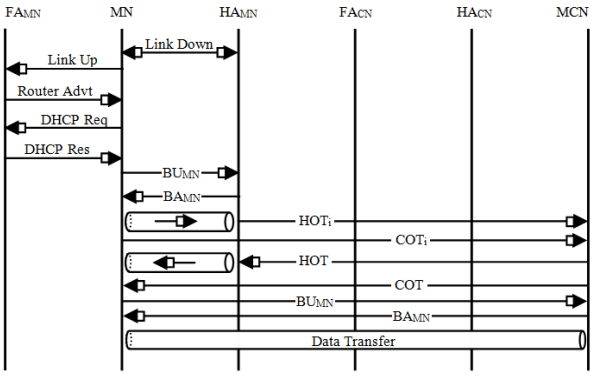

Figure 2: Mobility of MN

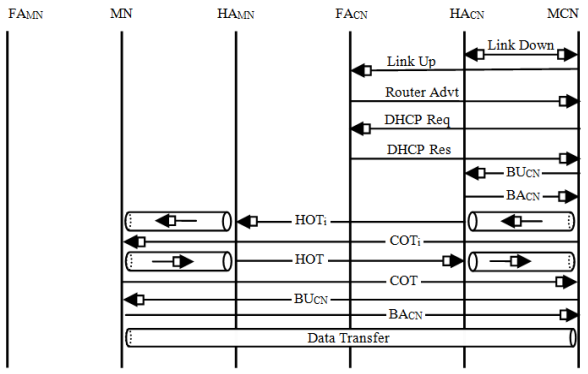

Figure 3: Mobility of CN

2. Reverse Return Routability Procedure (3RP)

3RP model proposed by Saxena & Jasola[1,2] is the addressable process that claims mobile node address through care-of-address of correspondent node during mobility. During authentication process it uses binding management key (K_{BM}) as proof. It uses Home Test initialisation(HOTi), Care-of-test initialisation(COTi), Home test (HOT) and Care-of-test(COT) messages. Home agent of registering node, HA_{XX}, sends HOTi to other node and gets response as HOT through HA_{XX}. Home agent of FN, where mobile node is currently located, sends COTi message directly to another node and gets response as COT message from that node.

The message is sent through moving nodes' (MN and CN both) home agents (HA_{MN} and HA_{CN}) directly to another communicating node (MN or CN). Afterwards it again gets binding update (BU) with other node by sending the BU and binding acknowledgement (BA) as shown in Figure 2 and Figure 3. Finally the data transfer proceeds.

Message Formats of 3RP[1,2]

There are four message formats for registration and the two messages for binding the values.

(i) **Home Test init (HOTi)-** HOTi message format contains Source Address, Destination Address and init cookies. The source is the home address, destination address is correspondent Address and init cookies is the key that should be remembered by mobile node to identify the correspondent node.

(ii) **Care of Test init (COTi)-** COTi message contains source Address, destination Address and init cookies. The source address is the care-of-address, corresponded node destination address is correspondent address and init cookies is the previous key which is sent by mobile node. Correspondent node compares these two cookies and identifies the mobile node.

(iii) **Home Test (HOT)-** HOT message format contains source address, destination address init cookies, keygen token and nonce index. The source is the correspondent address, destination address is home address. The correspondent node generates the keygen token by using the home address, nonce index and '0' bit appended at the end of message after applying the secure hash algorithm and send it to the home address.

(iv) **Care Of Test (COT)-** COT message contains source address, destination address, init cookies, keygen token and nonce index. The source is the correspondent address and destination address is care of address. At the correspondent node it sends the generated keygen token with other keys at care-of-address directly. Now the receiver again regenerates the keygen and compares for proper identification.

(v) **Binding Update (BU)-** All the above four messages are known as 3RP. And after this it (care of address node) sends binding update to correspondent node.

Now in the Binding Update the message format contains-source address, destination address, home Address, sequence number, nonce index, care of nonce index and encryption key K_{BN}.

The Source Address is care-of-address, Destination Address is correspondent address and K_{BN} is applied to SHA with care of address, correspondent and binding update message and sent to the destination.

(vi) **Binding Acknowledgement(BA)-** Similarly the binding acknowledgement message contains source address, destination address, sequence number and encrypted K_{BN}. Here source address is correspondent home address, Destination Address is care-of-address,

There are two problems in 3RP

(i). It takes six steps for a new registration process which takes good amount of time and affects the performance when link is broken due to change of network by a node. By the proposed model this time can be reduced.

(ii). It always requires fresh registration whenever the communication breaks. In the proposed model reduced steps will reestablish the communication.

3. PROPOSED MODEL: Circular Registration

The new reliable mobility model follows circular registration process which performs better in intermediate reestablishments of broken communication. The communication process is between the care-of addresses of MN and CN.

The basic structure of the mobility when MN and CN both move to foreign networks is shown in Figure 4. It is showing the sequence of the registering process when MN initiates the reestablishment of broken communication.

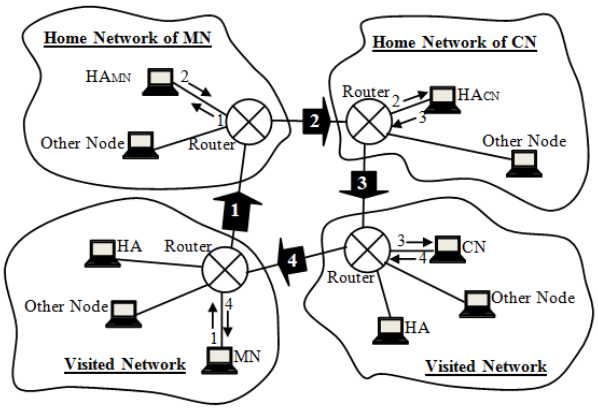

Figure 4: Circular registration process

BASIC MODEL- A moving Correspondent node (MCN) needs to communicate with other mobile node (MN). MCN just sends INIT message to Home of MN, considering that MN is in home network. The Home Agent of MN checks the list of nodes whether MN is in the home network or in some foreign network by checking binding information at Home Agent. Now there are two cases-

(i) MN is bound with its home network.

(ii) MN is not bound with its home network.

In the first case the related information is sent to MN at its current (home) location. In the second case, CN should be waiting until further information and acknowledgement message should be sent to CN. Here the proposed model works better and the registration takes four steps-

(i) From MN to HA_{MN}

(ii) From HA_{MN} to HA_{CN}

(iii) From HA_{CN} to CN at its current location

(iv) From CN to MN (direct).

$$\mathbf{MN \rightarrow HA_{MN} \rightarrow HA_{CN} \rightarrow CN \rightarrow MN}$$

Registration Process of MN- First it stores related information from INIT message about CN and generates the security key on the basis of message and apply security algorithm (if required) before sending REG message to HA_{MN}. HA_{MN} just forwards REG message to the Home Agent, HA_{CN}, of destination as mentioned in the message and HA_{CN} sends it to the current address of CN. CN analyzes the information and retrieves the Keys and compares with new created key. After editing the message it is sent to MN.

Finally MN gets the encrypted message which is decrypted with key and security level and compare with its original IP address. If successful, it sends BA to CN. Now both are registered for data transfer. The process is shown in the Figure 5.

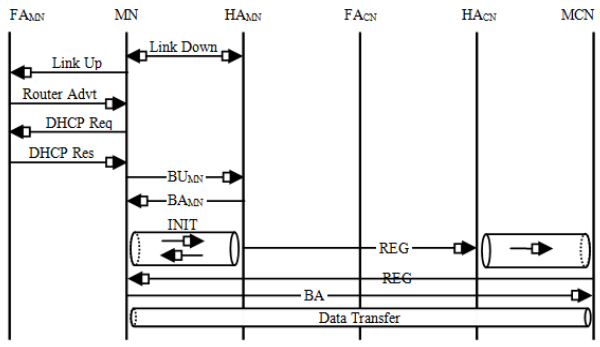

Figure 5: MN Registration

Registration Process of CN- Similar case as CN initiates the registering process when it binds up with its Home Agent (HA_{CN}). The process is shown in the Figure 6.

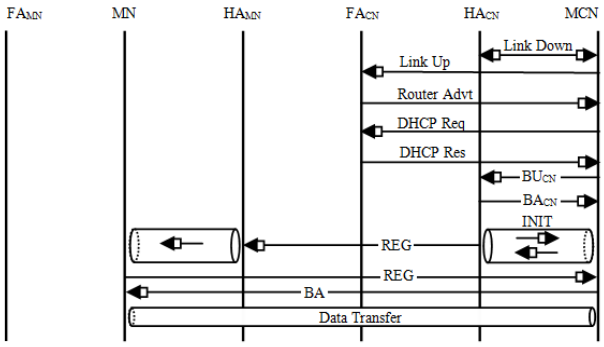

Figure 6: CN Registration

Binding Update by MN- During the mobility if communication fails between the MN and CN, first MN binds up with the new/changed foreign network (it may again enter into home). After binding, it checks the list of all previously communicating nodes and ends binding update to all instead of registering. During binding it gets new Key for further communication. On unsuccessful binding it follows the registering process again through HA_{MN}, HA_{CN}, CN and MN. The process is shown into Figure 7.

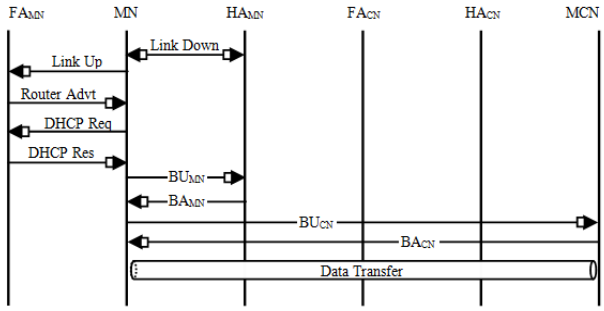

Figure 7: Binding update by MN

Binding Update by CN- Similarly as in the binding update of the MN but simple difference is that it is initiated by the CN instead of MN.

Message Formats- Four massage formats are required

(i) **INIT-** This is initiating message and sent on every first request made by initiator (the node which wants to start the communication). INIT message follows the path through homes. The INIT message has-Source address (CoA of MN), Destination address(Home Address of CN) and key K_1.

(ii) **REG-** Registration is circular process which starts and ends at REG initiator (CN). It goes through home agents and returns back directly to the REG initiating node. Initially, it has Source address(CoA of CN),Destination address(MN Home Address) and Keys K_1 & K_2. And finally REG initiator node(CN) receives directly modified version of REG- Source address(CoA of MN), Destination address(CoA of CN) and Keys K_2 & K_3.

(iii) **BU-** Binding update is special message and is used to reestablish the broken communication. This message is sent by the node that has changed its address(MN) recently. BU message uses the previous values that were used during last communication. BU message is same as registration message but with keys (K_1 and K_4), where K_1 is INIT message-key and K_4 is the one used during last communication (introduced by BA).

(iv) **BA-** The binding acknowledgement message is final binding message. This is sent to MN in response of REG or BU. In response of REG it simply adds new key (K_4) and sends communication establishment details. But in response of BU it sends new key replacing the old one.

$$K_4 \text{ (old)} \leftarrow K_4 \text{ (new)}$$

Exchange of keys in circular registration-

$$MN \xrightarrow[INIT]{K_1} CN \xrightarrow[REG]{K_1,K_2} MN \xrightarrow[REG]{K_2,K_3} CN \xrightarrow[BA]{K_1,K_4} MN$$

All keys are of 64 bits. K_0 is random number of 64 bits. K_i depends on K_{i-1}.

Exchange of keys to reestablish the communication after a break in communication:

$$MN \xrightarrow[BU]{K_1,K_4} CN \xrightarrow[BA]{K_1,K_4(new)} MN$$

4. IMPLEMENTAION

The proposed model is simulated in JAVA 1.5 on the Windows XP platform using JFC and threads. Initially there is a Network having 8 LANs. All LANs are LAN_0, LAN_1, LAN_2, LAN_3, LAN_4, LAN_5, LAN_6 and LAN_7. Each LAN has a different key to access network as shown in Table 6. LAN_2 has two nodes MN_2 & HA_{MN2}. Both have network ID 64 and 65 with different security keys to LAN access. MN_2 has its node ID as $MN_2(64)$ and a security key (K_c). Similarly its home has its ID and security key K_c. HA_{MN2} has a space for foreign node but now it is vacant and LAN access status which is initially free for both nodes (MN_2 & HA_{MN2}). Similarly all LANs have their nodes' list. All nodes and home are shown in Table 6,7 and 8.

After network initialization the communication is to be established between node $MN_3(96)$ and $CN_1(32)$. Here $MN_3(96)$ initiates the INIT process. The flow of the INIT message is $MN_3(96) \rightarrow HA_{MN3}(97) \rightarrow HA_{CN1}(33) \rightarrow CN_1(32)$. Here $HA_{MN3}(97)$ forwards the message to $HA_{CN1}(33)$ as shown in Table-1, where first five rows show the INIT process.

$MN_1(32)$ after receiving the INIT message starts REG process. The flow of REG process is $CN_1(32) \rightarrow HA_{CN1}(33) \rightarrow HA_{MN3}(97) \rightarrow MN_3(96) \rightarrow CN_1(32)$. This time REG message follows the reverse path followed

by INIT message. Home nodes forward message to destination MN_3(96). Table-1 shows the steps. MN_3(96) receives a REG message in response of INIT message. MN_3(96) edits message and forwards to CN_1(32) directly. The whole REG process is shown in Table-1 & 2- last four lines of Table-1 and first line of Table-2. CN_1(32) receives a REG message in response of REG message. Now it starts BA message.

Table:1: INIT and REG Process

Node	Local ID	Network ID	Process	Message
MN_3	3	96	Start	Initialization
MN_3	3	96	INI	Request Sent
HA_{MN3}	3	97	Forward	Message forwarded to
HA_{CN1}	1	33	Forward	Message forwarded to
CN_1	1	32	RQ	Registration started
HA_{CN1}	1	33	Forward	Message forwarded to
HA_{MN3}	3	97	Forward	Message forwarded to
MN_3	3	98	RQ	Registration process

Table 2: BA and Data Transfer.

Node	Local ID	Network ID	Process	Message
CN_1	1	32	BA	Binding Ack. Started
MN_3	3	96	BA	Binding Completed
MN_3	3	96	Data Trans	Data Transfer Started
CN_1	1	32	Data Trans	Data Transfer Started
MN_3	3	96	Data Trans	Data Transfer Started
CN_1	1	32	Data Trans	Data Transfer Started
MN_3	3	96	Data Trans	Data Transfer Started
CN_1	1	32	Data Trans	Data Transfer Started

Finally, BA message steps are $CN_1(32) \rightarrow MN_3(96)$. MN_3(96) received a BA message who was initiator of communication and is now ready for data transfer with authorization of correspondent CN_1(32). The communication is established. All remaining processes are shown into Table-3.

Table 3: Changing Address by MN3(96)

Node	Local ID	Network ID	Process	Message
MN_3	3	96	Changing	Changing Address
MN_3	3	96	Foreign	Sending Foreign Registration
HA_{MN2}	2	65	Forward	Registered into foreign network
MN_3	2	66	Request	Information sent to Home
MN_3	2	66	BU	Sending BU to 32
HA_{MN3}	3	97	Request	CoA updated of node 96→66
CN_1	1	32	BA	Binding Ack. started
MN_3	2	66	BA	Binding completed

Both MN-(96) and CN-(32) are communicating to each other. MN_3(96) moved to foreign network LAN_2. MN_3(96) first received a care-of address and new LAN-access key by LAN_2. By sending the foreign registration message node MN_3(96) received new ID 66 into LAN_2. After this it sent the information to its Home HA_{MN1}(97) to update care-of address and takes steps to reestablish the communication. The reestablishment of communication process is BU and BA messages in between $MN_1(66) \leftrightarrow CN_1(32)$. The BU message is sent to node CN_1(32). CN_1(32) analyzes whether to reply with BA message or not. The Table-4 shows the entire process of reestablishment of communication.

After reestablishment of communication between CN_1(32) & MN_3(66), CN_1(32) moved into foreign network LAN4. CN_1(32) first got a care-of address and new LAN access key by LAN_4. By sending the foreign registration message, node CN_1(32) got new ID 130 into LAN_4. Now this information is sent to its Home HA_{CN1}(33) to update care-of address and follows steps to reestablish the communication. The reestablishment of communication processes are BU and BA messages in between $MN_3(66) \leftrightarrow CN_1(130)$. The BU message is sent to node MN_3(66). MN_3(66) analyzes whether to reply with BA message or not. Table-4 shows the entire process of reestablishment of communication.

Table-4: Reestablishment of Communication.

Node	Local ID	Network ID	Process	Message
CN_1	1	22	Changing	Changing Address
CN_1	1	32	Foreign	Sending Foreign Registration
HA_{MN4}	4	129	Forward	Registered into foreign network
CN_1	4	130	Request	Information sent to Home
HA_{CN1}	1	33	Request	CoA updated of node 32→130
CN_1	4	130	BU	Sending BU to 66
MN_3	2	66	BA	Binding Ack. Started
CN1	4	130	Data Trans	Binding continued

All these steps show how to establish a new connection, change of address by correspondent node or mobile node or both. At the end the correspondent node CN_1(130) sends a message to close the communication. Table -5.

Table -5: Closing Communication.

Node	Local ID	Network ID	Process	Message
CN_1	4	130	Data Trans	Data transfer continue
MN_3	2	66	Data Trans	Data transfer continue
CN_1	4	130	Data Trans	Data transfer continue
MN_3	2	66	Data Trans	Data transfer continue
CN_1	4	130	Data Trans	Data transfer continue
MN_3	2	66	Data Trans	Data transfer continue
CN_1	4	130	Closed	Communication finished
MN_3	2	66	Finished	Communication finished

Table 6: LAN Details

Sr. No.	LAN ID	Network Key	Internal nodes' list		
			Home Name	Node Name	Foreign Node Name
1	0	-2796157908206859895	HA_{mn0}	MN_0	-
2	1	-4628641561949930066	HA_{cn1}	CN_1	-
3	2	1273808252703953671	HA_{mn2}	MN_2	-
4	3	-1587058469200310565	HA_{mn3}	MN_3	-
5	4	-3366644127751405509	HA_{mn4}	MN_4	-
6	5	540072993638041822	HA_{mn5}	MN_5	-
7	6	980717501151800054	HA_{mn6}	MN_6	-
8	7	-7671850706000975806	HA_{mn7}	MN_7	-

Table 7: Home List

SN	Node	LAN Name	Network ID	LAN access key	Node inside	Foreign Node Inside

1	HA_{MN0}	LAN_0	1	-699852102673795571	MN_0	-
2	HA_{CN1}	LAN_1	33	-5086360294108397192	CN_1	-
3	HA_{MN2}	LAN_2	65	-7217034949619537402	MN_2	-
4	HA_{MN3}	LAN_3	97	-4321165493066525820	MN_3	-
5	HA_{MN4}	LAN_4	129	-2742521606173754264	MN_4	-
6	HA_{MN5}	LAN_5	161	-2211604228482065662	MN_5	-
7	HA_{MN6}	LAN_6	193	9214057590934752163	MN_6	-
8	HA_{MN7}	LAN_7	225	-7671850706000975806	MN_7	-

Table 8: Moving Node List

SN	Node	LAN ID	Network ID	LAN access key	Home	
					ID	K_c
1	MN_0	LAN_0	0	4859524786204359779	1	-
2	CN_1	LAN_1	32	-7459458870876608887	33	8637522115308582251
3	MN_2	LAN_2	64	-2600126444617303549	65	-
4	MN_3	LAN_3	96	-671822774646447901	97	3298821842463134199
5	MN_4	LAN_4	128	-519272530817304060	129	-
6	MN_5	LAN_5	160	3368702412753809847	161	-
7	MN_6	LAN_6	192	-7730710215611681677	193	7013852424545880551
8	MN_7	LAN_7	224	-4816490087373103019	225	-

5. CONCLUSION

The proposed mobility model has only four message formats. Circular registration method follows circular path so no need to acknowledge separately. The registering process is situation dependent and divided into two parts. First one is initial registration setup and intermediate setup after link breakage whereas the binding update process is a better option when intermediate registration is needed. This model will be efficient if nodes are highly mobile and change of network is very frequent. Due to reduction in exchange of messages in various situations, this model will enhance the utilization of the available bandwidth. Throughput will be improved because the reduced exchange message will provide more time for data transfer. For real time applications delay due to handoff and bandwidth will be certainly improved. In case of that both nodes, MN and CN, changes their point of access simultaneously then it may take more time to reestablish the new connection.

REFERENCES

[1] P.C.Saxena, Sanjay Jasola, "Intelligent Model for Mobility of correspondent node in mobile IPv6", Computer Standards & Interface 28(2006) 737-751.

[2] P.C.Saxena, Sanjay Jasola, "A new model for Mobility of Correspondent Node in mobile IPv6". Journal of CSI,Vol. 36 No.1, January - March 2006.

[3] Nadjia Kara, "Mobility Management Approaches for Mobile IP Networks: Performance Comparison and Use Recommendations," *IEEE Transactions on Mobile Computing*, vol. 8, no. 10, pp. 1312-1325, Feb. 2009.

[4] Johnson, D., Parkins C., 2004, "Mobility support inIPv6", RFC 2462, IETF.

[5] Perkins C., Calhoun P., 2006, "Mobile IPv4 Challenges/Response Ext, RFC3012bis, IETF.

[6] Sanguankotchakorn, T. Jaiton, P. , Effect of Triangular Routing in Mixed IPv4/IPv6 Networks, IEEE, Networking, ICN2008,pp.357-362.

[7] Hinden R., Deering S., 1998, IP Version 6 Addressing Architecture, RFC 2373, IETF.

[8] Manoozi P., Ghosal D., 1995, Impact of mobility on TCP/IP: An integrated performance study, IEEE Journal of selected areas of communications, vol. 13, no. 5. Pp. 858-867.

[9] Mohebr Girgis, Tarek m. Mahmoud, Youssef s. Takroni and Hassan s. Hassan, "Performance Evaluation of a New Route Optimization Technique for Mobile IP", International Journal of Network Security & its Applications (IJNSA), V0l. 1, No 3; pp 63-73, October 2009.

[10] M. Song, J. Huang, R. Feng, and J. Song, "A Distributed Dynamic Mobility Management Strategy for Mobile IP Networks," *Proc. Sixth Int'l Conf. ITS Telecomm.*, 2006.

[11] Ruidong Li, Jie Li, Kui Wu, Yang Xiao, and Jiang Xie, "An Enhanced Fast Handover with Low Latency for Mobile IPv6," IEEE Transactions on Wireless Communications, vol. 7, no. 1, pp. 334-342, January 2008.

Munish Kumar- He obtained his B.E. in Computer Science & Engg from MNREC, University of Allahabad, in 1992 and Master of Computer Science & Engg from Jadavpur University, Kolkata.Tech. in 1995. Presently he is in School of IT, CDAC, Noida. His research area includes Ad-hoc Networks, Sensor Networks, Wireless Networks, Mobile Computing, Real-Time Applications

Prof Moin Uddin- He obtained his B. Tech and M.Tech in Electrical Engineering from Aligarh Muslim University, Aligarh, India in 1972 and 1978 respectively. He obtained his PhD degree from university of Roorkee in 1992. Dr. Moinuddin is the professor in the Department of Electrical Engineering, Jamia Millia Islamia, New Delhi and presently he is on deputation as Pro Vice Chancellor, Delhi Technological University, Delhi.. He has guided several PhD. His research area includes computer networking, soft computing and Artificial Intelligence.

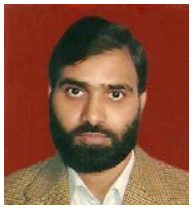

Dr. Z.A. Jaffery- He obtained his B. Tech and M.Tech in Electrical Engineering from Aligarh Muslim University, Aligarh, India in 1987 and 1989 respectively. He obtained his PhD degree from Jamia Millia Islamia (a central Govt. of India university) in 2004. Presently he is the associate professor in the Department of Electrical Engineering, Jamia Millia Islamia, New Delhi. His research area includes Application of soft computing Techniques in Signal Processing, Communication engineering and Computer Networking.

Available online at www.pelagiaresearchlibrary.com

Pelagia Research Library

Advances in Applied Science Research, 2012, 3 (5):2648-2651

Pelagia Research Library

ISSN: 0976-8610
CODEN (USA): AASRFC

An Analytical Study of Potential Energy Term in Variable Moment of Inertia Nuclear Softness (MINS) Model

Hardik P. Trivedi[1], Pallavi Bhatt[1], Anil Kumar [1, 2]*, Lalit K. Gupta[3], Jai Prakash Gupta[4], Krishna Chandra[5], Than Singh Saini[6] and Archna Kansal[7]

[1]*Department of Physics, Mewar University, Chittorgarh (Rajasthan) INDIA*
[2]*Deptartment of Physics, Vivekananda College of Technology and Management, Aligarh (UP) – 202 002, INDIA*
[3]*Department of Physics, Krishna Engineering College, Ghaziabad, INDIA*
[4]*Department of Physics, D. S. College, Aligarh (UP) - 202 001, INDIA*
[5]*Department of Physics, Goldfield institute of Technology & Management, Faridabad-, INDIA*
[6]*Department of Physics, Delhi Technological University, Delhi-42 INDIA*
[7]*Department of Physics, ITM, Gwalior (MP) INDIA*

ABSTRACT

In this paper, we have calculated potential energy term in variable moment of inertia nuclear softness which shows the variation of potential energy term for the different even-even nuclei in the region of I-quadrant based on the valence particle and hole pairs consideration [8]{Ce (N=90), Nd (N=92), Dy (N=92) & Dy (N-94)} with spin (J). The value of potential energy term is increasing almost linear with increasing spin (J) for all the nuclei.

Key Words: *Ground State Moment of Inertia (θ_0); Softness Parameter (σ); Stiffness Constant (C)*

INTRODUCTION

Now, it has been experimentally [1] suggested that the ground state bands for even-even nuclei away from closed shells can be expected throughout the Periodic Table. Theoretically, a number of models [2-7] have been proposed to correlate such a data. In this attempt, the variable moment of inertia (VMI) model proposed by Mariscotti *et al;* [2] is one of the earliest and very popular among the nuclear science community. In this model, the excitation energy of the state J is defined as the sum of the rigid rotational energy (with moment of inertia 'θ' varying with angular momentum 'J') and a potential energy term (harmonic in angular momentum dependent moment of inertia θ_J about its mean ground state value θ_0. Latter this VMI model extended by Klein and his associates [5, 6] on the basis of the predictions of the Interacting Boson Model [IBM-1] in to two generalizations of VMI model, namely, the Variable An harmonic Vibrator Model (VAVM) and the Generalized VMI (GVMI) model. Batra *et al;* [7-10] extended VMI model by taking in to account the concept of nuclear softness. This extended version of VMI generally called VMINS model. In the present work we studied the importance of potential energy term using VMINS model.

MATERIALS AND METHODS

In the original variable moment of inertia (VMI) [2] model, the excitation energy of the member of the ground-state band with angular momentum J is given by

$$E(J)=\frac{\hbar^2}{2I}J(J+1)+\frac{c}{2}(I-I_0)^2 \qquad \text{----------} \quad \text{(i)}$$

Here the potential term is added to the usual rotational term. The coefficients c and I_0 are parameters, characteristic for each nucleus. Where I_0 is called the ground state moment of inertia and c is denoted as stiffness parameter.

Gupta *et al;* [7, 8] expressed the Variable Moment of Inertia (VMI) model for the ground state band in even-even nuclei in terms of his Nuclear Softness (NS) model [3]. In NS model the variation of moment of inertia θ with J is given by

$$\theta=\theta_0(1+\sigma J) \qquad \text{----------} \quad \text{(ii)}$$

Where θ_0 is the ground state moment of inertia and σ is the softness parameter. After putting the value of Moment of Inertia (I) in terms of Nuclear Softness Parameter (σ) in equation (i) we get the following expression:-

$$E(J)=\frac{\hbar^2 J(J+1)}{2\theta_0(1+\sigma J)}+\frac{C}{2}\sigma^2\theta_0^2 J^2 \qquad \text{----------} \quad \text{(iii)}$$

Equation (iii) has three parameters
(a) Ground State Moment of Inertia (θ_0)
(b) Softness Parameter (σ)
(c) Stiffness Constant (C)

Two of the parameters Ground State M I (θ_0) and Stiffness Parameter (C) are same as 'I_0' and 'c' in original VMI model, while the Softness Parameter (σ) is different parameter which represents the softness of a particular nucleus. The first term in right hand side of equation (iii) has two parameters (i.e. θ_0 & σ), while the second term has three parameters (i.e. C, θ_0 & σ). The parameters θ_0 and σ are calculated by following the conditions given in reference [9].

In the present work we study the second term of equation (iii) i.e. (Potential Energy Term, $E_{pot.}$) with spin 'J' of the nucleons and with ground state of moment of inertia and with nuclear softness parameters of different nuclei of quadrant-I.

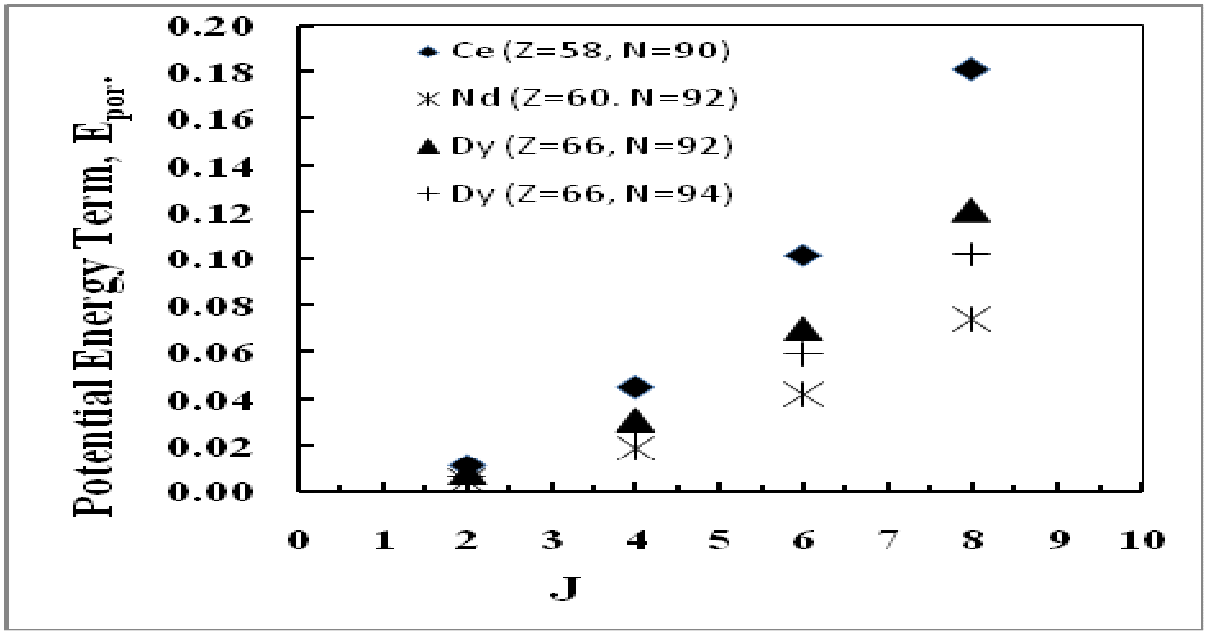

Fig.-(1): Variation of Potential Energy Term ($E_{pot.}$) with Spin (J).

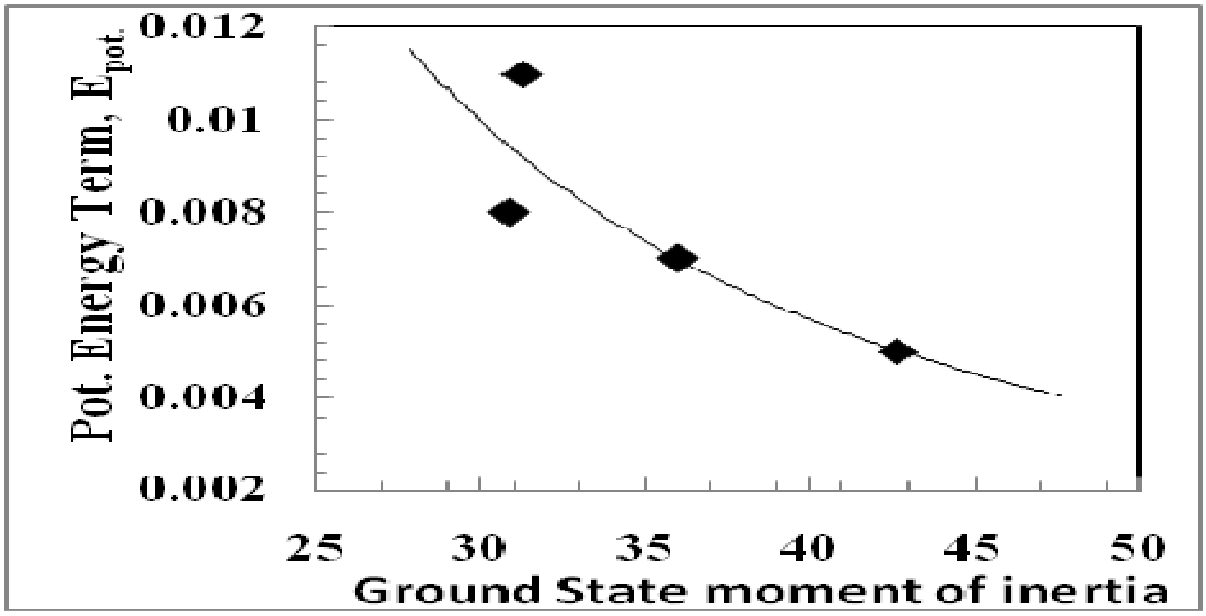

Fig.-(2): The Variation of Potential Energy Term ($E_{pot.}$) with Ground State Moment of Inertia.

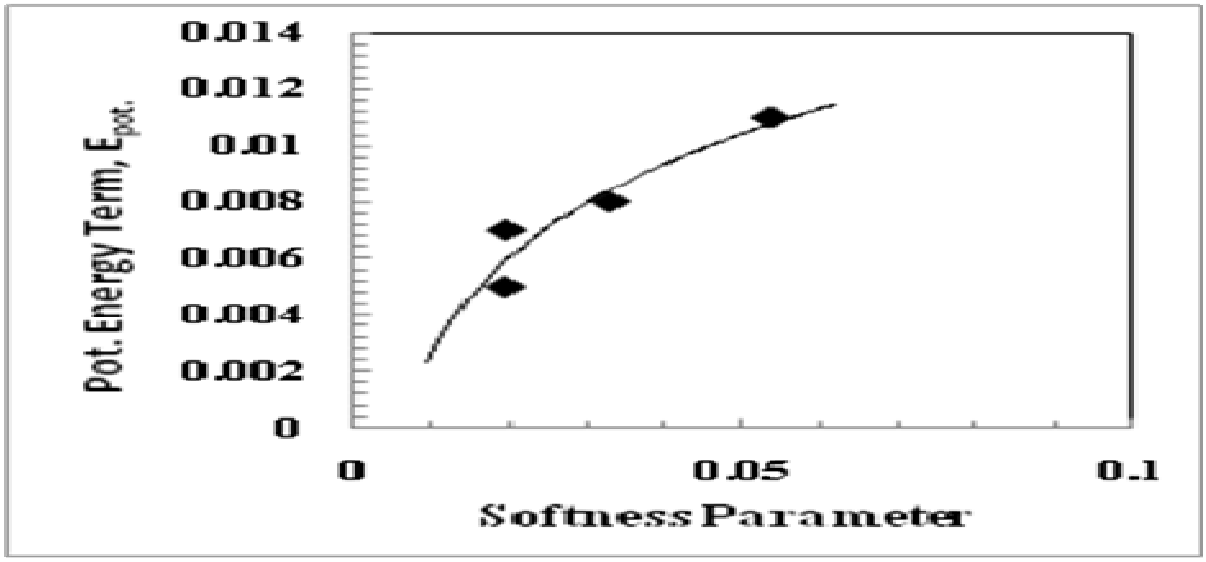

Fig.-(3): The Variation of Potential Energy Term ($E_{pot.}$) with Nuclear Softness Parameter.

RESULTS AND DISCUSSION

(a) Dependence of E_{pot} on Spin J

The variation of potential energy term for the different even-even nuclei in the region of I-quadrant based on the valence particle and hole pairs consideration [8]{Ce (N=90), Nd (N=92), Dy (N=92) & Dy (N-94)} with spin (J) has been shown in fig. (1). It is clear from fig. (1), that the value of potential energy term is increasing almost linear with increasing spin (J) for all the nuclei. In case of Dy (D=92) the potential energy term is less than that of Dy (N=94) for a particular value of spin (J).

(b) Dependence of E_{pot} on Ground State Moment of Inertia

In figure (2) the variation of potential energy, $E_{pot,}$ with ground state moment of inertia is shown. It is apparent from this figure that the potential energy term is decreases almost exponentially with ground state moment of inertia.

(c) Dependence of E_{pot} on Nuclear Softness Parameter

In figure (3) the variation of potential energy, E_{pot}, with nuclear softness parameter has shown. The nuclear softness parameter of nuclei is increases with nuclear softness parameter in the same way as that of decreases with ground state moment of inertia.

Acknowledgement

Hardik P. Trivedi. is very grateful to the Dr. Ajay Kumar Mahur and Dr. R. K. Saraswat Associate Professor, Department of Applied Science, VCTM, Aligarh for fruitful discussion and proper guidance.

REFERENCES

[1] M. Sakai, Quasi-Bands (Institute for Nuclear Study, University of Tokyo, Tokyo, **1982**)
[2] M. A. J. Mariscotti, G. Scharff-Foldhaber and B. Buck, Phys. Rev. 178, 1864 (**1969**)
[3] R. K. Gupta, Phys. Lett. 36B, 173 (**1971**)
[4] M. Satpathy and L. Satpathy, Phys. Lett. 34B 377 (**1971**)
[5] D. Bonatsos and A. Klein, Phys. Rev. C29, 1879 (1984), Atomic data and Nuclear Data Tables 30, 27 (**1984**)
[6] A. Klein, Nucl. Phys. A 347, 3(**1980**)
[7] R. K. Gupta, *et al;* Nucl. Data for Sci. & Tech. (Mito, Japan), 729 (**1988**)
[8] J. S. Batra, *et.al;* Phys. Rev. C43, 1725(**1991**)
[9] J. B. Gupta, *et al;* Phys. Rev. C56, 6, 3417 (**1997**)
[10] J. H. Hamilton, *et.al;* Bull. Am. Phys. Soc. 32, 2130 (**1987**)

Current Advances and Applications of Microbial Bio-Fuel Cells

R.C.Sharma* and Naveen Kumar
Delhi Technological University
Shahbad Daulatpur, Bawana Road, Delhi-110042 (India)

*Corresponding Author Email: rcsharma_263@yahoo.co.in

ABSTRACT:

Microbial bio-fuel cell technology has a immense potential and will emerge gradually as an essential element for renewable power generations, wastewater treatment process, fuel-batteries for automobile, self powered medical implants and environment sensors, bio-remediation and many more applications. In a microbial bio-fuel cell (MBFC), microbes/ enzymes are used as a catalyst to convert chemical energy, available in a bio-convertible substrate, directly into electricity. The main focus of MBFC research is on the study of microbe/ enzyme, the substrate and the mediator. ***E. Coli, Nocardia, Pseudomonas methanica,*** C. ***butyricum, Lactobacillus plantarum. Streptococcus lactis, Erwinia dissolvens, Proteus vulgaris, Bacillus subtilis, Alcaligenes eutrophus, Enterobacter aerogenes and Desulfovibrio desulfuricans*** microbes have been widely used in MBFCs**.** Carbohydrates (glucose, sucrose, cellulose, starch), volatile fatty acids (formate, acetate, butyrate), alcohols (ethanol, methanol), amino acids, proteins and sulfides or acid mine drainages have been used as energy source (substrates) and MB, HNQ, TH, MelB and NR have been used as mediators. Today, the major problems before MBFCs research are- short active lifetimes, low power densities, low efficiency, to engineer optimal functioning of microbes, electron transport between the microbes and the current collector, multi- microbes systems, and standardized characterization protocols. In this paper, an effort has been made to compile the R&D outcome of large number of researchers on different microbes, substrates and mediators being investigated in the last five decades.

INTRODUCTION:

How would you feel if your cell phone battery is instantly charged by the addition of a small amount of glucose or sucrose? Implant a power source into a human body and get infinite supply of power for heart pacemaker, hearing devices, artificial kidneys, insulin pumps, gluco-sensors and other micro-medical devices. Power a robot using fruits, sugars, meat and insects. Treat the waste water in to potable water and simultaneously generate electricity, and many more innovations. All this can be made possible by a bio-fuel cell; this being feasible since fuel, oxidant, and by-products are harmless and often biologically endogenous. Galvani first observed that an electrical action can induce a biological reaction. The converse is also true and in this way biological processes can be used to generate electricity. Bio-fuel cells were first introduced in 1911 when Potter[1] cultured yeast and E. Coli cells on platinum electrodes. A variety of microbe/ bacteria, substrates and mediators were used to generate electricity in microbial bio-fuel cells. Cohen[2] in 1931 developed a microbial fuel cell battery capable of generating potentials of order of ~35V. But it was not until 1962 that a bio-fuel cell based on enzyme glucose oxidase to oxidize glucose at the anode was invented and used to generate current. More recently, there has been an upsurge in research in bio-fuel cells[3-21], an alternative energy devise based on bio-electro-catalysis of agri-based, biological and organic substrates by enzymes or microorganisms. A bio-fuel cell generates electricity from carbohydrates utilizing bacteria/ enzymes as the catalyst. The basic components of bio-fuel cell are- an anode, a cathode, and a separator. However, the bio-catalysts used are oxido-reductase enzymes or bacteria. These bio-catalysts can catalyze oxidation-reduction reactions. Since these bio-catalysts are selective electro-catalysts, the separator could be an electrolyte solution, gel, or polymer. The bio-fuel cell incorporates an anode consisting of sugar-digesting microbe/ enzyme and mediator, and a cathode comprising oxygen-reducing microbe/ enzyme and mediator, either side of a cellophane separator. The anode extracts electrons and H^+ ions from the sugar (glucose) through enzymatic oxidation as follows:

$$\text{Glucose} \longrightarrow \text{Gluconolactone} + 2H^+ + 2e^- \quad (1)$$

The H^+ ion migrates to the cathode through the separator, where the H^+ ions and electrons absorb oxygen from the air to produce water:

$$O_2 + 4H^+ + 4e^- \longrightarrow 2H_2O \quad (2)$$

Figure 1 shows a schematic of a generic bio-fuel cell oxidizing glucose as fuel at the bio-anode and reducing oxygen to water at the bio-cathode. During this electrochemical reaction, the electrons pass through the outer circuit to generate electricity. It is interesting to note that the catalytic four-electron reduction of oxygen to water could take place at an enzyme electrode in neutral solution. Due to the selective reactivity of the enzymes at each electrode, no cross reaction occurs between the anode and cathode.

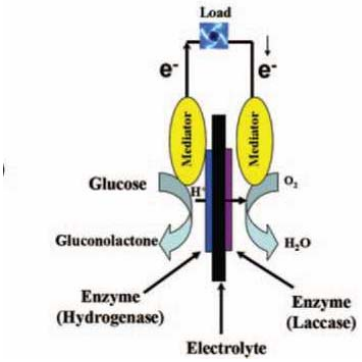

Fig. 1. Schematic presentation of a bio-fuel cell[22].

Over the last 5 decades, many improvements have been made in bio-fuel cells and these are the subject matter of several review articles[11,12,15,16]. However, there are several major issues to be considered in respect of bio-fuel cells for further improvement. Short active lifetimes, low power densities, and low efficiency of bio-fuel cells can be solved by new strategies for immobilization and stabilization of the bio-catalysts; for engineering of bio-catalyst to function optimally at electrode surfaces; for electron transport between the bio-catalyst and the current collector; for optimization of multi- bio-catalyst systems, and for developing standardized characterization protocols for the bio-fuel cell research community at large.

Dr Serge Cosnier and his team [23] at the Joseph Fourier University of Grenoble have built a bio-fuel cell that uses glucose and oxygen at concentrations found in the human body to generate electricity. They are the first group in the world to demonstrate their device working while implanted in a living animal. Recent advances by the Heller group have shown that bio-fuel cells can be implanted and can continue to function in a living organism. For *ex vivo* applications, many fuels are being considered, from alcohols to sugars.

Szczupak ***et al***. [24] reported that bio-fuel cells implanted in living clams were able to generate electrical power using physiologically produced glucose as fuel. The living batteries generated open circuitry voltage (Voc), short circuitry current (Isc) and maximum power (Pmax) of ca. 800 mV, 25 μA, 5.2 μW and ca. 360 mV, 300 μA, 37 μW for the serial and parallel connections of 3 "electrified" clams, respectively. Pan ***et al***.[25] designed a nano-wire-based bio-fuel cell (NBFC) which consists of a single proton conductive polymer nano-wire for converting chemical energy from bio-fluids into electricity, using glucose oxidase and laccase as catalyst. This innovative single nano-wire bio-fuel cell is capable of producing an output which is sufficient to drive pH, glucose or photon sensors. The high output power, low cost and easy fabrication process, large-scale manufacturability, high 'on-chip' integrability and stability demonstrates its great potential for *in vivo* bio-sensing. The NBFC can be accomplished at nano/micron scale, and the bio-fuel cell of a single nano-wire generates an output power as high as 0.5-3 μW in glucose solution, in human blood and the juice of a watermelon. It has been integrated with a set of nano-wire based sensors for performing self-powered sensing.

Cinquin ***et al*** [24] reported the first functional implantable glucose based bio-fuel cell (GBFC), working in the retroperitoneal space of freely moving rats. The breakthrough relies on the design of a new family of GBFCs, characterized by an innovative and simple mechanical confinement of various enzymes and redox mediators: enzymes are no longer covalently bound to the surface of the electron collectors, which enables use of a wide variety of enzymes and redox mediators, augments the quantity of active enzymes, and simplifies GBFC construction. The most efficient GBFC was based on composite graphite discs containing glucose oxidase and ubiquinone at the anode, polyphenol oxidase (PPO) and quinone at

the cathode. PPO reduces O_2 into water, at pH 7 and in the presence of chloride ions and urates at physiological concentrations. This GBFC, with electrodes of 0.133 mL, produced a peak specific power of 24.4 $\mu W\ mL^{-1}$, which is better than pacemakers' requirements and paves the way for the development of a new generation of implantable artificial organs.

Bio-fuel cells are expected to revolutionize medical implants, from sensors and drug delivery devices to entire artificial organs. A new range of artificial, electrically-powered organs are now under development, including hearts, kidneys, and bladder sphincter, and work has begun on fully-functioning artificial limbs such as hands, fingers, and even eyes. But they need electricity to run. Batteries are good enough for implants but they run out fast and have a fixed lifespan- normally 5 years after implantation. One study in the US found that one in five 70 year-olds implanted with a pacemaker, survived for another 20 years - meaning this group needed around 3 additional operations after the initial implant, just to replace the battery. Each operation is accompanied by the risk of complications of surgery, not something anybody should have to face if it is avoidable. Other devices such as artificial kidneys, limbs or eyes, would have such high energy demands that users would have to change their power source every few weeks to keep them working. It is simply impractical to use batteries in these devices.

Scientific research focusing on the technical challenges[3, 22] surrounding a bio-fuel cell has been taken as a team work by the University Professors in US and other developing countries. These cells will run on simple sugars or similar compounds. Researchers are turning to the natural world in an effort to see how sugars are oxidized by animals to produce power.

ADVANTAGES OF BIO-FUEL CELLS [26-28]:

- Bio-fuel cells replace expensive precious metal catalysts with low cost, renewable enzymes for the catalysis of redox-reactions.
- Bio-fuel cells utilize bio-waste, alcohols, glucose, and carbohydrates etc which, theoretically, give high energy. For example, if a molecule of glucose is oxidized completely, there are 24 electrons available for current generation.

- Bio-fuel cells are nontoxic and environmentally friendly. Glucose and other bio-molecules used in a bio-fuel cell are produced as a by-product of photosynthesis, and thus make the total process carbon neutral.
- Bio-fuel cells have ability to metabolize glucose and other carbohydrates present in human body fluids and the enzymes are biocompatible, which allow bio-fuel cells to implant into a human body and use them as power sources for pacemakers and other implants.
- Wide range of available enzymes with high catalytic activities superior to that of platinum, allow working in different experimental conditions.
- Substrate specificity of enzymes eliminates the need of existing expensive polymer electrolyte membranes.
- Bio-fuel cells do not require nutrients or biomass acclimation and the whole process can be controlled more easily.
- Bio-fuel cells produce higher power output densities.
- Bio-fuel cells can be easily engineered for a miniaturized system.
- Bio-fuel cells have very long life. An implanted bio-fuel cell would produce electrical current as long as a person is ticking.
- In a bio-fuel cell, a hydrogenase-coated anode and a laccase-coated cathode can be placed in the same compartment, meaning that, there is no need to separate the fuel and oxidant.
- In a bio-fuel cell, enzymes can also be tolerant of chemical species that are usually considered as poisons to conventional catalysts. For example, the membrane-bound hydrogenases from *Ralstonia eutropha* H16 and *Ralstonia metallidurans* CH34 can oxidise H_2 even in an excess of CO.

Bio-fuel cell could be classified into many types based on fuel containment, fuel and catalyst sources, origin of the catalytic enzymes and the method of electron transfer between reaction site and electrode. In this paper an attempt has been made to compile R&D findings of different researchers on the types of bacteria, substrates and mediators being studied in respect of microbial bio-fuel cell(MBFCs), and also assess the possible applications and advantages of different bio-fuel cells.

MICROBIAL BIO-FUEL CELLS:

A microbial bio-fuel cell (MBFC) converts chemical energy, available in a bio-convertible substrate, directly into electricity. To achieve this, bacteria are used as a catalyst to convert substrate into electrons. Bacteria are very small (size=1 μm) organisms which can convert a huge variety of organic compounds into CO_2, water and energy. The micro-organisms use the produced energy to grow and to maintain their metabolism. However, by using a MBFC one can harvest a part of this microbial energy in the form of electricity. A MBFC consists of an anode, a cathode, a proton or cation exchange membrane and an electrical circuit.

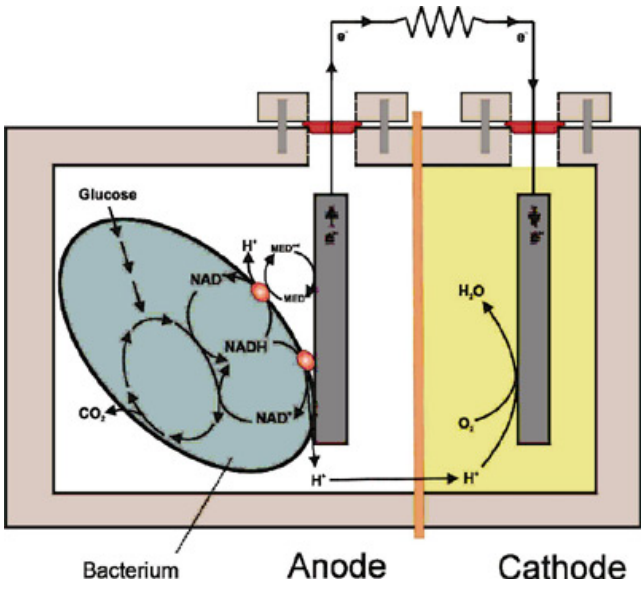

Fig. 2. Layout of a microbial bio-fuel cell [29].

In the anode compartment, the bacteria convert a substrate such as glucose, carbohydrate, acetate into CO_2, protons and electrons. Under aerobic conditions, bacteria use oxygen or nitrate as a final electron acceptor to produce water. However, in the anode of a MBFC, no oxygen is present and bacteria need to

switch from their natural electron acceptor to an insoluble acceptor, such as the MBFC anode. Due to the ability of bacteria to transfer electrons to an insoluble electron acceptor, one can use a MBFC to collect the electrons originating from the microbial metabolism. The electron transfer can occur either via membrane-associated components, soluble electron shuttles or nano-wires. The electrons then flow through an electrical circuit with a load or a resistor to the cathode. The potential difference (Volt) between the anode and the cathode, together with the flow of electrons (Ampere) results in the generation of electrical power (Watt). The protons flow through the proton or cation exchange membrane to the cathode. At the cathode, an electron acceptor is chemically reduced. Ideally, oxygen is reduced to water. To obtain a sufficient oxygen reduction reaction (ORR) rate a Platinum-catalyst has to be used. However, many researchers have tried to use other non-noble metal catalyst.

ENERGY SOURCES FOR MBFCs:

Energy source (a substrate) is important for any biological process as it serves as carbon or nutrient or raw material for the production of energy. The efficiency and economic viability of converting organic wastes to bio-energy depend on the characteristics and components of the waste material, especially the chemical composition and the concentrations of the components that can be converted. Many organic substrates have been investigated as possible energy sources to generate electricity using MBFCs. These include carbohydrates (glucose, sucrose, cellulose, starch), volatile fatty acids (formate, acetate, butyrate), alcohols (ethanol, methanol), amino acids, proteins and even inorganic components such as sulfides or acid mine drainages. An exhaustive list of different substrates (Table 1) studied in MBFCs has been given in the review paper of Pant D. et. al.[30] published in Bioresource Technology in 2009. In order to scale new MBFC components, reactor designs or operational conditions, acetate is commonly used as a substrate because of its inertness towards alternative microbial conversions (fermentations and methanogensis) at room temperature. Using a single-chambered MBFC, Liu ***et al***. [31] reported that the power generated with acetate (506 mW/m^2, 800 mg/L) was up to 66% higher than that produced with butyrate (305 mW/m^2, 1000 mg/L). Very recently, Chae ***et al.*** [32] compared the performance of four different substrates in terms of CE and power output. Acetate-fed MBFC showed the highest CE (72.3%), followed by butyrate (43.0%), propionate (36.0%) and glucose (15.0%). Also, when acetate was compared

with a protein-rich wastewater as substrate in MBFC, the MBFC based on acetate-induced consortia achieved more than 2-fold maximum electric power, and one half of optimal external load resistance compared to the MBFC based on consortia induced by a protein-rich wastewater. However, the protein-rich wastewater being a complex substrate provides the possibility of enriching more diverse microbial community than acetate. Having a more diverse microbial community helps to use various substrates or to convert complex organics to simpler compounds such as acetate which is used as electron donor for current production. This results in high Coulombic efficiencies of up to 98% and high power outputs of up to 115 $W.m^3$ for mixed anodophylic cultures.

TABLE 1(TO BE INSERTED HERE)

The use of a pure or single substrate allows study of metabolic processes and conversion products during the microbial conversion; it is not realistic to power full scale MBFCs with pure substrates from economic point of view. In that perspective, the use of second generation bio-fuels or organic waste is highly promising because it allows to combine the actual treatment of the waste with the generation of energy.A range of more complex organics, containing a large variety of different readily and non-readily degradable molecules such as domestic wastewater[33], brewery wastewater[34], paper recycling wastewater[35] or the effluent of anaerobic digesters [36] have been demonstrated to generate electrical power in MBFCs. However, the power outputs using wastewater are 10 times lower compared to pure substrates, and the composition of the wastewater is strongly affecting the power output of MBFCs. Rabaey ***et al.***,[29] found that spiking the wastewater with acetate resulted in an increase of the power output, indicating that the higher the rapidly biodegradable fraction within the wastewater is, the higher the power output will be. The type of substrate fed to a MFC potentially has an impact on the structure and composition of the microbial community. The more reduced the substrate is, the more energy there is available to divide across the community. This may lead to an increase of the possible interactions and niches. Rabaey ***et al.***[10] showed that microbial communities in fuel cells evolve specifically, resulting in an optimized bioelectrocatalyzer. Both membrane-bound electron transfer and transfer through soluble redox mediators were observed for the bacterial species analyzed. The bacteria facilitated the extracellular electron transfer and reduced the overpotential at the anode, thereby increasing the power output. The fact that bacteria can produce, and moreover use, redox mediators as electron shuttles enables them to thrive in

a microbial fuel cell. While the redox conditions in a microbial fuel cell are disadvantageous for an aerobic bacterial species, such as *P. aeruginosa*, this species can become dominant. In another study, Rabaey[29] reported that no significant difference exist in bacterial growth by addition of different substrates.

BACTERIA FOR MBFCs:

Logan and Regan[15, 37] observed that the bacterial communities that develop show great diversity, ranging from primarily δ-Proteobacteria that predominate in sediment MBFCs to communities composed of α-, β-, γ- or δ-Proteobacteria, Firmicutes and uncharacterized clones in other types of MFCs. Different scientists have used different bacteria in MBFC which include ***E. Coli, Nocardia, Pseudomonas methanica,*** C. ***butyricum, Lactobacillus plantarum. Streptococcus lactis, Erwinia dissolvens, Proteus vulgaris, Bacillus subtilis, Alcaligenes eutrophus, Enterobacter aerogenes and Desulfovibrio desulfuricans.*** The studies of anode bio-film community composition have revealed the persistence of phenotypically uncharacterized bacteria with wide phylogenetic diversity that contributes in unknown ways to the bio-film ecology. Ecological studies show that competition for a limited resource leads to a successive maturation of the community, beginning with early colonizers and invaders that give way to the final dominant organisms. The limited surface area of a non-corrosive carbon electrode in an MFC might represent a unique opportunity to study the effect of limited space for cell respiration on microbial growth and competition.

Logan & Regan[15, 37] advocated that understanding how the microbial ecology of electricity producing communities develops and changes over time, in terms of colonization, invasion and succession, therefore opens the door on a new world of exploration and insight into complex microbial communities and the evolution of life. At the same time, it might also open the door to a new method for renewable and sustainable energy production.

Davis and Yarbrough[38] showed that electrical energy can be produced using both microorganisms and enzymes. The microorganisms used in the MFC were ***Nocardia*** and ***Escherichia coli*** and the enzyme used was glucose oxidase (GOx), a dimeric protein that catalyses the oxidation of glucose

to hydrogen peroxide and D-glucono-δ-lactone. They began their study using a fuel cell configured with GOx, presumably containing bound flavin adenine dinucleotide (FAD), glucose, buffer, and a Pt-sheet electrode in the N_2-purged anodic compartment. The cathodic compartment, containing a Pt-sheet electrode and buffer, was saturated with O_2. GOx catalyzes the oxidation of p-D-glucose to 6-D-gluconolactone with the concomitant reduction of FAD to $FADH_2$ (eq. 3). Under biological conditions, $FADH_2$ is reoxidized by dioxygen (eq. 4), but because the anodic chamber had been purged to remove dioxygen, this reaction did not occur. Methylene blue (MB) was added to the anode compartment both to reoxidize FADH2 and to shuttle the reducing equivalents made available by the enzymatic reaction to the anode (eqs. 5 and 6).

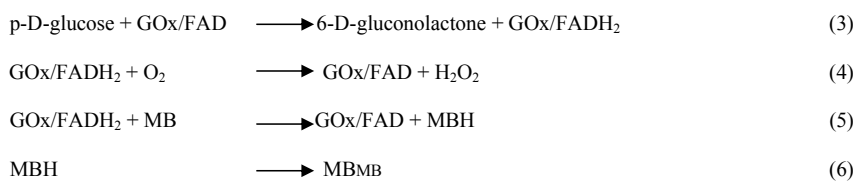

$$\text{p-D-glucose} + \text{GOx/FAD} \longrightarrow \text{6-D-gluconolactone} + \text{GOx/FADH}_2 \quad (3)$$

$$\text{GOx/FADH}_2 + \text{O}_2 \longrightarrow \text{GOx/FAD} + \text{H}_2\text{O}_2 \quad (4)$$

$$\text{GOx/FADH}_2 + \text{MB} \longrightarrow \text{GOx/FAD} + \text{MBH} \quad (5)$$

$$\text{MBH} \longrightarrow \text{MB}_{\text{MB}} \quad (6)$$

In the absence of MB, the fuel cell yielded no electricity. Voltage(V_c) at open-circuit was 0.28 V and voltages between 0.075 to 0.09 V could be maintained under a load of 1 **kn.** Because the glucose-GOx-MB system under a N_2 atmosphere generated reduced MB that produced electricity, the authors reasoned that a facultative anaerobe would also produce measurable current. ***Escherichia coli*** were added to the anode compartment in place of GOx, and a V_c of 0.625 V at open-circuit was obtained. Under a 1 ki2 load, V_c could be maintained at 0.52 V for over 1 h. The use of ethane as fuel was attempted using an ethane-oxidizing ***Nocardia*** as catalyst. No current was produced even in the presence of MB. When glucose was substituted for ethane, metabolic activity increased. An open-circuit voltage of 0.3 V and a maximum current of 2 mA under a 1 **kn** load was reported. This value of maximum current seems unlikely, given the upper limit of 0.3 mA imposed by Ohms law (V = IR).

A unique MBFC that utilized methane as fuel was demonstrated by van Hees [39]. The anodic compartment, containing ***Pseudomonas methanica,*** l-naphthol-2-sulfonate indo-2,6-dichlorophenol (NSIDCP), and a platinum anode, was purged of O_2 and supplied with methane. The cathode compartment housed a platinum cathode in a sterile medium and was supplied with O_2 in the form of air. Inclusion of NSIDCP in the anode compartment had no effect on Vceii at open-circuit, suggesting that this dye did not

function as an electrochemical mediator. This conclusion was further supported by enclosing the microorganisms in dye-permeable dialysis tubing and observing that the value for V_C at open-circuit was established only very slowly even in the presence of NSIDCP; this observation suggests that microbial contact with the anode was necessary for electron transfer. The power density was low 0.98 (iW cm^{-2}) and prolonged open-circuit conditions or high current drain were observed to be detrimental to the obligate aerobe used in this fuel cell. The explanation given for these observations was elaborate and the reader is referred to the original text. In summary, the authors concluded that bio-fuel cells utilizing obligate aerobes are best suited to functioning under moderate current drain.

Suzuki ***et al.*** [40-44] studied several microorganisms for their production of H_2 from glucose**.** Of the organisms studied, ***Clostridium butyricum*** IF03847 produced H_2 at the highest rate and was therefore used to supply H_2 to the anode compartment of a conventional fuel cell. Immobilization of the microorganism in a gel of agar-acetylcellulose both stabilized the H_2-producing system and increased the rate of H_2 production. For every mol of glucose consumed, 0.6 mol of H_2 and 0.2 mol of formic acid were produced. Two kg of wet gel containing -200 g of wet microorganism produced 40 ml (1.7 mmol) of H_2 per min, equivalent to ~5 A.

Four different fuel cell configurations were studied. One configuration, a fuel cell stack of five fuel cells using Pt- blackened Ni-gauze anodes and Pd-blackened Ni-gauze cathodes, was operated at room temperature. H_2 was passed from a 5L reservoir containing 2 kg of immobilized whole cells to the anode compartments of the fuel cell stack at a rate of 40 ml min^{-1} while O_2 was passed through the cathode compartments. The fuel cell system (H_2 producing microbial reservoir and five fuel cells) was operated for 7 days and maintained a current of 0.8 A at 2.2 V. The poor current efficiency was not noted.

A second configuration used ~3 kg of immobilized microorganisms in a 200 L fermentation vessel containing 150 L of molasses. The biogas produced, containing both H_2 and carbon dioxide, was passed into the anode compartment of a phosphoric acid fuel cell stack (two fuel cells in parallel operated at 200 ^{0}C) at a rate of 400-800 ml min^{-1} while O_2 was passed into the cathode compartment at a rate of 1-1.5 L

min^{-1}. The open-circuit voltage was between 0.9-0.93 V and a stable current of 10-14 A was maintained for four hours with a power output of 9-13 W.

Habermann and Pommer[45] demonstrated a microbial fuel cell utilizing the sulfate-reducing microorganism, ***Desulfovibrio desulfuricans.*** Sulfide, produced from the metabolic reduction of sulfate, was oxidized at the anode using air as the terminal oxidant according to equations 7-9:

$$SO_4^{2-} + 8\ H^+ + 8\ e^- \longrightarrow S^{2-} + 4\ H_2O \quad (7)$$

$$S^{2-} + 4\ H_2O \longrightarrow SO_4^{2-} + 8\ H^+ + 8\ e^- \quad (8)$$

$$2\ O_2 + 8\ H^+ + 8\ e^- \longrightarrow 4H_2O \quad (9)$$

The authors listed glucose, fructose, cane sugar, starch, and hydrocarbons as the substances selected to provide the reducing equivalents required to convert SO_4^{2-} to S^{2-}, and to meet the nutrient requirements of the microorganism.

The fuel cell consisted of an anode fabricated from porous graphite impregnated with cobalt hydroxide. In the presence of sulfate-reducing microorganisms, cobalt hydroxide was converted into a cobalt oxide/ cobalt sulfide mixture. As a result, reducing equivalents in the form of sulfide were concentrated within the porous network of the graphite anode during conditions of open-circuit. The cathode was fabricated from graphite activated with iron-phthalocyanine [Fe(phthal)]. The electrolyte used was a solution containing between 0.1 and 5% by weight sodium sulfate, 0.1% by weight urea and dextrose, and trace elements. The highest percentage of sulfate reduction by ***Desulfovibrio desulfuricans*** occurred when using 0.5% by weight sodium sulfate (pH 8.5) electrolyte. Three fuel cells were connected in series and gave an open-circuit voltage of 2.8 V. The current level after one day of operation was < 1 mA.

MEDIATOR FOR MBFCs:

Ieropoulus ***et al.***[46-48] studied five different synthetic mediators in MFCs to investigate their performance in both electron extraction and speed of response. Table 2. shows the average power output for the five mediators in MBFCs over 5 days. MB produced the highest average power whilst NR produced the lowest, approximately, 40% that of MB. The final pH values were close to neutral with the exception of MelB, which was more acidic at pH 6.2. The calculated values for *R*INT showed that MB had the lowest internal resistance value whilst NR had the highest.

Table 2. Averaged power output for MFC for five different mediators

Mediator	P_{ave} **(μW)**
MB(Methylene blue)	31.77
HNQ(2-hydroxy-l,**4**-naphthoquinone)	29.83
TH(Thionine)	28.84
MelB(Meldola's blue)	26.12
NR(Neutral red)	12.73

Delaney, ***et al.***,[49] studied fuel cell performance using different microorganism-mediator-substrate combinations**.** $V_C$eii at open-circuit was predicted to range from 0.9-1.2 V based on the difference between E° of the different mediators used in the anode compartment and E° of the potassium ferricyanide used in the cathode compartment. V_C, however, was found to be 0.2-0.4 V lower than predicted, indicating activation overpotentials at the electrodes. The fuel cell that gave the best performance contained ***Proteus vulgaris,*** thionine (TH+), and glucose in the anodic compartment. Typical current-voltage curves were obtained by discharging the fuel cell through a range of loads. The coulombic yield of the fuel cell was determined by integration of the area under the current-time curve. (Coulombic yield is the total number of coulombs passed through the fuel cell, as determined by integration of the current-time curve in units of amp-s = coulombs, relative to the theoretical number that might be obtained by complete conversion of the reactants to products). Coulombic yields of 32-62% were obtained based on the theoretical maximum coulombic equivalent for complete oxidation of glucose in accordance with equation 5. (The theoretical

maximum coulombic equivalent of glucose is 24 mol electron mol^{-1} glucose x 96,487 C mol^{-1} electron = 2.3 x 10^6 C mol^{-1} glucose):

$$C_6H_{12}O_6 + 6H_2O \longrightarrow 6CO_2 + 12H^+ + 24e^- \quad (10)$$

Thurston ***et al.*** [50] argue that if fuels such as carbohydrates are to be used, microorganisms will be more economical catalysts than individual enzymes because the multi-step oxidations involved with complex fuels would require multiple, expensive enzyme purifications***. Proteus vulgaris*** was chosen as the biocatalyst for glucose oxidation and ^{14}C-labeled glucose was used as fuel to establish the distribution of products. The amount of CO_2 evolved from the oxidation of glucose was determined by scintillation methods and a sodium hydroxide trap. Conversion of glucose to CO_2 was 40-50%, and coulombic yields indicated near unit current efficiency (based on 50% conversion of glucose). The most significant loss in energy was from the conversion of 30% of glucose to acetate; it is possible that this side reaction might be avoided by metabolic or genetic modification of the microorganism.

Bennetto ***et al***. [51-54] used sucrose as fuel in a TH^+ mediated microbial biofuel cell containing ***Proteus vulgaris*** as biocatalyst [44]. Equation 11 gives the stoichiometry of complete oxidation of sucrose.

$$C_{12}H_{22}O_{11} + 13\ H_2O \longrightarrow 12\ CO_2 + 48\ H^+ + 48\ e^- \quad (11)$$

The biofuel cell was discharged through a resistance of 100 n after the addition of various amounts of sucrose. The amount of CO_2 evolved from the anode compartment confirmed near complete oxidation of sucrose. The cell current peaked at 3.5 mA and the production of electricity from the oxidative conversion of sucrose was >95%, determined from both coulombic yield and CO_2 evolution. At higher concentrations of sucrose, the buffering capacity of the anodic medium was exceeded due to acid formation. Preliminary tests using molasses as fuel suggested that >70% of the carbohydrate was oxidized. Neither the open-circuit voltage nor electrode size were given.

Since TH^+ has frequently been used as a mediator in biofuel cells, Lithgow ***et al.*** [55] prepared sulfonated derivatives of thionine to determine the effect of ring substitution

on mediation of electron transfer from ***E. Coli*** to the anode. Changing from TH^+ to 2-sulfonated thionine (DST-1) and 2,6-disulfonated thionine (DST-2) resulted in an increase in the efficiency of mediated electron transfer. This increase was reflected by changes in cell current under a 560 n load: 0.35 mA for TH^+, 0.45 mA for DST-1, and 0.6 mA for DST-2. The low efficiencies of the fuel cells operating with TH^+ and DST-1 were attributed to interference with electron transfer by adsorption of mediator to the microbial membrane, and a resulting decrease of the rate of oxidation of glucose at that membrane.

The authors [55] also compared the thionine derivatives to ferric cyclohexane-1,2-diamine-N,N,N',N'-tetraacetic acid (FeCyDTA) and found that lower concentrations of both TH^+ and the sulfonated derivatives gave better mediation than the iron chelate. The significant inference from this report was that the power output of microbial biofuel cells could be improved by introducing hydrophilic groups into several mediators.

Vega ***et al.*** [56] studied mediation using several ferric chelates ~ FeCyDTA, ferric diethylenetriamine pentaacetic acid (FeDTPA), ferric ethylenediamine diacetic acid dipropionic acid (FeEDADPA), ferric ethylenediamine tetraacetic acid (FeEDTA), and ferric triethylenetetramine hexaacetic acid (FeTTHA) ~ with microbial biofuel cells containing ***Lactobacillus plantarum. Streptococcus lactis,*** and ***Erwinia dissolvens). Lactobacillus plantarum*** and ***Streptococcus lactis*** grow on dairy products and ***Erwinia dissolvens*** grows on coffee wastes. The objective of this study was to determine which microorganism/mediator combination would be the most efficient in a microbial biofuel cell. Fuel cells using ***Erwinia dissolvens*** mediated with FeCyDTA ran for five consecutive days, with coulombic yields between 80% and 90%. ***Lactobacillus plantarum*** and ***Streptococcus lactis*** did not produce any significant electrical output with any of the ferric chelates. The main

results from this study were: 1) different microorganisms, using the same mediators and the same amount of fuel, gave different coulombic yields, 2) biofuel cells using ***E. dissolvens*** as the biocatalyst gave higher coulombic yields than those using ***E. Coli.*** The interaction of the microbial membrane with the mediator was suggested to be the source of these effects.

Akiba ***et al.***[57]studied a microbial biofuel cell that operated at basic pH**.** Operating a fuel cell at basic pH circumvents problems associated with fuel cells operated at neutral pH, such as low ionic conductivity and inefficient operation of the O_2 cathode. Problems associated with CO_2 rejection are significant however, in fuel cells operating at basic pH. Methyl viologen (MV^{2+}), brilliant cresyl blue (BCB), and 2-hyclroxy-l**,**4-naphthoquinone (HNQ) were employed as mediators, either alone or in combination with FeEDTA. The anode compartment was loaded with 35-50 mgo f ***Bacillus W1,*** an unstated amount of mediator, 10 nmol of glucose, and 0.1 M KH_2PO_4 buffer (pH ranging between 10.0-11.0). The fuel cell was discharged through resistors of 300 or 500 n at 35°C. The coulombic yields were highest at pH 10.5 and were > 93.5% with the different mediators. The rate of mediator reduction was however, found to be an order of magnitude slower than that at neutral pH. Because the reduced mediators are less stable at higher operating temperatures, the cells were not examined at such temperatures. No open-circuit voltages were given.

Clostridia are known for their production of dihydrogen, and they have frequently been used in microbial fuel cells. Because ***Clostridia*** are obligate anaerobes, however, both dihydrogen production and microbial growth are oxygen sensitive. Tanisho ***et al.***[58] isolated a strain of the facultative anaerobe, ***Enterobacter aerogenes,*** and found it to produce dihydrogen from glucose**.** This microorganism, grown under aerobic conditions, consumes dioxygen to oxidize organic substrates; under anaerobic conditions, it degrades substrate into dihydrogen.

During operation of the fuel cell, the anolyte was circulated between the microbial reservoir and the anodic chamber of the fuel cell with a peristaltic pump. The reservoir contained microorganisms, phosphate buffer, ammonium sulfate, sodium citrate, magnesium sulfate, and glucose. Peptone, typically included in culture broth, was not included as it often causes microorganisms to adhere to the electrode. The fuel cell was operated with circulating microorganisms for 35 h; nutrients were added after 25 h. Whenever the anode compartment was opened to the atmosphere, the operating voltage would temporarily decrease, but would recover within ten minutes. The microorganisms were reported to produce 11 mol of dihydrogen/L culture/h (equivalent to 269 L dihydrogen/h at 1 atm and 25°C). The researchers assert that if all dihydrogen produced by the 330 ml of culture contained in the reservoir were utilized by the fuel cell (we calculate this to be 3.63 mol dihydrogen/h based on 11 mol of dihydrogen/L culture/h), then 330 mA would be generated. In fact, complete oxidation of 3.63 mol of dihydrogen/h would generate a current of 195 A; some elements of the report are thus internally incompatible. Experimentally, an average current of only 1.4 mA was observed. The authors suggested switching to a molten carbonate fuel cell (MCFC) working on a gas mixture of dihydrogen and carbon dioxide to obtain higher current densities. Operating a MCFC at 650°C has, of course, a substantial cost in energy relative to cells operating close to room temperature.

Sell ***et al.*** [59-60] employed HNQ as a redox mediator in a fuel cell using ***E. coli*** as the biocatalyst for the oxidation of glucose**.** The fuel cell was operated for 10 h under a 250 ***n*** load, during which time $V_C$eii decayed from 250 mV to 75 mV, presumably due to glucose consumption. The mechanism for HNQ reduction was not identified, but it was determined that HNQ is not reduced by isolated ADH. The significant finding in this report was that higher voltage and current density could be

obtained by switching from a glassy carbon (GC) disc anode (0.18 mA/cm^2) to a packed bed of graphite particles (1.3 mA/cm^2 of cross-sectional area of bed); thus the rate of electron transfer at the electrode seemed to limit current.

Table 3. Performance of MBFCs based on both axenic (single bacterial species) and mixed culture systems

	Substarte	Electrode Type	Redox Mediated	I (Current, mA)	P (mW/m^2)	P (W/m^3)
Auxenic Culture						
Proteous Vulgaris	Glucose	Glassy carbon	X	0.8	4.5	18
Erwinia dissolvens	Glucose	Woven Graphite	X	0.7	0.27	n.a.[e]
Proteous Vulgaris	Glucose	Glassy carbon	X	0.7	85	9.0
Shewanella putrefaciens	Lactate	Woven graphite		0.04	0.00032	0.08
Geobactor sulfurreducens	Acetate	Plain Graphite		0.4	13	0.35
Rhodoferax ferrireducens	Glucose	Plain Graphite		0.2	8	0.25
		Woven Graphite		0.57	17	1.7
		Graphite foam		0.4514	33	0.96
Pseudomonas aeruginosa	Glucose	Plain Graphite		0.1	88	8.8
Escherichia coli	Lactate	Woven Graphite[c]	X	3.3	1.2	7.6
		Graphite foam[c]	X	2.6	91	3.6
Mixed Culture						
Mixed, saltwater	Acetate	Plain graphite		0.23	10	n.a.[e]
	S^{2-}/ Acetate	Plain graphite		60	3200	n.a.[e]
Mixed consortium, batch	Glucose	Plain graphite		60[d]	36	206
Activated sludge	Wastewater	Woven graphite		0.2	8	1.6
	Lactate	Woven graphite[b]	X	11	5.3	34
		Plain graphite[b]	X	2.6	788	32

	Waste water	Woven graphite		4.85	26	1.6
	Glucose	Woven graphite		0.9	494	13
Mixed consortium, continous	Sucrose	Granular graphite		6.2	23	47
	Glucose	Granular graphite		5.4	18	37
	Acetate	Carbon paper		1.27	506	13
	Butyrate	Carbon paper		0.46	305	7.6

a No surface data available, value in absolute mW.

b Power output was calculated as average power output where possible because peak power outputs are less representative.

c Mediator immobilized in/on electrode matrix.

d Data as mA/m2 anode surface.

e n.a, unsufficient data available, or not applicable.

APPLICATIONS OF BIO-FUEL CELLS

There are several potential uses of biofuel cells as described below.

1. Power Generation:

Abundance of agri-based feed materials, biological waste & organic compounds, especially high concentrations of sugars e.g. glucose, make it as a very suitable fuel for enzyme-based power production. Dual and single chambered mediator less microbial fuel cells (MFCs) can be readily used for harvesting bio-electricity. A variety of substrates and waste material from the water can be utilized to harvest bio-electric power for the plant. Higher power production can be achieved with bio-film covered anode (graphite). MFCs also use energy much more efficiently than standard combustion engines; an MFC being capable of 50% or more energy efficiency. According to René Rozendal [21, 61] new microbial fuel cells are capable of converting 8 times hydrogen than can be achieved using conventional hydrogen production technologies, keeping energy inputs the same. The advantages of MFCs include: i) it uses a renewable form of energy and would not need to be recharged like a standard battery. ii) it operates in mild conditions, 20°C to 40°C and also at pH of around 7. Power in an MFC can also be derived directly from wastewater, plants & crops, algae & other aquatic plants.

2. Transport

Most of the automobiles are driven either by using fossil fuels or by the power derived from fossil fuels. According to one estimate, in about 200 years from now, vehicles will run on carbohydrate solutions using biological fuel cells. The energy liberated during the complete oxidation of a monosaccharide like glucose or a disaccharide such as sucrose to carbon dioxide and water is about 16 x 10^6 J/kg, which is about 5 kWh of electrical energy and is just less than half the energy that can be obtained from equivalent amounts of fuels such as octane. But the efficiency of burning carbohydrate in biological fuel cells is potentially greater than burning gasoline. It has been calculated [30] that a litre of a concentrated carbohydrate solution could power a car for 25-30 km. The car fitted with a 50L tank could travel over 1000 km without re-fuelling. This offers environment benefits as well as removes the risk associated with transport of large amounts of volatile, flammable fuels apart from the risk of fire following a road traffic accident.

Formatted: Not Highlight

3. Self Powered Medical Implants

Biofuel cells can be employed as an *in vivo* power sources for implantable medical devices such as pacemakers, microdrug pumps, deep brain stimulators or integrated, disposable and subcutaneously implanted glucose monitoring sensor-transmitters.

3.1 Bio-fuel cells for cardiac pacemakers

The most promising application for abiotically catalyzed glucose fuel cell is to implant it in a human body for powering cardiac pacemaker. Based on potentially long-term stable catalysts such as platinum or activated carbon, it is intended to generate electrical energy directly within the human body, using glucose (blood sugar) and oxygen from blood or tissue fluid. This way the necessity for regular surgical replacement of spent batteries could be circumvented. Since these fuel cells typically exhibit power densities of 2-4 cm^{-2}, these are highly suitable to power cardiac pacemakers. The challenges before scientific community are biocompatibility, proper functionality in a body-tissue environment, and long-term stability of the device. The envisioned integration of GFC directly on the casing of a medical implant will circumvent the need for intra-body wire connections or additional surgical procedures to place the fuel cell within the body.

3.2 Bio-fuel cells for Functional Electrical Stimulation**:**

A growing field of "functional electrical stimulation" exists wherein artificially applied electrical current is used to control the nervous system, allowing limited control of leg, arm, and finger movement. The power requirements of such systems greatly exceed that of pacemakers, and power for one such device, along with control signals, is provided by radio-frequency induction via a coil implanted in the patient's chest. Implantable power supplies providing milliwatt-scale power would greatly simplify the design of such systems. Other prosthetic applications such as artificial hearing or vision might also benefit from such a device.

3.3 Bio-fuel cells for implantable sensors

Bio-fuel cells can potentially be run in living systems, since the oxygen and fuel required for their operation can conceivably be taken from their immediate environment, and this offers great potential as power sources within a range of possible implantable medical devices. For example, a biosensor for glu*cose* has been developed utilising a glucose oxidase-based anode and cytochrome *c* cathode to generate electrical current. This process can be used in a biosensor format to give a measurement of the glucose concentration in the range of 1-80 mM. A similar sensor for lactate has also been developed. Other potential uses for miniature fuel cells include power sources for drug delivery systems. Glucose fuel cells based on enzymatic catalyst can be used to power the short-term implantable glucose sensors. Heller ***et al***. presented a glucose fuel cell, consisting of 2 thin graphite fibers serving as anode and cathode. The device exhibited a power density of ~ 430 cm^{-2} under physiological conditions; its projected lifetime is 2 weeks. However, due to instability of the cathode enzyme bilirubin oxidase in human serum, so far no *in-vivo* demonstration of the technology has been reported. Enzymatic glucose fuel cells can also function as sensors. Kakehi ***et al***. [62] have demonstrated that the open circuit voltage of an enzymatic glucose fuel cell can be used to continuously monitor glucose levels. They integrated the fuel cell together with a commercial wireless RF-transmission system and envisioned that with further optimization a subcutaneously implantable continuous glucose monitoring system can be realized.

Mano ***et al***.[27] described a miniature bio-fuel cell operating at 37°C in a glucose containing, aerated, pH 7.2, physiological buffer solution (0.14 M NaCl, 20 mM phosphate). It consists of two 7-μm diameter, 2-cm long, 0.44 mm^2, electrocatalyst-coated, and carbon fibers. Glucose is electrooxidized to gluconolactone on the anode fiber, and dissolved O_2 is electroreduced to water on the cathode fiber. When the cell operates continuously for one week at 37°C, its 1.9 μW power output (50 nW per mm of fiber) at 0.52 V declines to 1.0 μW. In its weeklong operation the cell generates 0.9 J of electrical energy while passing 1.7 C charge. The 1.7 C charge is 100 times higher than the 0.016 C charge that would have been generated at 100% current efficiency through the oxidation of a 7-μm diameter, 2-cm long zinc fiber in a battery. The authors hope that the simple miniature bio-fuel cells will be of value in powering small autonomous sensor/transmitter systems in animals and in plants

The future applications of biological fuel cells will be more attractive. One could construct

molecular biological cells, which could deliver electrical energy to remove tumors and cancerous cells, and could act as drug-delivery systems

4. Self-powered environmental sensors:

Bio-fuel cells could be ideally used to power *wireless sensor networks* (WSN). Applications of WSN are ranging from residential home automation, commercial building developments, to industrial monitoring and control as well as military.

4.1 Unattended ground sensors

Outside the medical sector the use of bio-fuels such as tree-sap has been suggested to power e.g. tree-mountable forest fire sensors. Both, abiotically catalyzed and enzymatic glucose fuel cell concepts have been under consideration. However, so far only preliminary studies have been reported, and in particular the poisoning of abiotic catalysts by tree-sap components and the limited lifetime of enzymatic catalysts have been named as main challenges hindering practical application of the concept.

4.2 Benthic microbial fuel cell powering a meteorological buoy

A more mature application example is the realization of energy-autonomous senor nodes, powered by a benthic microbial fuel cell embedded within the marine sediment. Recently, Tender ***et al***. reported the first demonstration of such a microbial fuel cell in which sufficient electrical power to power a meteorological buoy was generated. Their fuel cell had a total weight of 16 kg and a volume of 30 L. Constructed from graphite-plate anodes embedded in the marine sediment and a graphite brush cathode positioned in the overlying water, the fuel cell delivered 36 mW of continuous electrical energy (16 mW m^{-2} per geometric anode surface). The electrical output was transformed to a voltage of 6 V by means of a DC-DC-converter and supplied a set of sensors (temperature, air pressure, and relative humidity) as well as a low-power line-of-sight RF transceiver, which transmitted the data in 5-min intervals. The current challenges in this technology are the cost and power output.

4.3 Miniature Bio-fuel cell for Autonomous sensor-transmitter

Heller[63] argued that the feasibility of miniaturization of implantable sensor-transmitter systems to volumes smaller than 1 mm^3 are likely to create a demand for a miniature, low cost glucose-O_2 bio-fuel cell that would power the autonomous sensor–transmitters for a few weeks to meet the demand for spatially and temporally resolved information on local temperature, flow, pressure and chemical concentrations,. Prototypes of these cells are in hand. The cells consist merely of two 7 μm diameter carbon fibers, each coated with a different "wired" enzyme bio-electro-catalyst. On one, catalyzing the two-electron electro-oxidation of glucose at a reducing potential, glucose oxidase is co-immobilized in and electrically connected ("wired") by an electron conducting hydrogel of a reducing redox potential. On the other, catalyzing the four electron electroreduction of O_2 to water, bilirubin oxidase is co-immobilized in and electrically "wired" by an electron conducting hydrogel of an oxidizing potential. The cells are the smallest ever built. When the volume of the fibers is 0.0026 mm^3, the current of the cell operating at 0.52 V in a physiological buffer solution at 37°C is 8.3 μA. The 4.3 μW power output of the cell is expected to suffice for the operation of implanted sensors and for the intermittent transmission of the data collected to an external receiver.

5. Energy-autonomous robots

A fascinating application of microbial fuel cells is the realization of autonomous robots that feed from the environment. Kelly ***et al***. [64] first presented their slugbot in 2003 as a robotic predator that utonomically collected snails and carried them to a central fermenter unit. Here the snails were "digested" in a microbial fuel cell, and the generated electricity was in turn used to re-charge the battery packs of the robots. While in this first design the microbial fuel cell had to be stationary due to its size and weight, a later robot called "Eco-Bot II" was powered by several on-board microbial fuel cells operating on fuels such as sugar, fruit, and insects. The same research group also suggested the use of microbial fuel cells as power supply for energy-autonomous under-water robots. Another "gastropod" named "Chew-Chew" has also been produced and is capable of "feeding" and so running via consumption of meat.

6. Wastewater treatment:

Bio-fuel cells are useful for waste water treatment as it can remove organic compounds from the waste stream and can also generate electrical power. Logan[16] calculated that the wastewater from a town of 150,000 people could potentially be used to generate up to 2.3 MW of power (assuming a 100% efficiency), although a power of 0.5 MW might be more realistic. It should be mentioned in this context that up to 80% of the chemical oxygen demand of wastewater can be removed by treatment in a microbial fuel cell and it is possible that the electricity generated in this manner could be used on site to power further treatment of the wastewater. Another important application of microbial fuel cells is in the field of waste water engineering. Microorganisms can discharge the dual duty of degrading effluent and generating power. When microorganisms oxidize organic compounds present in waste water, electrons are released yielding a steady source of electrical current. If power generation in these systems can be increased, microbial fuel cells may provide a new method to offset operating costs of waste water treatment plant, making advanced waste water treatment more affordable in both developing and industrialized nations. Different designs of fuel cell reactors based on chemical engineering principles like fluidized bed reactors, packed bed reactors, etc. are under trial. Tests have been conducted using single chamber microbial fuel cell (SCMFC) containing eight graphite electrodes as anodes and a single air cathode. The system was operated under continuous-flow conditions with waste water. The prototype SCMFC reactor generated an electric power of 26 mW/m^2, while removing up to 80% of chemical oxygen demand of the waste water.

7. Bioremediation:

An MBFC can be modified for its use in bioremediation. The MBFC is not used to produce electricity; instead, power can be put into the system to drive desired reactions to remove or degrade chemicals, such as converting soluble U(VI) to insoluble U(IV). Bacteria are not only able to donate electrons to an electrode but can also accept electrons from the cathode. By poising the electrodes at –500 mV, Gregory ***et al***. [66] were able to precipitate uranium directly onto a cathode because of bacterial reduction. It has been shown that MBFC-based technologies could be used to remove nitrate, conversion to nitrite, even N_2 gas by receiving electrons from the cathode [67]. Electrolytic cultivation has been used to extend the growth rates of suspensions of iron-oxidizing bacteria in the laboratory [68]. It is known that nutrient removal is critical to treatment objectives of most wastewater treatment.

8. Hydrogen production:

MBFCs can also be modified to produce hydrogen gas (H_2). This can be done by removing oxygen at the cathode and adding in a small voltage via the bioelectrochemically assisted microbial reactor (BEAMR) process or the biocatalyzed electrolysis process [37, 69]. Bacteria produce an anode working potential of ~–0.3 V. Liu ***etal.*** [69] showed that the protons and electrons that are produced at the anode can combine at the cathode to produce H_2 with only an additional total cell potential of 0.11 V. A recent US Department of Energy report that one mole of glucose can produce 10-12 mol-H_2, making this route of H_2 production economically viable. Bio-hydrogen production via the BEAMR process is not limited to glucose. Any biodegradable substrate that produces electricity in an MFC should work in a BEAMR system. Recent research has shown that H_2 can also be produced using wastewaters via BEAMR process for which high-strength wastewaters is more appropriate.

FUTURE OF BIOFUEL CELLS:

Microbial biofuel cell technology has a huge amount of potential and will emerge gradually an essential element for both renewable energy resource and wastewater treatment process. The development of bio-fuel cells for practical applications is a field which is still in its infancy. A possible avenue include exploiting enzymes harvested from the lysis of living cells as catalysts, thereby combining the power output of enzyme-based bio-fuel cells with the versatility of microbial-based bio-fuel cells.

The high turnover of a "wired" enzyme electrode in medical implant BFCs could generate power levels capable of meeting the needs of many devices without the need for a mediator. One is required to address the problem that most of the enzyme electrodes have lifetimes in the order of weeks whereas for in vivo implanted devices, longevities of years would be required for practical application. Enzymes are to be modified through genetic engineering to meet the demand of stability. Adaptability to the physiological environment and resistance to bio-fouling over extended periods of time is much more needed, otherwise would lead to harm to the patient.

Although some specialist devices for medical, environment and military purposes could now be considered feasible, it is obvious that a continuing research effort need to be made before we will see large scale use of biofuel cells. Problems of lifetime, stability and power density all need to be addressed; and we need to improve our knowledge of biocatalysis, electron processes at surfaces, biological and other material stability to realise this vision.

REFRENCES:

1. Potter M. C. Electrical effects accompanying the decomposition of organic compounds. Proc. Royal Soc. 1911; B84: 260-276
2. Cohen B. The Bacterial Culture as an Electrical Half-Cell. Journal of Bacteriology. 1931; 21:18–19
3. Logan B. E. Feature Article: Biologically extracting energy from wastewater: biohydrogen production and microbial fuel cells. Environ. Sci. Technol. 2004; 38: 160-167.
4. Kim H. J. Park H. S. Hyun M. S. Chang I. S. Kim M.. and Kim B. H. A mediator-less microbial fuel cell using a metal reducing bacterium, Shewanella putrefaciens. Enzyme Microb. Technol. 2002; 30: 145-152.
5. Park D. H.and Zeikus J. G. Electricity generation in microbial fuel cells using neutral red as an electronophore. Appl. Environ.Microbiol. 2000; 66: 1292-1297.
6. Pizzariello A. Stred'ansky M. and Miertus, S. A glucose/hydrogen peroxide biofuel cell that uses oxidaseandperoxidase as catalysts by composite bulk-modified bioelectrodes based on a solid binding matrix. Bioelectrochemistry. 2002; 56: 99-105.
7. Chaudhuri S. K. and Lovley D. R. Electricity generation by direct oxidation of glucose in mediatorless microbial fuel cells. Nat. Biotechnol. 2003; 21: 1229-1232.
8. Bennetto H. P. Electricity generation by microorganisms. Biotechnology Education 1990; 1: 163-168.
9. Rabaey K.. Lissens G. Siciliano S. D. and Verstraete W. Amicrobial fuel cell capable of converting glucose to electricity at high rate and efficiency. Biotechnol. Lett. 2003; 25: 1531-1535.
10. Rabaey K. Boon N. Siciliano S. D. Verhaege M. and Verstraete W. Biofuel cells select for microbial consortia that self-mediate electron transfer. Appl. Environ. Microbiol. 2004; 70: 5373- 5382.

11. Du Z. Li H. and Gu T. A state of the art review on microbial fuel cells: a promising technology for wastewater treatment and bioenergy. Biotech. Adv. 2007; 25: 464–482.

12. Logan B.E. Microbial Fuel Cells. John Wiley & Sons, Inc., Hoboken, N. J. 2008; 200.

13. Logan B.E. Exoelectrogenic bacteria that power microbial fuel cells. Nat. Rev. Microbiol. 2009; 7: 375–381.

14. Logan B.E. Cheng S. Watson V. and Estadt, G. Graphite fiber brush anodes for increased power production in air-cathode microbial fuel cells. Environ. Sci. Technol. 2007; 41: 3341–3346.

15. Logan B.E. Hamelers B. Rozendal R. Schroder U. Keller J. Freguia S. Aelterman P. Verstraete W. and Rabaey K. Microbial fuel cells: methodology and technology. Environ. Sci. Technol. 2006; 40: 5181–5192.

16. Logan B.E. Murano C. Scott K. Gray N.D. and Head I.M. Electricity generation from cysteine in a microbial fuel cell. Water Res. 2005; 39: 942–952.

17. Pham H. Boon, N. Marzorati M. and Verstraete W. Enhanced removal of 1,2-dichloroethane by anodophilic microbial consortia. Water Res. 2009; 43: 2936–2946.

18. Pham T.H. Aelterman P. and Verstraete, W. Bioanode performance in bioelectrochemical systems: recent improvements and prospects. Trends Biotechnol. 2009; 27 (3): 168–178.

19. Pham T.H. Rabaey K. Aelterman P. Clauwaert P. Schamphelaire L.D. Boon N. and Verstraete, W. Microbial fuel cells in relation to conventional anaerobic digestion technology. Eng. Life Sci. 2006; 6 (3): 285–292.

20. Rismani-Yazdi H. Carver S.M. Christy A.D. and Tuovinen A.H. Cathodic limitations in microbial fuel cells: an overview. J. Power Sources. 2008; 180: 683–694.

21. Rozendal R.A. Hamelers H.V.M. Rabaey K. Keller J. and Buisman C.J.N. Towards practical implementation of bioelectrochemical wastewater treatment. Trends Biotechnol. 2008; 26(8): 450–459.

22. Kannan A.M. Renugopalakrishnan V. Filipek S. Li P. Audette G.F. and Munukutla L. Bio-Batteries and Bio-Fuel Cells: Leveraging on Electronic Charge Transfer Proteins, Nanoscience & nanotech. 2008; 8: 1-13.

23. Cinquin P. Gondran C. Giroud F. Mazabrard S. Pellissier A. Boucher F. Alcaraz Jean-Pierre. Gorgy K. Lenouvel F. Mathé S. Porcu P. and Cosnier S. A Glucose BioFuel Cell Implanted in Rats. PLoS ONE. 2010; 950: e10476

24. Halámková L. Halámek J. Bocharova V. Szczupak A. Alfonta L. and Katz E. Implanted Biofuel Cell Operating in a Living Snail. J. Am. Chem. Soc. 2012

25. Pan C. Wu H. Wang C. Wang B. Zhang L. Cheng Z. Hu P. Pan W. Zhou Z. Yang X. and Zhu J. Nanowire-Based High-Performance "Micro Fuel Cells": One Nanowire, One Fuel Cell. Advanced Materials. 2008; 20 (9): 1644-1648

26. S´eamus F.D. and Higson P.J. Biofuel cells—Recent advances and applications. Biosensors and Bioelectronics. 2007; 22: 1224–1235

27. Mano N. Mao F. and Heller A. A Miniature Biofuel Cell Operating in A Physiological Buffer, JACS Comm. 2002; 124: 12962

28. Bullen R.A. Arnot T.C. Lakeman J.B. and Walsh F.C. Biofuel cells and their development, Biosensors and Bioelectronics. 2006; 21: 2015–2045

29. Rabaey K. and Verstraete W. Microbial fuel cells: novel biotechnology for energy generation. Trends in Biotech. 2005; 23: 291

30. Pant D. Bogaert G.B. Diels L. Vanbroekhoven K. A review of Substrates in a microbial fuel cell for sustainable energy production. Bioresour. Techno. 2009; 100: 1

31. Liu H. Cheng S.A. and Logan B.E.Production of electricity from acetate or butyrate using a single-chamber microbial fuel cell. Environ. Sci. Technol. 2005; 39: 658–662.

32. Chae K.-J. Choi M.-J. Lee J.-W. Kim K.-Y. Kim I.S. Effect of different substrates on the performance, bacterial diversity, and bacterial viability in microbial fuel cells. Biores. Technol. 2009; 100: 3518–3525.

33. Liu H. and Logan B.E. Electricity generation using an air-cathode single chamber microbial fuel cell in the presence and absence of a proton exchange membrane. Environ. Sci. Technol. 2004; 38: 4040–4046.

34. Feng Y. Wang X. Logan B.E. and Lee H. Brewery wastewater treatment using air-cathode microbial fuel cells. Appl. Microbiol. Biotechnol. 2008; 78: 873–880.

35. Huang L. and Angelidaki I. Effect of humic acids on electricity generation integrated with xylose degradation in microbial fuel cells. Biotechnol. Bioeng. 2008; 100 (3): 413–422.

36. Aelterman P. Rabaey K. Pham T. H. Boon N. and Verstraete, W. Continuous electricity generation at high voltages and currents using stacked microbial fuel cells. Environ. Sci. Technol. 2006; 40: 3388-3394.

37. Logan B.E. and Regan J.M. Microbial Challenges & Fuel cell-applications, Envron. Sc. & Tech. 2006; 40: 5172.

38. Davis J. B. and Yarbrough H. F. Preliminary experiments on a microbial fuel cell. Science. 1962; 137: 615-616.

39. Von Hees W. A Bacterial Methane Fuel Cell. J. Electrochem. Soc. 1965; 112(3): 258-262

40. Karube I. Matsunaga T. Tsuru S. and Suzuki S. Biochemical cells utilizing immobilized cells of Clostridium butyricum. Biotechnol. Bioeng. 1977; 19: 1727.

41. Suzuki S. Karube I. Matsunaga T. Kuriyama S. Suzuki N. Shirogami T. and Takamura T. Biochemical energy conversion using immobilized whole cells of Clostridium butyricu., Biochimie. 1980; 62:353.

42. Karube I. Suzuki S. Matsunaga T. and Kuriyama S. Biochemical Energy Conversion By Immobilized Whole Cells. Ann. N. Y. Acad. Sci. 1981; 369: 91.

43. Suzuki S. Karube I. Matsuoka H. Ueyama S. Kawakubo H. Isoda S. and Murahashi T. Biochemical Energy Conversion By Immobilized Whole Cells , Ann. N. Y. Acad. Sci. 1983; 413: 133.

44. Suzuki S. and Karube I. Energy production with Immobilized Cells. Appl. Biochem. Bioener. 1983; 4: 281.

45. Habermann W. and Pommer E.-H. Appl. Microbiol. Biotechnol. 1991; 35: 128.

46. Ieropoulos I.A. Greenman J. Melhuish C. and Hart J. Comparative study of three types of microbial fuel cell. Enzyme & Microbial Techno., 2005

47. Ieropoulos I. Greenman J. and Melhuish C. Imitating metabolism: energy autonomy in biologically inspired robotics. In: Proceedings of the AISB'03, 2nd Int Symp. Imitat Animals and Artifacts. 2003; 191–4.

48. Ieropoulos I. Melhuish C. and Greenman J. Artificial metabolism: towards true energetic autonomy in artificial life. In: Proceedings of the 7th ECAL. 2003; 792–9.

49. Delaney G.M. Bennetto H.P. Mason J.R. Roller S.D. Stirling J.L. and Thurston C.F. Electron-transfer coupling in microbial fuel cells. 2. Performance of fuel cells containing selected microorganism-mediator-substrate combinations. J Chem Tech Biotechnol. 1984; 34B: 13–27.

50. Thurston C.F. Bennetto H.P. Delaney G.M. Mason J.R. Roller S.D. and Stirling J.L. Glucose metabolism in a microbial fuel cell. Stoichiometry of product formation in a thionine-mediated Proteus vulgaris fuel cell and its relation to coulombic yields. J Gen Microbiol, 1985;131:1393–401.

51. Bennetto H.P. Delaney G.M. Mason J.R. Roller S.D. Stirling J.L. and Thurston C.F. The sucrose fuel cell: efficient biomass conversion using a microbial catalyst. Biotechnol Lett 1985; 7: 699–704.

52. Bennetto H.P. Electricity generation by microorganisms. Biotechnol. 1990; 1: 163–8.

53. Bennetto H.P. Stirling J.L. Tanaka K. and Vega CA. Anodic reactions in microbial fuel cells. Biotechnol Bioeng 1983; XXV: 559–68.

54. Bennetto H.P. Delaney G.M. Mason J.R. Roller S.D. Stirling J.L. and Thurston C.F. An electrochemical bioreactor for treatment of carbohydrate wastes and effluents. In: Alternative energy sources, VII 4, bioconversion/hydrogen. New York, NY: Hemisphere Publishing Corporation; 1987; 143–57.

55. Lithgow A.M. Romero L. Sanchez I.C. Souto F.A. and Vega C.A. Interception of the electron transport chain in bacteria with hydrophilic redox mediators. 1. Selective improvement of the performance of biofuel cells with 2,6-disulphonated thionine as mediator. J Chem Research (S) 1986:178–9.

56. Vega C.A. and Fernandez I. Mediating effect of ferric chelate compounds in microbial fuel cells with Lactobacillus plantarum, Streptococcus lactis and Erwinia dissolvens. J Bioelectrochem Bioenerg 1987; 17: 217–22.

57. Akiba T. Bennetto H. P. Stirling J. L. and Tanaka K. Electricity production from alkalophilic organisms, Biotechnol. Lett. 1987; 9: 611 – 616

58. Tanisho S. Kamiya N. and Wakao N. Microbial fuel cell using Enterobacter aerogenes. J Bioelectrochem Bioenerg 1989; 21: 25–32

59. Sell D. Kraemer P. and Kreysa G. Use of an oxygen gas diffusion cathode and a three-dimensional packed bed anode in a bioelectrochemical fuel cell, Appl. Microbiol. Biotechnol. 1989; 31: 211.

60. Kreysa G. Sell D. and Kraemer P. Bioelectrochemical Fuel Cells, Ber. Bunsen-Ges. Phys. Chem. 1990; 94: 1042.

61. Rozendal R. Hamelers H.M. and Buisman C.N.,Effects of Membrane Cation Transport on pH and Microbial Fuel Cell Performance. Envion. Sc & Techno. 2006; 40: 5211

62. Kakehi N. Yamazaki T. Tsugawa W. and Sode K. A novel wireless glucose sensor employing direct electron transfer principle based enzyme fuel cell. Biosensors & Bioelectronics. 2007; 22: 2250.

63. Heller A. Miniature biofuel cells. Phys. Chem. Chem. Phys. 2004; 6: 209-216.

64. Kelly I. and Melhuish C. Slugbot: a robot predator. Robotica. 2003; 21: 399–406.

65. Ieropoulos I. Greenman J. Melhuish C. and Horsfield I. EcoBot-III: a robot with guts. Proc. of the Alife XII Conference, Odense, Denmark, 2010; 733.

66. Gregory K. B. and Lovley D. R. Remediation and Recovery of Uranium from Contaminated Subsurface Environments with Electrodes. Environ. Sci. Technol. 2005; 39: 8943– 8947.

67. Gregory K. B. Bond D. R. and Lovley D. R. Graphite Electrodes as Electron Donors for Anaerobic Respiration. Environ. Microbiol. 2004; 6: 596–604.

68. Hedrich S. Schomann . and Johnson D.B. The iron oxidizing proteobacteria. Microbiology. 2011;157:1551-1564

69. Liu H. Grot S. and Logan B. E. Electrochemically Assisted Microbial Production of Hydrogen from Acetate. Environ. Sci. Technol. 2005; 39: 4317–4320.

Table 1. Substrates used by different researchers in microbial bio-fuel cells [Pant et.al 30].

Type of substrate	**concentration**	**Source inoculation**	**Type of MFC (with electrode surface area and/or cell volume)**	**Current density (mA/cm2) at max power**
Acetone	1 g/L	Pre-acclimated bacteria from MFC	Cube shaped one-chamber MFC with graphite fibre brush anode(7170 m^2/m^3 brush volume)	0.8
Arabitol	1220 mg/L	Pre-acclimated bacteria from MFC	One chamber air-cathode MFC(12mL) with non-wet proofed carbon cloth as anode (2 cm^2) and wet proofed carbon cloth as cathode (7 cm^2)	0.68
Azo dye with glucose	300 mg/L	Mixture of aerobic and anaerobic sludge	One chamber air-cathode MFC with carbon paper anode (36 cm^2)	0.09
Carbomethyl cellulose	1 g/L	Co-culture of Clostridium cellulolyticum & G. sulfureducens	Two chambered MFC with graphite plates as electrodes (16 cm^2) and ferricyanide catholyte	0.05
Cellulose particles	4 g/L	Pure culture of Enterobactor cloacae	U tube MFC with carbon cloth anode (1.13 cm^2) and carbon fibers as cathode	0.02
Corn stover biomass	1 g/L COD	Domestic wastewater	One chamber membrane less air cathode MFC with carbon paper anode (7.1 cm^2) and carbon cloth cathode	0.15
Cysteine	385 mg/L	Sediment sample from 30 cm depth	Two chambered MFC with carbon paper as	0.0186

			electrodes (11.25 cm^2)	
1,2-dichloroethane	99 mg/L	Microbial consortia from acetate enrich MFC	Two chambered MFC with graphite plate anode (20cm^2) and graphite granules cathode	0.008
Ethanol	10mM	Anaerobic sludge from wastewater plant	Two chambered aqueous cathode MFC with carbon electrodes (22.5 $cm^{2)}$	0.025
Farm manure	3 kg in water (20%w/v)/L	Self build up of anaerobic environment	One reactor vessel of manure with anode at the bottom and cathode above the manure; carbon cloth electrodes (256 cm^2)	0.004
Furfural	6.8 mM	Pre-acclimated bacteria from anode of a ferricyanide cathode MFCMFC	One chamber air-cathode MFC with carbon paper anode and cathode (7cm^2)	0.17
Galacttitol	1220 mg/L	Pre-acclimated bacteria from MFC	One chamber air-cathode MFC (12mL) with non-wet proofed carbon cloth as anode (2 cm^2) and wet proofed carbon cloth as cathode (7 cm^2)	0.78
Glucose	6.7 mM	Mixed bacterial culture maintained on sodium acetate for 1 year(rhodococcus & Paracoccus)	One chamber air-cathode MFC (12mL) with non-wet proofed carbon cloth as anode (2 cm^2) and wet proofed carbon cloth as cathode (7 cm^2)	0.70
Glucuronic acid	6.7 mM	Mixed bacterial culture	One chamber air-cathode MFC (12mL) with non-wet proofed carbon cloth as anode (2 cm^2) and wet proofed carbon cloth as cathode (7 cm^2)	1.18

Lactate	18 mM	Pure culture of S.oneidensis MR-1	Two chambered MFC with graphite felt electrode (20 cm^2)	0.005
Landfill leachate	6000 mg/L	Leachate & sludge	Two chambered MFC with carbon veil electrode (30 cm^2)	0.0004
Macroalgae,Ulva lactuca	2500 mg/L COD	Primary clarifier overflow of wastewater plants	One chamber air-cathode MFC (25 mL) with graphite brush anodes and platinized cathode	0.25
Malt extract, yeast extract 1% & glucose		Pure culture of E.cloacae	Two chambered salt bridge MFC with mediators and graphite plate as electrode (15 cm^2)	0.067
Mannitol	1220 mg/L	Pre-acclimated bacteria from MFC	One chamber air-cathode MFC (12mL) with non-wet proofed carbon cloth as anode (2 cm^2) and wet proofed carbon cloth as cathode (7 cm^2)	0.58
Microalgae, Chorella vulgaris COD	2500 mg/L	Primary clarifier overflow of wastewater plants	One chamber air-cathode MFC (25 mL) with graphite brush anodes and platinized cathode	0.20
Microcrystalline cellulose	7.5 g/L	Rumen microorganism from rumen of a cow	Two chambered MFC with graphite plates as electrodes (84 (cm^2)	0.02
Nitrilitriacetic acid	48.5 mg/L	Oligotrophic consortium enriched with river water	Two chambered MFC with graphite felt as electrodes (24 cm^2)	0.0005
Phenol	400 mg/L	Mixed aerobic activated sludge & anaerobic sludge (1:1 v/v)	Two chambered MFC with aqueous air cathode, carbon paper electrode (25 cm^2)	0.1
Propiaonate	0.53 mM	Anaerobic sludge	Two chambered MFC with carbon paper as	0.035

			electrodes (22.5 cm^2)	
Ribitol	1220 mg/L	Pre-acclimated bacteria from MFC	One chamber air-cathode MFC (12mL) with non-wet proofed carbon cloth as anode (2 cm^2) and wet proofed carbon cloth as cathode (7 cm^2)	0.73
Sodium formate	20 mM	Anaerobic digested fluid from a sewage treatment plant	Two chambered MFC with graphite felt as electrodes (4.5 cm^2)	0.22
Sodium fumarate	25 mM	Pure culture of G.sulfurreducens	Stainless steel cathode (2.5 cm^2) half cells poised at -600mV versus Ag/ AgCl	2.05
Sorbitol	1220 mg/L	Pre-acclimated bacteria from MFC	One chamber air-cathode MFC (12mL) with non-wet proofed carbon cloth as anode (2 cm^2) and wet proofed carbon cloth as cathode (7 cm^2)	0.62
Starch	10 g/L	Pure culture of Clostridium butyricum	Two chambered MFC with woven graphite anode (7 cm^2) and ferricyanide catholyte	1.3
sucrose	2674 mg/L	Anaerobic sludge from septic tank	Two chambered mediator less MFC with stainless steel mesh as anode (213.29 cm^2) and cathode (176.45 cm^2); $KMnO_4$ (0.2 g/L) as catholyte	0.19
Xylitol	1220 mg/L	Pre-acclimated bacteria from MFC	One chamber air-cathode MFC (12mL) with non-wet proofed carbon cloth as anode (2 cm^2) and wet proofed carbon cloth as cathode (7 cm^2)	0.71

Xylose	6.7 mM	Mixed bed culture	One chamber air-cathode MFC (12mL) with non-wet proofed carbon cloth as anode (2 cm^2) and wet proofed carbon cloth as cathode (7 cm^2)	0.74
Xylose & humic acid	10 mM	Domestic wastewater	Two chambered MFC with plain carbon paper as electrode (76.5 cm^2)	0.06
Wastewaters artificial wastewater with glucose & glucomate	300 mg/L	Anaerobic sludge	Membrane less MFC with anode (465 cm^2) at bottom and cathode (89 cm^2) at top of cylinder; graphite felt as both electrode	0.02
Brewery wastewater	2240 mg/L	Full strength brewery wastewater	One chamber air-cathode MFC with non-wet proofed carbon cloth as anode (7 cm^2) and wet proofed carbon cloth containing Pt as cathode	0.2
Beer brewery Wastewater	600 mg/L	Anaerobic mixed consortia	One chamber air-cathode MFC with carbon fibers as anode	0.18
Chocolate industry Wastewater	1459 mg/L COD	Activated sludge	Two chambered MFC with graphite rods as electrodes (16.485 cm^2) and ferricyanide as catholyte	0.302
Domestic Wastewater	600 mg/L	Anaerobic sludge	Two chambered mediator less MFC with plain graphite electrode (50 cm^2)	0.06
Food processing Wastewater	1672 mg/L COD	Anaerobic sludge	Two chambered MFC with carbon paper as electrode (22.5 cm^2)	0.05
Meat processing	1420 mg/L	Domestic wastewater	One chamber (28 mL)	0.115

Wastewater			MFC with carbon paper electrodes (25 m^2/m^3)	
Paper recycling Wastewater	2.452 g/L	Diluted paper recycling wastewater	One chamber MFC with graphite fiber brush anode (5418 m^2/m^3 brush volume)	0.25
Protein –rich Wastewater	1.75 g/L COD	Mesophilic Anaerobic sludge	Two chambered MFC with graphite rods as electrode (65 cm^2)	0.008
Real urban Wastewater	330 mg/L	Domestic wastewater	Separate anolyte (1000 cm^3) and catholyte chambers (100 cm^3) connected with a salt bridge; graphite cylinder anode (20 cm^2)	0.018
Starch processing Wastewater	4852 g/L COD	Starch processing wastewater	One chamber air-cathode MFC with carbon paper anode (25 cm^2)	0.09
Swine Wastewater	8320 mg/L COD	Full strength swine wastewater	One chamber MFC (28 mL) with Toray carbon paper as anode (25 $m^{2/}m^3$) and carbon cloth as cathode	0.015
Synthetic acid mine drainage Wastewater	0.007 M Fe2+	Medium with NaCl and NaHCO3 sparged with Na and CO2	Two chambered MFC with carbon cloth anode (7 cm^2) and platinized carbon cloth anode	0.064
Synthetic Wastewater	12.1 g/L COD	Anaerobic mixed consortia producing hydrogen	Dual chamber MFC with graphite plate electrode (83. 56 cm^2)	0.086
Synthetic Wastewater	16 g COD/day	Granular sludge from a upflow of anaerobic sludge blanker(UASB) reactor	Membrane-less, mediator-less MFC with glassy carbon electrode (160 cm^2)	0.017
Synthetic Wastewater	510 mg/L	Anaerobic culture froma pre-existing	Dual chamber MFC with stainless tell as anode	0.008

		MFC	(170 cm^2) and graphite rods as cathode (150 cm^2)	
Synthetic Wastewater with urea and molasses	1000 mg/L	Anaerobic mixture from a wastewater plant	Two chambered MFC with copper wires as anode (20.1 cm^2) and gold covered copper wires as cathode	0.005
Wastewater amended with acetate	1600 mg/L	Domestic wastewater	Submersible MFC, with an immersed anode (carbon paper, 16 cm^2) and an air-cathode chamber in an anaerobic reactor	0.08

Title: Dielectric behavior of (1-x) Ba $Zr_{0.025}Ti_{0.975}O_3$–(x) $BiFeO_3$ solid solutions

Authors: Priyanka A. Jha, Pardeep K. Jha, A.K.Jha, R.K. Dwivedi

PII: S0025-5408(12)00773-8
DOI: doi:10.1016/j.materresbull.2012.10.017
Reference: MRB 6168

To appear in: *MRB*

Received date: 20-6-2012
Revised date: 29-8-2012
Accepted date: 5-10-2012

Please cite this article as: P.A. Jha, P.K. Jha, R.K. Dwivedi, Dielectric behavior of (1-x) Ba $Zr_{0.025}Ti_{0.975}O_3$ndash(x) $BiFeO_3$ solid solutions, *Materials Research Bulletin* (2010), doi:10.1016/j.materresbull.2012.10.017

Dielectric behavior of (1-x) Ba $Zr_{0.025}Ti_{0.975}O_3$ – (x) $BiFeO_3$ solid solutions

Priyanka A. Jha[1, 3], Pardeep K. Jha[3], A.K.Jha[1, 2] and R.K. Dwivedi[*3]

[1]Thin Film & Material Science Laboratory

Department of Applied Physics

Delhi Technological University (Formerly Delhi College of Engineering)

Bawana Road, Delhi- 110042, India.

[2]Department of Applied Science

A. I. A. C. T. R. (GGSIPU), Geeta Colony

Delhi- 110031, India.

[3]Department of Physics and Material Science & Engineering

Jaypee Institute of Information Technology

A-10, Scetor-62, Noida, U. P.-201307, India.

Email: rkdwivedi.jiit@gmail.com

Ph. No. : +91 120 2 59 43 66, Fax No. : +91 120 2 40 09 86

Abstract

Barium zirconate titanate is a very promising material having good ferroelectric properties while bismuth ferrite is a well known multiferroic material. In the present work, the compounds (1-x) Ba $Zr_{0.025}Ti_{0.975}O_3$ – (x) $BiFeO_3$ (x = 0.1-0.4) have been synthesized using solid state reaction method and structural analysis reveal the formation of single phase solid solution. Initially, the Curie temperature increases with increasing bismuth ferrite up to x = 0.2 and with the further increase in bismuth ferrite content, the Curie temperature decreases. There is an increase in the value of dielectric constant at 1 kHz from 551 for x = 0.1 to 3509 for x = 0.4 at their Curie temperatures. The values of coercive field decrease with the increasing bismuth ferrite

content resulting in slim ferroelectric loops which confirms the formation of relaxor multiferroics.

Keywords: A. ceramics, C. X-ray diffraction, D. Dielectric Properties, D. ferroelectricity.

1. Introduction:

The term Multiferroics is used for those multifunctional materials in which two or more kinds of fundamental ferroic properties coexist. These materials have become one of the hottest topics of research in condensed matter physics and materials science in the recent years. Various strategies have been followed to combine the two types of ferroic properties in a single phase system. In particular, special attention is paid to the three novel mechanisms for ferroelectricity (i) the ferroelectricity induced by spin orders such as spiral and E- phase antiferromagnetic spin orders, which break the spatial inversion symmetry; (ii) the ferroelectricity originating from the charge ordered states; and (iii) the ferrotoroidic systems [1]. The multiferroic materials are expected to show the magnetoelectric effect (ME). Magnetoelectric effect is defined as the appearance of a dielectric polarization in a material upon applying a magnetic field and it is also known as direct magnetoelectric effect designated as ME_H effect ($P= \alpha H$) or vice versa, i.e., converse magnetoelectric effect defined as the appearance of magnetization upon applying an electric field designated as ME_E effect ($M = \alpha E$) [2, 3]. Such effect facilitates an effective conversion between electric energy and magnetic energy. The literature shows the problems regarding the multifunctionality of the single phase materials, not only the low magnetoelectric effect but some other problems are also observed such as (i) high leakage current, (ii) structural distortion and instability and (iii) magnetic ordering in low temperature (<77K) range [4-6]. In order to solve these problems, various attempts are being made including the

modification of the chemical composition of the magneto electric materials by suitable substitutions at different atomic sites and design and fabrication of multicomponent system with Fe [7, 8].

Detailed literature survey reveals there is hardly any detailed study on combination of $BiFeO_3$ with $BaTiO_3$ – $BaZrO_3$ system. It is well known that a solid solution of ferroelectric $BaTiO_3$ and antiferroelectric $BaZrO_3$ provides a very interesting stable system for many applications [9]. Therefore, in order to solve the inherent problems of $BiFeO_3$, new compositions $BiFeO_3$ - $BaTiO_3$ – $BaZrO_3$ (i.e. Bi_x Ba_{1-x} (Fe_x $Zr_{0.025(1-x)}$ $Ti_{0.975(1-x)}$) O_3) (BBFZT) have been synthesized in order to get stable structure, which may be useful for making a new lead-free system for data storage and sensors - actuators applications.

2. Experimental

Polycrystalline samples of composition (1-x) [Ba $Zr_{0.025}Ti_{0.975}O_3$] – (x) [$BiFeO_3$] [x = 0.1- 0.4] were prepared by the solid state reaction method by taking high purity $BaCO_3$, TiO_2, ZrO_2, Bi_2O_3 and Fe_2O_3 (all from M/s Aldrich, USA) in their stoichiometric proportions. The powder mixtures were thoroughly ground in an agate mortar and passed through a sieve of appropriate size. The powder mixture was then calcined at 700^{o}C for 2 hours in an alumina crucible. The calcined mixtures were ground and admixed with polyvinyl alcohol (PVA) as a binder and then pressed at 150 MPa into disk shaped pellets. The pellets were then sintered at 830^{o}C for 2 hours in air. X- ray diffractograms of the sintered samples were recorded using a Bruker X-ray diffractometer with CuKα (λ=1.5406 A^o) radiations in the range $10^o \leq 2\theta \leq 70^o$ at a scanning rate of 2^o/ minute. The microstructural studies of the samples were carried out using Scanning Electron Microscope (Hitachi S-3700N). The sintered pellets were polished to a thickness of 1 mm and coated with silver paste on both sides to act as

electrodes and then finally cured at 300 ^{o}C for 30 min. The dielectric measurements were carried out in the temperature range of room temperature to 300^{o}C at 1 kHz, 10 kHz and 100 kHz using a precision LCR meter (HP 4284A) at an oscillation amplitude of 1 volt. P-E hysteresis loops were recorded at room temperature for frequency 1 kHz using an automatic P-E loop tracer based on Sawyer- Tower circuit.

3. Results and Discussions

3.1 XRD Analysis

Single phase solid solution is observed in the X-ray diffractograms (Fig. 1(a)). It reveals the formation of perovskite structure with orthorhombic phase and with the increase in concentration of BFO, the transformation from orthorhombic to pseudocubic is observed [10]. The indexing of BFO can be done either for rhombohederal or pseudocubic phase [11]. However, splitting observed in the (111) peak in the compositions up to x=0.3 has gradually disappeared in x= 0.4; hence cannot be indexed according to the rhombohederal symmetry [12]. It is also observed that the diffraction peaks shift towards higher angle with the increase in concentration of bismuth ferrite. However, for x= 0.4, the peaks are observed to shift towards the lower angle. At x = 0.4 the transformation from orthorhombic to pseudocubic has just started. This is also evident from the tetragonal splitting in (200) peak gradually seem to be disappearing from x = 0.1 to x = 0.4 (Fig.1 (b)) [13].

3.2 Dielectric Study

Fig.2 shows the temperature dependence of dielectric constant of the studied specimens at 1 kHz, 10 kHz and 100 kHz. It is observed that the value of permittivity increases gradually to a maximum value (ε_m) with the increase in temperature up to the transition temperature and then decreases gradually indicating a phase transition. The broadness of the permittivity peaks increases with the increasing content of BFO

[14] and with the increase in concentration of BFO, the permittivity peak shifts with the frequency indicating a relaxor behavior. There is an increase in the value of dielectric constant from 551 (for x=0.1) to 579 (x=0.2), 580 (x= 0.3) and 3509 (x=0.4) at 1 kHz.

A diffuse phase transition is characterized by broadening in the dielectric constant (ε) versus temperature (T) curve. There is broad permittivity temperature curve in the transition temperature region, as seen in Fig. 2, which can be attributed to mismatch in the ionic size, valence state and electronegativity difference between the solute and solvent atoms in accordance with the Hume rothery rules for solid solutions [15]. The broad permittivity temperature curve can also be attributed to the tolerance factor of the perovskite structure.

For the compositions in the present work, the following equation has been used to calculate the value of tolerance factor [16]:

$$t = \frac{R_O + xR_{Bi^{+3}} + (1-x)R_{Ba^{+2}}}{\sqrt{2}((1-x)(0.025)R_{Zr^{+4}} + (1-x)(0.975)R_{Ti^{+4}} + xR_{Fe^{+3}} + R_O)} \quad \text{.....(1)}$$

For a stable perovskite structure, value of tolerance factor (t) should be greater than unity. As t increases, the normal ferroelectric phase gets stabilized [17]. In case of $BaTiO_3$ value of t is greater than unity and hence the normal ferroelectric phase is stable. With the increasing BFO fraction, the tolerance factor decreases from 0.948 to 0.937 showing a small distortion in the lattice and the consequent broadening.

A modified Curie-Weiss law [18] has been proposed to describe the diffuseness of a phase transition

$$1/\varepsilon - 1/\varepsilon_m = (T - T_m)^{\gamma} / C' \text{.....(2)}$$

where γ and C' are constants. The parameter γ is regarded as a measure of the diffuseness of the phase transition: γ = 1 corresponds to the normal ferroelectric behavior, while 1< γ < 2 corresponds to the diffuse phase transition and γ = 2 refer to a relaxor ferroelectric behavior. The plots of ln ($1/\varepsilon - 1/\varepsilon_m$) as a function of ln ($T-T_m$) for the different compositions (x =0.1 and 0.2) at 1 kHz frequency (with the calculated values of diffusivity constant, γ) are shown in Fig. 3.

For the composition x=0.3 and x=0.4, the dielectric permittivity peak shifts with the increase in frequency showing the relaxor behavior (Fig.3 (inset)) shows the Volgel- Fulcher fitting according to the expression (3),

$$\upsilon = \upsilon_o \exp\left(-\frac{E_a}{k_B(T_m - T_{VF})}\right).....(3)$$

where E_a and υ_o are the activation energy and the Debye frequency of the dipole reorientation, respectively, and T_{VF} is the freezing temperature of the polarization fluctuations.

It is observed in Fig. 2 that the permittivity increases with increase in BFO content. This can be understood as follows. In the present compositions, Bi^{+3} ions substitute Ba^{+2} ions and Fe^{+3} ions substitute Zr^{+4} or Ti^{+4} ions as illustrated in the equation (4)

$$xBiFeO_3 \xrightarrow{In(1-x)BaZr_{0.025}Ti_{0.975}O_3 matrix} xBi^{\bullet}_{Ba} + x(0.025Fe'_{Zr} + 0.975Fe'_{Ti}) + 3xO^{\times}_{O}.....(4)$$

It is well known that the Bi-O (337.2 KJ/mol) bond and Fe-O (407 KJ/mol) bond are weaker in comparison to Ba-O (562 KJ/mol) as well as Zr-O (766.1 KJ/mol) and Ti-O (668 KJ/mol) bonds. At the same time enthalpy of formation of Fe gas (Fe-Fe = 415.5

KJ/mol) is higher than that for Bi gas (Bi-Bi bond = 209.6 KJ/mol). Simultaneously the formation of Oxygen gas is equally probable (O-O bond = 249.18 KJ/mol) [19]. This leads to the formation of charge carriers as depicted in the following equation (5) These charge carriers accumulate near the grain boundaries and this accumulation results in high interfacial polarization and increase in dielectric constant [13].

$$xBi_2O_3 + xFe_2O_3 + (1-x)BaO + 0.025(1-x)ZrO_2 + 0.975(1-x)TiO_2 \xrightarrow{700^{\circ}C}$$
$$(1-x)BaZr_{0.025}Ti_{0.975}O_3 + \{2(x-n\delta)Bi^{\bullet}_{Ba} + (2x)Fe'_{Ti,Zr} + 6(x-n\delta)O^{\times}_{o}\} +$$
$$(n\delta)Bi_2 \uparrow + (3n\delta)O_2 \uparrow + (6n\delta)V^{\bullet\bullet}_{O} + (2n\delta)V'''_{Bi} + 2(n\delta - x)BaO$$
$$+ 2n\delta V''_{Ba} + 2n\delta Ba'_{Bi} + 2(x-n\delta)O^{\times}_{O} \ldots\ldots\ldots\ldots\ldots(5)$$

Here, δ is % Bismuth loss per mole at 700°C; x is concentration in mol% `

$$\delta \propto x$$
$$\Rightarrow \delta = mx \ldots\ldots\ldots(i)$$

where m is constant of proportionality and n is multiplier related to δ such that it tells about the concentration of bismuth ferrite where it leads to the formation of Ba-O as a secondary peak (Fig.1(a)).

$$n\delta - x > 0$$
$$\Rightarrow \delta > \frac{x}{n} \ldots\ldots\ldots(ii)$$

Hence from equations (i) and (ii), it can be deduced that mn should be less than 1 to eliminate the secondary phase formation of Ba-O. Therefore, at low concentration of BFO, there is a secondary peak formation of Ba-O showing some of the Ba-O has left unreacted in the matrix while at higher concentration of BFO, due to bismuth volatilization the matrix has widened and hence showing no secondary phase of Ba-O.

The Curie temperature of barium zirconate titanate is 115°C and that of bismuth ferrite is 830°C. Hence the Curie temperature of the Ba-Bi

composite should lie between 115^{o}C and 830^{o}C according to the Home Ruthery rules. This can then be possibly due to the weak bonding force between the Fe^{+3} and the oxygen ion structure. As the Ti-O bonds are stronger than Fe-O bonds, the Ti^{+4} ions can be substituted at lower temperature for cubic phase formation; resulting in the reduction of the phase transition temperature [20]. Also, the weakening of Fe-O bond leads to a weaker distortion of the octahedron and the substitution of Fe-O might induce a "break" of the Ti-O chains; this could bring about a decrease in the c/a ratio as depicted in Table 1. This "break" is also responsible for the drop in the Curie temperature [21, 22].

The dielectric anomalies are also observed with the increase in fraction of bismuth ferrite (Fig. 2). These anomalies can be attributed to the increase in concentration of charge carriers, represented by the expression (5). These anomalies indicate the formation of several kinds of dipoles or polar clusters for different dielectric modes [23]. The possibility of two kinds of polarization is supported by the Z'' with frequency plots as shown in Fig. 4. The peaks exhibit the frequency dispersion and these peaks are highly influenced by the bismuth ferrite fraction. The peaks formed at certain temperatures in the paraelectric region may be attributed to the orientational polarization existing in the bulk specimens [24]. Oxygen vacancies exist as intrinsic type donors. Trivalent Bi^{+3} ions are substituted onto the Ba^{+2} site which act like extrinsic acceptors. Similarly, Fe^{+2} or Fe^{+3} ions may substitute the Ti^{+4}/ Zr^{+4} sites which act as extrinsic acceptors. The dipoles of following type may be formed due to coulombian interaction.

$$V_O^{\bullet\bullet} - 2Bi'_{Ba} \quad \text{or} \qquad V_O^{\bullet\bullet} - 2Fe'_{Ti/Zr}$$

The relaxation time (τ) for all the samples follows the well known Arrhenius law:

$$\tau = \tau_o \exp\left(\frac{E_a}{k_B T}\right) \quad \text{.....(6)}$$

Fig. 5 shows the variation of relaxation time for all the samples. The activation energy has been calculated using the relation (6). The values of activation energy are found to be nearly 1eV which is the value required for the formation of doubly ionized oxygen vacancies [25]. The higher values of τ (Table1) also support the formation of dipoles with doubly ionized oxygen vacancies [24].

The dielectric loss of the studied samples from room temperature to 300^{o}C is shown in Fig. 2. At the lower frequencies the loss is nearly independent of temperature up to about 200^{o}C and then increases rapidly with increasing temperature. This sharp increase of dielectric loss in the high temperature region may be attributed to the increased mobility of charge carriers arising from defects or vacancies in the sample [26]. It is observed that the loss peak is formed at Curie temperature showing the phase transition. This can be understood as follows. At some suitable frequencies of the applied alternating field, resonance in dielectric behavior is often observed [27]. Moreover, it is also observed that the sudden increase in loss is frequency dependent but independent of concentration and temperature which has also been observed in the barium zirconate titanate specimen [13].

3.4 Hysteresis Loops

Fig.6 shows the P-E loops of the studied specimens measured at room temperature. Unsaturated loops are observed in all the samples indicating poor ferroelectricity [28]. The values of remanent polarization ($2P_r$) decreases with the increase in bismuth ferrite fraction as depicted in Fig.6. There are two major effects of grain boundaries on polarization. As the grain size is small, there is large number of

grain boundaries [29] and it is well known that grain boundaries are low permittivity region, hence poor ferroelectric. On the other hand, there is polarization discontinuity between grain boundary and grain surface and hence polarization ($2P_r$) decreases. It is also seen that coercive field decreases with increase in bismuth ferrite content. This may be due to the fact that energy barrier for switching ferroelectric domain with the change in concentration of charge carriers which leads to the domain pinning [12]. The relaxor behavior of x=0.3 and x=0.4 has been confirmed with the help of ferroelectric loops as the slim loops are a characteristic of relaxor ferroelectrics [30].

Conclusions:

The multiferroic compounds with compositions (x) = 0.1- 0.4 in the system (1-x) Ba $Zr_{0.025}Ti_{0.975}O_3$ – (x) $BiFeO_3$ were synthesized and studied for the structural and electrical properties. X-ray diffractograms reveal the transformation from orthorhombic to pseudocubic phase of perovskite structure with the increase in concentration of bismuth ferrite. A significant increase in dielectric constant at Curie temperature is observed for the specimen with the higher bismuth ferrite content. The decrease in the value of tolerance factor from 0.948 to 0.937 with the increasing content of bismuth ferrite leads to the structural distortion in the lattice. The transformation from normal ferroelectrics to relaxor ferroelectrics has been confirmed from the values of diffusivity constant (γ). This is also supported by the appearance of the slim hysteresis loop.

Acknowledgement

Authors RKD and PAJ express their thanks to Department of Science and Technology (DST) for the research grant (SR/S3/ME/0048/2009-SERC). One of the authors PKJ is thankful to DRDO for the financial support (ERIPR/ER/0803744/M/01/1246).

References:

1. K. F. Wang, J. M. Liu and Z. F. Ren, Adv. Phys. 58 (4) (2009) 321-448.

2. L D Landau, E M Lifschitz, Electrodyanamics of continuous media, Oxford; Pergamon; 1960.

3. T Z Wang, You-He Zhou, Compos Struct 93 (5) 2011; 1485-1492.

4. R. N. P. Choudhary, K. Perez, P. Bhattacharya, R. S. Katiyar, Mater Chem Phys 105 (2007) 286-292.

5. Y. P. Wang, L. Zhon, M. F. Zhang, X. Y. Chen, J. M. Liu, Z. G. Liu, Appl. Phys. Lett. 84 (2004) 1713.

6. W. Eerenstein, F. D. Morrison, J. Dho, M. G. Blamire, J. F. Scott, D. Mathur, Science 307 (2005) 1203a.

7. J. Ryu, S. Priya, K. Uchino, H. E. Kim, J. Electroceram. 8 (2002) 107.

8. M. Fiebig, J. Phys. D: Appl. Phys. 38 (2005) R123 - R152.

9. F. Moura, A. Z. Simoes, B. D. Stojanovic, M. A. Zaghete, E. Longo, J. A. Varela, J. Alloys and Comp. 462 (2008) 129-134.

10. F Sanchez Bajo, Isidro Cachadina, Juan de Dios Solier, Fernando Guiberteau and Francisco L Cumbrera, J. Am. Ceram. Soc. 80 (1) (1997) 232-236.

11. C. J. Cheng, D. Kan, S. H. Lim, W. R. McKenzie, P. R. Munroe, L. G. Salamanca Riba, R. L. Withers, I. Takeuchi and V. Nagarajan Phys. Rev. b 80 (2009) 014109.

12. Sandra M Moussa, Brendan J Kennedy, Brett A Hunter, Christopher J Howard and Tom Vogt, J. Phys.: Condens. Matter 13 (9) (2001) L203-L209.

13. Priyanka A. Jha and A. K. Jha, Journal of Alloys and Compounds 513 (2012) 580-585.

14. D Hennings, A Schnell, G Simon, J Am Ceramic Society 1982, 65, 539.

15. W. Hume-Rothery, Atomic Theory for Students of Metallurgy, The Institute of Metals, London, 1969 (fifth reprint).

16. S. K. Rout, E. Sinha, S. Panigrahi , Mater. Chem. Phys. 101 (2007) 428.

17. H.T. Martirena, J. C. Burfoot, J. Phys. C : Solid State Phys 7, 3162 (1976).

18. G. Burns, Phys. Rev. B 13, 215 (1976).

19. D. R. Lide, CRC Handbook of Chem. and Phys., 87th Edition, (CRC, 2007).

20. S.G. Lee, D. S. Kan, Mater. Lett. 57 (2002) 1629.

21. W. R. Huo, Y. F. Qu, Sens. Actuators A 128 (2006) 265.

22. N. Sawangwan, J. Barrel, K. Mackenzie, T. Tunaksiri, Appl. Phys. A 90 (2008) 723.

23. Chen Ang, Zhi Yu, P. Lunkenheimer, J. Hemburger and A. Loidl, Phys. Rev. B 59 (1999) 6670-6674.

24. R. K. Dwivedi, D. Kumar and O. Prakash, J. Mater. Sci. 36 (2001) 3641-3648.

25. A Pelaiz-Barranco, J D S Guerra, R L´opez-Noda and E B Araujo, J. Phys. D: Appl. Phys. 41 (2008) 215503 (5pp).

26. Prasun Ganguly, A.K. Jha, J. of Alloys and Comp.495 (2010) 7-12.

27. R. C. Buchanan, Ceramic Materials for electronics, Marcel Dekker, New York, 1991.

28. N. Nanakorn, P. Jalupoom, N. Vaneesorn, A. Thanaboonsombut, Ceram. Int. 34 (2008) 779-782.

29. Wei Cai , Chunlin Fu, Jiacheng Gao, Huaqiang Chen, J Alloys Comp. 480 (2009) 870-873.

30. L E Cross, Ferroelectrics 76 (1987) 241-267.

FIGURE CAPTIONS

Fig. 1 (color online) X- Ray Diffractograms of the compositions (1-x) [Ba $Zr_{0.025}Ti_{0.975}O_3$] – (x) [$BiFeO_3$] [x = 0.1- 0.4]

Fig. 2 (color online) Variation of permittivity and dielectric loss tan δ with temperature at frequencies 1 kHz, 10 kHz and 100 kHz of the compositions (1-x) [Ba $Zr_{0.025}Ti_{0.975}O_3$] – (x) [$BiFeO_3$] [x = 0.1-0.4].

Fig. 3(color online) The plots of ln ($1/\varepsilon - 1/\varepsilon_m$) as a function of ln ($T- T_m$) for the different compositions (x =0.1 and 0.2) at 1 kHz frequency (with the calculated values of diffusivity constant, γ)

Fig. 3 inset (color online) The plots of Volgel- Fulcher fitting for the compositions x = 0.3 and 0.4.

Fig.4 (color online) Variation of Z'' with frequency of the studied specimens.

Fig. 5 (color online) The plots of relaxation time and 1000/T for the studied specimens.

Fig. 6 (color online) Ferroelectric hysteresis loops showing remanent polarization (P_r) and coercive field of the studied specimens.

TABLE CAPTIONS

Table 1 Variation in the tolerance factor, lattice parameters, tetragonal strain, dielectric constant, relaxation time and activation energy with concentration of bismuth ferrite (x).

***Graphical Abstract (for review)**

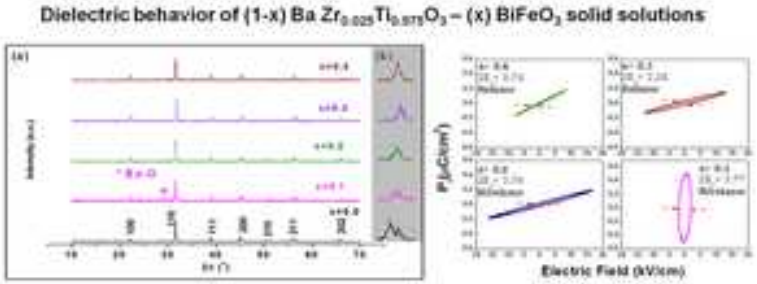

- The compositions (1-x) BZT-x BFO (x=0.1-0.4) have been synthesised using SSR.
- The samples showed Relaxor behaviour with the increasing concentration of BFO.
- Single phase at higher conc. of BFO has been justified through Defect Equation.
- The relaxor behaviour has been supported by the slim ferroelectric loops.

Figure(s)

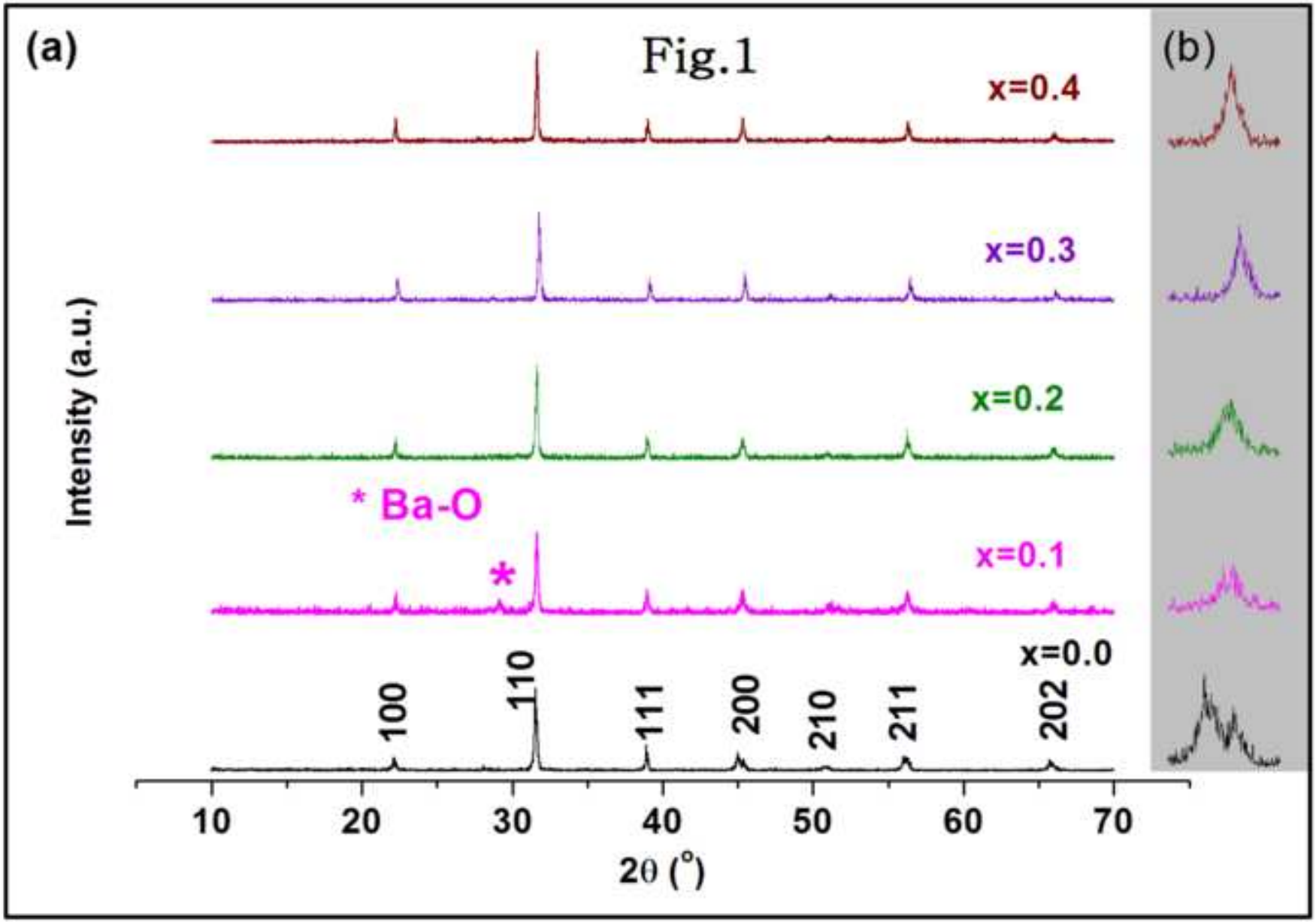
(a)
Fig.1
(b)
x=0.4
x=0.3
x=0.2
* Ba-O
x=0.1
x=0.0
Intensity (a.u.)
100
110
111
200
210
211
202
10
20
30
40
50
60
70
2θ (°)

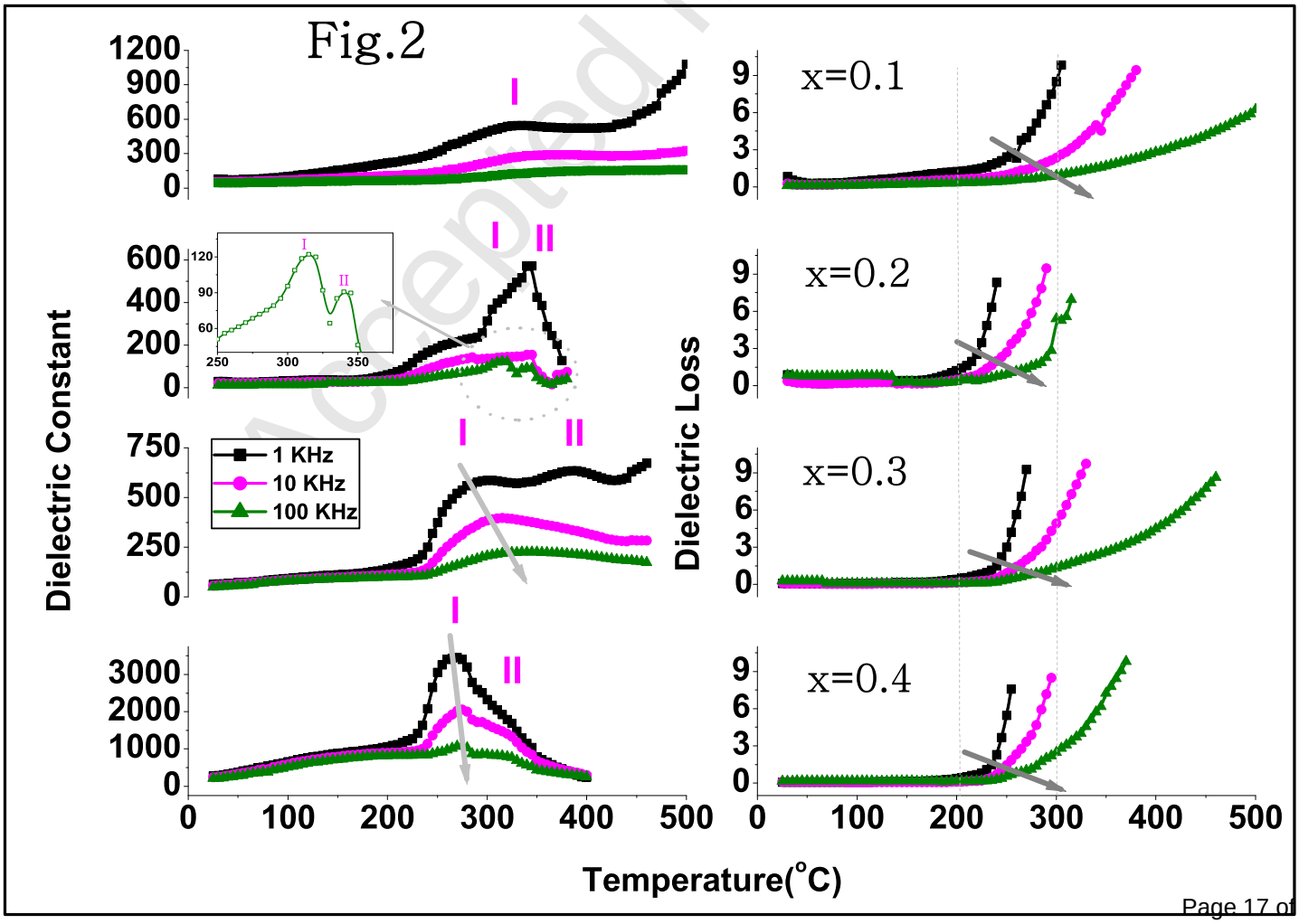

Fig. 3

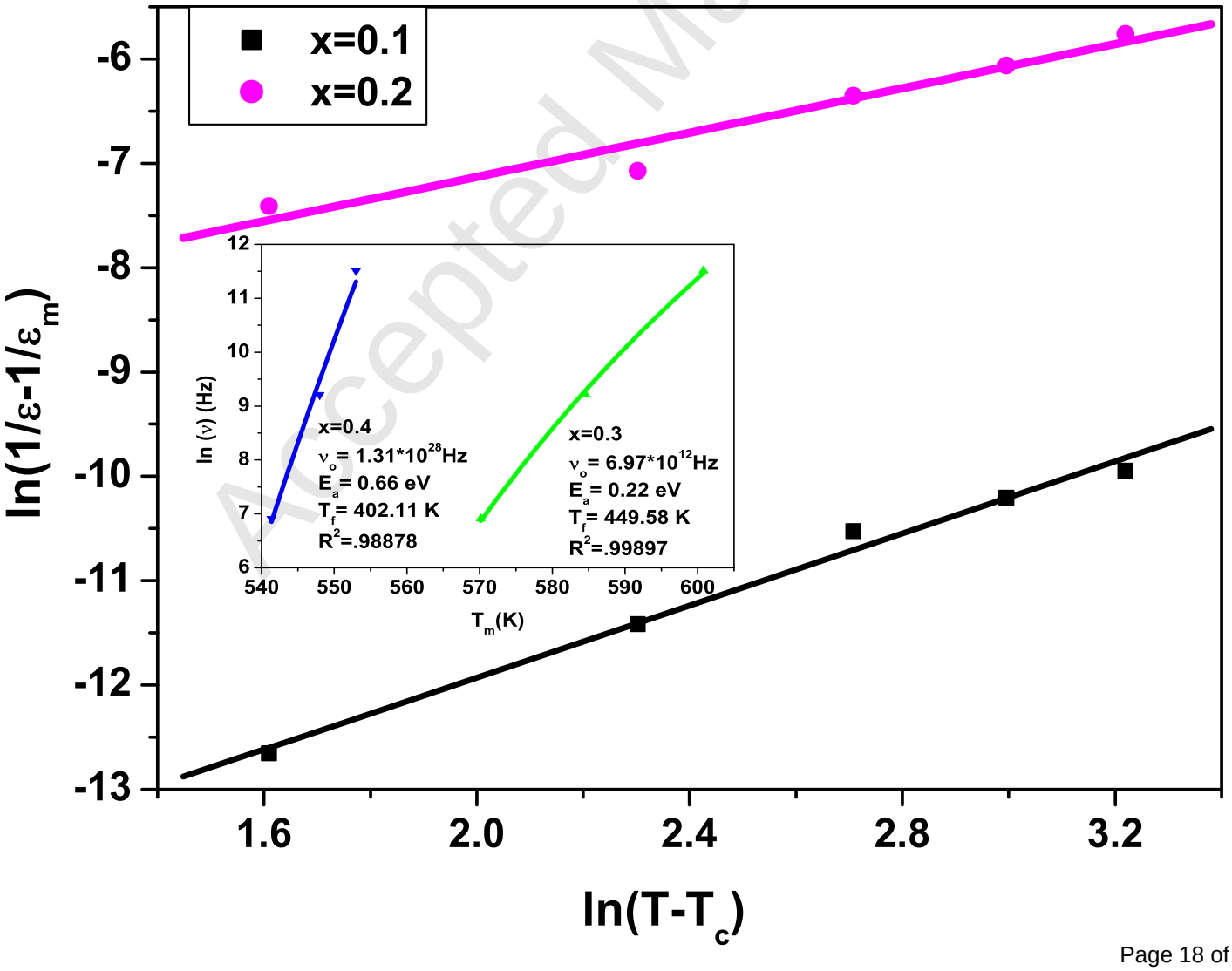

Fig.4

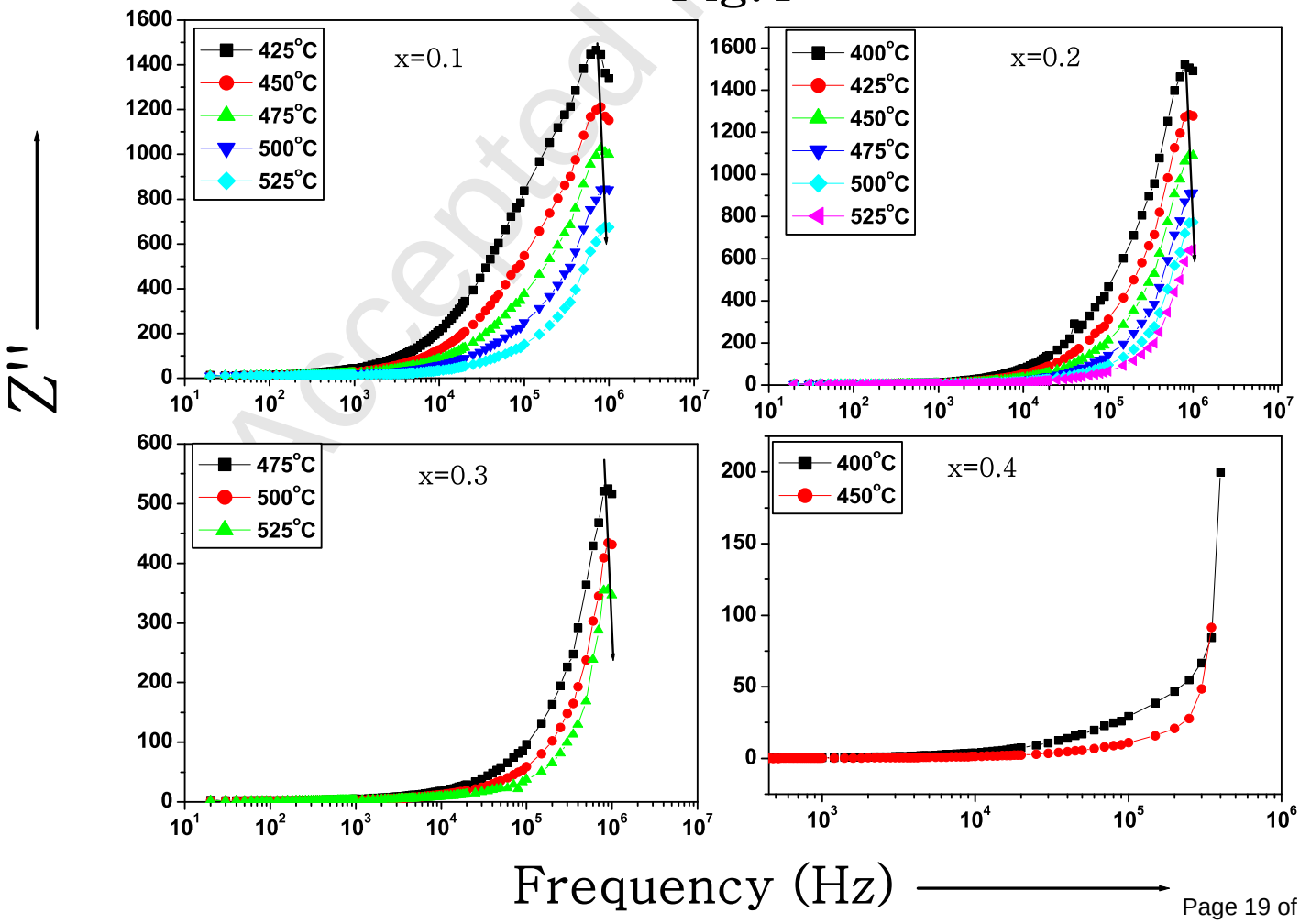

Fig.5

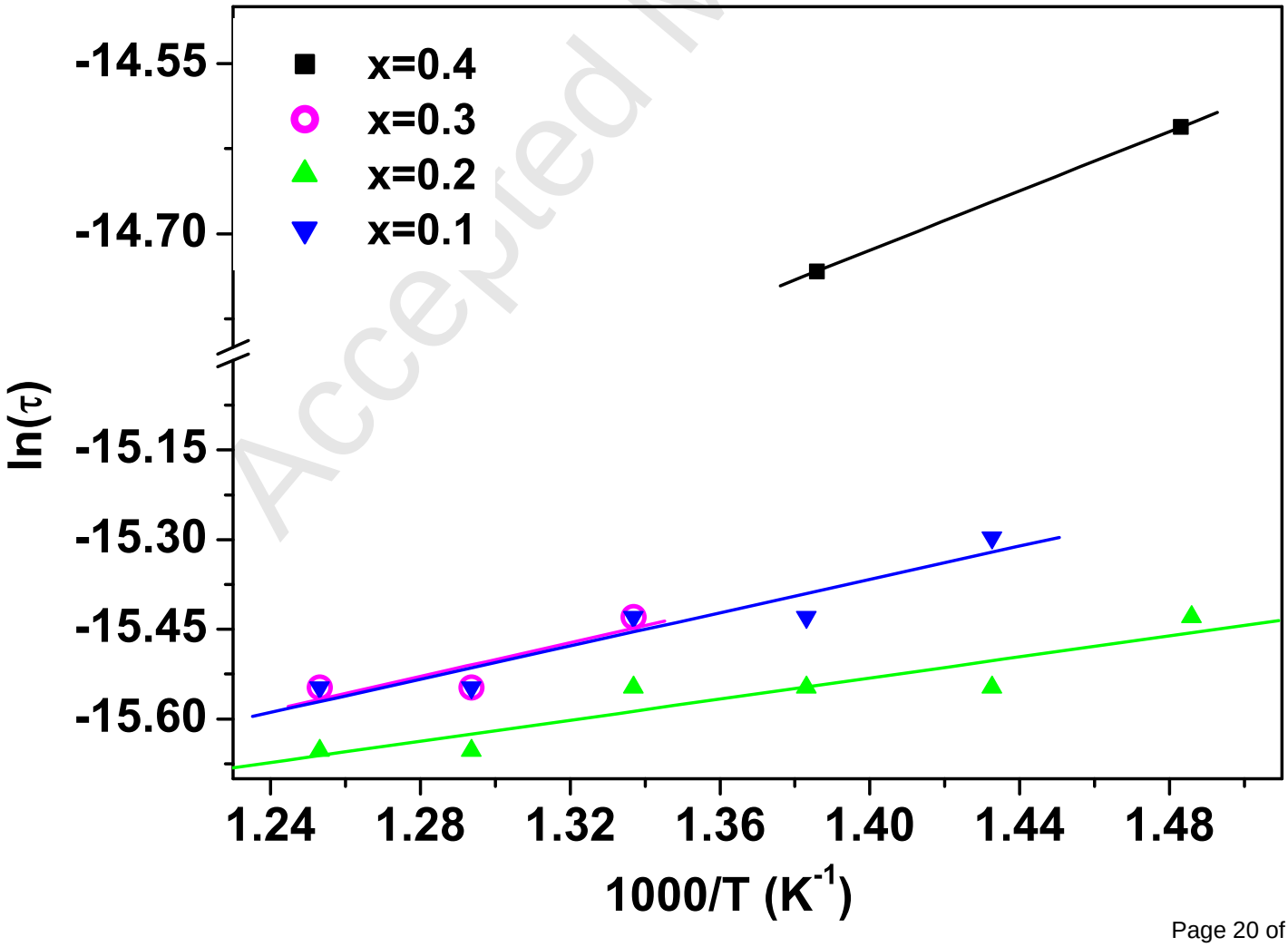

Fig.6

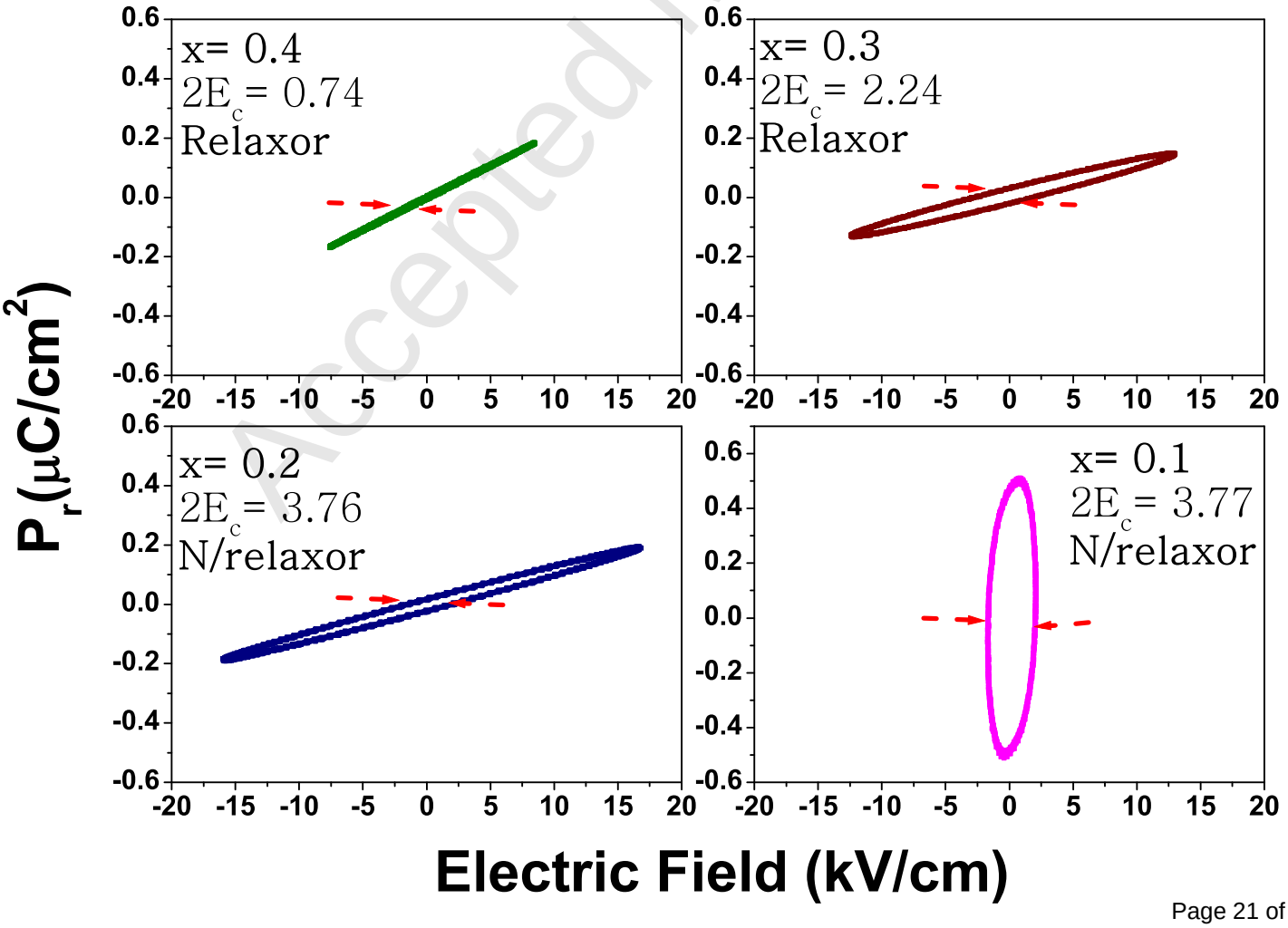

Table1

Sample	Tolerance factor	a	b	c	c/a	ε_m	τ_o	E_a (eV)
x=0.1	0.948	3.98348	4.013072	4.0136428	1.007572	551.26	6.60E-08	1.2008
x=0.2	0.945	3.97183	3.995046	3.9918248	1.005034	579.11	2.92E-08	1.09617
x=0.3	0.941	3.99627	3.998591	4.0002516	1.000996	580.73	5.22E-08	1.22541
x=0.4	0.937	3.99129	3.9971	4.0015962	1.002582	3509.16	3.02E-08	1.12079

International Scholarly Research Network
ISRN Electronics
Volume 2012, Article ID 303191, 6 pages
doi:10.5402/2012/303191

Research Article

DVCCCTA-Based Implementation of Mutually Coupled Circuit

Neeta Pandey, Sakshi Arora, Rinku Takkar, and Rajeshwari Pandey

Department of Electronics and Communications, Delhi Technological University, Delhi 110042, India

Correspondence should be addressed to Neeta Pandey, n66pandey@rediffmail.com

Received 5 July 2012; Accepted 9 August 2012

Academic Editors: H. A. Alzaher, H.-C. Chien, D. Rossi, and D. Takashima

This paper presents implementation of mutually coupled circuit using differential voltage current-controlled conveyor transconductance amplifier (DVCCCTA). It employs only two DVCCCTAs, one grounded resistor, and two grounded capacitors. The primary, secondary, and mutual inductances of the circuit can be independently controlled and tuned electronically. The effect of non-ideal behaviour of DVCCCTA on the proposed circuit is analyzed. The functionality of the proposed circuit is verified through SPICE simulation using 0.25 μm TSMC CMOS technology parameters.

1. Introduction

Since the beginning of current-mode circuit concept, a lot of research has been directed towards the development of active inductance and immittance simulator circuits. A limited literature is available on active realizations (simulators) of mutually coupled circuit (MCC). The MCC is characterized by primary inductance, secondary inductance, mutual inductance, and the coupling factor. The MCC simulators can be integrated easily and have reduced possibility of magnetic interference due to absence of inductive components. Also, there exists a possibility of tunability of inductance values along with the coupling coefficient. Considering this, some MCC simulators have recently been reported in literature that uses different active building blocks [1–8]. The study of MCC simulators [1–8] shows that the circuits reported in [1, 2, 7] are based on operational transconductance amplifier (OTA), [2–4] that uses second-generation current conveyors (CCII), [5, 6] employ second-generation current-controlled conveyors (CCCII), [7] uses differential voltage current conveyors (DVCC) and CCIIs, [8] and utilizes current-controlled current backward transconductance amplifier (CC-CBTA). Some of these implementations [1–7] realize grounded MCC whereas a floating MCC realization is reported in [8]. The OTA-based MCC [1, 2] employs eight OTAs and two grounded capacitors. The CCII-based structures [2–4] use four to eight active elements, four to six resistors, and two to four capacitors. The CCCII-based MCC [5] employs four CCCIIs, five resistors, and two capacitors [5]. Reference [6] reports another CCCII-based MCC that uses five CCCIIs, two capacitors, and an inductor. Two circuits are reported in [7], the first circuit uses four OTAs, two resistors, and two capacitors whereas the second circuit makes use of two DVCCs; two CCIIs, six resistors, and two capacitors. The recently reported MCC [8] uses three CC-CBTAs and three capacitors. The circuits reported in [1, 5–8] are electronically tunable MCC parameters.

In this paper, a new DVCCCTA- [9] based MCC is proposed that uses Gorski Popiel Technique [10]. It is floating in nature and uses only two DVCCCTAs, one resistor, and two grounded capacitors. The primary inductance (L_1), secondary inductance (L_2), and mutual inductance (M) can be electronically and independently controlled. The effect of nonideal behaviour of DVCCCTA on the proposed circuit is discussed. The functionality of the proposed circuit is tested under open-circuit condition. Its performance is exhibited by connecting it as a double-tuned band pass filter by using two additional resistors and two capacitors. The theoretical proposition has been verified with SPICE simulations using the parameters of 0.25 μm TSMC CMOS Technology.

2. Circuit Description

2.1. DVCCCTA. The DVCCCTA [9] is based on differential voltage current conveyor transconductance amplifier (DVCCTA) [11] and consists of differential amplifier, translinear

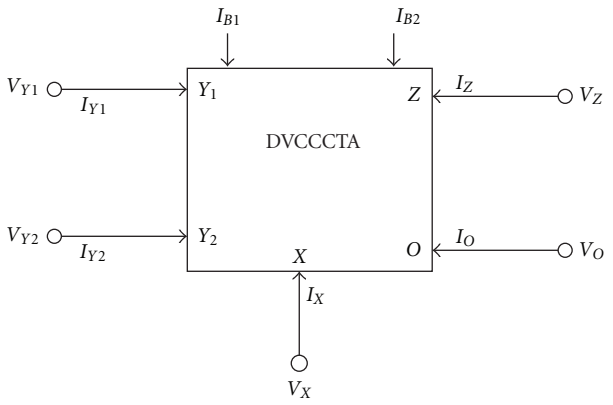

Figure 1: Circuit symbol of DVCCCTA.

loop and transconductance amplifier. The port relationships of the DVCCCTA as shown in Figure 1 can be characterized by the following matrix:

$$\begin{bmatrix} I_{Y1} \\ I_{Y2} \\ V_X \\ I_Z \\ I_O \end{bmatrix} = \begin{bmatrix} 0 & 0 & 0 & 0 & 0 \\ 0 & 0 & 0 & 0 & 0 \\ 1 & -1 & R_X & 0 & 0 \\ 0 & 0 & 1 & 0 & 0 \\ 0 & 0 & 0 & g_m & 0 \end{bmatrix} \begin{bmatrix} V_{Y1} \\ V_{Y2} \\ I_X \\ V_Z \\ V_O \end{bmatrix}, \tag{1}$$

where R_X is the intrinsic resistance at X terminal and g_m is the transconductance from Z terminal to O terminal of the DVCCCTA.

The CMOS-based internal circuit of DVCCCTA [9] in CMOS is depicted in Figure 2. The values of R_X and g_m depend on bias currents I_{B1} and I_{B2}, respectively, which may be expressed as

$$R_X = \frac{1}{\left(\sqrt{2\mu_n C_{ox}(W/L)_{18,19} I_{B1}} + \sqrt{2\mu_p C_{ox}(W/L)_{16,17} I_{B1}}\right)}, \tag{2}$$

$$g_m = \sqrt{\mu_n C_{ox}(W/L)_{24,25} I_{B2}}. \tag{3}$$

2.2. DVCCCTA-Based Floating Mutually Coupled Circuit. In this section, firstly the port equations for a floating MCC are stated. Then, Gorski Popiel technique is outlined which is followed by realieation of the proposed DVCCCTA-based floating mutually coupled circuit.

2.2.1. Floating Mutually Coupled Circuit. A floating MCC is shown in Figure 3(a) and is functionally represented as

$$\begin{aligned} V_{1F} &= sL_P I_1 + sM_{12} I_2 + V_{3F}, \\ V_{2F} &= sM_{21} I_1 + sL_S I_2 + V_{3F}, \end{aligned} \tag{4}$$

where $L_P = L_1 + M_{11}$ and $L_S = L_2 + M_{22}$, and M_{12} and M_{21} represent mutual inductances of MCC.

Alternately, (4) can be represented as

$$\begin{aligned} V_{1F} - V_{3F} &= s(L_1 + M_{11}) I_1 + sM_{12} I_2, \\ V_{2F} - V_{3F} &= sM_{21} I_1 + s(L_2 + M_{22}) I_2. \end{aligned} \tag{5}$$

Representing the voltages $V_{1F} - V_{3F}$ and $V_{2F} - V_{3F}$ as V_{1D} and V_{2D}, respectively, (5) reduces to

$$\begin{aligned} V_{1D} &= s(L_1 + M_{11}) I_1 + sM_{12} I_2, \\ V_{2D} &= sM_{21} I_1 + s(L_2 + M_{22}) I_2. \end{aligned} \tag{6}$$

Equation (6) can be represented pictorially in Figure 3(b) which can be realized using Gorski Popiel technique [10] described in the following section.

2.2.2. Gorski Popiel Technique [10]. This technique is generalization of inductor simulation method and uses generalized impedance converter (GIC). The GICs are circuits whose input impedance can be changed by appropriate selection of components and load. A simplified pictorial representation of GIC is shown in Figure 4. The characteristic equation of GIC may be written as

$$\begin{aligned} V_1 &= V_2, \\ I_2 &= sTI_1, \end{aligned} \tag{7}$$

where T represents time constant of GIC. In Figure 5, a GIC connected to a resistor in input branch makes the input impedance inductive. The value of the inductance would be TR.

This technique implies that a resistive network embedded in GICs appears like an inductive network of same topology with the inductance matrix $L_i = TR_i$. Thus it allows replacement of complete inductor networks by similar resistive networks rather than treating each inductor separately. Thus, this technique can be easily applied to T-shaped resistive network to get the mutually coupled circuit as shown in Figure 6.

2.2.3. Proposed Floating Mutually Coupled Circuit. The method outlined in preceding section can be used for floating MCC realization if the voltages V_1 and V_2 (Figure 6) represent differential voltage as shown in Figure 7. The DVCCCTA, being capable of processing differential inputs through Y_1 and Y_2 terminals, can be used to implement floating mutually coupled circuit.

The proposed floating MCC circuit is shown in Figure 8 where each DVCCCTA realizes GIC block $(sT:1)$ and a series resistance. Thus the circuit uses X-port resistances of 1st and 2nd DVCCCTA for realization of inductances L_1 and L_2 whereas resistance R_M provides mutual coupling. The analysis of the circuit in Figure 8 gives

$$\begin{aligned} V_{1D} &= \frac{sC_1(R_{X1} + R_M)}{g_{m1}} I_1 + \frac{sC_2 R_M}{g_{m2}} I_2, \\ V_{2D} &= \frac{sC_1 R_M}{g_{m1}} I_1 + \frac{sC_2(R_{X2} + R_M)}{g_{m2}} I_2, \end{aligned} \tag{8}$$

where $V_{1D} = V_{1F} - V_{3F}$, $V_{2D} = V_{2F} - V_{3F}$, R_{Xi} and g_{mi} represent intrinsic X-port resistance and transconductance of ith DVCCCTA.

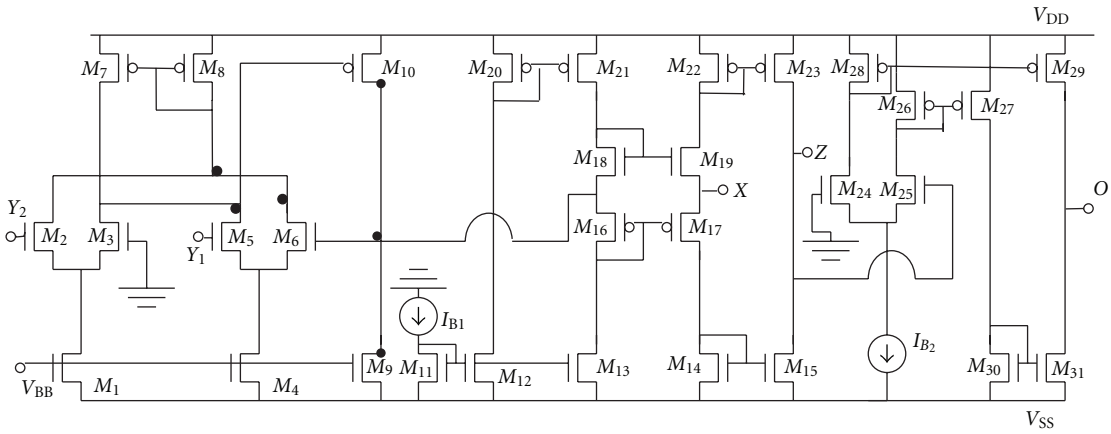

Figure 2: CMOS implementation of DVCCCTA [9].

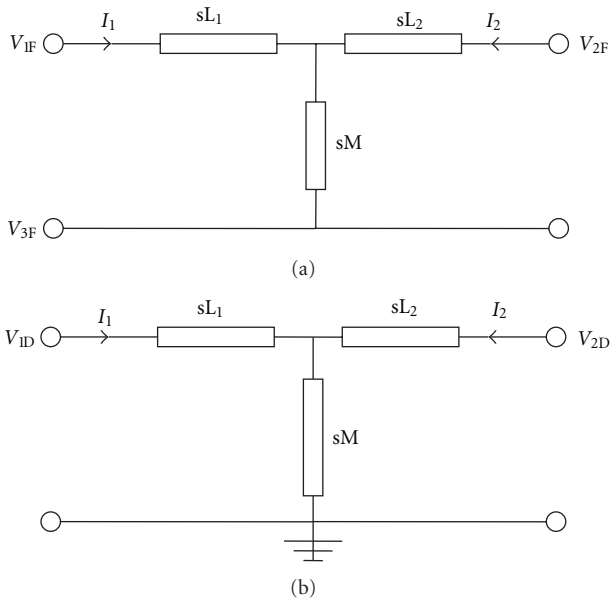

Figure 3: Pictorial representation of floating MCC.

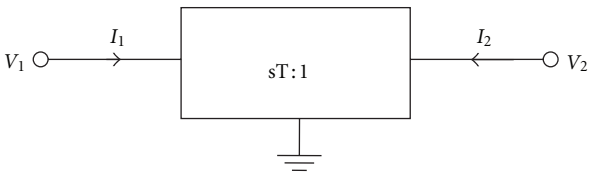

Figure 4: Symbolic Representation of GIC.

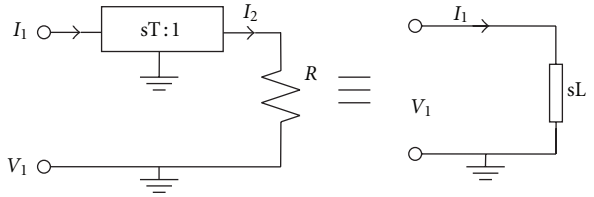

Figure 5: Inductance simulation using Gorski Popiel Technique.

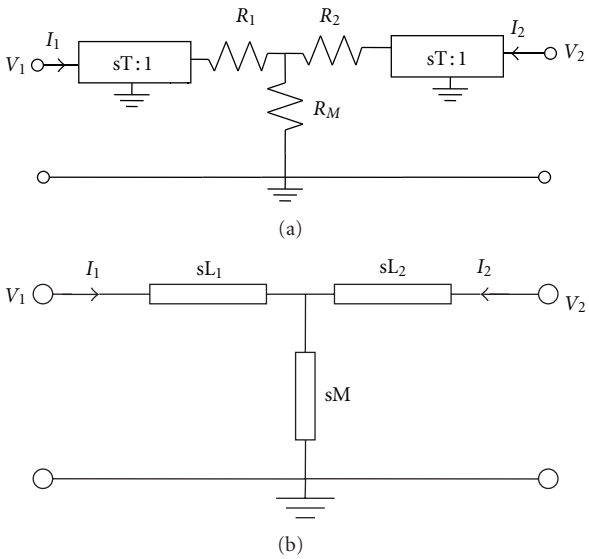

Figure 6: MCC implementation using Gorski Popiel Technique. (a) Resistive network with GIC, (b) its equivalent network.

Using (3) and (6), the values of various inductances L_1, L_2, M_{11}, M_{22}, M_{12}, and M_{21} can be computed as

$$L_1 = \frac{C_1 R_{X1}}{g_{m1}}, \qquad L_2 = \frac{C_2 R_{X2}}{g_{m2}},$$
$$M_{11} = \frac{C_1 R_M}{g_{m1}}, \qquad M_{12} = \frac{C_2 R_M}{g_{m2}}, \tag{9}$$
$$M_{21} = \frac{C_1 R_M}{g_{m1}}, \qquad M_{22} = \frac{C_2 R_M}{g_{m2}}.$$

For symmetrical coupling, $M_{12} = M_{21} = M$. Assuming $g_{m1} = g_{m2} = g_m$, and $C_1 = C_2 = C$, the inductances become

$$L_1 = \frac{CR_{X1}}{g_m}, \qquad L_2 = \frac{CR_{X2}}{g_m},$$
$$M = \frac{CR_M}{g_m}. \tag{10}$$

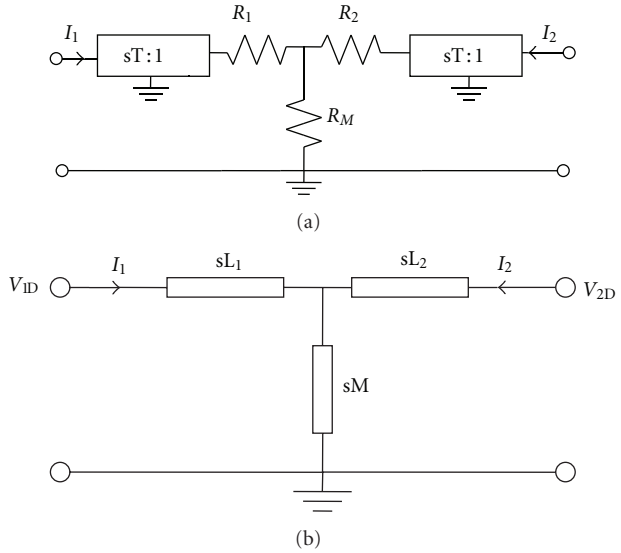

Figure 7: Floating MCC implementation using Gorski Popiel Technique.

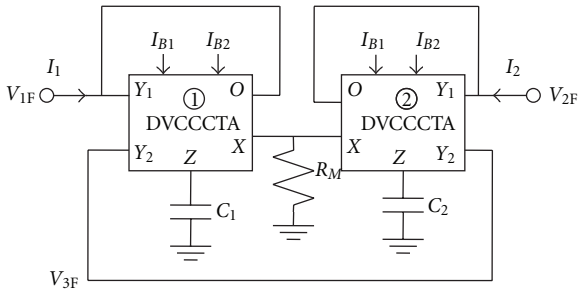

Figure 8: Proposed floating MCC circuit.

The coefficient of coupling (k) can be computed as

$$k = \frac{R_M}{\sqrt{(R_{X1} + R_M)(R_{X2} + R_M)}}. \tag{11}$$

The resistance R_M being grounded can easily be implemented with MOS transistor [12]. Thus, the inductances of MCC as well as coefficient of coupling can be electronically tuned.

2.3. Non-Ideal Analysis. The frequency performance of the proposed MCC may deviate from the ideal one due to nonidealities. The DVCCCTA nonidealities may be categorized in two groups. The first comes from nonunity internal current and voltage transfers in DVCCCTA. The modified port relationships may be written in matrix form as follows:

$$\begin{bmatrix} I_{Y1} \\ I_{Y2} \\ V_X \\ I_Z \\ I_O \end{bmatrix} = \begin{bmatrix} 0 & 0 & 0 & 0 & 0 \\ 0 & 0 & 0 & 0 & 0 \\ \beta_1 & -\beta_2 & R_X & 0 & 0 \\ 0 & 0 & \alpha & 0 & 0 \\ 0 & 0 & 0 & \gamma g_m & 0 \end{bmatrix} \begin{bmatrix} V_{Y1} \\ V_{Y2} \\ I_X \\ V_Z \\ V_O \end{bmatrix}, \tag{12}$$

where the voltage transfer functions $\beta_1 = 1 - \varepsilon_{v1}$ and $\beta_2 = 1 - \varepsilon_{v2}$. The ε_{v1} and ε_{v2} denote voltage tracking errors from Y_1 and Y_2 terminals to X terminal, respectively. The current transfer function $\alpha = 1 - \varepsilon_i$, where ε_i denote current tracking error from X to Z terminal. The coefficient γ denotes current transfer function from Z terminal to O terminals. Considering these deviations in the voltage and current transfers, (9) modifies to

$$L_1 = \frac{CR_{X1}}{(\alpha\beta\gamma g_m)}, \qquad L_2 = \frac{CR_{X2}}{(\alpha\beta\gamma g_m)}, \qquad M_{11} = M_{12} = M_{21} = M_{22} = \frac{CR_M}{(\alpha\beta\gamma g_m)}, \tag{13}$$

where equal values of α, β, and γ are assumed for both DVCCCTAs. Equation (9) clearly indicates that the nonunity voltage and current transfer functions of DVCCCTA affect various inductances. Apart from having non-unity values, the current and voltage transfer functions also have poles at high frequencies. Their effect on proposed MCC performance can however be ignored if the operating frequencies are chosen sufficiently smaller than voltage and current transfer pole frequencies of the DVCCCTA.

The second group of nonidealities comes from parasitics of DVCCCTA comprising of resistances and capacitances connected in parallel at terminals $Y1$, $Y2$, Z, and O (i.e., R_{Y1}, C_{Y1}, R_{Y2}, C_{Y2}, R_Z, C_Z, R_O, C_O). The effects of these parasitics on filter response depend strongly on circuit topology. In the proposed structure, the external capacitor appears in parallel to the parasitic capacitor, the effect of these may be accommodated by preadjusting the external capacitor value.

Table 1: Aspect ratios of CMOS transistors in DVCCCTA.

Transistors	Aspect ratio (W (μm)/L (μm))
M_1, M_4, M_9, M_{11}–M_{15}, M_{30}-M_{31}	3/0.25
M_2, M_3, M_5, M_6	1/0.25
M_7-M_8, M_{20}–M_{23}, M_{26}, M_{28}-M_{29}	5/0.25
M_{10}	12.5/0.25
M_{16}-M_{17}	8/0.25
M_{18}-M_{19}	5/0.25
M_{24}-M_{25}	5/0.25
M_{27}	4.35/0.25

3. Simulation Results

To verify the functionality of the proposed DVCCCTA-based MCC, SPICE simulations have been carried out using TSMC 0.25 μm CMOS process model parameters and power supplies of $V_{DD} = -V_{SS} = 1.25$ V and $V_{BB} = 0.8$ V. The aspect ratios of various transistors of DVCCCTA (Figure 2) are listed in Table 1. Firstly, the proposed circuit is tested under the open-circuit condition, that is, $I_2 = 0$, so the ratio between the secondary and the primary voltage can be expressed as

$$\frac{V_{\text{out}}}{V_{\text{in}}} = \frac{R_M}{R_M + R_{X1}}. \tag{14}$$

Equation (14) clearly shows that under the open-circuit condition the ratio between the output and input voltages

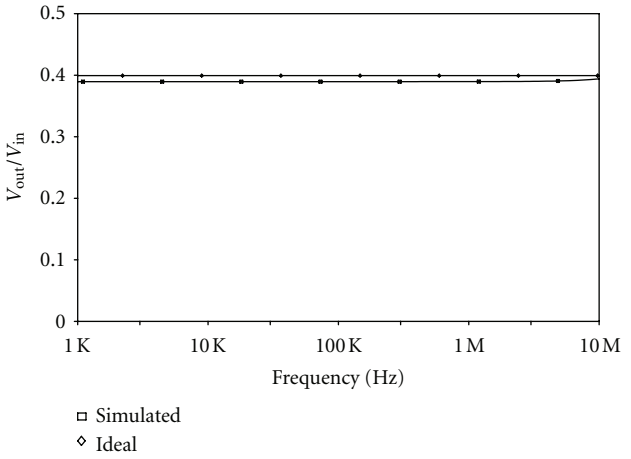

Figure 9: Simulated response of proposed MCC under open-circuit condition.

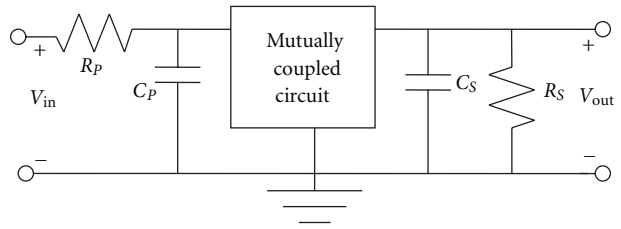

Figure 10: Double-tuned circuit.

will be frequency independent. The open circuit is tested for bias currents I_{B1} and I_{B2} taken as 10 μA and 160 μA, respectively, for both DVCCCTA. The values of C_1, C_2, and R_M are 10 pF, 10 pF, and 1.33 kΩ, respectively. The simulation result as shown in Figure 9 confirms the relation between V_{out} and V_{in}.

To illustrate an application of proposed mutually coupled circuit, a double-tuned circuit is constructed as shown in Figure 10. The primary and secondary side resonance frequencies (f_P and f_S) and quality factors (Q_P and Q_S) can be obtained as

$$f_P = \frac{1}{\left(2\pi\sqrt{C_P(L_1+M)}\right)}, \qquad f_S = \frac{1}{\left(2\pi\sqrt{C_S(L_2+M)}\right)},$$
$$Q_P = 2\pi f_P R_P C_P, \qquad Q_S = 2\pi f_S R_S C_S. \tag{15}$$

The performance of the double-tuned circuit is tested with following component values: $R_P = R_S = 11\,\text{k}\Omega$; $C_P = C_S = 20$ pF; for proposed MCC: $R_M = 1.33\,\text{k}\Omega$, $C_1 = C_2 = 10$ pF. The bias current I_{B1} and I_{B2} are selected as 10 μA and 160 μA, respectively, so as to provide $R_{X1} = R_{X2}$ as 2 kΩ and $1/g_{m1} = 1/g_{m2}$ as 1.5 kΩ. The resulting values of inductances are $L_1 = L_2 = 30\,\mu$H and $M_{11} = M_{12} = M_{21} = M_{22} = 19.95\,\mu$H. This selection results in $f_P = f_S = 5.035$ MHz and $Q_p = Q_s = 6.952$. The ideal and simulated responses of a double-tuned circuit are shown in Figure 11. There is a close agreement between the ideal and simulated values. The

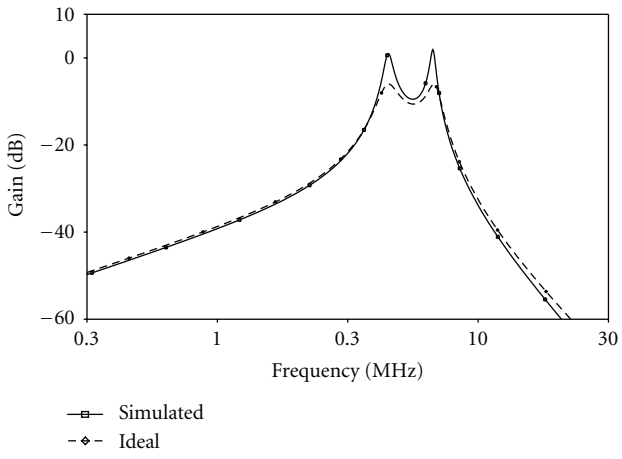

Figure 11: Simulated and ideal response of double-tuned circuit.

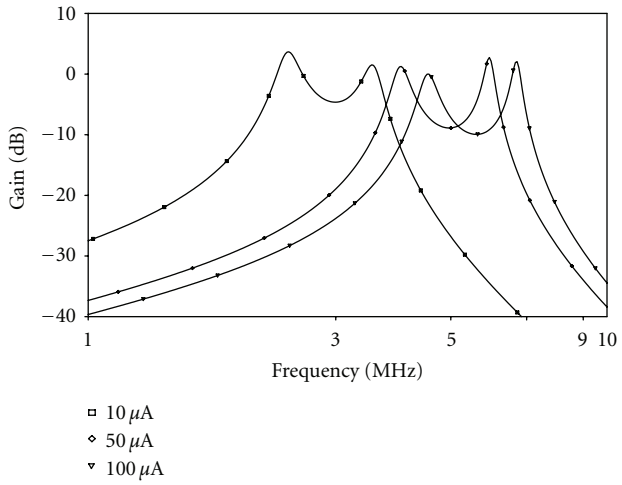

Figure 12: Simulated filter response with varying bias current I_{B2}.

electronic tunability is demonstrated by varying bias current I_{B2} of both the DVCCCTAs from 10 μA to 250 μA and the simulation results are shown in Figure 12.

To study the time domain behaviour of the double-tuned circuit (Figure 10), a sinusoidal signal of 300 mV amplitude and frequency of 5.035 MHz is applied as input. The transient response is depicted in Figure 13 which shows that ideal and simulated responses are in close approximation. The power consumption of the circuit was 2.77 mW. The double-tuned circuit is also tested to judge the level of harmonic distortion at the output of the signal. The %THD result is shown in Figure 14 which shows that the output distortion is low and within 3% up to about 800 mV.

4. Conclusion

In this paper, DVCCCTA-based circuit for simulation of floating mutually coupled circuit has been presented. The proposed circuit uses only two DVCCCTAs, one grounded resistor, and two grounded capacitors. The primary and

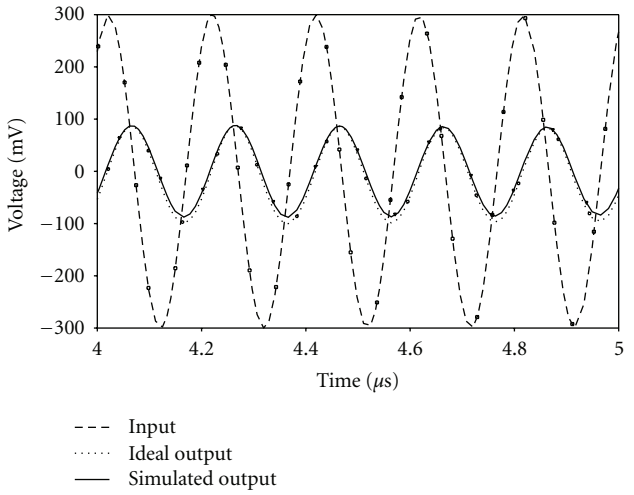

Figure 13: Transient response of double-tuned circuit of Figure 10.

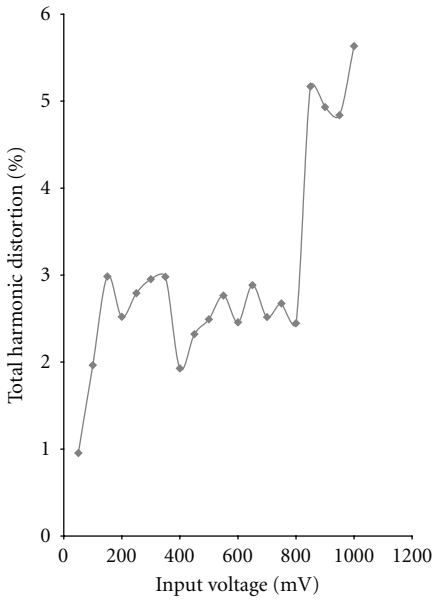

Figure 14: Variation of %THD with respect to input signal amplitude.

secondary inductances of the circuit can be independently controlled and tuned electronically via bias currents of DVCCCTAs whereas mutual coupling can be adjusted via grounded resistor. This resistor can be realized with MOS transistors. The nonideal analysis of circuit is included and as an application a double-tuned circuit is simulated.

References

[1] M. Higashimura and Y. Fukui, "Electronically tunable OTA-C mutually coupled circuit," *Electronics Letters*, vol. 27, no. 14, pp. 1251–1252, 1991.

[2] M. Higashimura and Y. Fukui, "RC active realization of mutually coupled circuit," in *1991 IEEE International Symposium on Circuits and Systems Part 4 (of 5)*, pp. 1343–1346, June 1991.

[3] M. T. Abuelma'atti, S. M. Al-Shahrani, and M. K. Al-Absi, "Simulation of a mutually coupled circuit using plus-type CCIIs," *International Journal of Electronics*, vol. 92, no. 1, pp. 49–54, 2005.

[4] E. Yuce, S. Minaei, and M. A. Ibrahim, "A new simulation of mutually coupled circuit based on CCIIs," *International Journal of Electronics*, vol. 94, no. 4, pp. 367–372, 2007.

[5] E. Yuce and S. Minaei, "Electronically tunable simulated transformer and its application to stagger-tuned filter," *IEEE Transactions on Instrumentation and Measurement*, vol. 57, no. 9, pp. 2083–2088, 2008.

[6] E. Yuce and S. Minaei, "A new active network suitable for realizing ladder filters and transformer simulator," *Journal of Circuits, Systems and Computers*, vol. 16, no. 1, pp. 29–41, 2007.

[7] E. O. Güneş, A. Zeki, and A. Toker, "Design of a high performance mutually coupled circuit," *Analog Integrated Circuits and Signal Processing*, vol. 66, no. 1, pp. 81–91, 2011.

[8] M. Koksal, U. E. Ayten, and M. Sagbas, "Realization of new mutually coupled circuit using CC-CBTAs," *Circuits, Systems, and Signal Processing*, vol. 31, no. 2, pp. 435–446, 2012.

[9] W. Jaikla, M. Siripruchyanun, and A. Lahiri, "Resistorless dual-mode quadrature sinusoidal oscillator using a single active building block," *Microelectronics Journal*, vol. 42, no. 1, pp. 135–140, 2011.

[10] R. Schaumann and M. E. V. Valkenburg, *Design of Analog Filters*, Oxford University press, Oxford, UK, 2003.

[11] H. O. Elwan and A. M. Soliman, "Novel CMOS differential voltage current conveyor and its applications," *IEE Proceedings of Circuits, Devices and Systems*, vol. 144, no. 3, pp. 195–200, 1997.

[12] H. P. Chen, "High-input impedance voltage-mode multifunction filter with four grounded components and only two plus-type DDCCs," *Active and Passive Electronic Components*, vol. 2010, Article ID 362516, 5 pages, 2010.

International Scholarly Research Network
ISRN Nanomaterials
Volume 2012, Article ID 809063, 6 pages
doi:10.5402/2012/809063

Research Article

Effect of Polyvinyl Alcohol on the Growth, Structure, Morphology, and Electrical Conductivity of Polypyrrole Nanoparticles Synthesized via Microemulsion Polymerization

Anurag Krishna,[1] Amit Kumar,[2] and Rajiv Kumar Singh[2]

[1] *Department of Applied Chemistry and Polymer Technology, Delhi Technological University, Bawana Road, New Delhi 110042, India*
[2] *National Physical Laboratory, Council of Scientific and Industrial Research, Dr. K. S. Krishnan Marg, New Delhi 110012, India*

Correspondence should be addressed to Rajiv Kumar Singh, rajivsingh@mail.nplindia.ernet.in

Received 6 July 2012; Accepted 27 August 2012

Academic Editors: A. Kajbafvala, B. Panchapakesan, A. Sorrentino, and C. Wang

Polypyrrole (PPy) nanoparticles were synthesized via microemulsion polymerization technique using sodium dodecyl sulfate as surfactant. Polyvinyl alcohol (PVA) was added as soft template during polymerization to modify the structure and properties of PPy nanoparticles. The synthesized materials namely, PVA-free and PVA added were characterized by Fourier transform infrared spectroscopy (FT-IR), X-ray diffraction (XRD), scanning electron microscopy (SEM), and DC electrical conductivity measurements. The sample synthesized in the presence of PVA has longer conjugation length as estimated from FT-IR investigation. Temperature dependence (4.2–300 K) of DC electrical conductivity measurement reveals that the PVA has a strong effect on the polymerization mechanism of PPy giving evidence of H-bonded assistance during polymerization leading to the synthesis of better ordered polymer. A growth mechanism has been proposed which explains the H-bonded assistance of PPy polymerization leading to enhanced structural ordering.

1. Introduction

Conjugated polymers have attracted considerable attention in the past few decades because of their potential application in electronic devices [1]. Their ease of processing and chemically tunable properties makes them useful for electronic, optoelectronic, electromechanical, and sensing device application [2, 3]. During the recent years conducting polymer nanostructures have received increasing attention from both fundamental research as well as application point of view. Conducting polymer nanostructures show high electrical conductivity, large surface area, short path lengths for the transport of ions, and high electrochemical activity as compared to its macrogranular structure or self-supporting films [4–7]. It can be synthesized by several approaches such as well-controlled solution synthesis [8, 9], soft-template methods [10], hard-template methods [11], and electrospinning technology [12]. Recently some conducting polymer nanowires and nanorods have been synthesized via hydrogen bonding [13].

Polypyrrole (PPy) is one of the most studied conducting polymers because of its good environmental stability, facile synthesis, ion exchange capacity, biocompatibility, and higher conductivity [14, 15]. It can be used in drug delivery, rechargeable batteries, supercapacitors, anhydrous electrorheological fluids, microwave shielding, and corrosion protection [16–18]. Soft template uses microemulsion polymerization which allows particles to transfer into spherical aggregates through the surfactant template for the production of PPy nanostructures. Conducting polymer nanoparticles (particle size) ~50–200 nm [19, 20] and ~20–50 nm [21] have been synthesized. It has been observed that the microemulsion polymerization has increased the yield of the PPy nanoparticles, the extent of the π-conjugation

Table 1: Peaks observed in FT-IR spectra of Sample A and B.

Absorption bands	Samples A (cm^{-1})	Sample B (cm^{-1})
C=C	1553.1	1538
C–C	1481.1	1453
C–N (in plane def.)	1280	1289
Vibration of pyrrole ring	1211	1156
N–H (in plane def.)	1044	1025
C–H out of plane vibrations	925	960
C–H wagging	787	764
N–H out of plane vibration	679	690

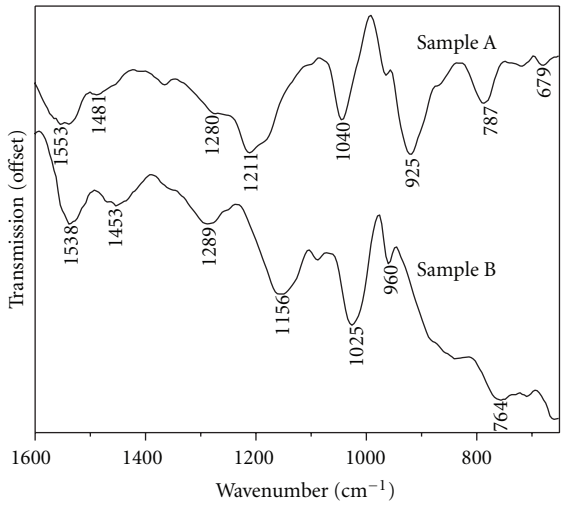

Figure 1: FT-IR spectra of PPy nanoparticles synthesized in the absence (sample A) and presence (sample B) of PVA.

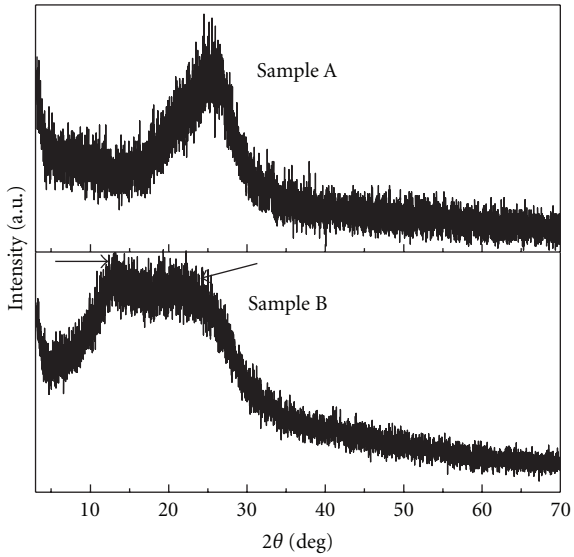

Figure 2: X-ray diffraction pattern of samples synthesized in the absence (sample A) and presence (sample B) of PVA.

along the polymer backbone, and the ordered arrangement of the macromolecular chains. Song et al. 2004 have reported the synthesis of PPy nanoparticles doped with a variety of alkylbenzenesulfonic acid (ABSA) [22]. PPy doped with short alkyl chain showed higher conductivity than long alkyl chain. These achievements indicate that the microemulsion polymerization is powerful technique for the fabrication of polymer nanostructures.

In the present paper, we report the synthesis of PPy nanoparticles by microemulsion polymerization. The temperature-dependent (4.2 to 300 K) dc conductivity measurement along with structural investigations indicates that the addition of PVA during the polymerization affects the polymerization mechanism.

2. Experimental

PPy nanoparticles were synthesized using doubly distilled 0.1 M pyrrole monomer (Fluka chemie) with 0.5 M ferric chloride ($FeCl_3$) (Sigma Aldrich). Sodium dodecyl sulfate (SDS) (Fluka) (0.03 M) was used as surfactant. The solution of SDS was prepared in distilled water (18 MΩ cm). Continuous stirring was carried out for 6 hrs at 275 K in inert atmosphere during polymerization. The black precipitate of PPy from the reaction mixture was filtered via vacuum filtration. The filtered precipitate was washed repeatedly with methanol and distilled water till clear and colorless filtrate was obtained. Finally, the PPy nanoparticles were dried for 6 hrs in vacuum oven at 333 K and was designated as sample A. PPy nanoparticles were also synthesized with the addition of polyvinyl alcohol (PVA) (5% by weight of pyrrole) in the abovementioned reaction mixture, and similar procedure was followed for polymerization and filtration and was designated as sample B.

Fourier transform infrared (FT-IR) spectra of both samples A and B were recorded using Smart orbit ATR-single reflection accessory of the Thermo Scientific Nicolet 5700 spectrometer, with a diamond crystal, taking four scans at a resolution of 4 cm^{-1}, and details of different vibration peaks are given in Table 1. X-ray diffraction of samples A and B was taken by Rigaku-make powder X-ray diffractometer for Cu-Kα (λ = 1.5404 Å) radiation. The scanning electron micrographs (SEMs) of samples A and B were taken using SEM model Zeiss EVO MA-10 microscope to investigate the surface morphology of the samples. A thin layer of gold was sputtered on the samples before loading in the microscope probe to nullify any charging effect. For dc electrical conductivity (σ_{dc}) measurement, circular pellets of both samples A and B having dia ~5 mm were made by using hydraulic press at $\sim 5 \times 10^8$ Pa. Conductivity measurements were performed by using four-probe technique. Keithley 238 high current source measuring unit was used for applying constant current and Keithley 6517A Electrometer/High Resistance meter was employed to measure the voltage. The thickness of the samples was accurately measured to calculate the bulk conductivity. Temperature-dependent (4.2–320 K) dc conductivity measurement was performed in liquid helium Dewar using Keithley's 224 Programmable Constant Current Source and 195 A Digital Multimeter.

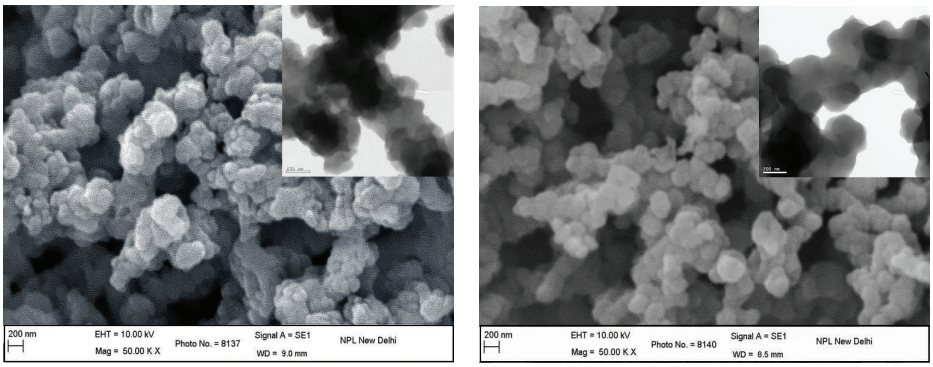

(a) (b)

Figure 3: (a) SEM of PPy nanoparticles (sample A) and (b) SEM of PPy (sample B). Inset shows their corresponding TEM images.

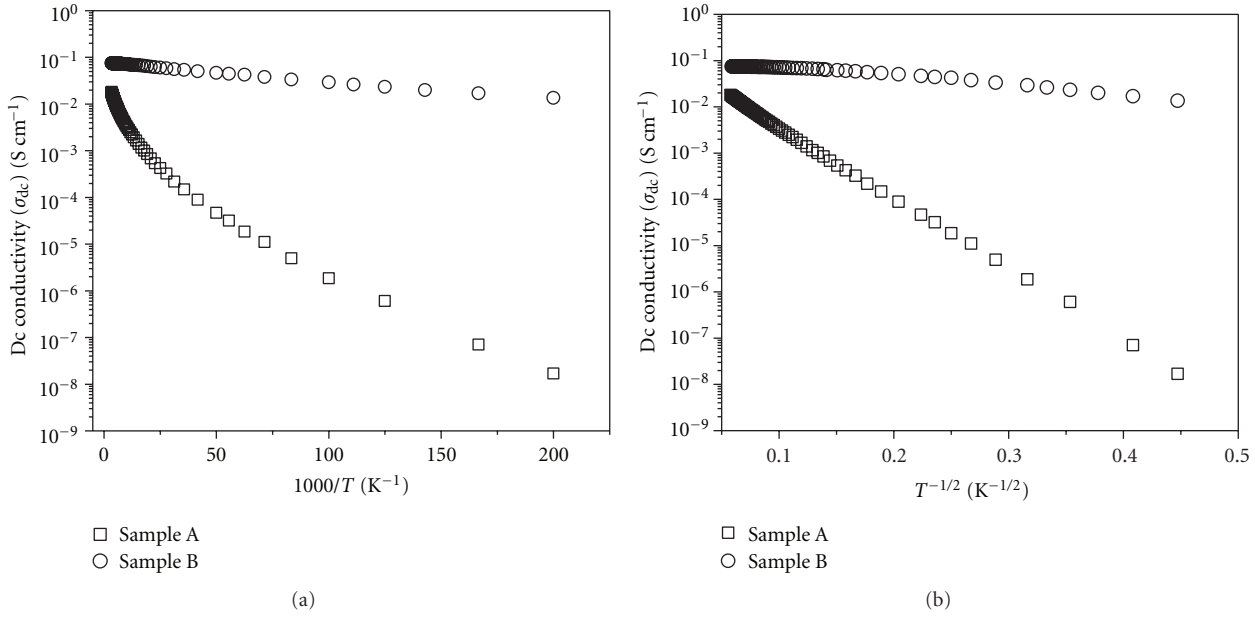

(a) (b)

Figure 4: Plot of dc conductivity (σ_{dc}) versus (a) 1000/T and (b) $T^{-1/2}$ for both the samples in the temperature range 4.2–320 K.

3. Results and Discussion

A key property of a conducting polymer is the presence of conjugated double bond which gives rise to the electrical conductivity, as it allows the efficient transfer of electrons or positive charges along the polymer backbone. Increasing conjugation length and improving order throughout polymer chain will allow charge to migrate along a longer distance and hence enhances the conductivity. In the present work, the conjugation length and structural ordering of PPy nanoparticles have been influenced by the addition of polyvinyl alcohol (PVA) during the microemulsion polymerization.

Figure 1 shows the FT-IR spectra of samples A and B confirming the synthesis of polymers. Sample A shows the peaks at 1553 and 1481 cm^{-1} which correspond to C=C-stretching and C–C-stretching vibrations, respectively [23]. The peaks at 1280 and 1211 cm^{-1} are attributed to the C–N in plane deformation and vibrations of the pyrrole ring. The peak at 1040 cm^{-1} is attributed to N–H in plane deformation vibration [23, 24]. The peaks at 787 and 925 cm^{-1} correspond C–H wagging and C–H out of plane vibrations, respectively. The peak at 679 cm^{-1} is attributed to N–H out of plane vibration [24].

Sample B shows the peaks at 1538 and 1453 cm^{-1} which correspond to the stretching vibration of C=C and C–C, respectively [23]. The peaks at 1289 cm^{-1} correspond to C–N in plane deformation. The peak at 1156 cm^{-1} is attributed to the vibration of the pyrrole ring. The band of N–H in plane deformation is located at 1025 cm^{-1} while C–H out of vibration is found at 960 cm^{-1} [23, 24]. The peaks at 764 and 690 cm^{-1} corresponds to C–H wagging vibration and N–H out of plane vibration, respectively [24]. The characteristic peaks of PVA could not be observed in the spectrum, indicating that alcohol has been washed out from the final PPy nanostructures.

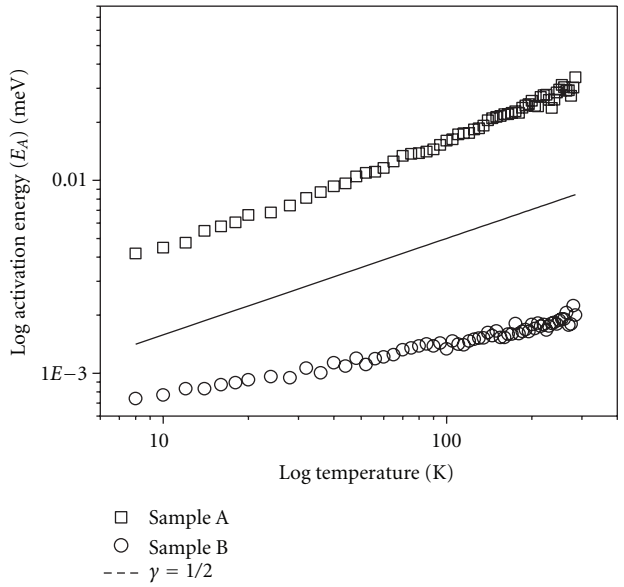

Figure 5: Plot of log E_A (E_A is the activation energy derived from Figure 4(a)) versus log T in the temperature range 8–290 K.

The FT-IR spectra for both samples A and B have all the characteristic peak of PPy, which suggest that it has been successfully synthesized. However, there are few differences between the spectra of samples A and B. The band of C=C stretching vibration located at 1553 cm^{-1} in the FT-IR spectrum of sample A synthesized in the absence of PVA shifts to 1538 cm^{-1} for sample B synthesized in the presence of PVA. Due to this shift the room temperature (~300 K) conductivity of sample B (~7.5×10^{-2} S/cm) is higher than sample A (~1.6×10^{-2} S/cm). The intensity of the C=C and C–C band in the two samples is different which can be linked with the conjugation length of PPy. The conjugation length is estimated from the ratio of peak intensity of C=C and C–C stretching vibrations [25]. The higher ratio represents longer effective π conjugation along the PPy chains and hence higher conductivity. PPy synthesized using PVA shows higher conjugation (~0.98) than the one synthesized without it (~0.91). This shows that the PVA considerably influenced the molecular structure of PPy. The hydrogen in the O–H group of PVA is capable of forming bond with the hydrogen in the N–H group of the pyrrole ring. These hydrogen bonds are known to be weak, and PVA is soluble in water, and quantity of PVA added was very small; therefore, these bonds get broken, and PVA is removed during the washing of the sample. FTIR confirms that this as no characteristic peak for PVA is observed.

Figure 2 shows the XRD pattern of the synthesized PPy nanoparticles with and without PVA. PPy nanoparticles synthesized in the absence of PVA (sample A) exhibit broad scattering peaks at 2θ value around 25.6°, which suggest that PPy is virtually amorphous. PPy nanoparticles synthesized in the presence of PVA (sample B) exhibit two peaks at 2θ values around 14.1° and 23.45° with almost same intensity which suggests that this sample B is less amorphous than sample A. It can be said here that sample synthesized in the presence of PVA is partially crystalline and has better ordering than sample synthesized in the absence of PVA. Higher ordering in PPy prepared in the presence of PVA may be attributed to the alignment given to the PPy chains via hydrogen bonding between N–H group of pyrrole ring and oxygen atom of PVA. The d spacing (interlayer spacing) value for the sample A is ~3.46 Å under whereas for sample B the values of d_1 and d_2 are ~6.28 Å and 3.79 Å, respectively.

The SEM micrograph in Figure 3(a) represents the general morphological features of the PPy nanoparticles obtained without using PVA (sample A) during the experiment process. The SEM image reveals the presence of globular particles with diameter ranging from 50 to 100 nm. These globular particles conglutinate together to form bigger aggregates. The size measured by particle size analyzer was found to around 80 to 100 nm (result not shown). Figure 3(b) shows the typical SEM images of PPy nanoparticles obtained when PVA was introduced to the experiment process (sample B). The SEM image reveals the existence of lamella disc-like structures with diameter ranging from 150 to 200 nm. The size measured by particle size analyzer was found to around 200 to 300 nm (result not shown). On careful observation it can be said that the sample looks well-ordered and the level of aggregation in this sample is very low as compared to the sample prepared in the absence of PVA. This suggests that the presence of the PVA in polymerization mixture has strongly influenced the morphology of synthesized PPy and is also responsible for better order and reduction in the aggregations. The inset in Figures 3(a) and 3(b) shows their respective transmission electron micrographs which further support the variation in particle size as well as a core-shell structure, the material of the shell being amorphous, and the core being formed by the more closely packed polymer macromolecules.

The variation of dc conductivity (σ_{dc}) for both the samples A and B is shown in Figure 4 as functions of (a) $1000/T$, (b) $T^{-1/2}$ in the temperature range 4.2–300 K. The temperature-dependent variation of dc conductivity data indicates that the charge transport seems to occur by phonon-assisted hopping or thermally activated jumps between localized states [26–28]. According to Mott and Davis, the dc conductivity (σ_{dc}) can be written [27] as

$$\sigma_{dc} = \sigma_o \exp\left\{-\left(\frac{T_0}{T}\right)^{\gamma}\right\}, \quad (1)$$

where σ_0 is the infinite temperature conductivity, σ_{dc} is the conductivity at temperature T, and T_0 is the Mott's characteristic temperature that determines the thermally activated hopping among localized states at different energies and is also considered as a measure of disorder. We have $\gamma = 1/(d+1)$, where d is the dimensionality. The values of $d = 1, 2, 3$ signify the 1-dimensional, 2-dimensional, and 3-dimensional Mott's VRH. A plot of log σ_{dc} versus $(1/T)^{\gamma}$ should give a straight line for proper value of γ. It is evident from this figure that for both the samples that is, prepared in presence (sample A) and absence of PVA (sample B) exhibits the linear dependence of log σ_{dc} versus $T^{-1/2}$ (Figure 4(b)) and is better than that of log σ_{dc} versus $T^{-1/4}$ (result not

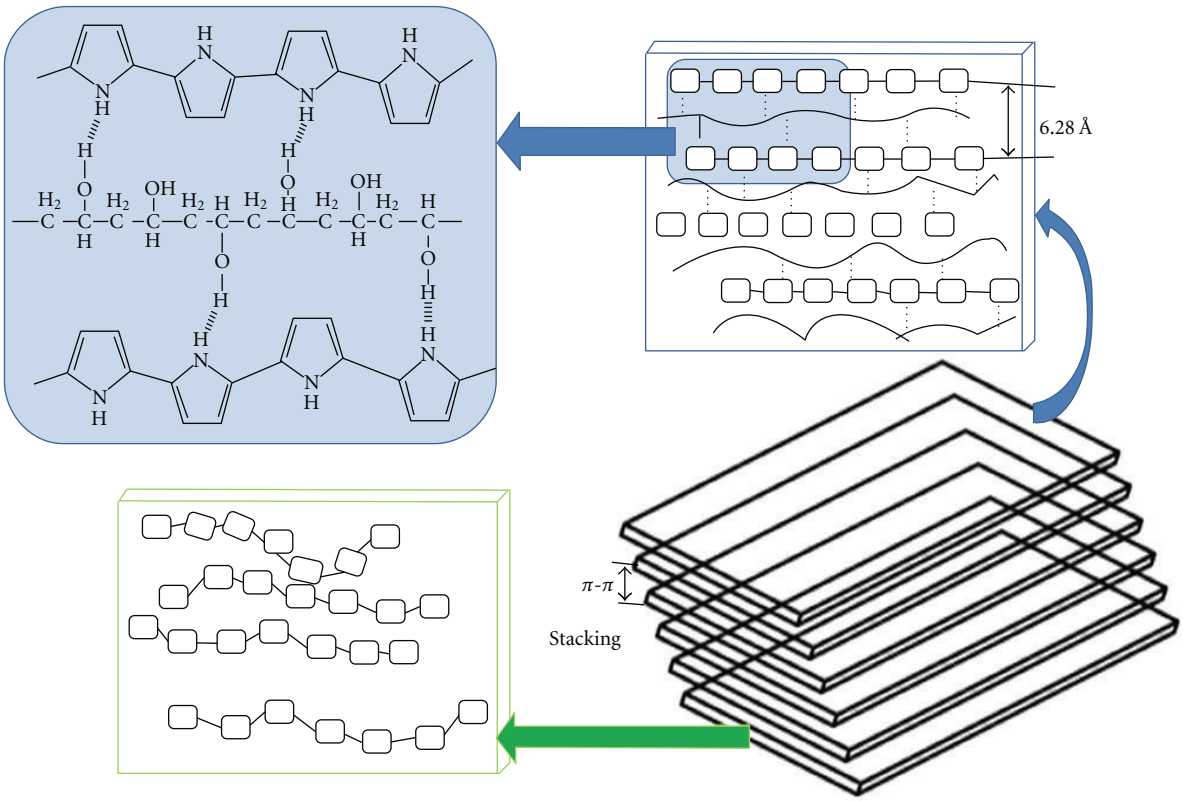

Figure 6: Mechanism of growth of PPy in presence of PVA showing the H-bonding assisted growth.

shown). The linearity factor of the PPy prepared in PVA is 0.99935 while for PPy prepared in absence of PVA is 0.96196. These linearity factors illustrate that the Mott's 1D-VRH mechanism of $T^{-1/2}$ type seems to be more appropriate [27, 29] for explaining the mechanism of dc conduction in both PPy samples.

The temperature region where (1) is valid should gives [26] the activation energy as

$$E_A = \frac{-d(\ln \sigma)}{d(1/k_B T)}, \tag{2}$$

where k_B is the Boltzmann's constant and E_A is the activation energy. Equation (2) can be correlated to the parameters of (1) and can be written as

$$E_A = \gamma k_B T_0 \left(\frac{T_0}{T}\right)^{\gamma-1}. \tag{3}$$

It is evident from (3) that a plot of log E_A versus log T should yield a straight line of slope = $(-(\gamma-1))$. To verify this, the activation energy (E_A) evaluated at different temperatures from Figure 4(a) has been plotted as log E_A versus log T in the temperature range 8–290 K and is shown in Figure 5. It can be clearly seen that the behavior of activation energy with temperature matches with a straight line corresponding to γ = 1/2 which is shown as a solid line in Figure 5. This gives a clear indication that the Mott's VRH mechanism of $T^{-1/2}$ type dominates the mechanism of charge transport in both PPy samples. Equations (1) and (3) give the slope T_0 from log σ_{dc} versus $T^{-1/2}$ plots (Figure 4) [27, 30] as

$$T_0 = \frac{B_0 \alpha^3}{k_B N(E_F)}, \tag{4}$$

where T_0 is the characteristic temperature, B_0 is dimensionless constant ~1.66 [27, 30], k_B is Boltzmann's constant, N (E_F) is the density of states at the Fermi level, and α (=1/r_P) is the coefficient of exponential decay of the localized states involved in the hopping process.

Based on the experimental observations, a mechanism explaining the role of PVA in improving the order and conjugation length has been proposed in Figure 6. The hydrogen in the O–H group of PVA is capable of forming bond with the hydrogen in the N–H group of the pyrrole ring. Thus hydrogen bonding takes place between the N–H group of the Pyrrole ring and O–H group of the PVA molecule. Now, PVA acts as a bridging agent between the PPy chains and forms a temporary soft template which controls the growth of the PPy chains as shown in Figure 6. PVA forms linkage between the PPy chains via hydrogen bonding. These hydrogen bonds act as temporary soft template which is responsible for increasing the order of the PPy nanoparticles and hence increase in conjugation length and conductivity.

4. Conclusion

PPy nanoparticles synthesized by microemulsion polymerization in the presence of PVA show better ordering and conjugation length than those synthesized in absence of PVA. This study shows the importance of H-bonding assistance during polymerization and gives rise to a promising method to the controllable synthesis of other conducting polymers with high conductivity.

Acknowledgments

The authors are thankful to Director of National Physical Laboratory, New Delhi for encouragement. The authors thank Dr. Ramadhar Singh for helpful discussions.

References

[1] Z. Yao, H. W. C. Postma, L. Balents, and C. Dekker, "Carbon nanotube intramolecular junctions," *Nature*, vol. 402, no. 6759, pp. 273–276, 1999.

[2] K. Ramanathan, M. A. Bangar, M. H. Yun, W. Chen, A. Mulchandani, and N. V. Myung, "Individually addressable conducting polymer nanowires array," *Nano Letters*, vol. 4, no. 7, pp. 1237–1239, 2004.

[3] J. W. Gardner and P. N. Bartlett, "Brief history of electronic noses," *Sensors and Actuators B*, vol. B18, no. 1, pp. 211–220, 1994.

[4] J. Huang, S. Virji, B. H. Weiller, and R. B. Kaner, "Polyaniline nanofibers: facile synthesis and chemical sensors," *Journal of the American Chemical Society*, vol. 125, no. 2, pp. 314–315, 2003.

[5] H. Peng, L. Zhang, C. Soeller, and J. Travas-Sejdic, "Conducting polymers for electrochemical DNA sensing," *Biomaterials*, vol. 30, no. 11, pp. 2132–2148, 2009.

[6] R. J. Tseng, J. Huang, J. Ouyang, R. B. Kaner, and Y. Yang, "Polyaniline nanofiber/gold nanoparticle nonvolatile memory," *Nano Letters*, vol. 5, no. 6, pp. 1077–1080, 2005.

[7] N. R. Chiou, C. M. Lui, J. J. Guan, L. J. Lee, and A. J. Epstein, "Growth and alignment of polyaniline nanofibres with superhydrophobic, superhydrophilic and other properties," *Nature Nanotechnology*, vol. 2, pp. 354–357, 2007.

[8] D. Li and R. B. Kaner, "Shape and aggregation control of nanoparticles: not shaken, not stirred," *Journal of the American Chemical Society*, vol. 128, no. 3, pp. 968–975, 2006.

[9] N. R. Chiou and A. J. Epstein, "Polyaniline nanofibers prepared by dilute polymerization," *Advanced Materials*, vol. 17, no. 13, pp. 1679–1683, 2005.

[10] M. X. Wan, "A template-free method towards conducting polymer nanostructures," *Advanced Materials*, vol. 20, no. 15, pp. 2926–2932, 2008.

[11] M. Yang, J. Ma, C. L. Zhang, Z. Z. Yang, and Y. F. Lu, "General synthetic route toward functional hollow spheres with double-shelled structures," *Angewandte Chemie International Edition*, vol. 44, no. 41, pp. 6727–6730, 2005.

[12] M. K. Shin, Y. J. Kim, S. I. Kim et al., "Enhanced conductivity of aligned PANi/PEO/MWNT nanofibers by electrospinning," *Sensors and Actuators B*, vol. 134, no. 1, pp. 122–126, 2008.

[13] J. Zang, C. M. Li, S. J. Bao, X. Cui, Q. Bao, and C. Q. Sun, "Template-free electrochemical synthesis of superhydrophilic polypyrrole nanofiber network," *Macromolecules*, vol. 41, no. 19, pp. 7053–7057, 2008.

[14] Y. C. Liu and C. J. Tsai, "Enhancements in conductivity and thermal and conductive stabilities of electropolymerized polypyrrole with caprolactam-modified clay," *Chemistry of Materials*, vol. 15, no. 1, pp. 320–326, 2003.

[15] B. R. Saunders, R. S. Fleming, and K. S. Murray, "Recent advances in the physical and spectroscopic properties of polypyrrole films, particularly those containing transition-metal complexes as counteranions," *Chemistry of Materials*, vol. 7, no. 6, pp. 1082–1094, 1995.

[16] J. M. Pernaut and J. R. Reynolds, "Use of conducting electroactive polymers for drug delivery and sensing of bioactive molecules. A redox chemistry approach," *The Journal of Physical Chemistry B*, vol. 104, no. 17, pp. 4080–4090, 2000.

[17] K. Jurewicz, S. Delpeux, V. Bertagna, F. Béguin, and E. Frackowiak, "Supercapacitors from nanotubes/polypyrrole composites," *Chemical Physics Letters*, vol. 347, no. 1–3, pp. 36–40, 2001.

[18] J. W. Goodwin, G. M. Markham, and B. Vinent, "Studies on model electrorheological fluids," *The Journal of Physical Chemistry B*, vol. 101, no. 11, pp. 1961–1967, 1997.

[19] J. Jang and J. H. Oh, "Novel crystalline supramolecular assemblies of amorphous polypyrrole nanoparticles through surfactant templating," *Chemical Communications*, no. 19, pp. 2200–2201, 2002.

[20] Y. Liu and Y. Chu, "Surfactant-assisted synthesis of single crystal $BaWO_4$ octahedral microparticles," *Materials Chemistry and Physics*, vol. 92, no. 1, pp. 59–63, 2005.

[21] F. Yan, G. Xue, and M. Zhou, "Preparation of electrically conducting polypyrrole in oil/water microemulsion," *Journal of Applied Polymer Science*, vol. 77, no. 1, pp. 135–140, 2000.

[22] M. K. Song, Y. T. Kim, B. S. Kim, J. Kim, K. Char, and H. W. Rhee, "Synthesis and characterization of soluble polypyrrole doped with alkylbenzenesulfonic acids," *Synthetic Metals*, vol. 141, no. 3, pp. 315–319, 2004.

[23] Y. Liu, Y. Chu, and L. Yang, "Adjusting the inner-structure of polypyrrole nanoparticles through microemulsion polymerization," *Materials Chemistry and Physics*, vol. 98, no. 2-3, pp. 304–308, 2006.

[24] M. Omastová, M. Trchová, J. Kovarová, and J. Stejskal, "Synthesis and structural study of polypyrroles prepared in the presence of surfactants," *Synthetic Metals*, vol. 138, no. 3, pp. 447–455, 2003.

[25] V. P. Menon, J. Lei, and C. R. Martin, "Investigation of molecular and supermolecular structure in template-synthesized polypyrrole tubules and fibrils," *Chemistry of Materials*, vol. 8, no. 9, pp. 2382–2390, 1996.

[26] R. K. Singh, A. Kumar, K. Agarwal et al., "DC electrical conduction and morphological behavior of counter anion-governed genesis of electrochemically synthesized polypyrrole films," *Journal of Polymer Science Part B*, vol. 50, no. 5, pp. 347–360, 2012.

[27] N. F. Mott and E. A. Davis, *Electronic Processes in Noncrystalline Materials*, Oxford University Press, London, UK, 2nd edition, 1979.

[28] R. K. Singh, A. Kumar, and R. Singh, "Mechanism of charge transport in poly(2,5-dimethoxyaniline)," *Journal of Applied Physics*, vol. 107, no. 11, Article ID 113711, 7 pages, 2010.

[29] Z. H. Wang, A. Ray, A. G. MacDiarmid, and A. J. Epstein, "Electron localization and charge transport in poly(o-toluidine): a model polyaniline derivative," *Physical Review B*, vol. 43, no. 5, pp. 4373–4384, 1991.

[30] D. S. Maddison and T. L. Tansley, "Variable range hopping in polypyrrole films of a range of conductivities and preparation methods," *Journal of Applied Physics*, vol. 72, no. 10, pp. 4677–4682, 1992.

ISSN: 2278 – 909X
International Journal of Advanced Research in Electronics and Communication Engineering (IJARECE)
Volume 1, Issue 4, October 2012

Evaluating Modified-BLEU Metric for English to Hindi Language Using ManTra Machine Translation Engine

Neeraj Tomer[1]
Banasthali University Banasthali

Deepa Sinha[2]
South Asian University

Piyush Kant Rai[3]
Banasthali University Banasthali

Abstract: Evaluation of MT is required for Indian languages because the same MT is not works in Indian language as in European languages due to the language structure. So, there is a great need to develop appropriate evaluation metric for the Indian language MT. The main objective of MT is to break the language barrier in a multilingual nation like India. The present research work aims at studying the Evaluation of Machine Translation Evaluation's Modified-BLEU Metric for English to Hindi for tourism domain. This work will help to give the feedback of the MT engines. We may make the changes in the MT engines and further we may revise the study.

Keywords: MT – Machine Translation, MTE-Machine Translation Evaluation, EILMT –Evaluation of Indian Language Machine Translation, ManTra – MAchiNe Assisted TRAnslation Technology, Tr – Tourism.

INTRODUCTION

Indian languages are highly inflectional, with a rich morphology, relatively free word order, and default sentence structure as Subject-Object-Verb. In addition, there are many stylistic differences. So the evaluation of MT is required for Indian languages because the same MT is not works in Indian language as in European languages. The same tools are not used directly because of the language structure. So, there is a great need to develop appropriate evaluation metric for the Indian language MT.

English is understood by less than 3% of Indian population. Hindi, which is official language of the country, is used by more than 400 million people. MT assumes a much greater significance in breaking the language barrier within the country's sociological structure. The main objective of MT is to break the language barrier in a multilingual nation like India. English is a highly positional language with rudimentary morphology, and default sentence structure as Subject-Verb-Object. The present research work aims at studying the "Evaluation of Machine Translation Evaluation's Modified-BLEU Metric for English to Hindi" for tourism domain. The present research work is the study of statistical evaluation of machine translation evaluation for English to Hindi. The research aims to study the correlation between automatic and human assessment of MT quality for English to Hindi. The main goal of our experiment is to determine how well a variety of automatic evaluation metric correlated with human judgment.

In the present work we propose to work with corpora in the tourism domain and limit the study to English – Hindi language pair. It may be assumed that the inferences drawn from the results will be largely applicable to translation for English to other Indian Languages. Our test data consisted of a set of English sentences that have been translated from expert and non-expert translators. The English source sentences were randomly selected from the corpus of tourism domain. These sentences are taken randomly from the different resources like websites, pamphlets etc. Each output sentence was score by Hindi speaking human evaluators who were also familiar with English. It may be assumed that the inferences drawn from the results will be largely applicable to translation for English to other Indian Languages, as assumption which will have to be tested for validity. We used ManTra MT engine for this work.

ManTra: C-DAC Pune has developed a translation system called ManTra. The work in ManTra has to be viewed in its potentiality of translating the bulk of texts produced in daily official activities. The system is facilitated with pre-processing and post-processing tools, which enables the user to overcome the problems/errors with minimum effort.

OBJECTIVE

The main goal of this work is to determine how well a variety of automatic evaluation metrics correlated with human scores. The other specific objectives of the present work are as follows.

1. To design and develop the parallel corpora for deployment in automatic evaluation of English to Hindi machine translation systems.
2. Assessing how good the existing automatic evaluation metrics Modified-BLEU, will be as MT evaluating strategy for evaluation of Indian language machine translation systems by comparing the results obtained

by this with human evaluator's scores by correlation study.

3. To study the statistical significance of the evaluation results as above, in particular the effect of-
   - size of corpus
   - sample size variations
   - increase in number of reference translations

Creation of parallel corpora: Corpus quality plays a significant role in automatic evaluation. Automatic metrics can be expected to correlate very highly with human judgments only if the reference texts used are of high quality, or rather, can be expected to be judged high quality by the human evaluators. The procedure for creation of parallel corpora is as under:

1. Collect English corpus from the domain from various resources.
2. Generate multiple references (we limit it to three) for each sentence by getting the source sentence translated by different expert translators.
3. XMLise the source and translated references for use in Automatic evaluation

Table 1: Description of Corpus

Domain	Source Language	Target Language	No. of Sentences	No. of Human Translation	Name of MT Engine
Tourism	English	Hindi	1000	3	Mantra

For the corpus collection our first motive was to collect as possible to get better translation quality and a wide range vocabulary. For this purpose the first corpus we selected to use in our study is collected from different sources. We have manually aligned the sentence pairs.

In our study for tourism domain we take 1000 sentences. When the text has been collected, we distributed this collected text in the form of Word File. Each word files having the 100 sentences of the particular domain. In this work our calculation will be based on four files- source file and three reference files. Reference files are translated by the language experts. We give the file a different identification. For e.g. our first file name is Tr_0001_En where Tr_ for tourism 0001 means this is the first file and En means this is the Candidate file. We treat this as the candidate file. In the same way our identification for the Hindi File is Tr_0001_Hi, in this Hi is for the Hindi file and we have called this a reference file. As we already mention that we are taking the three references we named them reference 1(R1), reference 2(R2), reference 3(R3). In the study we take the candidate sentence and the reference sentences, as shown below. For e.g.

Source Sentence: Known for their fine architecture, elegant speech and intellectual pursuits, they were the ancestors of the famous Aztecs.

Candidate Sentence: प्रसिद्ध के लिए उनका अच्छे अर्चिटेक्चर , सुंदर भाषण और बुद्धि जीवी अनुसरण , वे मशहूर अज़टेक्स का पूर्वजों थे

Reference Sentences: R1: अपने उत्तम स्थापत्य कला, सुन्दर भाषा और बौद्धिक अनुसरण के लिए जाना जाने वाला, वे प्रसिद्ध ऐज़टेक्स के पूर्वज थे ।

R2: अपने उत्कृष्ट स्थापत्य कला तथा सहज भाषा तथा बौद्धिक शौकों के लिए जाने गये, वे प्रसिद्ध एजटैक्स के पूर्वज थे ।

R3: वे प्रसिद्ध एजटेक्स के पूर्वज थे, उत्तम शिल्प, शिष्ट वाणी और मानसिक खोज के लिए जाने जाते हैं ।

HUMAN EVALUATION

Human evaluation is always best choice for the evaluation of MT but it is impractical in many cases, since it might take weeks or even months (though the results are required within days). It is also costly, due to the necessity of having a well trained personnel who is fluent in both the languages, source and targeted. While using human evaluation one should take care for maintaining objectivity. Due to these problems, interest in automatic evaluation has grown in recent years. Every sentence was assigned a grade in accordance with the following four point scale for adequacy.

	Score
• Ideal	1
• Acceptable	.5
• Not Acceptable	.25
• If a criterion does not apply to the translation	0

AUTOMATIC EVALUATION BY MODIFIED-BLEU METRIC

We used Modified-BLEU evaluation metric for this study. This metric is specially designed for English to Hindi. Modified-BLEU metric, designed for evaluating MT quality, scores candidate sentences by counting the number of n-gram matches between candidate and reference sentences. Modified-BLEU metric is probably known as the best known automatic evaluation for MT. To check how close a candidate translation is to a reference translation, an n-gram comparison is done between both. Metric is designed from matching of candidate translation and reference translations. We have chosen correlation analysis to evaluate the similarity between automatic MT evaluations and human evaluation. Next, we obtain scores of evaluation of every translated sentence from both MT engines. The outputs from both MT systems were scored by human judges. We used this human scoring as the benchmark to judge the automatic evaluations. The same MT output was then evaluated using both the automatic scoring systems. The automatically scored segments were analyzed for Spearman's Rank Correlation with the ranking defined by the categorical scores assigned by the human judges. Increases in correlation indicate that the automatic

systems are more similar to a human in ranking the MT output.

Statistical significance is an estimate of the degree, to which the true translation quality lays within a confidence interval around the measurement on the test sets. A commonly used level of reliability of the result is 95%. To reach at decision, we have to set up a hypothesis and compute p-value to get final conclusion.

The present research is the study of statistical evaluation of machine translation evaluation's Modified-BLEU metric. The research aims to study the correlation between automatic and human assessment of MT quality for English to Hindi. While most studies report the correlation between human evaluation and automatic evaluation at corpus level, our study examines their correlation at sentence level. The focus in this work is to examine the correlation between human evaluation and automatic evaluation and its significance value, not to discuss the translation quality. In short we can say that this research is the study of statistical significance of the evaluated results, in particular the effect of sample size variations.

So, firstly we take source sentences and then get these sentences translated by our MT engine, here we consider the Anuvadaksh. We have the different references of these sentences. After doing this we do the evaluations of these sentences human as well as the automatic evaluations and we collect the individual scores of the given sentences considering all the three references one by one. The following table shows the individual scores of the five sentences (particular sentences can be seen at the end of the paper) using different no. of references.

Table 2: Human Evaluation and Modified-BLEU Evaluation scores

S. No.	Modified-BLEU Score			
	Human Eval.	one no. of reference	two no. of references	three no. of references
1.	0.25	0.1503	0.1679	0.1679
2.	0.75	0.4971	0.6717	0.801
3.	1	0.2649	0.2727	0.2727
4.	0.5	0.1747	0.2513	0.3602
5.	0.75	0.1152	0.1171	0.1171

In this way we also collect the individual scores of all the sample sizes like 20, 60,100,200,300,500 and 1000 sentences. After this we do the correlation analysis of these values. In order to calculate the correlation with human judgements during evaluation, we use all English–Hindi human rankings distributed during this shared evaluation task for estimating the correlation of automatic metrics to human judgements of translation quality, were used for our experiments. In our study the rank is provided at the sentence level.

For correlation analysis we calculate the correlation between human evaluation and automatic evaluations one by one by the Spearman's Rank Correlation method. The Spearman's rank correlation coefficient is given as (when ranks are not repeated)-

$$\rho = 1 - \left(\frac{6\sum_{i=1}^{n} d^2}{n(n^2-1)} \right)$$

where d is the difference between corresponding values in rankings and n is the length of the rankings. An automatic evaluation metric with a higher correlation value is considered to make predictions that are more similar to the human judgements than a metric with a lower value. Firstly, we calculate the correlation value in between the human evaluation and automatic evaluation Modified-BLEU metric means human evaluation with Modified-BLEU for sample size 20, 60, 100, 200, 300, 500 and 1000.

Table 3: Correlation (ρ) values

Sample Size	ρ values		
	one no. of reference	two no. of references	three no. of references
20	.270	-.104	.196
60	.287	.245	.289
100	.183	.179	.187
200	.046	.008	.046
300	.050	-.024	-.054
500	-.002	-.050	-.056
1000	-.027	-.053	-.033

After calculating the correlation, we need to find out which type of correlation is there between the variables and of which degree and whether the values of the correlation are significant.

ANALYSIS OF STATISTICAL SIGNIFICANCE TEST FOR HUMAN EVALUATION AND AUTOMATIC EVALUATION

Statistical significance is an estimate of the degree, to which the true translation quality lays within a confidence interval around the measurement on the test sets. A commonly used level of reliability of the result is 95%, for e.g. if, say, 100 sentence translations are evaluated, and 30 are found correct, what can we say about the true translation quality of the system? To reach at decision, we have to set up a hypothesis and compute p-value to get final conclusion that whether there is any correlation between the human evaluations and automatic evaluations. If yes, then what is the type and degree of correlation? Also what is the significance of the correlation value? In this work we set the hypothesis that there is no correlation between the values of human and automatic evaluation. The p-value will provide the answer about the significance of the correlation value.

A Z-test is a statistical test for which the distribution of the test statistic under the null hypothesis can be approximated by a normal distribution. For each significance level, the Z-test has a single critical value (for example, 1.96 for 5% two

tailed) which makes it more convenient than the Student's t-test which has separate critical values for each sample size. The test statistic is calculated as:

$$Z = \frac{\bar{x}_1 - \bar{x}_2}{\sqrt{\frac{S_1^2}{n_1} + \frac{S_2^2}{n_2}}}$$

where $\bar{x}_1$ and $\bar{x}_2$ are the sample means, s_1^2 and s_2^2 are the sample variances, n_1 and n_2 are the sample sizes and z is a quartile from the standard normal distribution.

Table 4: p-values of output of Anuvadaksh using different no. of references

Sample Size	p-values		
	one no. of reference	two no. of references	three no. of references
20	0.0001	0.0001	0.0001
60	0.0001	0.0001	0.0001
100	0.0001	0.0001	0.0001
200	0.0183	0.0183	0.0183
300	0.0262	0.0594	0.0594
500	0.0314	0.0375	0.0375
1000	0.0322	0.0336	0.0336

Now on the basis of these values we conclude our results like which type and degree of correlation is there between the given variables and whether the correlation results are significant. In the above example we have done all the calculations by considering the single reference sentence and in tourism domain using 5 numbers of sentences.

But in our research work we consider the different references like 1, 2, 3 and we use the different sample sizes like 20, 60, 100, 200, 300, 500, and 1000. We see whether the results remains uniform for different sample sizes and different number of references in particular domains.

For above calculation we used following sentences:
English Sentences:

1. The other factor on Cortes side was the lucky coincidence that 1519 was the exact year when legend had it that the Aztec god, Quetzalcoatl, would return from the east and so Cortes was mistaken for a god.
2. Mexico City has a peculiar charm, possessing Mexico in microcosm: pollution and poverty intermingled with streets named after philosophers.
3. For those who love sailing, yachting and windsurfing, there are facilities in Goa as well as at Kovalam beach in Kerala.
4. Traverse the lonely stretches of the That Desert, like the travelers of old.
5. Boparais organization is situated on Chandigarh Shimla highway.

Candidate Sentences (translated by ManTra):

1. अन्य तत्व सौभाग्यशाली संयोग वह 1519 पर दन्तकथा जब वर्ष सटीक यह था कि अज़टेक ईश्वर , कुएट्ज़ल्कोअट्ल , पूर्व से प्रतिलाभ करेंगे और ऐसा था
2. मेक्सिको नगर निश्चित मनोहरता , स्वामी होने वाले मेक्सिको में लघु जगत् : प्रदूषण और गरीबी ने सड़कें नाम पर दार्शनिकों के साथ परस्पर मिश्रित किया जाए
3. उनके लिए जो प्रेम जलयात्रा करने वाले , नौका विहार और विंड्सुर्फिंग , वहाँ गोवा के रूप में अच्छा के रूप में कोवलाम समुद्र तट में केरला में सुविधा हैं
4. थार मरूस्थल का मालारेखा अकेला भूखंडों , यात्रियों का पुरानी को पसंद करते हैं
5. बोपरैस संगठन स्थित पर चंडीगढ़ शिमला राजपथ

RESULTS

In the domain tourism there is significance difference between the average evaluation score of human with Modified-BLEU at 5% level of significance and this is for sample sizes 20, 60 and 100.

In Table 2 (Correlation (ρ) values) correlation value for Modified-BLEU is .046 and .050 these values are for sample size 200 and 300 for three and tone number of references which is insignificant at 5% level of significance and same result are seen for the sample sizes 500 and 1000.

I. CONCLUSION

Corpus quality plays a significant role in automatic evaluation. This work will help to give the feedback of the MT engines. In this way we may make the changes in the MT engines and further we may revise the study.

II. ACKNOWLEDGMENT

The present research work was carried under the research project "English to Indian Languages Machine Translation System (EILMT)", sponsored by TDIL, Ministry of Communications and Information Technology, Government of India. With stupendous ecstasy and profundity of complacency, we pronounce utmost of gratitude to Late Prof. Rekha Govil, Vice Chancellor, Jyoti Vidyapith, Jaipur Rajasthan.

REFERENCES

1. Ananthakrishnan R, Bhattacharyya Pushpak, M. Sasikumar, Shah Ritesh, (2007): "Some Issues in Automatic Evaluation of English-Hindi MT", more blues for BLEU in proceeding of 5th International Conference on Natural Language Processing (ICON-07), Hyderabad, India.

2. Andrew FINCH, Eiichiro SUMITA, Yasuhiro AKIBA, "How Does Automatic Machine Translation Evaluation Correlate With Human Scoring as the Number of Reference Translations Increases?" ATR Spoken Language Translation Research Laboratories, 2-2-2 Hikaridai "Keihanna Science City" Kyoto, 2004, 619-0288, Japan, 2019-2022.
3. Bandyopadhyay S., "Teaching MT: an Indian perspective", Sixth EAMT Workshop "Teaching machine translation", November 14-15, UMIST, Manchester, 20002, England. 13-22.
4. Bandyopadhyay Sivaji, "State and Role of Machine Translation in India", Machine Translation Review, 2000, 11: 25-27.
5. Deborah Coughlin, "Correlating Automated and Human Assessments of Machine Translation Quality", In Proceedings of MT Summit IX. New Orleans, 2003, 63-70.
6. Donaway, R. L., Drummey, K. W., Mather, L. A., "A Comparison of Rankings Produced by Summarization Evaluation Measures", Proceedings of the Workshop on Automatic Summarization, 2000, 69-78.
7. Feifan Liu, Yang Liu, "Correlation between ROUGE and Human Evaluation of Extractive Meeting Summaries", the University of Texas at Dallas Richardson, TX 75080, USA, 2008, 201-208.
8. Gore Lata, Patil Nishigandha, "Paper on English To Hindi - Translation System", Proceedings of Symposium on Translation Support Systems STRANS-2002, IIT Kanpur.
9. Josan G. S., Lehal G. S.,"A Punjabi to Hindi machine Translation System", Coling 2008: Companion volume: Posters and Demonstrations, Manchester, UK, 2008, 157-160.
10. Keshav Niranjan, "Language Technology in India", Language in India, Strength for Today and Bright Hope for Tomorrow Volume 12: 4 April 2012 ISSN 1930-2040,187-195.
11. Lin C. Y., E. hovy., "Manual and Automatic Evaluations of Summaries", In Proceedings of the Workshop on Automatic Summarization, post-Conference Workshop of ACL.2002, 45-52.
12. Murthy, Deshpande B. K., W. R., " Language technology in India: past, present and future", http://www.cicc.or.jp/english/ hyoujyunka/ mlit3/7-12.html
13. Papineni, K., Roukos, S., Ward, T., and Zhu, W. J., "BLEU: a method for automatic evaluation of machine translation" in ACL-2002: 40th Annual meeting of the Association for Computational Linguistics, 2002 311–318.
14. Paula Estrella, Andrei Popescu-Belis , Maghi King (2007): "A New Method for the Study of Correlations between MT Evaluation Metrics", ISSCO/TIM/ETI University of Geneva 40, bd. du Pont-d'Arve 1211 Geneva, Switzerland, 35-43.
15. Philipp Koehn (2004): "Statistical Significance Tests for Machine Translation Evaluation" Computer Science and Artificial Intelligence Laboratory Massachusetts Institute of Technology, The Stata Center, 32 Vassar Street, Cambridge, MA 02139.
16. S.Niessen, F.J.Och, G. Levsch, and H.Ney., "An Evaluation Tool for Machine Translation: Fast Evaluation for Machine Translation Research", In Proceedings of the Second International Conference on Language Resources and Evaluation. Athens, Greece, 2000, 39-45.
17. Sanjay Kumar Dwivedi, Pramod Premdas Sukhadeve (2010): "Machine Translation System in Indian Perspectives", Department of Computer Science, Babasaheb Bhimrao Ambedkar University, Lucknow, India.
18. Sinha R. Mahesh K., Thakur Anil, "Machine translation of bi-lingual Hindi-English (Hinglish) text", MT Summit X, Phuket, Thailand, September 13-15, 2005, Conference Proceedings: the tenth Machine Translation Summit; 2005, 149-156.
19. Sitender, Bawa Seema, "Survey of Indian Machine Translation Systems", Department of CSE, Thapar University Patiala, Punjab 2010.
20. Stephan Minnis, "A Simple and Practical Method For Evaluating Machine Translation", Machine Translation 9: 133-149, 1994.
21. Tomer Neeraj and Sinha Deepa, "Evaluating Machine Translation Evaluation's BLEU Metric for English to Hindi Language Machine Translation", in The International Journal of Computer Science & Application, Vol-01-NO-06-Aug-2012, 48-58.
22. Tomer Neeraj and Sinha Deepa: "Evaluating Machine Translation Evaluation's NIST Metric for English to Hindi Language Machine Translation", paper accepted in The International Journal of Multidisciplinary Academy IJMRA for November-2012 issue.
23. Tomer Neeraj, "Evaluating Machine Translation (MT) Evaluation Metrics for English to Indian Language Machine Translation", Ph.D. Thesis 2012, Banasthali University, Banasthali.
24. Tomer Neeraj, Sinha Deepa and Rai Piyush Kant, "Evaluating Machine Translation Evaluation's F-Measure Metric for English to Hindi Language Machine Translation", in International Journal of Academy Research Computer Engineering and Technology, volume1, Issue 7, September 2012, 151-156.
25. Yanli Sun, "Mining the Correlation between Human and Automatic Evaluation at Sentence Level", School of Applied Language and Intercultural Studies, Dublin City University, 2004, 47-50.

Author 1

Neeraj Tomer
tneeraj12@rediffmail.com
9460762117

Area of Interest:

- Machine Translation and Indian Language Technology
- Theoretical Computer Science and related technologies

Academic Qualification:

Ph.D (thesis submitted) in Computer Science, Banasthali University, Banasthali.
MCA, Maharishi Dayanand University, Rohtak 2005.
Master of Economics, Kurukshetra University Kurukshetra 1999.
Bachelor of Economics, Kurukshetra University Kurukshetra 1997.

Employment History:

Post graduate and graduate teaching at Mahatma Gandhi Institute of Applied Sciences, Jaipur as a lecturer from July 2003 to August 2006. As a Research Associate at Banasthali University Banasthali in 2007. As a lecturer at LCRT College of Education Panipat from August 2007 to July 2010. As an Assistant Professor at SINE International Institute of Technology, Jaipur from August 2010 to March 2012.

- Papers Published : 2
- In Press : 2
- Communicated : 3

Seminar and Conferences Attended: 5

Research Guidance:

Guided 3 students for their dissertation work at PG (M.Sc) level.

Future Plans: To grow academically

Author 2

Deepa Sinha
Associate Professor
Department of Mathematics
South Asian University
Akbar Bhawan
Chanakyapuri, New Delhi 110021 (India)
Cell No: 08744022273
deepasinha2001@gmail.com

Research Area: **Graph Structures**

Academic Qualification:

M.Sc., Ph. D. (University of Delhi), CSIR-NET (twice)

Future Plans: To grow academically

Achievements: CSIR_NET (qualified Twice)

Publications:

(a) Books: one
(b) Research Papers: 27

Conference/workshop/symposium attended: 39
Invited talks delivered: Ten
Papers presented: 23
Work experience: 16 years

Served several Institutions for graduate and post graduate courses, particularly Khalsa Girls Degree College (1996-1999), Delhi College of Engineering (1999-2004), Banasthali University (2004-2012).
Seven students got awarded their M. Phil. Degree under her supervision.
Three students got awarded their Ph.D. in the year 2011-2012.
Have refereed several research papers for National and international Journal of high impact factor like Discrete Applied Mathematics, Graphs and Combinatorics, International Journal of Physical Sciences etc.
Sessions chaired in the National/ International conferences: four

Author 1

Name: Piyush Kant Rai
Date of Birth: February 5, 1980
E-Mail: raipiyush5@gmail.com

Current Affiliation:

Working as Assistant Professor (Senior-Scale) (Statistics) in the Department of Mathematics & Statistics (AIM & ACT), Banasthali University, Rajasthan.

Working Experience: Eight years of teaching and research experience including one year experience as a Project Assistant at Banaras Hindu University (BHU), U.P. and five months as a Statistical Fellow at Sanjay Gandhi Post Graduate Institute of Medical Sciences (SGPGIMS) Lucknow, U.P.

UGC Major/Minor Project: One Minor Research Project as Principal Investigator and one Major Research Project as Co-Principal Investigator.

Academic Qualification:

- Ph.D. (Statistics) from Banasthali University, Rajasthan.
- M.Phil. (Statistics), 2008, with First Class from Periyar Institute of Distance Education (PRIDE), Periyar University, Salem Tamilnadu.
- M.Sc. (Statistics), 2003, with First Rank (Gold Medal) from Banaras Hindu University (BHU), Varanasi, U.P.
- B.Sc. (Hons., Statistics), 2001, with First Class (5^{th} Rank in Faculty of Science) from Banaras Hindu University (BHU), Varanasi, U.P.
- Intermediate (Physics, Chemistry, Math, Hindi and English), 1996, with First Class (1^{st} Rank in College) from U.P. Board.
- High School (Hindi, English, Science, Math, Social Science and Biology), 1994, with first-Honours (1^{st} Rank in School) from U.P. Board.

Qualified National Eligibility Test:

- UGC NET, June 2004, UPSLET, August 2004 and ISI-JRF, May 2005.

Scholarships:

- 10^{th} to 12^{th} standard, 8^{th} to 10^{th} standard and 6^{th} to 8^{th} standard scholarship by Education Department U.P.

Publication: (National/International):

- Papers Published: 8, In Press: 1, Communicated: 3
- Books Published: Two Book Chapters are published and two are in Press.

Supervisor of 2 Ph.D. Scholars and 5 M.Phil. Scholars
Workshop and Training Program Attended /Organized: 17
Seminar and Conference Attended/Organized: 12

2012 Fourth International Conference on Computational Intelligence, Modelling and Simulation

Extended Species Abundance Models of Biogeography Based Optimization

[1]Lavika Goel, [1] Daya Gupta
[1]Department of Computer Engineering,
Delhi Technological University,
Delhi, India.
e-mail: goel.lavika@gmail.com, dgupta@dce.ac.in

[2]Vinod Panchal
[2]Defense and Terrain Research Lab (DTRL),
Defense and Research Development Organization,
Delhi, India.
e-mail: vkpans@ieee.org

***Abstract* --- This paper is an extension to the models of species abundance in biogeography based optimization technique. We present the extended species abundance models by defining the parameter species growth rate as a function of species evolution rate and the species immigration rate and species decline rate as a function of species extinction rate and emigration rate for the determination of the total species count at a given time instant on a single habitat, as opposed to the Simon's model which relies upon migration only for the determination of the species count. We also introduce an additional dependency factor which signifies the interdependence of migrating species on each other such as the predator-prey relationships; to be considered for the determination of immigration and emigration rates and hence further extend the original model of species abundance in a single habitat. We discuss the extended BBO and its mathematics and then go on to present the extended forms of each of the six representative migration models that were originally proposed by Haiping Ma as an extension to the work by Simon. We demonstrate the performance of each of the extended models of BBO by running them on standard benchmark functions and found that the average convergence of each of the proposed extended species abundance models is faster leading to better optimization results than the original species abundance model of BBO.**

Keywords--- biogeography based optimization; species population modeling; evolutionary algorithms; benchmark functions.

I. INTRODUCTION

Biogeography based Optimization (BBO) is a new population based evolutionary optimization method which is inspired from the migration mechanism of ecosystems [14]. As a global optimization method, BBO is an original algorithm based on the mathematical model of organism distribution in biological systems. Biogeography based optimization is a technique that has been adaptively applied in various areas of computer intelligence [1], including genetic algorithms (GAs) [10], ant colony optimization (ACO) [3], and particle swarm optimization (PSO) [7]. This evolutionary algorithm was introduced by Simon [14] in 2008 and demonstrated good optimization performance on various benchmark functions. In the original BBO paper, it was illustrated that BBO is competitive with other EAs. It could become a popular EA if it continues to improve with additional extensions and modifications (for example, oppositional BBO [4] and blended BBO [9]), and if it is applied to additional practical engineering problems (for example, ECG diagnosis [11], power system optimization [13], economic load dispatch [2], and satellite image classification [5, 12]).

This paper is an extension to the Simon's model of species abundance in biogeography based optimization technique. The paper introduces an additional dependency factor which signifies the interdependence of migrating species on each other such as the predator-prey relationships to be considered for the determination of immigration and emigration rates and hence modifies the Simon's model of species abundance in a single habitat. Motivated by natural biogeography, new migration models were incorporated in BBO [8] and six representative migration models were formulated. We discuss the extended BBO and its mathematics and then go on to present the extended forms of each of the six representative migration models that were originally proposed by Haiping Ma [8] as an extension to the work by Simon [14].

The rest of this paper is organized as follows. Section 2 gives a brief overview of the BBO algorithm as an optimizing approach. Section 3 first describes the theoretical foundations of the extended model of species abundance in biogeography, and proves new theorems about species count probabilities; second, it extends the six representative migration models by Ma [8] and presents our extended species abundance models. Section 4 presents the performance analysis of the extended models of BBO and compares their performance with the Simon's model of BBO on standard benchmark functions. Section 5 presents the conclusions and directions for future research.

II. BIOGEOGRAPHY BASED OPTIMIZATION (BBO)

BBO is a population based EA motivated by the migration mechanisms of ecosystems. It is based on the mathematics of biogeography. In BBO, problem solutions are represented as islands, and the sharing of features between solutions is represented as emigration and immigration. The idea of BBO was first presented in December 2008 by D. Simon [14]. It is an example of a natural process that can be modeled to solve general optimization problems. One characteristic of BBO is that the original population is not discarded after each generation; it is rather modified by migration. Also for each generation, BBO uses the fitness of each solution to

2166-8531/12 $26.00 © 2012 IEEE
DOI 10.1109/CIMSim.2012.30

determine its emigration and immigration rate [8, 14]. In a way, we can say that BBO is an application of biogeography to EAs. In BBO, each individual is considered as a habitat with a HSI [8, 14], which is similar to the fitness of EAs, to measure the individual fitness. Also, an SIV which characterizes the habitability of an island is used. A good solution is analogous to an island with a high HSI, and a poor solution indicates an island with a low HSI. High HSI solutions tend to share their features with low HSI solutions. Low HSI solutions accept a lot of new features from high HSI solutions [14]. The algorithm for biogeography based optimization is given in fig. 1.

Initialize the BBO parameters, the maximum species count S_{max} and the maximum migration rates E and I, the maximum mutation rate m_{max} , an elitism parameter and a random set of habitats, each habitat corresponding to a potential solution to the given problem.
For each habitat
Map the HSI to the number of species K, the immigration rate λ, and the emigration rate μ.
Probabilistically use immigration and emigration to modify each non-elite habitat.
Re-compute each HSI.
Update the probability of its species count using (4). Then mutate each non-elite habitat based on its probability and re-compute each HSI.
End For
End.

Figure 1: Algorithm for biogeography based optimization

III. EXTENDED MODELS OF SPECIES ABUNDANCE IN BIOGEOGRAPHY

This section presents the theoretical framework and the proposed extended models of species abundance in biogeography.

A. Biogeography with species population modeling

This section presents the concepts of biogeography with species population modeling for the development of the extended BBO models. Biogeography theory proposes that the number of species found on a habitat is mainly determined by immigration and emigration. Immigration is the arrival of new species into a habitat or population, while emigration is the act of leaving one's native region. In addition there are other important factors which increase the species count other than the immigration rate between habitats, including the cross-breeding rate, reproduction rate, human activity, bringing in species through wind, or natural causes, etc. We consider these factors as contributors to the population evolution rate [6]. Factors which lead to a decrease in the species count include predator-prey relationships, competition for available resources, etc. These factors contribute to the population extinction rate [6]. Hence, these factors make the immigration and the emigration curves complicated as was presented in our paper [6], contrary to those described in the original BBO [14] and the models proposed by Haiping Ma [8].

We also introduce a factor called the dependency factor (φ) with the emigration rate. The factor is an important factor in the determination of the emigration rate since species tend to resist migration because of the dependency on other species until this dependence questions the survivability of the species themselves because of a deteriorating habitat suitability index. The HSI value of a habitat decreases with the deterioration of favorable factors (SIVs) such as rainfall, temperature, diversity of vegetation, topography, etc. Thus, the dependency factor (φ) signifies the interdependence of migrating species on each other one such example being the predator-prey relationships. We model our dependency factor as the ratio of the number of groups of dependent species (N) and the total number of species S for a non-zero value of $N\ and\ 1$ for $N = 0$ in equation (1). Thus,

$$\varphi = \begin{cases} \dfrac{Number\ of\ groups\ of\ dependent\ species\ (N)}{S}, & N \neq 0 \\ 1, & N = 0 \end{cases} \quad (1)$$

Hence, we extend the original model proposed by Simon [14], and propose an extended species abundance model where we define two factors namely, the growth rate and the decline rates [6] as below in equations (2) and (3) respectively. (The mathematical formulations for the derivation of evolution and extinction rates are discussed in our paper [6]).

$$Species\ Growth\ Rate = Immigration\ Rate + Evolution\ Rate = \sigma_k = I\left(1 - \frac{k}{n}\right) + \frac{c}{k} \quad (2)$$

And, $Species\ Decline\ Rate = Emigration\ Rate + Extinction\ Rate = \rho_k = \frac{Ek}{n} + 2\sqrt{n.k}$

Since, some species' movement is interdependent, we add a dependency factor φ to our mathematical formulation of the decline rates and the growth rates $\rho_k\ and\ \sigma_k$ in order to account for this dependency.

Thus,

$$Species\ Decline\ Rate = Emigration\ Rate(with\ the\ effect\ of\ dependency\ factor) + Extinction\ Rate = \rho_k = \frac{Ek\varphi}{n} + 2\sqrt{n.k} \quad (3)$$

B. Extended Models of species abundance

According to different mathematical models of biogeography [8], various migration curves were proposed by Ma in his paper [8]. To explore the influence of migration curve shape on optimization performance, he listed six representative migration models. We extend these migration models by considering factors other than migration (as discussed in the previous section) to formulate the extended species abundance model. We thereby present the modified forms of each of the six migration models proposed by Ma [8] and call these as the generalized species abundance models. The first three are extended versions of the linear models [8], which means that the immigration rate λ_k and the emigration rate μ_k are linear (or at least affine) functions of the number of species k, and the other three are extended versions of the nonlinear models [8].

1) Linear models

Model 1: (constant immigration and linear emigration model)

The emigration rate μ_k is linear with respect to the number of species k, and the immigration rate λ_k is constant and equal to half of I. The proposed extended species abundance curve is illustrated in fig. 2(a) and the probability curve is shown in fig. 2(b). The growth rate and the decline rate are as derived below in equations (4) and (5) respectively.

$$\text{Growth rate } \sigma_k = \frac{I}{2} + \frac{c}{k} \tag{4}$$

$$\text{Decline rate } \rho_k = \frac{Ek\varphi}{n} + 2\sqrt{nk} \tag{5}$$

Model 2: (linear immigration and constant emigration model)

The immigration rate λ_k is linear with respect to the number of species k, and the emigration rate μ_k is constant and equal to half of E. The proposed extended species abundance model is illustrated in fig. 2(a) and the probability curve is shown in fig. 2(b). The growth rate and the decline rate are as derived below in equations (6) and (7) respectively.

$$\text{Growth rate } \sigma_k = I\left(1 - \frac{k}{n}\right) + \frac{c}{k} \tag{6}$$

$$\text{Decline rate } \rho_k = \frac{E\varphi}{2} + 2\sqrt{nk} \tag{7}$$

Model 3: (linear immigration and linear emigration model)

This model was presented in the original BBO paper [14]. The immigration rate λ_k and the emigration rate μ_k are linear functions of the number of species k in the habitat. The proposed extended species abundance model is illustrated in fig. 2(a) and the probability curve is shown in fig. 2(b). The growth rate and the decline rate are as derived below in equations (8) and (9) respectively.

$$\text{Growth rate } \sigma_k = I\left(1 - \frac{k}{n}\right) + \frac{c}{k} \tag{8}$$

$$\text{Decline rate } \rho_k = \frac{Ek\varphi}{2} + 2\sqrt{nk} \tag{9}$$

2) Non-Linear Models

Ma proposed three nonlinear migration models, a trapezoidal migration model, a quadratic migration model and a sinusoidal migration model. We present the extended forms of each of these non-linear models.

Model 4: (Trapezoidal migration model)

The immigration rate λ_k and the emigration rate μ_k are trapezoidal functions of the number of species k. The proposed extended species abundance model is illustrated in fig. 2(a) and the probability curve is shown in fig. 2(b). The growth rate and the decline rate are as derived below in equations (10) and (11) if $k \leq i'$ and (12) and (13) if $k \leq n$ respectively.

If $k \leq i'$ $\quad (I \geq E)$

$$\text{Growth rate } \sigma_k = I + \frac{c}{k} \tag{10}$$

$$\text{Decline rate } \rho_k = \frac{2Ek\varphi}{2} + 2\sqrt{nk} \tag{11}$$

$Else \quad k \leq n \qquad (I < E)$

$$\text{Growth rate } \sigma_k = 2I\left(1 - \frac{k}{n}\right) + \frac{c}{k} \tag{12}$$

$$\text{Decline rate } \rho_k = E\varphi + 2\sqrt{nk} \tag{13}$$

where i' is the smallest integer that is greater than or equal to $(n + 1)/2$; that is, $i_0 = ceil((n + 1)/2)$.

Model 5: (quadratic migration model)

The migration rate λ_k and μ_k are convex quadratic functions of the number of species k. The proposed extended species abundance model is illustrated in fig. 2(a) and the probability curve is shown in fig. 2(b). The growth rate and the decline rate are as derived below in equations (14) and (15) respectively.

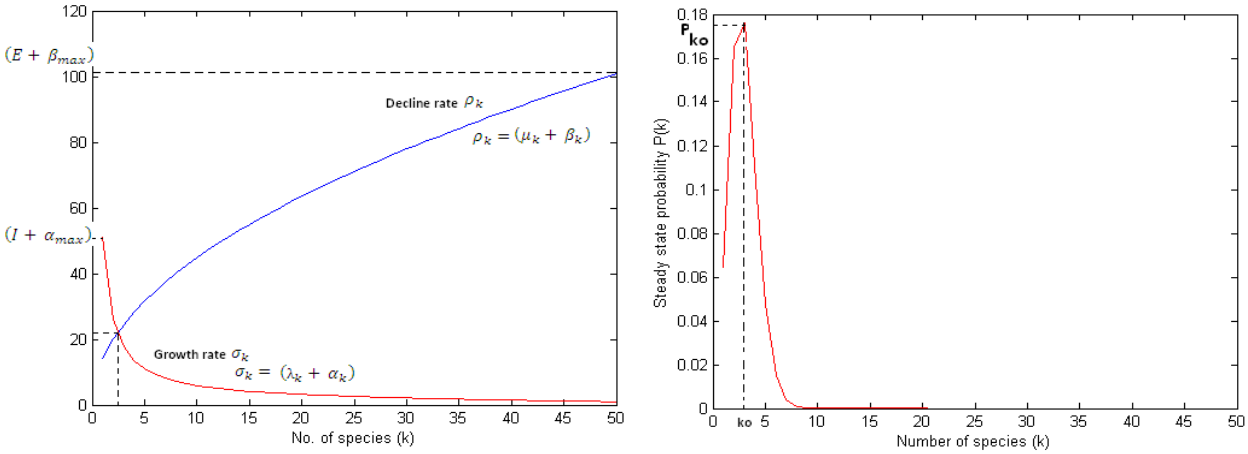

Figure 2: (a) Proposed extended species abundance model. (b) Steady state probability P_k as a function of species count k , where k_0 is the equilibrium number of species , and P_{k_0} is its corresponding probability.

$$\text{Growth rate } \sigma_k = I\left(\frac{k}{n} - 1\right)^2 + \frac{c}{k} \quad (14)$$

$$\text{Decline rate } \rho_k = E\varphi\left(\frac{k}{n}\right)^2 + 2\sqrt{nk} \quad (15)$$

Model 6: (sinusoidal migration model)

The migration rate μ_k and λ_k are sinusoidal functions of the number of species k, resulting in a bell-like shape. The proposed extended species abundance model is illustrated in fig. 2(a) and the probability curve is shown in fig. 2(b). The growth rate and the decline rate are as derived below in equations (16) and (17) respectively.

$$\text{Growth rate } \sigma_k = \frac{I}{2}\left(cos\left(\frac{k\pi}{n}\right) + 1\right) + \frac{c}{k} \quad (16)$$

$$\text{Decline rate } \rho_k = E\varphi\left(-cos\left(\frac{k\pi}{n}\right) + 1\right) + 2\sqrt{nk} \quad (17)$$

It is to be noted that the extended species abundance model as well as the corresponding probability curve is same for all the six migration models. This is because of the overshadowing effect of the evolution and extinction curves on the migration curves. The evolution curve which is basically a rectangular hyperbola overshadows the effect of the species growth by immigration and the extinction curve which is a y-axis centered parabola scales down the effect of the species decline by emigration. This means that evolution and extinction play a major role in the determination of the species count on a habitat at a given time instant and hence the species growth rates and decline rates are primarily determined by evolution and extinction of species rather than by migration under normal circumstances. Also, the addition of the dependency factor in the determination of the emigrating species further diminishes the role of emigration in the determination of species count on a habitat and hence, we propose our species abundance model as presented in fig. 2(a) and the corresponding probability curve as given by fig. 2(b). We therefore model the species count on a habitat not as a function of migration only but as a function of migration (modeling the effect of dependency factor) as well as evolution / extinction of species on the habitat under consideration. Hence, we extend each of the migration models by Ma [8] and define the growth and the decline rates as a function of migration and evolution / extinction. The modified definitions of growth rates and decline rates for each of the six representative models are as presented above.

Fig. 2(a) presents our species abundance model in a single habitat. Maximum values of immigration and emigration are E and I. The equilibrium point is k_0 at which the species immigration rate and the emigration rates are equal. The figure presents our model of species abundance where the species abundance is a function of species growth and species decline rate. Species growth rate is a function of the immigration λ_k and the evolution rates α_k and is equal to $(\lambda_k + \alpha_k)$. Species decline rate is the function of emigration μ_k and the extinction rates β_k and is equal to $(\mu_k + \beta_k)$. The equilibrium point is k_0 at which the species growth rate and the decline rates are equal. The maximum value of the growth rate curve and decline rate curves are achieved at $I + \alpha_{max}$ and $E + \beta_{max}$ respectively. Hence, we can see how the inclusion of the two additional factors as well as the dependency factor which characterize the population growth rates and the decline rates [6] have affected the species abundance model. For the proposed model, the probability P_k is an even function with respect to its midpoint, as shown in fig. 2(b). By looking at the equilibrium point on the probability curve of fig. 2(b), we see that there is high probability near the equilibrium point k_0. We also observe that the equilibrium point k_0 is reached earlier than indicated by Simon's model. This means that the habitat is the most stable when there are fewer species. The point k_0 can be found by equating the growth rates and the decline rates.

IV. PERFORMANCE ANALYSIS

In order to explore the benefits of the proposed models of BBO, we compare their performance on two standard benchmark functions, the Step function and the Griewank function. Each algorithm had a population size of 50, an elitism parameter of 2. We ran 50 Monte Carlo simulations of each algorithm on the benchmark to get representative performances.

Tables I and II show the absolute best minima and the *average* minima found by each model, averaged over 50 Monte Carlo runs for the Step and the Griewank functions respectively. The tables show the *average* performance of each model, as well as the *best* performance of each model for the step as well as the Griewank functions. It can be observed from the tables that the best and the average performances of each of the proposed extended species abundance models is better than the original Simon's species abundance model [14] which is evident from the fact that the average and the absolute minimal cost found for each of the extended models is much lower than that found by the original BBO model. For example, the absolute minima for model 3 is 70 and 9 for the Step and the Griewank functions respectively whereas for original BBO it is 102 and 20, almost half of that of the Simon's model, that for model 2 is 286 and 12 whereas for Simon's model, it is 564 and 16 for the Step and Griewank functions

TABLE I: MEAN OPTIMIZATION RESULTS AND CPU TIMES ON BENCHMARK FUNCTION 'STEP'. THE NUMBERS SHOWN ARE THE MINIMUM AND THE AVERAGE FUNCTION VALUES FOUND BY THE MODELS, AVERAGED OVER 50 MONTE CARLO SIMULATIONS.

Step function	Models of BBO			BBO		
	Best	Mean	CPU Time	Best	Mean	CPU Time
Model 1	22	793.84	0.5470	103	1081.32	0.5470
Model 2	286	1194.02	0.6410	564	1318.26	0.5160
Model 3	70	1079.74	0.5470	102	1104.14	0.5000
Model4(a)	270	714.90	0.5630	537	1629.44	0.4850
Model4(b)	149	738.72	0.5000	199	986.88	0.5160
Model 5	11	1171.68	0.5310	22	1824.02	0.5150
Model 6	79	396.44	0.5000	182	531.50	0.5310

TABLE II: MEAN OPTIMIZATION RESULTS AND CPU TIMES ON BENCHMARK FUNCTION 'GRIEWANK'. THE NUMBERS SHOWN ARE THE MINIMUM AND THE AVERAGE FUNCTION VALUES FOUND BY THE MODELS, AVERAGED OVER 50 MONTE CARLO SIMULATIONS.

Griewank function	Models of BBO			BBO		
	Best	Mean	CPU Time	Best	Mean	CPU Time
Model 1	3	40.27	2.6250	4	51.36	2.6250
Model 2	12	62.52	2.6400	16	72.16	2.6100
Model 3	9	66.49	2.5940	20	68.38	2.6090
Model4(a)	11	32.17	2.6720	15	63.11	2.6090
Model4(b)	11	44.35	2.5780	17	75.05	2.5940
Model 5	13	65.73	2.5630	16	83.32	2.5780
Model 6	12	83.32	2.5780	15	92.55	2.8120

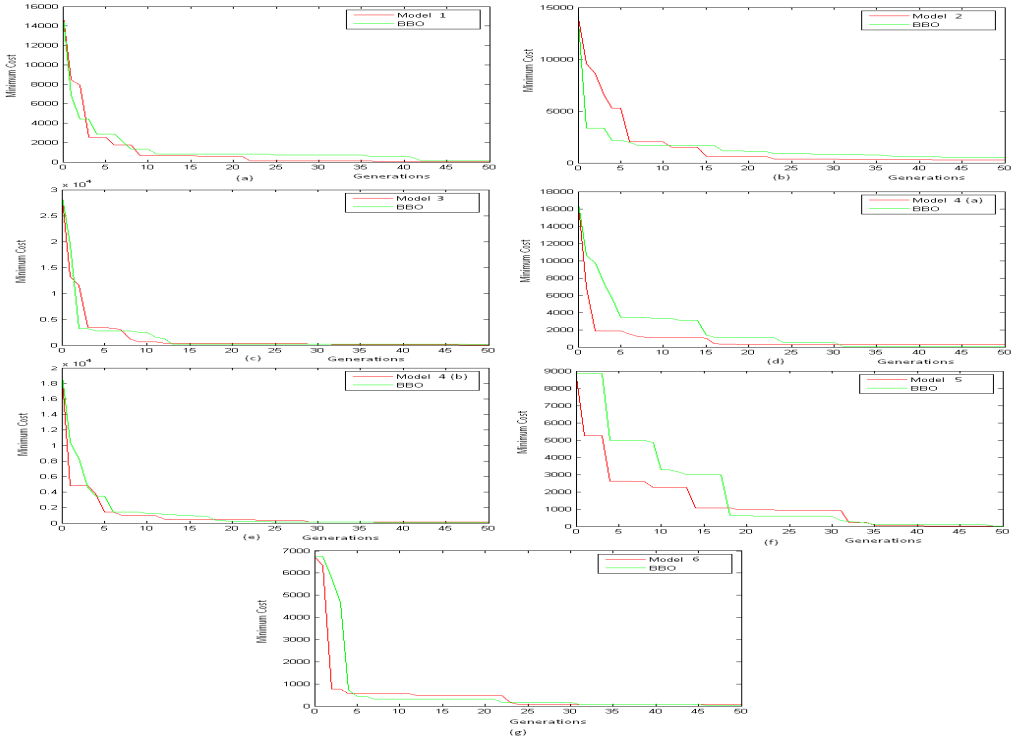

[2]Figure 3 (a) - (f): Graph plot of the minimum cost values for each of the proposed extended migration models of BBO over 50 simulations for the Step function. The color codes are: 'red' – proposed extended model and 'green' – original Simon's model of BBO [2].

respectively and similarly for the other models too. This can be explained by the fact that with the incorporation of other factors of evolution / extinction, the equilibrium point k_0 is reached earlier than that indicated by Simon's model and hence, convergence to a minimal cost value is faster in the proposed model. Also, the inclusion of the concept of dependency in migration of species in the determination of true migration rates further decreases the minimal cost value found by the proposed model thereby increasing the efficiency of optimization leading to better optimization results. From Tables I and II, we also observe that the CPU times have not increased substantially as opposed to the decrease in the cost functions that they provide for each of the models.

The CPU times are greater than the Simon's model for model 2 and 4(a) only for both the Step and the Griewank functions while they are comparable for rest of the other models. Figs. 3(a) - (f) present the graph plot of the minimum cost values for each of the proposed extended species abundance models of BBO for the Step function over 50 simulations. The color codes are 'red' for the minimum cost graph plot for the proposed extended model and 'green' for the minimum cost values found by the original Simon's model of BBO over 50 monte carlo simulations [14]. From the graphs, it can be easily observed that the absolute minima found by each of the proposed extended models of BBO is lower than that found by the Simon's model.

V. CONCLUSION AND FUTURE SCOPE

This paper is an extension to the Simon's model of species abundance in biogeography based optimization technique wherein the determining factor for the species count at a given time instant on a single habitat has been redefined by the inclusion of evolution and extinction factors along with the migration rates. Hence, we reformulate the governing factors of the species count function as the species growth rates and the species decline rates. We also presented the extended forms of each of the six representative migration models that were originally proposed by Haiping Ma [8] as an extension to the work by Simon [14]. We also demonstrated the performance of each of the extended models of BBO by running them on standard benchmark functions and found that the average convergence of each of the proposed extended species abundance models is faster than the original Simon's species abundance model of BBO hence leading to better optimization results than the original model. We note that CPU time is a bottleneck to the implementation of many population-based optimization algorithms. If an algorithm does not converge rapidly, it will be impractical, since it would take too long to find a near-optimal solution. However, the proposed extended models of BBO do not seem to require an unreasonable amount of computational effort; and require CPU times comparable with that of the Simon's model of BBO which further adds to the strengths of these models.

BBO presents promising potential but still requires additional theoretical and empirical investigations. For future work, we can further tune the extended species abundance models as inspired by other aspects of biogeography, seeking the best possible performance for BBO. We can also incorporate features from other EAs into BBO to improve optimization performance.

REFERENCES

[1] Ethem Alpaydin, "Introduction to machine learning", MIT Press, 2004.

[2] A. Bhattacharya, P. Chattopadhyay, "Solving complex economic load dispatch problems using biogeography-based optimization", Expert Systems with Applications 37 (5) (2010) 3605–3615.

[3] M. Dorigo, V. Maniczzo, A. Colomi, "Ant system: optimization by a colony of cooperating agents", IEEE Transaction on Systems, Man, and Cybernetics Part B 26 (1996) 29–41.

[4] M. Ergezer, D. Simon, D.W. Du, "Oppositional biogeography-based optimization", in: Proceeding of IEEE the Conference on Systems, Man, and Cybernetics, San Antonio, TX, 2009, pp. 1035–1040.

[5] Lavika Goel, Daya Gupta, V.K. Panchal, "Hybrid bio-inspired techniques for land cover feature extraction: A remote sensing perspective," Applied Soft Computing, Elsevier publications, 12, pp. 832-849, 2012.

[6] Lavika Goel, Daya Gupta, V.K. Panchal, "Dynamic model of blended biogeography based optimization for land cover feature extraction", Springer CCIS 306 (LNCS), pp. 8-19, IC3, 2012.

[7] J. Kennedy, R.C. Eberhart, "Particle swarm optimization", in: Proceedings of the IEEE International Conference on Neural Networks, Piscataway, NJ 1995, pp. 1942-1948.

[8] Haiping Ma, "An analysis of the equilibrium of migration models for biogeography-based optimization", Information Sciences 180, pp. 3444–3464, 2010.

[9] H.P. Ma, D. Simon, "Biogeography-based optimization with blended migration for constrained optimization problems", in: Proceedings of GECCO-2010, Portland, Oregon, July, 2010.

[10] H. Muhlenbein, D. Schlierkamp-Voosen, "Predictive models for the breeder genetic algorithm", I. Continuous parameter optimization, Evolutionary Computation 1 (1993) 25–49.

[11] M. Ovreiu, D. Simon, "Biogeography-based optimization of neuro-fuzzy system parameters for diagnosis of cardiac disease", in: Proceedings of GECCO-2010, Portland, Oregon, July, 2010.

[12] Panchal, V., Singh, P., Kaur, N., Kundra, H., "Biogeography based satellite image classification", International Journal of Computer Science and Informa- tion Security 6 (2), 269–274, 2009.

[13] R. Rarick, D. Simon, F.E. Villaseca, B. Vyakaranam, "Biogeography-based optimization and the solution of the power flow problem", in: Proceedings of the IEEE on Systems, Man, and Cybernetics, San Antonio, Texas, 2009, pp. 1029–1034.

[14] Dan Simon, "Biogeography based optimization", IEEE Transactions on Evolutionary Computation, Vol. 12, No. 6, 2008.

Feasibility Evaluation of VANET using Directional-Location Aided Routing (D-LAR) Protocol

Ram Shringar Raw[1], Sanjoy Das[2], Nanhay Singh[1], Sanjeet Kumar[3], and Shailender Kumar[1]

[1]Ambedkar Institute of Advanced Communication Technologies & Research, Delhi, India

[2]School of Engineering and Technology, Galgotias University, Uttar Pradesh, India

[3]Dr. Bhimrao Ambedkar University, Agra, India

Abstract

Vehicular Ad hoc Networks (VANETs) allow vehicles to form a self-organized network without any fixed infrastructure. VANETs have received wide attention and numerous research issues have been identified in the recent time. The design and implementation of efficient and scalable routing protocols for VANETs is a challenging task due to high dynamics and mobility constraints. In this paper, we have proposed D-LAR (Directional-Location Aided Routing), is an extension of Location Aided Routing (LAR) with Directional Routing (DIR) capability. D-LAR is a greedy approach based-position based routing protocol to forward packet to the node present in request zone within the transmission range of the source node as most suitable next-hop node. We have justified the feasibility of our proposed protocol for VANET.

Keywords: *VANET, Routing Protocol, DIR, LAR, D-LAR, Feasibility Evaluation.*

1. Introduction

Vehicular Ad hoc Network (VANET) is a rapidly emerging new class of mobile ad hoc networks. VANET consists of a large number of vehicles providing connectivity to each other. We assume that vehicles move in every direction with high mobility. Neighboring vehicles that are within a transmission range directly communicate over a wireless links. Ifsource and destination vehicle are not in direct communication range of each other, then they communicate through intermediate node in multi-hop fashion.

VANETs have a large potential to improve the traffic safety and travel comfort of drivers and passengers [1]. For example vehicles can communicate detour, traffic congestion, and accident information with the nearby vehicles to reduce the traffic jam near the affected areas. Rescue vehicles could instantly receive exact location information of the accident site to reach there faster. Toll could be automatically paid, traffic signals equipped with communication equipments could more accurately control intersection traffic. Although fixed infrastructure is not required for VANET, however fixed network nodes may be used in the form of roadside units. These roadside units open up a wide variety of services for vehicular ad hoc networks such as serving as a gateway to the Internet, serving up geographical data etc [2].

The work in this paper involves two steps.First, we explain the proposed routing protocol in VANET which is very essential to establish a path for packet transmission between nodes. In second step,we evaluatethe feasibility of VANET for the dense traffic scenario using proposed routing protocol [3]. Our work only focuses on a densely connected city network.

Unlike traditional ad hoc and other routing protocols, position-based routing protocols present challenging and interesting properties of VANETs [4,5]. A position-based routing protocol does not require any information on the global topology, but uses the local information of neighboring nodes that restricted to the transmission range of any forwarding node. Due to this restrictions, it gives low overhead of their creation and maintenance. Generally position-based routing is based on greedy forwarding scheme that guarantees loop-free operation. The local information about the physical location of nodes can be provided by the Global Positioning System (GPS), if vehicular nodes are equipped with a GPS receiver [6, 7]. Over the last few years, there have been numerous variations of position-based routing protocols such as LAR and DIR protocols examined in the literature [8, 9].

In this work, we study the performance of both LAR and DIR protocolsand propose a new protocol based on greedy forwarding approach, that we call Directional-Location

AidedRouting (D-LAR) protocol. In this protocol, we first draw a straight line between source and destination. Then the packet is forwarded in the request zone to the direct neighbor having direction closest to the line drawnbetween source and destination.

The rest of the paper is organized as follows. We discuss the related work in section 2. In section 3, the design of D-LAR routing protocol is introduced. Section 4 presents the performance analysis of the proposed protocol. Finally, we conclude the paper in section 5.

2. Related Work

Ad-hoc routing protocols are classified into two categories: topology-based routing protocols and position-based routing protocols. Topology-based routing protocols are not more suitable in VANETs where the network topology is changing frequently. To cope with the dynamic network, position-based routing protocols are used. In this section, we introduce two existing position-based routing protocols like DIR and LAR protocols.

2.1DIrectional Routing (DIR)

Kranakis [10] proposed the Directional Routing (DIR) (referred as the Compass Routing) is based on the greedy forwarding method in which the source node uses the position information of the destination node to calculate its direction. In DIR protocol next-hop neighbor node is decided through unicast forwarding by using the position information of the sender node, its next-hop neighbor nodes, and the destination node. Then the message is forwarded to the nearest neighbor having direction closest to the line drawn between source and destination. Thus a message is forwarded to the neighboring node minimizing the angle between itself, the previous node, and the destination.

The performance of DIR depends on the network density. DIR have high packet delivery rates for dense vehicular networks and low delivery rates for sparse vehicular networks. In the Fig. 1 (a), source node S has five neighbors in it transmission range. Among these nodes, node F has the closest direction (node F has minimum angle among all the neighbors within the communication range) to line *SD* and is the selected next-hop node for further packet transmission. Figure 1 (b), shows the direction of path selection by DIR protocol.

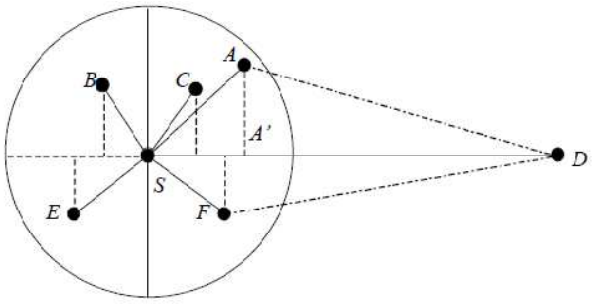

(a)

(b)

Fig. 1 (a) DIR forwarding method, (b) Path selected by DIR

2.2 Location-Aided Routing (LAR)

Several routing protocols have already been proposed for ad hoc networks. Young-BaeKo and Nitin H. Vaidyaproposed the LAR protocol [8]. LAR is an on-demand routing protocol whose operation is similar to DSR (Dynamic Source Routing) [11]. As like DSR, LAR utilizes location information using GPS to limit the area for discovering a new route to a smaller "request zone". The location information is used to reduce routing overhead and improve the performance of routing protocols for ad hoc networks. In LAR, instead of flooding the route requests into the entire network, only those nodes in the request zone will forward packets.

In LAR, two zones are defined: expected zone and request zone [12]. The source node estimates a circular area (expected zone) in which the destination is expected to be found at the current time. The position and the size of the circle are calculated based on the location information and speed of destination (v) at time t_0. The request zone is the smallest rectangular region that includes the expected zone of radius R ($= v\ (t_1\text{-}t_0)$) and the source nodes that should forward the route request packets to the destination.

The coordinates of the four corners of the request zone are included in the route request packet when initiating the route discovery process. RREQ broadcast is limited to this request zone. Thus, when the node in the request zone receives RREQ, it forwards the packet normally. However when a node which is not in the request zone receives an RREQ, it drops the packet. Therefore, the overhead of control packets is reduced. In Fig. 2, for example, if node *I* receives the RREQ from another node, node *I* forwards the RREQ to its direct neighbors because it is located in the

request zone. However, when node *J* which is not in the request zone receives an RREQ, it discards the request.

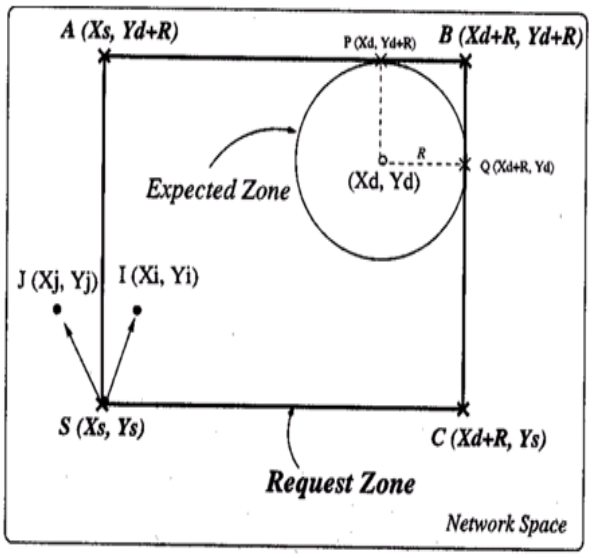

Fig. 2 Request and expected zones in LAR[12]

3. Proposed Scheme

This section is divided into two parts: Section 3.1 describes the assumptions of the proposed model while section 3.2 introduces our proposed scheme.

3.1 System Model

Since this scheme is improved based on DIR and LAR position-based routing protocol, some assumptions are made as follows:

- A large vehicular ad hoc network is considered.
- Vehicles forward packet only in ad hoc mode.
- Each vehicle is equipped with GPS to obtain the position information of itself.
- Every vehicle finds its own coordinates through receiver.
- The source vehicle forwards its own position through beacon message so that the neighboring vehicles forward packets to the destination.
- Impact of signalslocked by obstacles or buildings not included.

3.2 Directional-Location Aided Routing (D-LAR) Protocol

In this section, we propose a Directional Location-Aided Routing (D-LAR) scheme to improve the performance of LAR scheme. D-LAR uses the advantage of DIR and LAR both. In DIR, the source node forward packets in a geographical area towards the direction of the destination node. LAR uses this directional forwarding method to forward the packet between source and destination node. This scheme is based on greedy forwarding approach which uses the location and direction of motion of their neighbors to select the next-hop node for further transmission.

The packet delivery ratio in position-based routing protocols depends on the position information of nodes obtained from the GPS. Each node finds its own location information once in every beacon interval. In high mobility network such as VANET, beacon interval has to be small to find more accurate position information but it gives high communication overhead that affect the overall performance of the network. Therefore, we need a method to find current position and direction of nodes towards destination in highly mobile network with low control packets overhead. So our proposed routing protocol finds the position of nodes using direction of nodes within beacon interval during packet transmission.

In D-LAR, the sender node selects the next-hop forwarding node having direction closest to the straight line drawn between source and destination. D-LAR selects the next-hop node from the nodes running in the same direction as the forwarding node because moving direction can help to build a stable route between forwarding and next-hop node. Therefore, a message is forwarded to the next-hop node in the request zone minimizing the angle between itself, the previous node and the destination node.

In D-LAR, the straight line drawn between source and destination node in the requested zone is used to determine the angle of the nodes within the transmission range. Then D-LAR select the node having minimum angle as a next-hop node for further transmission. In this method, angle (direction closest to the straight line, *SD*) of nodes can be determined through directional routing scheme as given below:

The positions of the two mobile nodes *S* and *A* in Fig. 3 are (x_1,y_1) and (x_2,y_2) respectively. In Fig. 3, when node *A* receives the RREQ from source node *S*, node *A*will calculate the distance *d* between the source node and itself as

$$d = \sqrt{(x_2 - x_1)^2 + (y_2 - y_1)^2} \quad (1)$$

Similarly, the angle θ for node *A* with respect to straight line *SD* is calculated as

$$\theta = tan^{-1}\frac{(y_2 - y_1)}{(x_2 - x_1)} \quad (2)$$

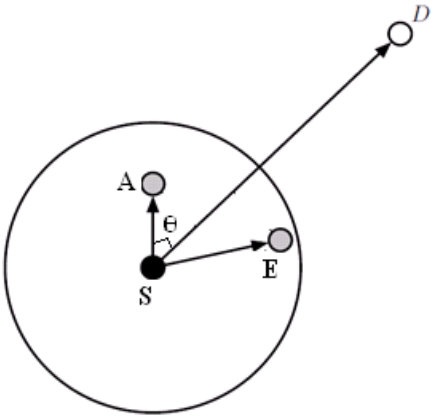

Fig. 3 Angle calculated by DIR Scheme

In Fig.4, node*S* and *D* are source and destination nodes. Node *A* is a next-hop node of source node *S*because node *A* has minimum angle between itself, source node *S*, and the destination node *D*. Therefore, node *A* is selected as the next-hop forwarding node when it receives the message from *S*. It uses the same method, to find the next-hop forwarding node with minimum angle with line *SD*. In this way, node *B* is selected as a next-hop node of *A* for forwarding packets to destination. Finally node *C* directly delivers the packet to destination node *D*. During the whole D-LAR process route request packet is forwarded using LAR scheme.

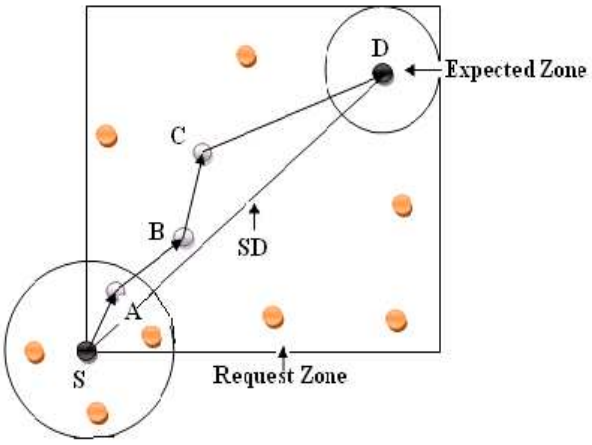

Fig. 4 Directional- location aided routing scheme

The D-LAR scheme is more suitable for dense vehicular network such as city traffic scenario, where an adequate number of vehicles in the city road at any given time in order to make connectivity between vehicles.

4. Feasibility Evaluation of VANET using D-LAR

The number of vehicles in the vehicular network has a crucial impact on network performance, when a high number of nodes are available in the network, which will increase the probability of finding the most suitable node to forward the packet to its desired destination. If there is link breakage has occurred, an alternative node can be selected immediately with a minimum time delay and the packet delivery ratio will increase when increasing the number of nodes in the network.

In VANET, vehicles can move into many different traffic environments that can interfere with wireless communication. Velocities of vehicles are restricted by speed limits, road traffic condition, and traffic control mechanism. Usually, there are large numbers of vehicles in city roads available at any given time. Take the metropolitan city Delhi in India for example, where plenty of vehicles like car, truck, buses, motorcycles etc. run on the road at any given time. Delhi has huge population and with respect to population, vehicles population in Delhi is large among all metropolitan cities in India. On an average about 800 new vehicles are added in Delhi every day [13]. According to Department of Transportation (DOT) annual reports, there are 50 thousand to 100 thousand of vehicles in the city in day times. Therefore, vehicle density can vary in day times. A number of road-based routing protocols have been designed to study the feasibility of VANET. In this work, the feasibility evaluation of VANET has explained using D-LAR routing protocol.

In D-LAR, the process of selecting the next-hop node in the network has an impact on the connectivity and reliability of the network, and selecting the suitable next-hop node will increase the feasibility of obtaining a high network performance. Let *S* be the forwarding node. Since as per the D-LAR scheme, the next-hop node must be present in the request zone for further transmission. Therefore, search for a next-hop node of *S* is restricted to the one fourth of the circular region of the source node *S*. In case of multi-hop VANET, each vehicle must be within the range of at least one other vehicle to maintain the link in the network. Let *N* be the number of nodes located in the circular area are followsPossion distribution with parameter λ, where λ is the node density per unit area. We assume that each node has the same transmission and receiving range of *R*, therefore, the average number of nodes within a circular area can be calculated as:

$$\textit{Number of nodes } (N) = \lambda \times \textit{Area of the region}$$

$$= \lambda \pi R^2$$

Similarly if n nodes are distributed according to Possion process in one fourth area of the circular region (shaded area) of S, which is the part of request zone, then the number of nodes n in the shaded area as shown in the Fig. 5 is

$$n = \lambda\pi R^2/4 \quad (3)$$

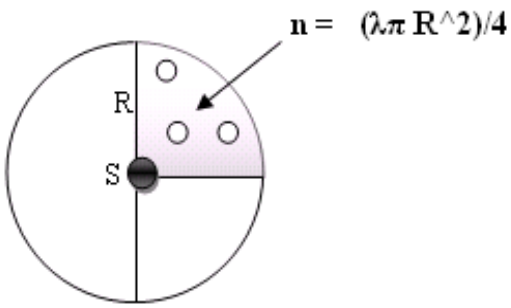

Fig. 5 Showing the shaded area of the circle

Since nodes are Possion distributed, then the probability that *n*other nodes located in the shaded area is given by [14]

$$P(n, A) = \frac{(\lambda A)^n \cdot e^{-\lambda A}}{n!}$$

$$= \frac{\left(\frac{\lambda\pi R^2}{4}\right)^n \cdot e^{-\frac{\lambda\pi R^2}{4}}}{n!}, \qquad n = 0, 1, 2, 3, \ldots \qquad (4)$$

Thus, the probability to select at least k out of n within the shaded area is

$$P_k = 1 - \sum_{n=0}^{k-1} \frac{\left(\frac{\lambda\pi R^2}{4}\right)^n \cdot e^{-\frac{\lambda\pi R^2}{4}}}{n!} \qquad (5)$$

Figure 6 shows the probability of selecting at least k nodes in the transmission range of the source node. We have taken node density 0.0002 and 0.0004 nodes/km^2. In Fig. 7, the probability of selecting at least k nodes in the shaded area has shown for the same node densities. Based on these observations, we can say that the probability that a vehicle has at least k neighbors in the shaded area within the transmission range is relatively high.

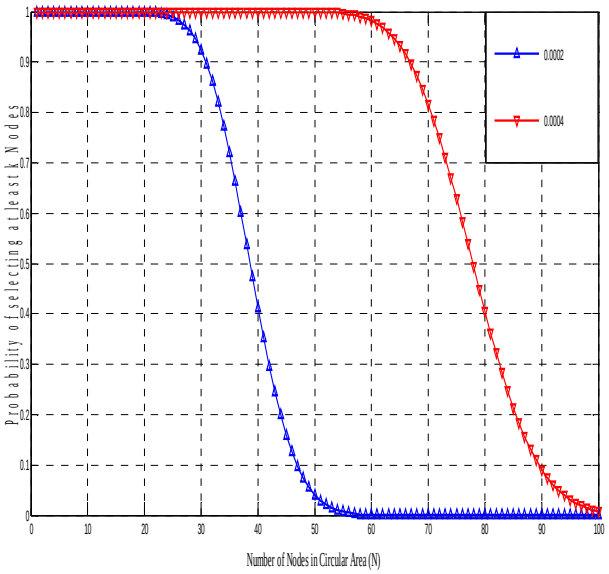

Fig. 6 Probability of selecting at least k nodes in the circular area

This study shows that shaded area belonging to request zone of the transmission range has less number of nodes compare to whole circular region of the source node. Less number of nodes in the shaded area improving the individual reachable neighbors will improve the connectivity between nodes in the network. Thus, Fig. 7 clearly shows that the probability to select a node as a next-hop node in shaded area is higher than the probability to select a node in whole circular area (as shown in Fig. 6) within the transmission range for further transmission.

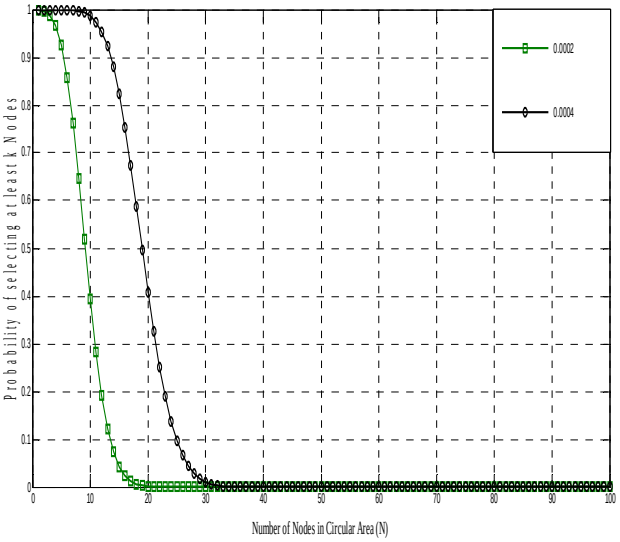

Fig. 7 Probability of selecting at least k nodes in the shaded area

5. Conclusion

In this paper, a new position-based routing protocol, D-LAR which uses the advantage of DIR and LAR routing protocols is proposed. In this scheme, the next-hop node is selected with minimum angle along with the straight line drawn between source and destination node in the requested zone as per DIR protocol. During the whole D-LAR packet transmission process route request packet is forwarded using LAR scheme.The D-LAR scheme is more suitable for dense vehicular network such as city traffic scenario, where an adequate number of vehicles in the city road at any given time in order to make connectivity between vehicles.

We studied the characteristics of VANET for dense network and the feasibility of VANET for D-LAR routing protocol have been justified. The performance of D-LAR protocol can be compared in terms of end-t-end delay, packet delivery ratio, and route costs with DIR and LAR routing protocols in the next step of work.

References

[1] Hassnaa Moustafa and Yan Zhang, Vehicular networks: techniques, standards, and applications,Boca Raton London, New York:CRC Press, 2009.

[2] JinhuaGuo and Nathan Balon, "Vehicular Ad Hoc Networks and Dedicated Short-Range Communication," University of Michigan – Dearborn, 2006.

[3] Sun Xi, LI Xia-miao, "Study of the Feasibility of VANET and its Routing Protocols," IEEE, 2008, pp. 1-4.

[4] Kevin C. Lee, Uichin Lee, and Mario Gerla, " Survey of Routing Protocols in Vehicular Ad Hoc Networks," IGI Global, 2010, pp. 149-170.

[5] Hirozumi Yamaguchi, Weihua Sun, and TeruoHigashino, "Geographic Routing on Vehicular Ad Hoc Networks," IGI Global, 2010, pp. 171-178.

[6] Azzedine Boukerche, Horacio A.B.F. Oliveira, Eduardo F. Nakamura, and Antonio A.F. Loureiro, "Vehicular Ad Hoc Networks: A New Challenge for Localization-Based Systems," Computer Communication, Elsevier (ScienceDirect), 2008, pp.1-12.

[7] G. Dommety and R. Jain, "Potential networking applications of global positioning systems (GPS)," Tech. Rep. TR-24, CS Dept., The Ohio State University, April 1996.

[8] Young-BaeKo and Nitin H. Vaidya, "Location-aided routing (LAR) in mobile ad hoc networks," ACM/IEEE, MOBICOM'98, 1998, pp. 66-75.

[9] I. Stojmenovic, A. P. Ruhil, and D. K. Lobiyal, "Voronoi diagram and convex hull based Geocasting and routing in wireless networks", Wireless Communications and Mobile Computing Special Issue on Ad Hoc Wireless Networks, John Wiley & Sons, Ltd., Vol.6, Issue.2, 2006,pp.247-258.

[10]E. Kranakis, H. Singh and J. Urrutia, "Compass routing on geometric networks," Proceedings of the 11th Canadian Conference on Computational Geometry (CCCG'99), 1999, http:www.cs.ubc.ca/ conferences/CCCG/elec_proc/c46.ps.gz.

[11]David B. Johnson and David A. Maltz, "Dynamic Source Routing in Ad Hoc Wireless Networks," Kluwer Academic Publishers, 1996.

[12]Neng-Chung Wang, Jong-Shin Chen, Yung-Fa Huang, and Si-Ming Wang, "A Greedy Location-Aided Routing Protocol for Mobile Ad Hoc Networks," Proceedings of the 8th WSEAS International Conference on Applied Computer and Applied Computational Science, 2002, pp. 175-180.

[13]Rites Ltd. Urban environmental engineering household survey, Delhi, 1994.

[14]SUN Xi, LI Xia-miao, "Study of the Feasibility of VANET and its Routing Protocols", IEEE 4th International Conference on Wireless Communications, Networking and Mobile Computing (WOCOM), Dalian, 2008, pp.1-4.

Dr. Ram Shringar Raw received his B. E. (Computer Science and Engineering) from G. B. Pant Engineering College, Pauri-Garhwal, UK, India and M. Tech (Information Technology) from Sam Higginbottom Institute of Agriculture, Technology and Sciences, Allahabad (UP), India in 2000 and 2005, respectively. He has obtained his Ph.D (Computer Science and Technology) from School of Computer and Systems Sciences, Jawaharlal Nehru University, New Delhi, India in 2011. He is currently working as Assistant Professor in the Department of Computer Science and Engineering, Ambedkar Institute of Advanced Communication Technologies & Research, GGSIP University, New Delhi, India. His current research interest includes Mobile Ad hoc Networks and Vehicular Ad hoc Networks. Dr. Raw has published papers in International Journals and Conferences including IEEE, Springer, Inderscience, American Institute of Physics, AIRCC, etc.

Mr. Sanjoy Das did his B. E. and M.Tech in Computer Science. He has submitted his Ph.D in Computer Science, School of Computer and Systems Sciences, Jawaharlal Nehru University, New Delhi, India. He has worked as an Assistant Professor, Department of Computer Science and Engineering in G. B. Pant EngineeringCollege, Uttarakhand , India. Also, he has worked as an Assistant Professor in thedepartment of Information Technology, School of Technology, Assam University (A Central University),Silchar, Assam, India. Presently, working as an Assistant Professor, in Computer Science and Engineering Department, School of Engineering and Technology, Galgotias University, Greater Noida, UP, India. His current research interest includes Mobile Ad hoc Networks and Vehicular Adhoc Networks, Distributed Systems.

Dr. Nanhay Singh, working as Associate Professor in Ambedkar Institute of Advanced Communication Technologies & Research, Govt. of NCT, Delhi-110031 (Affiliated to Guru Gobind Singh Indraprastha University, Delhi) in the Department of Computer Science & Engineering. He received his Ph.D (Computer Science and Technology) & M. Tech. (Computer Science & Engineering) from the Kurukshetra, University, Kurukshetra, Haryana. He has rich experience in teaching the classes of Graduate and Post-Graduate in India. He has contributed to numerous International journal & conference publications in various areas of Computer Science. He published more than 11 Research Paper in International Journals and Conferences. . He has also written an International book Titled as "Electrical Load Forecasting Using Artificial Neural Networks and Genetic Algorithm", in Global Research Publications New Delhi (India). His area of interest includes Distributed System, Parallel Computing, Information Theory & Coding, Cyber Law, and Computer Organization.

Mr. Sanjeet Kumar received his B. E. (Computer Science and Engineering) from IET, Dr. Bhimrao Ambedkar University, Agra, India in 2005. He is pursuing M. Tech. from Integral University Lucknow. He has five years of experience in teaching as well as in industry. His area of interest includes Mobile Computing, Ad hoc Network and Sensor Network.

Mr. Shailender Kumar obtained his B.E. (CSE) from MDU Rohtak and M.Tech. from Rajasthan University. He has more than 10 years of experience in teaching at various esteemed engineering colleges in India, like Delhi College of Engineering, Netaji Subhas Institute of Technology etc. Currently he is working as Assistant Professor (Pre-revised) at AIACTR, Delhi, India. His area of interest is Databases,Compiler Construction,Computer Network, Ad hoc Network etc.

IOSR Journal of Applied Physics (IOSR-JAP)
ISSN: 2278-4861. Volume 2, Issue 1 (Sep-Oct. 2012), PP 41-42
www.iosrjournals.org

Fiction Supporting Decelerated Expansion of the Universe

Umesh Kumar
(Student, VLSI & ESD, Delhi Technological University, India)

Abstract : *It has always been a topic of interest whether Universe is expanding or collapsing, if anyone of them is happening then whether the phenomena is accelerating or decelerating. This paper is a fiction supported by the basic principles of physics and Nebula hypothesis.*
Keywords: *Nebula Theory, Supernova, Gravity.*

I. INTRODUCTION

The **Big Bang** theory is the prevailing cosmological model that explains the early development of the Universe. According to the Big Bang theory, the Universe was once in an extremely hot and dense state which expanded rapidly. This rapid expansion caused the young Universe to cool and resulted in its present continuously expanding state. According to the most recent measurements and observations, this original state existed approximately 13.7 billion years ago, which is considered the age of the Universe and the time the Big Bang occurred.

In my opinion it is hard to say whether the universe is expanding or collapsing because only of the observation of a few supernovae and their rate of expansion can never predict the complete nature of the Universe. So here we go for a fiction like explanation of the above mentioned phenomena.

II. BEFORE BIG BANG

It might have happened that before the Big-Bang, the system would have looked like a super-giant sun with extremely super-high temperature that could have ever been imagined. Now one question may be asked how such a system could be stable. The answer lies in the present Universe system's sun stability. It has been observed that big suns (stars) have higher temperature compared to smaller suns. It seems like the stability, mass and temperature of a star are parameters of a single equation (like the following one)

$$S=f(T,M)= a. T^{b}. M^{-c}$$

Where S is stability factor, T is temperature and M is the mass of the star. a, b and c are constants (or can be variables dependent of few more nature's parameters). If the mass and the temperature of the star are unbalanced, the star will not be able to survive i.e. less mass and high temperature will create a supernova and less temperature and high mass will turn system to go cold into a system like planets.

III. AFTER BIG BANG

After the super-explosion (The Big-Bang), according to the nebula hypothesis [1], the solar system began as a nebula, an area in the Milky Way Galaxy that was a swirling concentration of cold gas and dust. Due to some perturbation, possibly from the nearby supernova this cloud of gas and dust began to condense (fig. 1), or pull together under the force of its own gravity. Condensation was slow at first, but increase in speed as more material was drawn towards the centre of the nebula. This made gravity stronger, making condensation faster. This theory was justified by a well know experiment in which astronomers used a transparent glass tube of water with dissolved salt crystals (mingled in spaces). It was observed that salt crystals started to condense with many locality of condensation region. During the Nebulae formation the whole system still kept expanding with a very high velocity.

IV. REASON FOR DECELERATED EXPANSION

According to my view nebula theory is not just only for the dust particles and gases created during the supernovae but can also be applied for the whole Universe system where all the galaxies are tiny particles in comparison of the center of the super-explosion (the big-bang). It may be possible that one day the expansion will stop and the whole universe will collapse into a single Star (sun or a super-nebula) and once again big-bang will occur and again the universe will be formed.

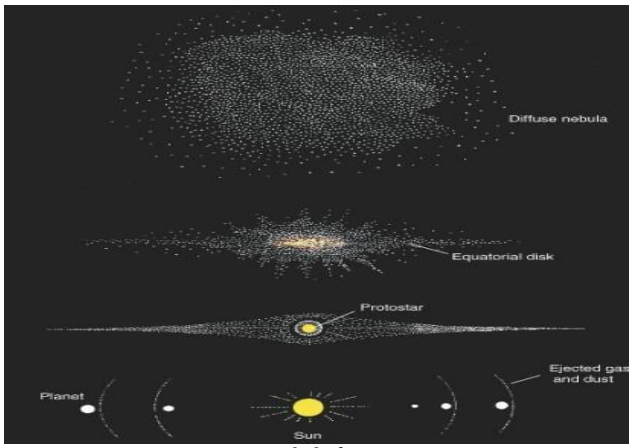

Fig.1. Nebula formation

V. CONCLUSION

History repeats itself.

REFERENCES

[1] Swedenborg, Emanuel (1734). *(Principia) Latin: Opera Philosophica et Mineralia (English: Philosophical and Mineralogical Works)*.

[2] Woolfson, M.M. (1993). "Solar System – its origin and evolution". *Q. J. R. Astr. Soc.* **34**: 1–20. Bibcode 1993QJRAS..34....1W. For details of Kant's position, see Stephen Palmquist, "Kant's Cosmogony Re-Evaluated", *Studies in History and Philosophy of Science* 18:3 (September 1987), pp.255-269.

[3] Kokubo, Eiichiro; Ida, Shigeru (2002). "Formation of protoplanet systems and diversity of planetary systems". *The Astrophysical Journal* **581** (1): 666–680.

ISSN: 2278 – 1323
International Journal of Advanced Research in Computer Engineering & Technology (IJARCET)
Volume 1, Issue 7, September 2012

F-Measure Metric for English to Hindi Language Machine Translation

Neeraj Tomer [1] Deepa Sinha [2] Piyush Kant Rai [3]

Abstract: The main objective of MT is to break the language barrier in a multilingual nation like India. Evaluation of MT is required for Indian languages because the same MT is not works in Indian language as in European languages due to the language structure. So, there is a great need to develop appropriate evaluation metric for the Indian language MT. The present research work aims at studying the Evaluation of Machine Translation Evaluation's F-Measure Metric for English to Hindi for tourism domain. This work will help to give the feedback of the MT engines. We may make the changes in the MT engines and further we may revise the study. We see that as we increase the number of references there is improvement in our results.

Keywords: MTE- Machine Translation Evaluation, MT-Machine Translation, SVO- Subject-Verb-Object, SOV-Subject-Object-Verb, Tr.-Tourism.

INTRODUCTION

India is a highly multilingual country with 22 constitutionally recognized languages. Still, English is understood by less than 3% of Indian population. Hindi, which is official language of the country, is used by more than 400 million people. Therefore, Machine Translation (MT) assumes a much greater significance in breaking the language barrier within the country's sociological structure. The main objective of MT is to break the language barrier in a multilingual nation like India. English is a highly positional language with rudimentary morphology, and default sentence structure as Subject-Verb-Object. Indian languages are highly inflectional, with a rich morphology, relatively free word order, and default sentence structure as Subject-Object-Verb. In addition, there are many stylistic differences. So the evaluation of MT is required for Indian languages because the same MT is not works in Indian language as in European languages. The same tools are not used directly because of the language structure. So, there is a great need to develop appropriate evaluation metric for the Indian language MT.

The present research work aims at studying the "Evaluation of Machine Translation Evaluation's F-Measure metric for English to Hindi" for tourism domain. The present research work is the study of statistical evaluation of machine translation evaluation for English to Hindi. The research aims to study the correlation between automatic and human assessment of MT quality for English to Hindi. The main goal of our experiment is to determine how well a variety of automatic evaluation metric correlated with human judgment.

MATERIALS AND METHODS

In the present work we propose to work with corpora in the tourism domain and limit the study to English – Hindi language pair. It may be assumed that the inferences drawn from the results will be largely applicable to translation for English to other Indian Languages. Our test data consisted of a set of English sentences that have been translated from expert and non-expert translators. The English source sentences were randomly selected from the corpus of tourism domain. These samples are taken randomly from the tourism domain in which we have the 15200 sentences and from the health care domain in which we have the 10000 sentences. Each output sentence was score by Hindi speaking human evaluators who were also familiar with English. It may be assumed that the inferences drawn from the results will be largely applicable to translation for English to other Indian Languages, as assumption which will have to be tested for validity. We intend to be consider the following MT engine in our study-

- Anuvadaksh

OBJECTIVE

The main goal of this work is to determine how well a variety of automatic evaluation metrics correlated with human judges. A secondary goal is to determine for which the correlation of automatic and human evaluation is particularly good or bad. The other specific objectives of the present work are as follows.

1. To design and develop the parallel corpora for deployment in automatic evaluation of English to Hindi machine translation systems.
2. Assessing how good the existing automatic evaluation metric F-Measure, will be as MT evaluating strategy for evaluation of Indian language machine translation (EILMT) systems by comparing the results obtained by this with human evaluator's scores by correlation study.
3. To study the statistical significance of the evaluation results as above, in particular is the effect of-
   - size of corpus
   - sample size variations
   - increase in number of reference translations

Creation of parallel corpora: Corpus quality plays a significant role in automatic evaluation. Automatic

metrics can be expected to correlate very highly with human judgments only if the reference texts used are of high quality, or rather, can be expected to be judged high quality by the human evaluators. The procedure for creation of parallel corpora is as under:

1. Collect English corpus from the domain from various resources.
2. Generate multiple references (we limit it to three) for each sentence by getting the source sentence translated by different expert translators.
3. XMLise the source and translated references for use in automatic evaluation.

Description of Corpus

Domain	Tourism
Source Language	English
Target Language	Hindi
No. of Sentences	1000
No. of Words	23000
No. of Human Translation	3
No. of MT Engine	1

For the corpus collection our first motive was to collect as possible to get better translation quality and a wide range vocabulary. For this purpose the first corpus we selected to use in our study is collected from different sources. We have manually aligned the sentence pairs.

In our study for tourism domain we take 1000 sentences. When the text has been collected, we distributed this collected text in the form of Word File. Each word files having the 100 sentences of the particular domain. In this work our calculation will be based on four files- source file and three reference files. Reference files are translated by the language experts. We give the file a different identification. For e.g. our first file name is Tr_0001_En where Tr_ for tourism 0001 means this is the first file and En means this is the Candidate file. We treat this as the candidate file. In the same way our identification for the Hindi File is Tr_0001_Hi, in this Hi is for the Hindi file and we have called this a reference file. As we already mention that we are taking the three references we named them reference 1(R1), reference 2(R2), reference 3(R3). In the study we take the candidate sentence and the reference sentences, as shown below. For e.g.

Source Sentence: Internal problems dominated the agenda for the next 30 years, as a series of governments struggled to keep the economy, which was almost completely destroyed as a result of the Pacific War, from disintegrating.

Candidate Sentence:

उष्ण कटिबंधीय निम्नभूमियाँ वन्य जीवन का बहुत बड़ी क्रम छुपाती हैं, घनी वनस्पति और समान देश के अंतर्गत अभी तक नाटकीय जलप्रपातों ट्रेककरों औरपर्वतारोहियों को चुनौती देकर ऊँची एन्डियन चोटियाँ में है

Reference Sentences:

R1- अगले 30 वर्षों तक एजेण्डा में अन्दरूनि समस्याएं सर्वोच्च रही, जबकि एक के बाद एक सरकारें संघर्षरत थी उस अर्थव्यवस्था को विघटित होने से बचाने में जो कि पैसिफिक युध्द के परिणाम स्वरुप लगभग पूरी तरह नष्ट हो चुकी थी।

R2- जिस तरह अर्थव्यस्था को बनाए रखने के लिए सरकारों की श्रेणियों मेंसंघर्ष किया, आने वाले 30 वर्षों के लिए आन्तरिक समस्याओं ने कार्य सूचि को अधिकार में रखा जो विघटित होने से Pacific War के परिणामस्वरूप पूर्णतया समाप्त हो गयी थी।

R3- अगले तीस वर्षों के लिए आन्तरिक समस्याएं कार्यक्रम पर प्रभावी रहीं, क्योंकि सरकारों की एक श्रृंखला ने अर्थव्यवस्था, जो पेसिफिक युद्ध के परिणामस्वरूप पूर्णतः नष्ट हो गयी थी,विखण्डित होने से बचाए रखने के लिए संघर्ष किया।

HUMAN EVALUATION

Human evaluation is always best choice for the evaluation of MT but it is impractical in many cases, since it might take weeks or even months (though the results are required within days). It is also costly, due to the necessity of having a well trained personnel who is fluent in both the languages, source and targeted. While using human evaluation one should take care for maintaining objectivity. Due to these problems, interest in automatic evaluation has grown in recent years. Every sentence was assigned a grade in accordance with the following four point scale for adequacy.

	Score
• Ideal	1
• Acceptable	.5
• Not Acceptable	.25
• If a criterion does not apply to the translation	0

AUTOMATIC EVALUATION BY F-MEASURE METRIC

We used F-Measure evaluation metric for this study. This metric is specially designed for English to Hindi. F-Measure metric, designed for evaluating MT quality, scores candidate sentences by counting the number of n-gram matches between candidate and reference sentences. F-Measure metric is probably known as the best known automatic evaluation for MT. To check how close a candidate translation is to a reference translation, an n-gram comparison is done between both. Metric is designed from matching of candidate translation and reference translations. We have chosen correlation analysis to evaluate the similarity between automatic MT

evaluations and human evaluation. Next, we obtain scores of evaluation of every translated sentence from both MT engines. The outputs from both MT systems were scored by human judges. We used this human scoring as the benchmark to judge the automatic evaluations. The same MT output was then evaluated using both the automatic scoring systems. The automatically scored segments were analyzed for Spearman's Rank Correlation with the ranking defined by the categorical scores assigned by the human judges. Increases in correlation indicate that the automatic systems are more similar to a human in ranking the MT output.

Statistical significance is an estimate of the degree, to which the true translation quality lays within a confidence interval around the measurement on the test sets. A commonly used level of reliability of the result is 95%. To reach at decision, we have to set up a hypothesis and compute p-value to get final conclusion.

The present research is the study of statistical evaluation of machine translation evaluation's F-Measure metric. The research aims to study the correlation between automatic and human assessment of MT quality for English to Hindi. While most studies report the correlation between human evaluation and automatic evaluation at corpus level, our study examines their correlation at sentence level. The focus in this work is to examine the correlation between human evaluation and automatic evaluation and its significance value, not to discuss the translation quality. In short we can say that this research is the study of statistical significance of the evaluated results, in particular the effect of sample size variations.

So, firstly we take source sentences and then get these sentences translated by our MT engine, here we consider the Anuvadaksh. We have the different references of these sentences. After doing this we do the evaluations of these sentences human as well as the automatic evaluations and we collect the individual scores of the given sentences considering all the three references one by one. The following table shows the individual scores of the five sentences (particular sentences can be seen at the end of the paper) using different no. of references.

Table 1: Human Evaluation and F-Measure Evaluation scores

S. No.	F-Measure Score			
	Human Eval.	one no. of reference	two no. of references	three no. of references
1.	0.75	0.1286	0.1575	0.1575
2.	0.25	0.1814	0.1689	0.1865
3.	0.75	0.1917	0.2073	0.2472
4.	0.75	0.1352	0.1505	0.1679
5.	1	0.1336	0.1713	0.1868

In this way we also collect the individual scores of all the sample sizes like 20, 60,100,200,300,500 and 1000 sentences. After this we do the correlation analysis of these values. In order to calculate the correlation with human judgements during evaluation, we use all English–Hindi human rankings distributed during this shared evaluation task for estimating the correlation of automatic metrics to human judgements of translation quality, were used for our experiments. In our study the rank is provided at the sentence level.

For correlation analysis we calculate the correlation between human evaluation and automatic evaluations one by one by the Spearman's Rank Correlation method. The Spearman's rank correlation coefficient is given as (when ranks are not repeated)-

$$\rho = 1 - \left(\frac{6\sum_{i=1}^{n} d^2}{n(n^2-1)} \right)$$

where d is the difference between corresponding values in rankings and n is the length of the rankings. An automatic evaluation metric with a higher correlation value is considered to make predictions that are more similar to the human judgements than a metric with a lower value. Firstly, we calculate the correlation value in between the human evaluation and automatic evaluation F-Measure metric means human evaluation with F-Measure for sample size 20, 60, 100, 200, 300, 500 and 1000.

Table 2: Correlation (ρ) values

Sample Size	ρ values		
	one no. of reference	two no. of references	three no. of references
20	.384	.399	.410
60	.141	.151	.204
100	.071	.092	.106
200	.219	.212	.260
300	.216	.199	.232
500	.116	.256	.256
1000	.176	.256	.176

After calculating the correlation, we need to find out which type of correlation is there between the variables and of which degree and whether the values of the correlation are significant.

ANALYSIS OF STATISTICAL SIGNIFICANCE TEST FOR HUMAN EVALUATION AND AUTOMATIC EVALUATION

Statistical significance is an estimate of the degree, to which the true translation quality lays within a confidence interval around the measurement on the test sets. A commonly used level of reliability of the result is 95%, for e.g. if, say, 100 sentence translations are evaluated, and 30 are found correct, what can we say about the true translation quality of the system? To reach at decision, we have to set up a hypothesis and compute p-value to get final conclusion that whether there is any correlation

between the human evaluations and automatic evaluations. If yes, then what is the type and degree of correlation? Also what is the significance of the correlation value? In this work we set the hypothesis that there is no correlation between the values of human and automatic evaluation. The p-value will provide the answer about the significance of the correlation value.

A Z-test is a statistical test for which the distribution of the test statistic under the null hypothesis can be approximated by a normal distribution. For each significance level, the Z-test has a single critical value (for example, 1.96 for 5% two tailed) which makes it more convenient than the Student's t-test which has separate critical values for each sample size. The test statistic is calculated as:

$$Z = \frac{\bar{x}_1 - \bar{x}_2}{\sqrt{\frac{S_1^2}{n_1} + \frac{S_2^2}{n_2}}}$$

where $\bar{x}_1$ and $\bar{x}_2$ are the sample means, s_1^2 and s_2^2 are the sample variances, n_1 and n_2 are the sample sizes and z is a quartile from the standard normal distribution.

Table 3 : p-values of output of Anuvadaksh using different no. of references

Sample Size	p-values		
	one no. of reference	two no. of references	three no. of references
20	0.0001	0.0001	0.0001
60	0.0001	0.320	0.0001
100	0.0001	0.0001	0.450
200	0.0001	0.0001	0.0001
300	0.0001	0.0202	0.0162
500	0.2296	0.0069	0.0069
1000	0.0764	0.069	0.0754

Now on the basis of these values we conclude our results like which type and degree of correlation is there between the given variables and whether the correlation results are significant. In the above example we have done all the calculations by considering the single reference sentence and in tourism domain using 5 numbers of sentences.

But in our research work we consider the different references like 1, 2, 3 and we use the different sample sizes like 20, 60, 100, 200, 300, 500, and 1000. We see whether the results remains uniform for different sample sizes and different number of references in particular domains.

For above calculation we used following sentences:
English Sentences:

1. Little wonder, then, that its environment is so rich.
2. French Guiana is also home to a colorful blend of different cultural backgrounds.
3. All this combined with rich historical and archaeological past and enduring indigenous cultures.
4. The country enjoys 500km of fine sandy beaches on the Atlantic and the Río de la Plata, woods, hills, hot springs, hotels, casinos, art festivals and numerous opportunities for sport and entertainment.
5. First occupied by the French in 1764, the islands were quickly ceded to Spain, which then ruled the adjacent territory in Latin America.

Candidate Sentences:

1. थोड़ा सा विस्मय, तब जो अपनी पर्यावरण इसलिए समृद्ध है
2. फ्रेंज गुआना विभिन्न सांस्कृतिक पृष्ठभूमियाँ का रंगीन मिश्रण को आवास भी है
3. सभी यह समृद्ध ऐतिहासिक और पुरातात्त्विक भूतकाल और चिरस्थाई स्वदेशी संस्कृतियाँ के साथ सुमेलित किया
4. देश खेल और मनोरंजन के लिए ला प्लाटकड़ियाँ, पहाड़ों , गर्म वसंतों , होटलों , नृत्यशालाएँ , कला उत्सवों और अनेक अवसरों द अटलांटिक और आर. ओ पर अच्छे बालुकामय समुद्र तटों क500 किमी को आनन्द प्राप्त करता है
5. 1764 में फ्रेंच द्वारा पहला अधिकार किया गया द्वीपों स्पेन को शीघ्रतापूर्वक सौंप दिये गये थे जो लैटिन अमेरिका में संलग्न प्रांत को तब शासन किया

RESULTS

In the domain tourism there is significance difference between the average evaluation score of human with F-Measure at 5% level of significance and for the sample size 20. There is highest correlation between the evaluation score of human and F-Measure for MT engine Anuvadaksh.

We see that as we increase the number of references there is improvement in our results. In Table 2 (Correlation (ρ) values) correlation value for F-Measure is .399 and .410 these values are for sample size 20 and for two and three number of references which is significant at 5% level of significance. A similar result is seen in the case of sample size 60, 100 and 200 for two and three no. of references. But for the sample sizes 500 and 1000 value of correlation is .256 for two no. of references which is insignificant on the given level of significance. From the analysis on the basis of z-test used for the significance test of human evaluation and automatic evaluation we obtain the following important point; in the domain tourism there is significance difference between the average evaluation score of human with F- Measure at 5% level of significance and for the some sample sizes.

CONCLUSION

This work will help to give the feedback of the MT

engines. In this way we may make the changes in the MT engines and further we may revise the study. Corpus quality plays a significant role in automatic evaluation. Automatic metrics can be expected to correlate highly with human judgments only if the reference texts used are of high quality, or rather, can be expected to be judged of high quality by human evaluators. In this evaluating MT evaluation metrics for English to Indian Language machine translation work, we developed the tool SEMTE which is good enough according to the results obtained.

ACKNOWLEDGEMENT

The present research work was carried under the research project "English to Indian Languages Machine Translation System (EILMT)", sponsored by TDIL, Ministry of Communications and Information Technology, Government of India. With stupendous ecstasy and profundity of complacency, we pronounce utmost of gratitude to Late Prof. Rekha Govil, Vice Chancellor, Jyoti Vidyapith, Jaipur Rajasthan.

REFERENCES

1. Akiba, Yasuhir Taro Watanabe, Eiichiro Sumita, (2002): "Using Language and Translation Models to Select the Best among Outputs from Multiple {MT} System", Proceeding of Colong, 8-14.
2. Babych, Bogdan and Anthony Hartley, (2004): "Extending the BLEU MT Evaluation Method with Frequency Weightings", Proceedings of ACL, 621-628.
3. Bradley Efron and Robert Tibshirani, (1986): "Bootstrap Methods for Standards Errors, Confidence Intervals, and other Measures of Statistical Accuracy", Statistical Science, 54-77.
4. Calison-Burch, Chris and Raymond S. Flournoy, (2001): "A Program for Automatically Selecting the Best Output from Multiple Machine Translation Engines", Proceedings of MT Summit VIII, 63-66.
5. Calison-Burch, Chris and Raymond S. Flournoy, (2001): "A Program for Automatically Selecting the Best Output from Multiple Machine Translation Engines", Proceedings of MT Summit VIII, 63-66.
6. Deborah Coughlin, (2003): "Correlating Automated and Human Assessments of Machine Translation Quality", In Proceedings of MT Summit IX. New Orleans, 63-70.
7. Deborah Coughlin, (2003): "Correlating Automated and Human Assessments of Machine Translation Quality", In Proceedings of MT Summit IX. New Orleans, 63-70.
8. Doddington G., (2002): "Automatic Evaluation of Machine Translation Quality Using N-gram Co-Occurrences Statistics", Human Language Technology: Notebook Proceedings, San Diego, USA, 128-132.
9. Donaway, R. L., Drummey, K. W., Mather, L. A. (2000): "A Comparison of Rankings Produced by Summarization Evaluation Measures", Proceedings of the Workshop on Automatic Summarization, 69-78.
10. Donaway, R.L., Drummey, K.W., and Mather, L.A., (2000): "A Comparison of Rankings Produced by Summarization Evaluation Measures", In Proceedings of the Workshop on Automatic Summarization, 69-78.
11. Dunning, Td. (1993): "Accurate Methods for the Statistics of Surprise and Coincidence", Computational Linguistics. 61-74.
12. http://en.wikipedia.org/wiki/Evaluation_of_machine_translation
13. http://en.wikipedia.org/wiki/History_of_machine_translation
14. Joseph P. Turrian, Luke Shen and I. Dan Melamed, (2003): "Evaluation of Machine Translation and its Evaluation", In Proceedings of MT Summit IX. New Orleans, 63-70.
15. K.-Y.Su, M.-W.Wu, and J.-S.Chang., (1992): "A New Quantitative Quality Measures for Machine Translation System", In Proceedings of the 15th International Conference on Computational Linguistics (COLING) Nantes, France. 433-439.
16. Lin C. Y., E. hovy. (2002): "Manual and Automatic Evaluations of Summaries", In Proceedings of the Workshop on Automatic Summarization, post-Conference Workshop of ACL. 45-52.
17. Liu Ding and Gildea Daniel, "Syntactic Features for Evaluation of Machine Translation", Department of Computer Science University of Rochester, Rochester, NY 14627.
18. Meng, X., R. Rosenthal, and D. Rubim., (1992): "Comparing Correlated Correlation Coefficients", Psychological Bulletin-11, 172-175.
19. Rajman M., Hartley A. (2001): "Automatically predicting MT system rankings Compatible with Fluency, Accuracy or Informativeness scores", In Proceedings of the 4th workshop on MT Evaluation, MT Summit VIII, Santigo de Compostela, 29-34.
20. Rao, Durgesh (2001): "Machine Translation in India: A Brief Survey", National Centre for Software Technology Gulmohar Road 9, Juhu, Mumbai 400049, India, 21-23.
21. S.Niessen, F.J.Och, G. Levsch, and H.Ney. (2000): "An Evaluation Tool for Machine Translation: Fast Evaluation for Machine Translation Research", In Proceedings of the Second International Conference on Language Resources and Evaluation. Athens, Greece, 39-45.
22. T. Neeraj (2012): "Evaluating Machine Translation (MT) Evaluation Metrics for English to Indian Language Machine Translation", Ph.D. Thesis, Banasthali University, Banasthali.
23. T. Neeraj and Sinha Deepa (2012): "Evaluating Machine Translation Evaluation's BLEU Metric for English to Hindi Language Machine Translation", in The International Journal of Computer Science & Application , Vol-01-NO-06-Aug-12, 48-58.
24. T. Neeraj and Sinha Deepa (2012): "Evaluating Machine Translation Evaluation's NIST Metric for English to Hindi Language Machine Translation", paper accepted in The International Journal of Multidisciplinary Research Academy –IJMRA.
25. www.amadeus.net/home/destinations/en/guides/.../intro.htm
26. www.escapelets.com/en-GB/countryproperties/PE.aspx
27. www.iexplore.com/travel.../**french-guiana**/overview
28. www.noble-caledonia.co.uk/.../countries_information.asp?section
29. www.thetravelwebsite.co.uk/uruguay-c446.html
30. Y. Akiba, K.Imamura, and E. Sumita., (2001): "Using Multiple Edit Distances to Automatically Rank Machine Translation Output", In Proceedings of MT Summit VIII. Santiago de Compostela, Spain, 15-20.

Author 1

Neeraj Tomer
tneeraj12@rediffmail.com
9460762117

Area of Interest:

- Machine Translation and Indian Language Technology
- Theoretical Computer Science and related technologies

Academic Qualification:

Ph.D (thesis submitted) in Computer Science, Banasthali University, Banasthali.
MCA, Maharishi Dayanand University, Rohtak 2005.
Master of Economics, Kurukshetra University Kurukshetra 1999.
Bachelor of Economics, Kurukshetra University Kurukshetra 1997.

Employment History:

Post graduate and graduate teaching at Mahatma Gandhi Institute of Applied Sciences, Jaipur as a lecturer from July 2003 to August 2006. As a Research Associate at Banasthali University Banasthali in 2007. As a lecturer at LCRT College of Education Panipat from August 2007 to July 2010. As an Assistant Professor at SINE International Institute of Technology, Jaipur from August 2010 to March 2012.

- Papers Published : 1
- In Press : 3
- Communicated : 3

Seminar and Conferences Attended: 5

Research Guidance:

Guided 3 students for their dissertation work at PG (M.Sc) level.

Future Plans: To grow academically

Author 2

Deepa Sinha
Associate Professor
Department of Mathematics
South Asian University
Akbar Bhawan
Chanakyapuri, New Delhi 110021 (India)
Cell No: 08744022273
deepasinha2001@gmail.com

Research Area: **Graph Structures**

Academic Qualification:

M.Sc., Ph. D. (University of Delhi), CSIR-NET (twice)

Future Plans: To grow academically

Achievements: CSIR_NET (qualified Twice)

Publications:

(a) Books: one
(b) Research Papers: 27

Conference/workshop/symposium attended: 39

Invited talks delivered: Ten

Papers presented: 23

Work experience: 16 years

Served several Institutions for graduate and post graduate courses, particularly Khalsa Girls Degree College (1996-1999), Delhi College of Engineering (1999-2004), Banasthali University (2004-2012).

Seven students got awarded their M. Phil. Degree under her supervision
.
Three students got awarded their Ph.D. in the year 2011-2012.

Have refereed several research papers for National and international Journal of high impact factor like Discrete Applied Mathematics, Graphs and Combinatorics, International Journal of Physical Sciences etc.

Sessions chaired in the National/ International conferences: four

Author 3

Name: Piyush Kant Rai
Date of Birth: February 5, 1980
E-Mail: raipiyush5@gmail.com
Current Affiliation:
Working as Assistant Professor (Senior-Scale) (Statistics) in the Department of Mathematics & Statistics (AIM & ACT), Banasthali University, Rajasthan.

Working Experience: Eight years of teaching and research experience including one year experience as a Project Assistant at Banaras Hindu University (BHU), U.P. and five months as a Statistical Fellow at Sanjay Gandhi Post Graduate Institute of Medical Sciences (SGPGIMS) Lucknow, U.P.

UGC Major/Minor Project: One Minor Research Project as Principal Investigator and one Major Research Project as Co-Principal Investigator.

Academic Qualification:

- Ph.D. (Statistics) from Banasthali University, Rajasthan.
- M.Phil. (Statistics), 2008, with First Class from Periyar Institute of Distance Education (PRIDE), Periyar University, Salem Tamilnadu.
- M.Sc. (Statistics), 2003, with First Rank (Gold Medal) from Banaras Hindu University (BHU), Varanasi, U.P.
- B.Sc. (Hons., Statistics), 2001, with First Class (5^{th} Rank in Faculty of Science) from Banaras Hindu University (BHU), Varanasi, U.P.
- Intermediate (Physics, Chemistry, Math, Hindi and English), 1996, with First Class (1^{st} Rank in College) from U.P. Board.
- High School (Hindi, English, Science, Math, Social Science and Biology), 1994, with first-Honours (1^{st} Rank in School) from U.P. Board.

Qualified National Eligibility Test:

- UGC NET, June 2004, UPSLET, August 2004 and ISI-JRF, May 2005.

Scholarships:

- 10^{th} to 12^{th} standard, 8^{th} to 10^{th} standard and 6^{th} to 8^{th} standard scholarship by Education Department U.P.

Publication: (National/International):

- Papers Published : 8
- In Press : 1
- Communicated : 3
- Books Published : Two Book Chapters are published and two are in Press.

Supervisor of 2 Ph.D. Scholars and 5 M.Phil. Scholars
Workshop and Training Program Attended /Organized: 17
Seminar and Conference Attended/Organized: 12

Membership:
Membership of Actuarial Society of India and Indian Bayesian Society.

Ain Shams Engineering Journal (2012) xxx, xxx–xxx

Ain Shams University

Ain Shams Engineering Journal

www.elsevier.com/locate/asej
www.sciencedirect.com

MECHANICAL ENGINEERING

GTA-based framework for evaluating the role of design parameters in cogeneration cycle power plant efficiency

Nikhil Dev [a,*], Samsher [b], S.S. Kachhwaha [c], Rajesh Attri [a]

[a] Department of Mechanical Engineering, YMCA University of Science and Technology, Faridabad, Haryana, India
[b] Department of Mechanical Engineering, Delhi Technological University, Delhi, India
[c] Department of Mechanical Engineering, School of Technology, Pandit Deendayal Petroleum University, Raisan, Gandhinagar, India

Received 11 April 2012; revised 3 July 2012; accepted 9 August 2012

KEYWORDS
CGCPP;
Parameters;
Graph theory;
Efficiency

Abstract This paper presents a methodology based on graph theoretic approach (GTA) to design a new cogeneration cycle power plant (CGCPP), improvement of existing plant and comparison of two real life operating cogeneration cycle power plants. Different combinations may be suggested by a manufacturer to an organization for selecting or improving the efficiency of a power plant. This paper identifies various design parameters affecting cogeneration cycle power plant efficiency. All these parameters are interacting with each other by different amounts. An attempt has been made to develop a mathematical model of CGCPP from these interacting parameters using GTA. A CGCPP efficiency index is proposed which evaluates the influence power of these parameters.

1. Introduction

Cogeneration is the production of more than one useful form of energy (such as process heat and electric power) from the same energy source. Cogeneration systems often capture otherwise wasted thermal energy, usually from an electricity producing device like a heat engine (e.g., steam-turbine, gas-turbine, diesel-engine), and use it for space and water heating, industrial process heating, or as a thermal energy source for another system component [1,2].

Design of cogeneration cycle power plant, improvement in existing plant and comparison of two real life operating power plants require a multi attribute decision making (MADM) technique to analyze the effect of one system/design parameter on the other systems/design parameters. In multiple criteria decision making, a number of alternatives have to be evaluated and compared using several criteria. The aim of MADM techniques is to provide support to the decision-maker in the process of making the choice between alternatives.

From the literature review it has been revealed that there are two models i.e. thermodynamic and thermo-economic model for the analysis of power plants. Thermodynamic model of a power plant gives solution for optimum efficiency while thermo-economic model is useful for the analysis on efficiency and cost basis in association with each other. For the complete

* Corresponding author. Tel.: +91 9711812394.
E-mail addresses: nikhildevgarg@yahoo.com (N. Dev), Sam6764@yahoo.com (Samsher), sskachhwaha@rediffmail.com (S.S. Kachhwaha), rajeshattri2005@gmail.com (R. Attri).

Peer review under responsibility of Ain Shams University.

Production and hosting by Elsevier

2090-4479 © 2012 Ain Shams University. Production and hosting by Elsevier B.V. All rights reserved.
http://dx.doi.org/10.1016/j.asej.2012.08.002

analysis of a power plant (CGCPP for the present case) thermodynamic, economic, reliability, human being and environment aspects have to be studied in association with each other. At present there is no effective mathematical model for studying these aspects in association with each other for CGCPP. Simple model, easy to implement, lesser computational cost and flexible with changing environment is required to evaluate the cogeneration cycle power plant efficiency on design basis or analysis basis.

A number of MADM techniques have been suggested in the literature to model various systems and their elements. Graph theory is one of such methodologies. It is a systematical and logical approach. Digraph model representation has proved to be useful for modeling and analyzing various kinds of systems and problems in numerous fields of science and technology [3,4]. The matrix approach is useful in analyzing the graph/digraph models expeditiously to derive the system function and index to meet the objectives. Moreover, representation of the digraph by a matrix offers ease in computer handling. In view of these, GTA method is proposed in this paper for the prediction of efficiency of a CGCPP in terms of an index which takes into account various design parameters and interactions between them.

2. Identification of design parameters in cogeneration cycle power plant

In this part, system modeling of cogeneration cycle power plant and its analysis is described. Cogeneration cycle power plant considered for the present analysis is shown in Fig. 1.

The air at the ambient temperature is compressed by the air compressor and directed to the combustion chamber. The compressed air mixes with the natural gas from the fuel supply system to produce hot combustion gas in the combustor. The hot combustion gas is delivered to the gas turbine where the power is generated. The exhaust gas passes through a Heat Recovery Steam Generator where water is converted to steam. The steam produced is used as process steam.

For the graph theoretic analysis cogeneration cycle power plant is divided into following four systems:

1. Air compressor system (S_1).
2. Combustion chamber system (S_2).
3. Gas turbine system (S_3).
4. Heat Recovery Steam Generator (HRSG) system (S_4).

Based on the above analysis, a real life CGCPP has been converted into a well defined and bounded engineering representation based on these systems. These systems of the CGCPP are also connected with each other physically or indirectly at the level of their sub-systems. Efficiency of these systems and their interaction will decide the efficiency of CGCPP. In the present work, system is modeled by considering its structure on the basis of efficiency. Let each of the four systems of plant be represented by vertices S_i's ($i = 1, 2, 3, 4$) and interconnection between two systems (S_i, S_j) is represented by edges c_{ij}'s ($i = 1, 2, 3, 4$ and $i \neq j$) connecting the two vertices S_i and S_j.

In actual system all four system do not affect each other. The graph theoretic representation [S, c] of vertex and edge sets of the four system cogeneration cycle power plant, called system structure graph (SSG) is shown in Fig. 2. This system structure graph (Fig. 2) represents the internal structure of the CGCPP at system level. It clearly shows different systems and their interactions in the CGCPP as discussed above.

This is based upon the working of cogeneration cycle power plant as per the following:

1. The ambient air comes to the compressor after being filtered by air filters. Compressor and turbine are attached with a shaft. So the power to compress the air comes to the compressor from the turbine. This is represented by the edge c_{31}. S_1 is the compressor system.

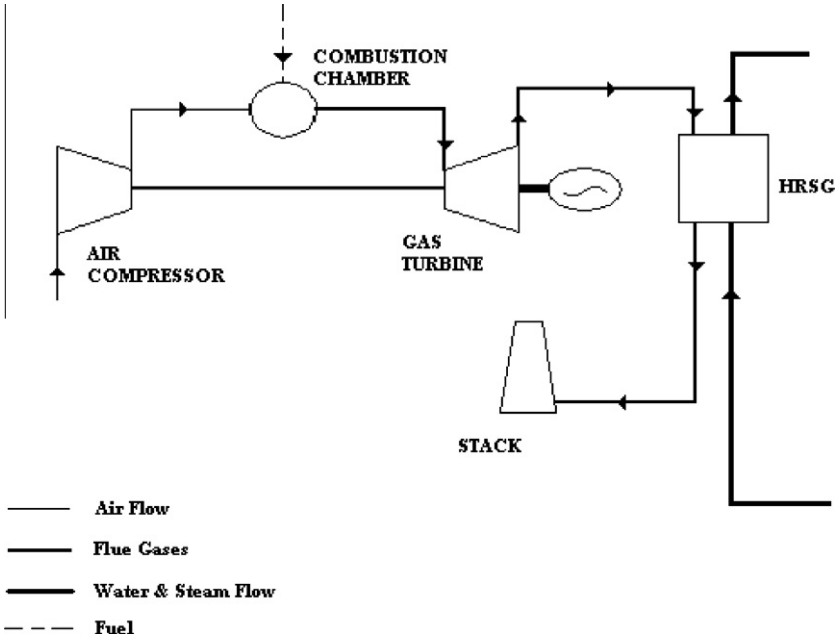

Figure 1 Schematic flow diagram of cogeneration cycle power plant.

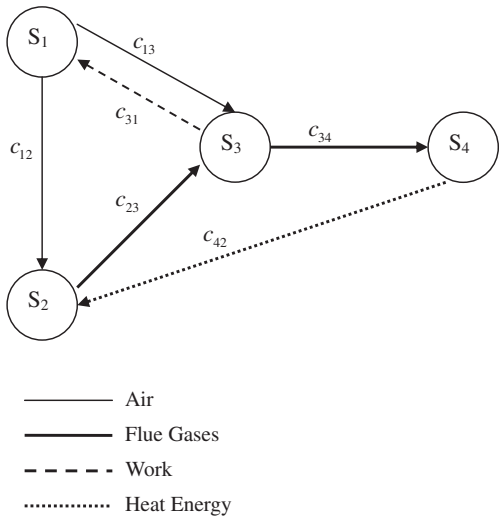

Figure 2 System structural graph of cogeneration cycle power plant: air compressor system (S_1), combustion chamber system (S_2), gas turbine system (S_3), Heat Recovery Steam Generator system (S_4).

2. After compression, air goes to the combustion chamber. This is represented by edge c_{12}. Fuel is added in the combustion chamber.
3. A blade is cooled by being made hollow so that a coolant air can circulate through it. Coolant air is obtained directly from the compressor, thus bypassing the combustion chamber. Edge c_{13} represents the bypassing of cooling air.
4. Fuel supplied to the combustion chamber is generally compressed natural gas (CNG). Fuel supply is taken as a part of combustion chamber system. Outlet temperature of combustion chamber system [S_2] depends upon thermal stress limit of gas turbine blade material. Highest temperature of flue gas coming out from combustion chamber is controlled by changing air–fuel (A/F) ratio. Combustion product flows to gas turbine as shown by edge c_{23}.
5. Depending upon the temperature of flue gas, HRSG [S_4] may be used for (i) partial heating (regeneration) of the compressed air leaving the compressor (c_{42}), or (ii) generating steam in a dual or multipressure steam cycle.
6. Flue gases coming out of combustion chamber and entering to HRSG system [S_4] are shown by the edge c_{34}.

The design parameters affecting the CGCPP efficiency have been identified on the basis of exhaustive literature survey and discussion with experts both from organization and academics. These parameters are epitomized in Fig. 3.

Rationales for selecting the design parameters for all systems are discussed below.

2.1. Compressor system

1. As the ambient temperature increases, density of air decreases. Due to which the compressor has to do more work to compress the same mass of air at high temperature than at lower temperature. Output of gas-steam cogeneration cycle is a strong function of the inlet air temperature. When the inlet air temperature drops, power output increases considerably and heat rate varies slightly. Where heat rate is heat input required to produce a unit quantity of power.
2. Enthalpy and specific heats (both at constant pressure and constant volume) for a gas at particular temperature and pressure have different values for humidified air and non-humidified air. This difference depends upon the relative humidity.
3. Compressor efficiency is a function of manufacturing quality and may vary from manufacturer to manufacturer.
4. The thermal efficiency of ideal Brayton Cycle is being given by the following relationship.

$$\eta_{TH} = 1 - \frac{1}{r_p^{(k-1)/k}}$$

r_p is the compressor pressure ratio; k is the ratio of specific heats

5. Compressor outlet temperature is the temperature at which compressed air will be entering the combustor. It will be affected by the pressure ratio and polytropic efficiency of compressor.

2.2. Combustion chamber system

1. If the inlet temperature to combustion chamber is higher then lower amount of fuel will be required to attain the combustion chamber outlet temperature or turbine inlet temperature (TIT).
2. Type of fuel used in combustion chamber will be a deciding factor that how much heat will be released by burning unit amount of fuel. Ratio of Carbon to Hydrogen (C/H) decides the calorific value of fuel. When the fuel-calorific value is higher then the combustion efficiency will be higher. With the increase in fuel-calorific value the burning velocity increases which decline the NOx conversion rate slightly [5].
3. Combustion chamber loses energy due to heat transfer, noise and vibration. Fuel utilization efficiency depends upon the design of combustion chamber.
4. Overall efficiency of cycle depends upon the amount of fuel injected in combustion chamber. There is no other supply of energy to the cycle for a fixed net output power, so mass of fuel injected will be deciding factor for cycle efficiency.
5. If the mass of air entering the combustion chamber gets changed and amount of fuel is not changed then combustion chamber outlet temperature will depend upon the mass of air. For a lean fuel–air mixture, if amount of fuel remains same and mass of air decreases then temperature of combustion gasses will be increased.
6. Combustion chamber outlet temperature is fixed by thermal stress limit of turbine blade material. As the turbine inlet temperature (TIT) increases the cycle efficiency will also increase.
7. Under high pressure conditions, combustion efficiency improves with increase in pressure [6].

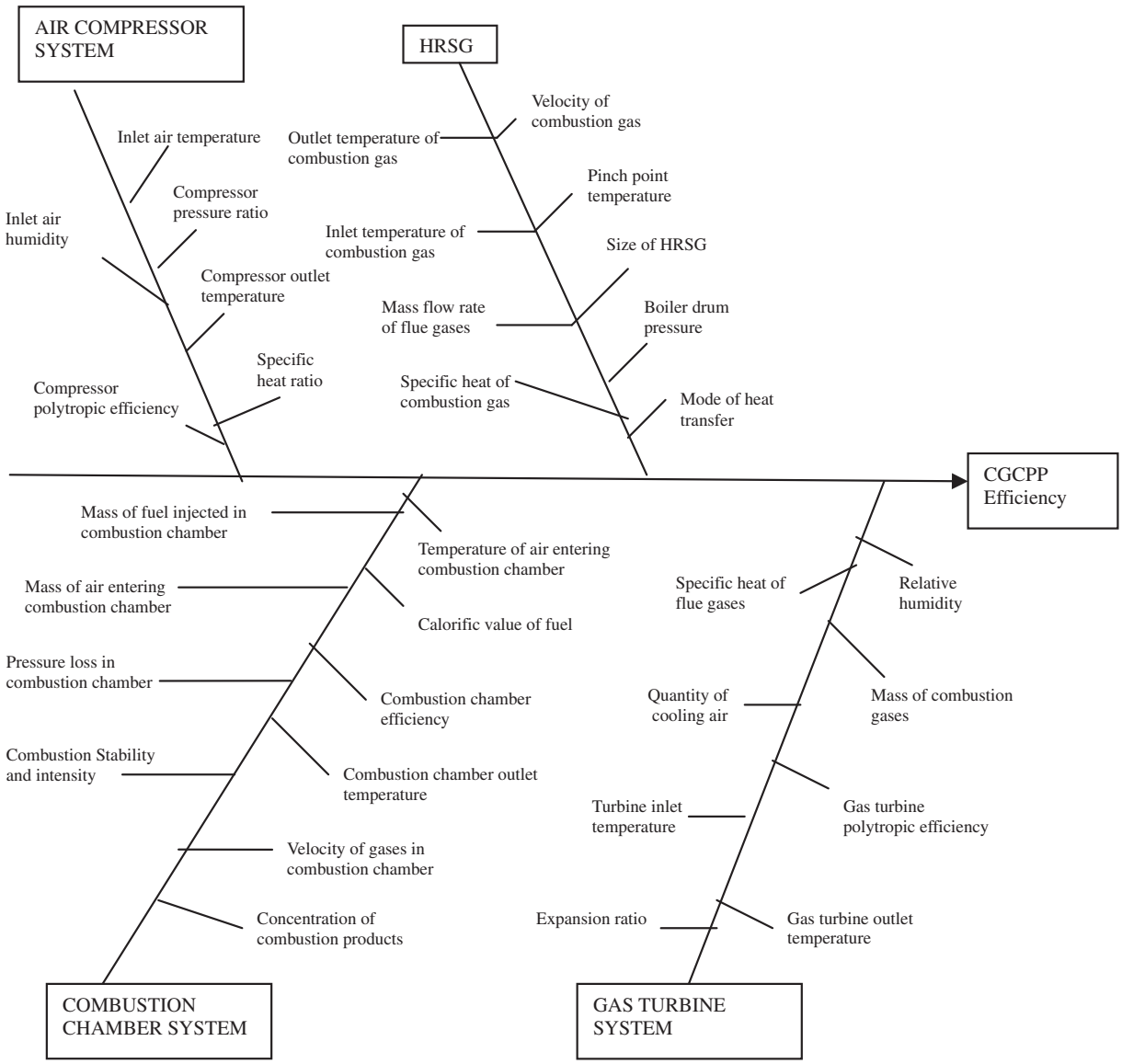

Figure 3 Diagram showing systems of CGCPP and design parameters.

2.3. Gas turbine system

1. Expansion ratio of gas turbine depends upon the pressure ratio of air compressor. Higher is the expansion ratio of gas turbine more will be the utilization of enthalpy across the gas turbine.
2. Higher TIT means that combustion gases are having higher enthalpy. It can be seen from the following relationship that work obtained from cycle is a function of TIT [6].

$$W = C_p T_3 \left(1 - \frac{1}{r^{\frac{(\gamma-1)}{\gamma}}}\right) - T_1 \left(r^{\frac{(\gamma-1)}{\gamma}} - 1\right)$$

where W is the net work obtained from a simple gas turbine cycle, C_p is the specific heat at constant pressure, γ is the ratio of specific heats, T_1 is ambient air temperature, T_3 is TIT and r is the pressure ratio. Higher is the TIT, higher will be work obtained. For all cooling modes, coolant requirement increases with increase in TIT.

3. If the efficiency of gas turbine is higher then the utilization of energy in gas turbine will be higher.
4. Flue gases coming out of gas turbine at lower pressure and high temperature are passed through HRSG for waste heat recovery.
5. Cooling air is passed through the blades for cooling. This air quantity is fixed by air-by-pass ratio.

2.4. Heat Recovery Steam Generator system

1. It is being found that introducing multipressure steam generation in the HRSG in place of single pressure improves the performance of a cogeneration power plant. HRSGs are classified into single, dual, and triple pressure types depending on the number of drums in the boiler [7].

2. Due to increased velocity of flue gases, convective heat transfer coefficient of flue gases gets increased. If the velocity of flue gases coming of gas turbine is high then more heat will be transferred to HRSG tubes and steam can be produced at high temperature and pressure [8].
3. Heat transfer by conduction mode is more than convection mode for the same temperature difference. Heat transfer by radiation is very less.
4. If the flue gases have high specific heat then there will be very less drop in temperature of flue gases while passing through HRSG for a specific amount of heat transfer.
5. A large size of HRSG will minimize the heat loss but this will increase the cost of HRSG [7].
6. Temperature of gases coming out from HRSG is being limited by the dew point temperature of flue gases. If it is kept high then energy will be lost to the environment and efficiency will be decreased.
7. The HRSG steam production for a given gas turbine goes down as the steam pressure and temperature goes up [9].
8. Higher pinch point leads to lesser efficiency. Where pinch point is the difference between gas temperature leaving an evaporating section and the temperature at which boiling is occurring.

3. Graph theoretic approach (GTA)

Graph theory is a logical and systematic approach useful for modeling and analyzing various kinds of systems and problems in numerous fields of science and technology [10–18]. GTA synthesizes the inter-relationship among different parameters or sub-system parameters and provides a synthetic score for the entire system. It also takes care of directional relationship and inter-dependence among parameters.

Graph theoretic and matrix model consists of digraph representation, matrix representation and permanent representation. The digraph characterizes the visual representation of the elements (parameters) and their interdependence. The matrix converts the digraph into mathematical form. The permanent function is a mathematical model that helps to determine index, which can be used for comparison.

3.1. Digraph representation of CGCPP system

Digraph is used to represent the parameters affecting the efficiency of CGCPP system and their interdependencies in terms of nodes and edges. The digraph consists of a set of nodes $N = \{n_i\}$ with $i = 1, 2, \ldots, M$ and a set of directed edges $E = \{c_{ij}\}$. A node n_i represents ith parameter and edges represent the interdependence between parameters. The total of nodes, M, is equal to the number of parameters considered for the system. If a node i has relative importance over another node j, then a directed edge or arrow is drawn from node i to node j (c_{ij}). If a node j is having relative importance over i, then a directed edge or arrow is drawn from node j to node i (c_{ji}). The digraphs are dependent on the subjective judgement. In the present case, to overcome this limitation different power plant expert (both academic and industry) has been consulted for the digraph preparation.

For the development of CGCPP system digraph, the four categories of system (as discussed in Section 2) are considered and represented by four nodes in the CGCPP system digraph, shown in Fig. 4. The directed edges are drawn according to the interdependence of these systems.

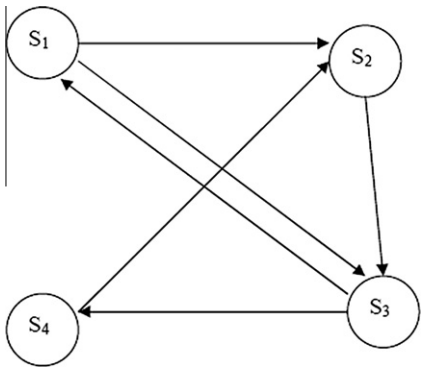

Figure 4 Digraph showing four attributes of cogeneration cycle power plant and their interdependencies in the system (attributes: air compressor system (S_1), combustion chamber system (S_2), gas turbine system (S_3), Heat Recovery Steam Generator system (S_4)).

3.2. Matrix representation of CGCPP system

Digraph helps the experts to visualize and analyze the proposed system. But as the number of nodes and their interdependence increase, the digraph becomes complex. In such cases, a visual analysis of the digraph is more difficult and complex. To overcome this difficulty, the digraph is represented in matrix form. Matrix representation of a digraph gives one-to-one representation.

In general, if there is M number of contributing categories of systems and interdependencies exists among all of these categories and there are no self loops, then the GTPP system matrix E for the GTPP system digraph is written as:

$$E = \begin{array}{c} \begin{matrix} 1 & 2 & 3 & - & - & M \end{matrix} \quad \text{Systems} \\ \begin{bmatrix} S_1 & c_{12} & c_{13} & - & - & c_{1M} \\ c_{21} & S_2 & c_{23} & - & - & c_{2M} \\ c_{31} & c_{32} & S_3 & - & - & c_{3M} \\ - & - & - & - & - & - \\ - & - & - & - & - & - \\ c_{M1} & c_{M2} & c_{M3} & - & - & S_M \end{bmatrix} \begin{matrix} 1 \\ 2 \\ 3 \\ - \\ - \\ M \end{matrix} \end{array} \tag{1}$$

Hence, the CGCPP system matrix, also known as variable permanent matrix (VPM_{CGCPP}), corresponding to CGCPP system digraph as shown in Fig. 4 is written as:

$$E^* = \begin{array}{c} \begin{bmatrix} 1 & 2 & 3 & 4 \end{bmatrix} \quad \text{Systems} \\ \begin{bmatrix} S_1 & c_{12} & c_{13} & 0 \\ 0 & S_2 & c_{23} & 0 \\ c_{31} & 0 & S_3 & c_{34} \\ 0 & c_{42} & 0 & S_4 \end{bmatrix} \begin{matrix} 1 \\ 2 \\ 3 \\ 4 \end{matrix} \end{array} \tag{2}$$

In this matrix E^*, the diagonal elements S_1, S_2, S_3, and S_4 represent the impact of different categories of systems on the CGCPP efficiency on the basis of their design parameters and c_{ij} represents the interdependency of the system category i and j, represented by the edge c_{ij} from i to j in the digraph.

Please cite this article in press as: Dev N et al., GTA-based framework for evaluating the role of design parameters in cogeneration cycle power plant efficiency, Ain Shams Eng J (2012), http://dx.doi.org/10.1016/j.asej.2012.08.002

3.3. Permanent representation of CGCPP system matrix

Both digraph and matrix representations are not unique in nature because they are altered by changing the labels of their nodes. Hence, to develop a unique representation that is independent of labeling, a permanent function of the CGCPP system matrix is proposed here. The permanent is a standard matrix function and is used in combinatorial mathematics [3,19,20]. The permanent function is obtained in a similar manner as the determinant but unlike in a determinant where a negative sign appears in the calculation, in a variable permanent function positive signs replace these negative signs.

The expression for permanent function corresponding to four-element digraph, as shown in Fig. 4, is written as:

$$\begin{aligned}\mathrm{Per}(E^*) &= S_1\,S_2\,S_3\,S_4 \\ &+ c_{12}\,c_{21}\,S_3\,S_4 + c_{13}\,c_{31}\,S_2\,S_4 + c_{14}\,c_{41}\,S_2\,S_3 \\ &+ c_{23}\,c_{32}\,S_1\,S_4 + c_{24}\,c_{42}\,S_1\,S_3 + c_{34}\,c_{43}\,S_1\,S_2 \\ &+ c_{12}\,c_{23}\,c_{31}\,S_4 + c_{13}\,c_{32}\,c_{21}\,S_4 + c_{12}\,c_{24}\,c_{41}\,S_3 \\ &+ c_{14}\,c_{42}\,c_{21}\,S_3 + c_{13}\,c_{34}\,c_{41}\,S_2 + c_{14}\,c_{43}\,c_{31}\,S_2 \\ &+ c_{23}\,c_{34}\,c_{42}\,S_1 + c_{24}\,c_{43}\,c_{32}\,S_1 \\ &+ c_{12}\,c_{21}\,c_{34}\,c_{43} + c_{13}\,c_{31}\,c_{24}\,c_{42} + c_{14}\,c_{41}\,c_{23}\,c_{32} \\ &+ c_{12}\,c_{23}\,c_{34}\,c_{41} + c_{14}\,c_{43}\,c_{32}\,c_{21} + c_{13}\,c_{34}\,c_{42}\,c_{21} \\ &+ c_{12}\,c_{24}\,c_{43}\,c_{31} + c_{14}\,c_{42}\,c_{23}\,c_{31} + c_{13}\,c_{32}\,c_{24}\,c_{41}\end{aligned} \tag{3}$$

Eq. (3), i.e., the permanent function of the CGCPP system matrix, is a mathematical expression in symbolic form and contains a number of terms which are structure invariants. These terms are arranged in groupings whose physical significance is explained below:

- The first group contains only one term and represents the presence of major systems i.e. $S_1\,S_2\,S_3\,S_4$.
- The second grouping is absent since these are no self-loops i.e. this grouping will occur in expression only if a system is connected to itself.
- The third grouping contains a set of 2 systems, interdependence and remaining N-2 (i.e., 2 here) systems.
- Each term of fourth grouping represents a set of 3 system, interdependence and remaining N-3 (i.e., 1 here) systems.
- The fifth grouping contains terms arranged in two-sub grouping. The first sub grouping contains a set of two systems, the interdependence and measure of remaining N-4 systems. The second sub grouping is a set of 4 systems, interdependence or its pair and the measure of remaining N-4 systems.

If the values of CGCPP system matrix, i.e. Eq. (2) are substituted in Eq. (3), then, some of the terms in various groupings are nullified and resultant permanent representation is as follows:

$$\begin{aligned}\mathrm{Per}[E^*] = [&S_1\,S_2\,S_3\,S_4 + (c_{13}\,c_{31})(S_2\,S_4) + (c_{31}\,c_{23})(S_1\,S_4) \\ &+ S_1\,(c_{23}\,c_{34}\,c_{42})]\end{aligned} \tag{3}$$

A computer program was developed using C^{++} language for calculating the values of permanent function for square matrix of M × M matrix.

3.4. Cogeneration cycle power plant efficiency index

CGCPP efficiency index is function of considered systems i.e. air compressor system, combustion chamber system, gas turbine system, and Heat Recovery Steam Generator system.

$$\begin{aligned}&\text{CGCPP efficiency index(CGCPPEI)} \\ &= f(\text{systems}) = f(\text{Air compressor system, Combustion chamber system,} \\ &\textit{turbine system, Heat Recovery Steam Generator system})\end{aligned}$$

The permanent function of CGCPP system (i.e. Eq. (3)) is proposed, here, for the evaluation of CGCPPEI because it contains all the possible components of CGCPP system and their interdependence. The numerical value of CGCPP system matrix is named as the CGCPPEI:

$$\begin{aligned}\text{CGCPPEI} &= \mathrm{Per}[E^*] \\ &= \text{Permanent function of CGCPP system matrix}\end{aligned}$$

To calculate this index, the values of S_i and c_{ij} are required. The values of these parameters and their interdependence are found on the basis of the production system data available in the organization and the experience of production personnel. If a quantitative value is not available, then a ranked value judgement on a scale (e.g., from 1 to 9) is adopted. Table 1 is suggested for this purpose. To assign numerical values to the interdependence of parameters c_{ij}, the opinions of production experts can be recorded. But this interdependence of parameters cannot be measured directly and, hence, qualitative values may be adopted. These qualitative values of the interdependence of parameters are also assigned on a scale (e.g., 1–5), as suggested in Table 2.

The efficiency index value for a number of cogeneration cycle power plants can be evaluated by substituting the values of S_i and c_{ij} in Eq. (3). Index values will differ for different cogeneration cycle power plants because of affect of different parameters to different extent on the system. In this way, different power plants may be arranged in ascending or descending order, according to their efficiency index value. Power plant with the higher value of efficiency index find better chance of higher work output for same consumption of fuel than the others.

4. Comparison of cogeneration cycle power plants

The identification of a new power plant and its comparison with other power plants based on efficiency index is carried out by considering their $\mathrm{VPF_{CGCPP}}$. Two organizations are similar the cogeneration cycle power plant system viewpoint if their digraphs are isomorphic at the system and subsystem level. Two CGCPP system digraphs are isomorphic if they have identical $\mathrm{VPF_{CGCPP}}$. This means that not only numbers of terms in each grouping/subgrouping are the same but also the value. Based on this fact, a composite CGCPP design parameter set for an organization is written as:

$$[(T_i^D/T_{ij}^D)(H_i^D/H_{ij}^D)] \tag{4}$$

where T_i^D represents the total number of terms in the ith grouping, T_{ij}^D represents the total number of terms in jth subgrouping of the ith grouping. In case there is no subgrouping, T_{ij}^D is same as T_i^D; similarly H_i^D is the value of the ith grouping. H_{ij}^D is the numerical value of the jth subgrouping in the ith grouping. Numerical values of the S_i's and c_{ij}'s are substituted in the subgrouping and grouping to obtain H_{ij}^D. In general, two power plants may not be isomorphic from the design parameter viewpoint. Comparison is also carried out on the basis of coefficient of similarity. The coefficient is derived from the structure, i.e., the number of terms in different groupings and the permanent function, i.e., $\mathrm{VPF_{CGCPP}}$ and compares

Table 1 Quantification of factors affecting cogeneration cycle power plant efficiency.

S. No.	Qualitative measure of parameters affecting cogeneration cycle efficiency	Assigned value of parameter
1	Exceptionally low	1
2	Very low	2
3	Low	3
4	Below average	4
5	Average	5
6	Above average	6
7	High	7
8	Very high	8
9	Exceptionally high	9

Table 2 Quantification of interdependencies.

S. No.	Qualitative measure of interdependencies	c_{ij}
1	Very strong	5
2	Strong	4
3	Medium	3
4	Weak	2
5	Very weak	1

two power plants or a set of power plants on the basis of similarity or dissimilarity.

If the values of distinct terms in the jth subgrouping of the ith grouping of $\mathrm{VPF_{CGCPP}}$ for two power plants under consideration are denoted by H_{ij}^{D} and $H_{ij}^{\prime D}$, then criterion of coefficient of dissimilarity (C_d^D) is given as

$$C_d^D = \frac{\sum_i \sum_j \phi_i}{Y} \tag{5}$$

where Y is the maximum of $\sum_i \sum_j |H_{ij}^{D}|$ and $\sum_i \sum_j |H_i^{\prime D}|$. When subgrouping are absent, $H_{ij}^{D} = H_i^{D}$ and $H_{ij}^{\prime D} = H_i^{\prime D}$; while $\phi_{ij} = |H_i^{D} - H_i^{\prime D}|$, when the subgrouping are absent. Once the coefficient of dissimilarity is known, then, coefficient of similarity (C_S^D) is calculated as follows:

$$C_S^D = 1 - C_d^D \tag{6}$$

It may be noted that the coefficient of similarity and dissimilarity lie in the range between 0 and 1. If two power plants are isomorphic or completely similar then, their coefficient of similarity is 1 and the coefficient of dissimilarity is 0. In a similar manner, if two power plants are completely dissimilar, their coefficient of dissimilarity is 1.

5. Methodology

A methodology for the evaluation of CGCPP efficiency index (CGCPPEI) for a cogeneration cycle power plant is proposed on the basis of GTA. The main steps of this methodology are as follows:

1. Identify the various system categories affecting the CGCPP efficiency.
2. Develop the CGCPP system digraph. This is the digraph at the system level.
3. Identify the various design parameters for each system category of CGCPP system.
4. For each system category, develop a digraph among the design parameters based on the interactions among them. This is the digraph at each sub-system level.
5. Based on the above-mentioned digraphs among sub-system design parameters, develop the variable permanent matrix for each system category.
6. Calculate the permanent function at each sub-system level. For avoiding the complexity, the numerical values of inheritance and interactions are used.
7. Develop the CGCPP system matrix for the CGCPP system digraph. This will be $\mathrm{M} \times \mathrm{M}$ matrix with diagonal elements of S_i and off-diagonal elements of c_{ij}. The value of the permanent function at each sub-system level provides inheritance (diagonal elements of S_i) for each system category. The values of interaction among these system categories (i.e. off-diagonal elements of c_{ij}) are to be decided by the experts on the basis of scale of 1–5.
8. Calculate the permanent function of CGCPP system matrix at the system level. This is the value of CGCPP efficiency which mathematically characterizes the efficiency of any cogeneration cycle power plant based on the different design parameters and their interdependence.
9. Compare different power plants in terms of CGCPP efficiency index and list them in descending order of their $\mathrm{VPM_{CGCPP}}$ values. The power plant having the lowest value of $\mathrm{VPM_{CGCPP}}$ has the best chance of efficiency improvement.
10. Record the results of this study and document them for future analysis.

6. Working example

For the demonstration of proposed methodology, a cogeneration cycle power plant is taken as an example. It is proposed to find the value of CGCPP efficiency index (CGCPEI). For this purpose, some numerical values of all parameters and their interdependencies are required i.e. the value of all terms of $\mathrm{VPM_{CGCPP}}$. The value of diagonal elements in $\mathrm{VPM_{CGCPP}}$, i.e., the value of all four systems S_1, S_2, S_3 and S_4 are evaluated by applying GTA for design parameters of the respective subsystem. The methodology explained in Section 4 is used to evaluate CGCPP efficiency index in this example.

1. Various system categories affecting the CGCPP efficiency (four categories of system in the present case) are identified and presented in Fig. 2.
2. A digraph is developed for these four system category as shown in Fig. 4.
3. Design parameters are identified for each category of CGCPP system and presented in Fig. 2.
4. Digraphs for each system category (Figs. 5–8) are developed considering the sub-systems design parameters. Nodes in the digraph represent the design parameters and their mutual interactions are depicted by different edges.

Please cite this article in press as: Dev N et al., GTA-based framework for evaluating the role of design parameters in cogeneration cycle power plant efficiency, Ain Shams Eng J (2012), http://dx.doi.org/10.1016/j.asej.2012.08.002

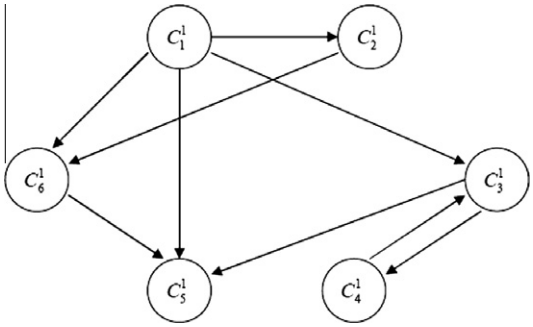

Figure 5 Digraph for air compressor system design parameters (attributes: inlet air temperature (C_1^1), inlet air humidity (C_2^1), compressor polytropic efficiency (C_3^1), compressor pressure ratio (C_4^1), compressor outlet temperature (C_5^1), and specific heat ratio (C_6^1)).

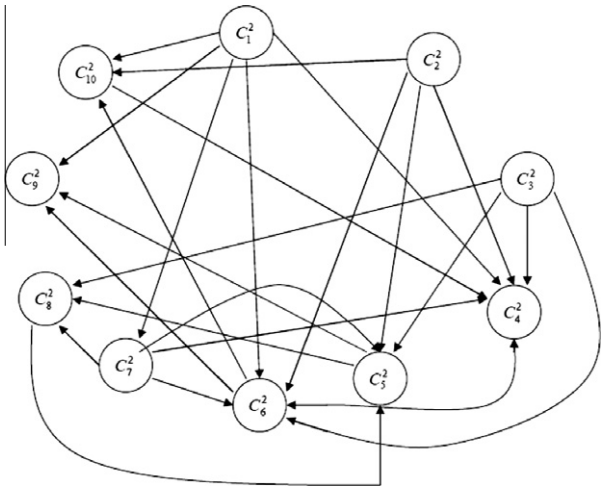

Figure 6 Digraph for combustion chamber system design parameters (attributes: Temperature of air entering combustion chamber (C_1^2), calorific value of fuel (C_2^2), combustion chamber efficiency (C_3^2), combustion chamber outlet temperature (C_4^2), velocity of gases in combustion chamber (C_5^2), mass of fuel injected in combustion chamber (C_6^2), mass of air entering combustion chamber (C_7^2), pressure loss in combustion chamber (C_8^2), combustion Stability and intensity (C_9^2), and concentration of combustion products (C_{10}^2)).

5. Variable permanent matrix for digraph for each subsystem is written. At the sub-system level, VPM for digraph for subsystem 1 (Fig. 5) in general form is considered. Similar to Eq. (1), VPM for air compressor system is given by:

$$\mathrm{VPM}_{\text{air compressor}} = \begin{array}{c} \begin{matrix} C_1^1 & C_2^1 & C_3^1 & C_4^1 & C_5^1 & C_6^1 \end{matrix} \\ \begin{bmatrix} c_{11}^1 & c_{12}^1 & c_{13}^1 & c_{14}^1 & c_{15}^1 & c_{16}^1 \\ c_{21}^1 & c_{22}^1 & c_{23}^1 & c_{24}^1 & c_{25}^1 & c_{26}^1 \\ c_{31}^1 & c_{32}^1 & c_{33}^1 & c_{34}^1 & c_{35}^1 & c_{36}^1 \\ c_{41}^1 & c_{42}^1 & c_{43}^1 & c_{44}^1 & c_{45}^1 & c_{46}^1 \\ c_{51}^1 & c_{52}^1 & c_{53}^1 & c_{54}^1 & c_{55}^1 & c_{56}^1 \\ c_{61}^1 & c_{62}^1 & c_{63}^1 & c_{64}^1 & c_{65}^1 & c_{66}^1 \end{bmatrix} \end{array} \begin{array}{l} \text{Design parameters} \\ C_1^1 \\ C_2^1 \\ C_3^1 \\ C_4^1 \\ C_5^1 \\ C_6^1 \end{array} \quad (7)$$

At subsystem level, Tables 1 and 2 are used to determine numerical values for inheritance of parameters and their interactions. The variable permanent matrices for different sub-systems (based on their digraph) are written through Eqs. (8)–(11).

For air compressor, the values taken from Table 1 are: $C_1^1 = 9,\ C_2^1 = 1,\ C_3^1 = 9,\ C_4^1 = 5,\ C_5^1 = 1,\ C_6^1 = 3.$

The values taken from Table 2 are: $c_{12}^1 = 3,\ c_{13}^1 = 4,\ c_{15}^1 = 3,\ c_{16}^1 = 5,\ c_{26}^1 = 2,\ c_{34}^1 = 5, c_{35}^1 = 4,\ c_{43}^1 = 3,\ c_{65}^1 = 1.$

Substituting these values in Eq. (7), $\mathrm{VPM}_{\text{air compressor}}$ is given as:

$$\mathrm{VPM}_{\text{air compressor}} = \begin{array}{c} \begin{matrix} C_1^1 & C_2^1 & C_3^1 & C_4^1 & C_5^1 & C_6^1 \end{matrix} \\ \begin{bmatrix} 9 & 3 & 4 & 0 & 3 & 5 \\ 0 & 1 & 0 & 0 & 0 & 2 \\ 0 & 0 & 9 & 5 & 4 & 0 \\ 0 & 0 & 3 & 5 & 0 & 0 \\ 0 & 0 & 0 & 0 & 1 & 0 \\ 0 & 0 & 0 & 0 & 1 & 3 \end{bmatrix} \end{array} \begin{array}{l} \text{Design parameters} \\ C_1^1 \\ C_2^1 \\ C_3^1 \\ C_4^1 \\ C_5^1 \\ C_6^1 \end{array} \quad (8)$$

In similar way, variable permanent matrices for other sub-systems are written as:

$$\mathrm{VPM}_{\text{Combustion chamber}} = \begin{array}{c} \begin{matrix} C_1^2 & C_2^2 & C_3^2 & C_4^2 & C_5^2 & C_6^2 & C_7^2 & C_8^2 & C_9^2 & C_{10}^2 \end{matrix} \\ \begin{bmatrix} 9 & 0 & 0 & 5 & 0 & 4 & 4 & 0 & 2 & 1 \\ 0 & 9 & 0 & 5 & 1 & 5 & 0 & 0 & 0 & 3 \\ 0 & 0 & 8 & 3 & 1 & 2 & 0 & 3 & 0 & 0 \\ 0 & 0 & 0 & 1 & 0 & 5 & 0 & 0 & 0 & 0 \\ 0 & 0 & 0 & 0 & 5 & 0 & 0 & 4 & 4 & 0 \\ 0 & 0 & 0 & 0 & 0 & 4 & 0 & 0 & 3 & 1 \\ 0 & 0 & 0 & 1 & 0 & 4 & 7 & 2 & 0 & 0 \\ 0 & 0 & 0 & 0 & 3 & 0 & 0 & 3 & 0 & 0 \\ 0 & 0 & 0 & 0 & 0 & 0 & 0 & 0 & 5 & 0 \\ 0 & 0 & 0 & 3 & 0 & 0 & 0 & 0 & 0 & 6 \end{bmatrix} \end{array} \begin{array}{l} \text{Design parameters} \\ C_1^2 \\ C_2^2 \\ C_3^2 \\ C_4^2 \\ C_5^2 \\ C_6^2 \\ C_7^2 \\ C_8^2 \\ C_9^2 \\ C_{10}^2 \end{array} \quad (9)$$

$$\mathrm{VPM}_{\text{GasTurbine}} = \begin{array}{c} \begin{matrix} C_1^3 & C_2^3 & C_3^3 & C_4^3 & C_5^3 & C_6^3 & C_7^3 & C_8^3 \end{matrix} \\ \begin{bmatrix} 9 & 0 & 4 & 5 & 0 & 0 & 0 & 0 \\ 0 & 8 & 1 & 0 & 4 & 5 & 0 & 3 \\ 0 & 0 & 9 & 4 & 0 & 0 & 0 & 0 \\ 0 & 0 & 0 & 4 & 0 & 0 & 0 & 0 \\ 0 & 0 & 0 & 4 & 6 & 0 & 0 & 0 \\ 0 & 0 & 3 & 0 & 0 & 6 & 0 & 1 \\ 0 & 0 & 0 & 0 & 0 & 1 & 1 & 0 \\ 0 & 0 & 0 & 0 & 0 & 0 & 0 & 2 \end{bmatrix} \end{array} \begin{array}{l} \text{Design Parameters} \\ C_1^3 \\ C_2^3 \\ C_3^3 \\ C_4^3 \\ C_5^3 \\ C_6^3 \\ C_7^3 \\ C_8^3 \end{array} \quad (10)$$

$$\mathrm{VPM}_{\text{HRSG}} = \begin{array}{c} \begin{matrix} C_1^4 & C_2^4 & C_3^4 & C_4^4 & C_5^4 & C_6^4 & C_7^4 & C_8^4 & C_9^4 \end{matrix} \\ \begin{bmatrix} 9 & 0 & 2 & 0 & 4 & 0 & 1 & 0 & 0 \\ 0 & 9 & 4 & 5 & 3 & 2 & 1 & 5 & 0 \\ 0 & 0 & 5 & 0 & 0 & 0 & 0 & 0 & 0 \\ 0 & 0 & 3 & 6 & 0 & 0 & 1 & 1 & 0 \\ 0 & 0 & 4 & 0 & 8 & 2 & 5 & 1 & 0 \\ 0 & 0 & 4 & 0 & 0 & 6 & 0 & 0 & 0 \\ 5 & 0 & 4 & 0 & 3 & 0 & 7 & 0 & 0 \\ 0 & 0 & 0 & 1 & 0 & 0 & 0 & 5 & 0 \\ 0 & 0 & 4 & 0 & 0 & 0 & 5 & 0 & 7 \end{bmatrix} \end{array} \begin{array}{l} \text{Design Parameters} \\ C_1^4 \\ C_2^4 \\ C_3^4 \\ C_4^4 \\ C_5^4 \\ C_6^4 \\ C_7^4 \\ C_8^4 \\ C_9^4 \end{array} \quad (11)$$

The value of permanent function for each category is calculated using a computer programme developed in language C^{++}. Substituting the values from Eq. (8) we get

Per $C_1 = 1620$

Similarly the values of permanent function of different sub-systems are evaluated from variable permanent matrices in Eqs. (9)–(11) and are written as under:

$$\mathrm{Per}C_2 = 2.3882 \times 10^7$$
$$\mathrm{Per}C_3 = 186624$$
$$\mathrm{Per}C_4 = 4.5730 \times 10^7$$

1. CGCPP system matrix at the system level is developed as per Eq. (1). In this matrix, values of diagonal elements are taken from the sub-system level as explained below:

S_1 = Per C_1, S_2 = Per C_2, S_3 = Per C_3, S_4 = Per C_4 and the values of the off-diagonal elements are taken form Table 2.

$$\mathrm{VPM}_{\mathrm{CCPP}} = T = \begin{array}{c} \begin{matrix} 1 & 2 & 3 & 4 & \text{Systems} \end{matrix} \\ \begin{bmatrix} 1620 & 5 & 3 & 0 \\ 0 & 23882000 & 5 & 0 \\ 3 & 0 & 18662 & 4 \\ 0 & 2 & 5 & 45730000 \end{bmatrix} \begin{matrix} 1 \\ 2 \\ 3 \\ 4 \end{matrix} \end{array} \quad (12)$$

7. Value of permanent function at the system level is evaluated and found to be 3.29434×10^{21} which indicates the value of CGCPP efficiency index for the case considered. CGCPP efficiency index depends upon the inheritance and interdependencies of system/sub-systems. As in present case, the system is large and the numbers of performance parameters are also large in number, so naturally index value comes out to be large digit number. In its present form it may be helpful in comparing the efficiency index of two or more similar cogeneration cycles. Moreover, as it is a new proposal in the field of cogeneration cycle power plant and no new work is a perfect one, so this matter can be discussed in future international meetings and conferences for the simplification of this index. By carrying out similar analysis, the efficiency index for different CGCPP system can be obtained. Higher value for the efficiency index of a CGCPP system indicates that its efficiency will be better than others. Monitoring at regular interval may be carried out by third party to assess power plant efficiency. Moreover, the analysis may be carried out at regular interval for self assessment.

Similarity and dissimilarity among CGCPP in terms of efficiency index may be estimated using methodology discussed in Section 4. Two cogeneration cycle power plants are considered which can be devided into four subsystems (1) air compressor system (2) combustion chamber system (3) gas turbin system (4) HRSG system. These are designated by H_1, H_2, H_3 and H_4 and H_1', H_2', H_3' and H_4' for the organization 1 and organization 2, respectively. Although the parameters identified are the same for both organizations, it is the inheritance and interaction of these design parameters that will lead to comparison. Based on the methodology discussed earlier in this paper, the VPM for organization 1 may be written as:

$$\begin{array}{c} \begin{matrix} 1 & 2 & 3 & 4 & \text{Systems} \end{matrix} \\ \begin{bmatrix} H_1 & h_{12} & h_{13} & 0 \\ 0 & H_2 & h_{23} & 0 \\ h_{31} & 0 & H_3 & h_{34} \\ 0 & h_{42} & 0 & H_4 \end{bmatrix} \begin{matrix} 1 \\ 2 \\ 3 \\ 4 \end{matrix} \end{array} \quad (13)$$

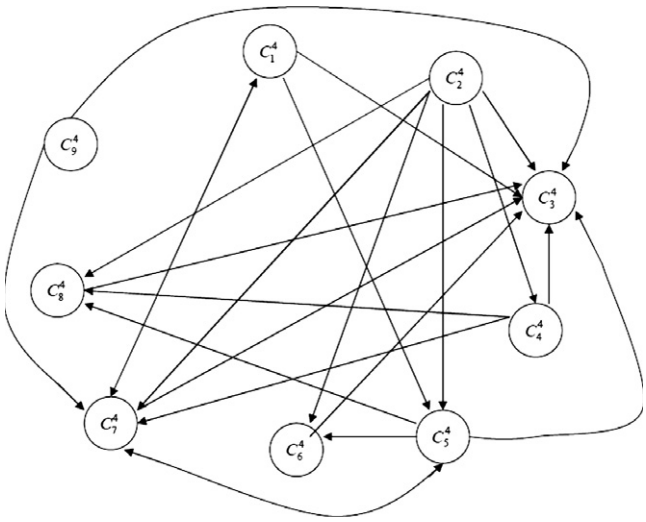

Figure 8 Digraph for HRSG system design parameters (attributes: mass flow rate of combustion gas (C_1^4), inlet temperature of combustion gas (C_2^4), outlet temperature of combustion gas (C_3^4), specific heat of combustion gas (C_4^4), velocity of combustion gas (C_5^4), pinch point of combustion gas and circulating water (C_6^4), size of HRSG (C_7^4), mode of heat transfer of combustion gas to circulating water (conduction, convection, radiation) (C_8^4), and pressure level of boiler water drums (single pressure, dual pressure, triple pressure) (C_9^4)).

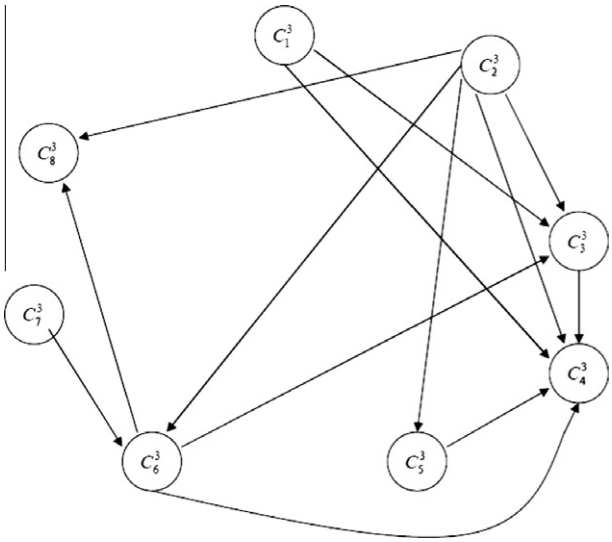

Figure 7 Digraph for gas turbine system design parameters (attributes: expansion ratio (C_1^3), turbine inlet temperature (C_2^3), gas turbine polytropic efficiency (C_3^3), gas turbine outlet temperature (C_4^3), quantity of cooling air (C_5^3), specific heat of flue gases (C_6^3), relative humidity (C_7^3), and mass/volume of combustion gases (C_8^3)).

The VPF of Eq. (13) will lead to the permanent of the matrix per E^* using Eq. (3).
The expression for Per H_1^* is arranged in $n + 1$, i.e., five groups

$$
\begin{aligned}
\text{Per}\,(H^{*}) = \quad & H_1\,H_2\,H_3\,H_4 && \text{First Grouping}\\
& + [h_{12}\,h_{21}\,H_3\,H_4 + h_{13}\,h_{31}\,H_2\,H_4 + h_{14}\,h_{41}\,H_2\,H_3 && \text{Third Grouping}\\
& \quad + h_{23}\,h_{32}\,H_1\,H_4 + h_{24}\,h_{42}\,H_1\,H_3 + h_{34}\,h_{43}\,H_1\,H_2] && \\
& + [h_{12}\,h_{23}\,h_{31}\,H_4 + h_{13}\,h_{32}\,h_{21}\,H_4 + h_{12}\,h_{24}\,h_{41}\,H_3 && \\
& \quad + h_{14}\,h_{42}\,h_{21}\,H_3 + h_{13}\,h_{34}\,h_{41}\,H_2 + h_{14}\,h_{43}\,h_{31}\,H_2 && \text{Fourth Grouping}\\
& \quad + h_{23}\,h_{34}\,h_{42}\,H_1 + h_{24}\,h_{43}\,h_{32}\,H_1] && \\
& + [h_{12}\,h_{21}\,h_{34}\,h_{43} + h_{13}\,h_{31}\,h_{24}\,h_{42} + h_{14}\,h_{41}\,h_{23}\,h_{32} && \\
& \quad + h_{12}\,h_{23}\,h_{34}\,h_{41} + h_{14}\,h_{43}\,h_{32}\,h_{21} + h_{13}\,h_{34}\,h_{42}\,h_{21} && \text{Fifth Grouping}\\
& \quad + h_{12}\,h_{24}\,h_{43}\,h_{31} + h_{14}\,h_{42}\,h_{23}\,h_{31} + h_{13}\,h_{32}\,h_{24}\,h_{41}] &&
\end{aligned}
\tag{14}
$$

(the second group is absent as there is no self-loops) and contains $n!$, i.e., 24 terms.

Similar to Eqs. (13) and (14), VPM and the permanent function for the organization 2 may be written down. The values of inheritance and interactions, i.e., H_i's and H_{ij}'s are to be determined by the experts. In present example only one parameter affecting the performance of air compressor is considered. For demonstration of methodology, these are taken from the Tables 1 and 2 as.

$$H_1 = 6,\quad H_2 = 7,\quad H_3 = 5,\quad H_4 = 6,\quad h_{12} = 5,\quad h_{13} = 3,\quad h_{23} = 5,\quad h_{31} = 3,\quad h_{34} = 4,\quad h_{42} = 2,\quad h_{43} = 5$$

$$H'_1 = 3,\quad H'_2 = 7,\quad H'_3 = 5,\quad H'_4 = 6,\quad h'_{12} = 5,\quad h'_{13} = 3,\quad h'_{23} = 5,\quad h'_{31} = 3,\quad h'_{34} = 4,\quad h'_{42} = 2,\quad h'_{43} = 5$$

Substituting the values, the permanent for organization 1 (Eq. (14)) may be written as:

$$\text{Per}\ H^{*}_1 = 1260 + 810 + 240 + 0 = 2310$$

Based on Eq. (4), Eq. (14) and the value of Per H*, the identification set for power plant one may be written as:

[1/0/2/1/0][1260/0/810/240/0]

On the similar lines, the permanent for organization 2 may be written as:

$$\text{Per}\ H^{*}_2 = 630 + 540 + 80 + 0 = 1250$$

The identification set for organization 2 may be written as:

[1/0/2/1/0][630/0/540/80/0]

Whereas the identification sets help in visually analyze the existence of various groups, Eq. (5) is used to compare similarities in power plants in terms of performance parameters. Based on this criterion, the coefficient of dissimilarity between the two power plants is .459. Thus, the coefficient of similarity is .541. The comparison procedure helps organizations compare different groups in identification sets, on which they can analyze and improve the weak parameter in power plant design or analysis. Moreover, organizations can be ranked in increasing or decreasing order of value of the coefficient of similarity or dissimilarity. The increasing or decreasing order is just for ranking of power plants but managers should mainly focus on the performance parameters according to which some major decision regarding power plant performance on efficiency basis can be taken.

7. Conclusion

1. A methodology based on GTA is proposed to evaluate the role of design parameters in calculating the efficiency of CGCPP. For this purpose, CGCPP has been divided into four systems as the CGCPP is a very large system. Design parameters affecting system efficiency are identified.
2. The methodology presented in this paper builds a flexible and comprehensive model, which has the capability to consider the inheritance and interdependencies between various systems and design parameters affecting efficiency of CGCPP.
3. The methodology helps in quantifying the influence of various design parameters on the efficiency of the system/subsystems. Accordingly, weak and strong design parameters can be identified.
4. Efficiency of CGCPP is expressed in terms of an index. The index value depends on inheritance of systems which further depends upon design parameters.
5. Using this methodology, efficiency of any system can be evaluated and compared under the impact of any number of design parameters.

Please cite this article in press as: Dev N et al., GTA-based framework for evaluating the role of design parameters in cogeneration cycle power plant efficiency, Ain Shams Eng J (2012), http://dx.doi.org/10.1016/j.asej.2012.08.002

6. This methodology permits to generate alternative for CGCPP efficiency improvement.
7. This methodology can be effective tool for evaluation, comparison, ranking and selection of an optimum CGCPP system on efficiency basis.

Practical implementation of the proposed methodology in a systematic manner will help power generation industry to identify, analyze and evaluate parameters responsible for CGCPP performance on efficiency basis. Evaluation and comparison will also lead to identify critical areas that are roadblock to CGCPP efficiency. The CGCPP efficiency index will help an organization to achieve profitability through productivity.

The world is dynamic in nature and new performance parameters may be identified in future. To overcome such situations, a computer program may be developed to expedite the process as the mathematical calculations are tedious, repetitive and more time consuming if they are done manually. With the help of computer program, new performance parameters may be introduced. The impact of these new parameters on system performance may be analyzed and a new mathematical model may be developed. From the results of new model, strategy for improving the power plant performance may be modified or developed.

References

[1] Lawn J. Cogenerators see new promise, face old problems. Energy Manage 1981:43–8.
[2] Kanoglu M, Dincer I. Performance assessment of cogeneration plants. Energy Convers Manage 2009;50:76–81.
[3] Deo N. Graph theory with applications to engineering and computer science. New Delhi: Prentice Hall India; 2007.
[4] Rao RV, Gandhi OP. Failure cause analysis of machine tools using digraph and matrix methods. Int J Machine Tools Manuf 2002;42:521–8.
[5] Poullikkas A. An overview of current and future sustainable gas turbine technologies. Renew Sustain Energy Rev 2005;9:409–43.
[6] Saravanamuttoo HIH, Rogers GFC, Cohen H. Gas turbine theory. Pearson Education; 2003.
[7] Shin JY, Son YS, Kim MG, Kim KS, Jeon YJ. Performance analysis of a triple pressure HRSG. KSME Int J 2003;17(11):1746–55.
[8] Carapellucci R, Milazzo A. Repowering combined cycle power plants by a modified STIG configuration. Energy Convers Manage 2007;48:1590–600.
[9] Pasha A, Jolly S. Combined cycle heat recovery system generators optimum capabilities and selection criteria. Heat Recovery Syst CHP 1995;15(2):147–54.
[10] Faisal MN, Banwet D, Shankar R. Mapping supply chains on risk and customer sensitivity dimensions. Ind Manage Data Syst 2006;106(6):878–95.
[11] Raj T, Attri R. Quantifying barriers to implementing total quality management. Eur J Ind Eng 2010;4(3):308–35.
[12] Garg RK, Agrawal VP, Gupta VK. Selection of power plants by evaluation and comparison using graph theoretical methodology. Electr Power Energy Syst 2006;28:429–35.
[13] Grover S, Agrawal VP, Khan IA. A digraph approach to TQM evaluation of an industry. Int J Prod Res 2004;42:4031–53.
[14] Raj T, Shankar R, Suhaib M, Khan RA. A graph-theoretic approach to evaluate the intensity of barriers in the implementation of FMSs. Int J Serv Oper Manage 2010;7(1):24–52.
[15] Raj T, Shankar R, Suhaib M. GTA-based framework for evaluating the feasibility of transition to FMS. J Manuf Techn Manage 2010;21(2):160–87.
[16] Gandhi OP, Agrawal VP. FMEA – a digraph and matrix approach. Reliab Eng Syst Saf 1992;35:147–58.
[17] Gandhi OP, Agrawal VP. Failure cause analysis – a structural approach. Trans ASME, J Pressure Vessel Technol 1996;118:434–40.
[18] Schumacker RE, Lomax RG. A beginner's guide to structural equation modeling. Pittsburgh, PA: Lawrence Erlbaum Associates; 1996.
[19] Jense JB, Gutin G. Digraph theory, algorithms and organisations. London: Springer; 2000.
[20] Jurkat WB, Ryser HJ. Matrix factorization of determinants and permanents. J Algebra 1966;3:1–27.

Mr. Nikhil Dev is an assistant professor of mechanical engineering at YMCA University of Science and Technology, Faridabad, India. He obtained his M.E. degree from the Panjab University, Chandigarh in 2005. Presently he is pursuing his PhD from Delhi University, Delhi. His areas of interest include combined cycle power plants, combustion and computational techniques. To his credit, he is having more than thirteen papers published in reputed national and international journals. He is an active member of combustion institute.

Dr Samsher did B.Tech in Mechanical Engineering from HBTI Kanpur and M.Tech and Ph.D fom IIT Delhi. He Served NTPC for about 5 years, National Power Training Institute about 8 years, NIT Jalandhar for 5 months and presently working in the Department of Mechanical Engineering for about 12 years and presently occupying the post of Professor. Thus, he has total about 25 years of experience. He has published number of research papers in various journals of high repute and presented many papers in the national/ international conferences. He has been awarded "Consistently High Performance award" in the year 2000 and also honoured by presenting "Scroll of honour" on millennium teacher's day in 2000. Dr Samsher also has discharged various administrative duties in the institutions he worked. He is fellow of institution of Engineers (India).

Dr. Surendra Singh Kachhwaha completed his BE degree in Mechanical Engineering from M. B. M. Engineering College, Jodhpur in 1985. He did his M.Tech. (1988) in Heat Power from Institute of Technology, BHU Varanasi and Ph.D in Evaporative Cooling from IIT Delhi in 1996. Presently he is working as Professor and Head of Mechanical Engineering Department, School of Technology, Pundit Deendayal Petroleum University since May 2012. He is also performing his duty as Dean, Faculty of Engineering and Technology. He has a teaching experience of more than 23 years in the field of thermal engineering at undergraduate and post graduate level. He has worked 17 years at Engineering College Kota and a tenure of 6 years at Delhi College of Engineering, Delhi. Dr. Kachhwaha has contributed around 16 technical publications in reputed national and international journals and more than 40 publications in national/international conferences. His research interests include **evaporative cooling, ice slurry generation, Trigeneration, and biodiesel production techniques**. Presently he is guiding five research students pursuing PhD degree. Dr. Kachhwaha has successfully completed various Research and consultancy projects sponsored by government agencies in last one decade. He is a recipient of young scientist award (1998), SERC visiting fellowship (1999), and INSA

visiting Fellowship (2003) due to his applied research contribution. He is also a life member of various societies.

Rajesh Attri is an Assistant Professor in the Mechanical Engineering Department at YMCA University of Science & Technology, Faridabad (Haryana), India. He received his B.E. in Mechanical Engineering from MD University, Rohtak, India, in 2005 with Honours and his M.Tech in Mechanical Engineering (Manufacturing & Automation) from the YMCA Institute of Engineering, Faridabad (Haryana), India, in 2008 with honours. Presently, he is pursuing his Ph.D from YMCA University of Science & Technology, Faridabad. He has published 15 papers in referred international journals and 5 papers in national & international conferences proceedings and reviewed many papers for international journals. His area of research is Quality management, Production system life cycle and Application of MADM approaches in manufacturing environment.

Please cite this article in press as: Dev N et al., GTA-based framework for evaluating the role of design parameters in cogeneration cycle power plant efficiency, Ain Shams Eng J (2012), http://dx.doi.org/10.1016/j.asej.2012.08.002

ISSN: 2229-6646 IJSTM, Vol. 3 Issue 2, September 2012
www.ijstm.com

MULTIDIMENSIONAL ROLE OF CD34 PROTEIN IN HEMATOPOIETIC STEM CELL BIOLOGY

Vimal Kishor Singh[1,$], Kohichiro Tsuji[2,] PB Sharma[1,] Ramesh Chandra[3]

[1]Department of Biotechnology, Delhi Technological University, Shahbad Daulatpur, Bawana road, Delhi-110042, India; [$]Stem Cell Gene Therapy Research Group, Institute of Nuclear Medicine & Allied Sciences, Lucknow Road, Delhi-110054, India; [2]The University of Tokyo Hospital The Institute of Medical Science Research Hospital Department of Pediatric Hematology/Oncology; Dr. B. R. Ambedkar Center for Biomedical Research, University of Delhi Delhi-110 007, India

Correspondence:
Prof. Ramesh Chandra, Founder Director Dr. B. R. Ambedkar Center for Biomedical Research, University of Delhi Delhi -110 007, India Tel: +91-11-27666245, 27666272 Fax: +91-11-27666248, 27667730 E-mail: acbrdu@hotmail.com ; vim_kissor@yahoo.co.in

Key words:
CD34, HSCs, Homing, Adhesion, Proliferation, Differentiation

Abstract

CD34 is a highly glycosylated surface-expressed sialomucin and, because it is present on hematopoietic stem cells (HSCs), has demonstrated immense clinical utility in their enumeration in aphaeresis products, immunoaffinity purification for transplantation, and disease monitoring. The success of CD34 based reagents in identifying hematopoietic progenitors led to the assumption that CD34 is expressed on cells with regenerative potential and is sufficient for hematopoietic reconstitution in marrow-ablated recipients. Recently, researchers have identified the existence of $CD34^{-neg}$ HSCs, which have also been shown to successfully reconstitute hematopoiesis in both human and primate models. These reports stymied efforts to precisely define a critical role for CD34 in hematopoietic biology. Preliminary reports indicated its role in the early hematopoiesis, differentiation, and proliferation of HSCs. However, evidences accumulated so far suggest that CD34 is predominantly an adhesion/anti-adhesion molecule playing crucial role in HSCs trafficking. These studies are still in the early stages and a detailed analysis of the structural and functional importance of CD34 is likely to enhance our understanding of its role in hematopoiesis. This article reviews the biological significance of CD34 in hematopoiesis.

Introduction

CD34 is a surface glycoprotein expressed on a variety of cells including immature hematopoietic progenitors (**1-3**), small vessel endothelial cells (**4, 5**), embryonic fibroblast cells (**6**), adipose tissue (**7**), and mesenchymal stem cells (**8, 9**). The expression of CD34 in bone marrow (BM) comprises about 1.5-3% population that includes all hematopoiet**ic** progenitors as evident by reconstitution of hematopoiesis by $CD34^+$ progenitors in myeloablated mice, primates and human recipients (**1-3**). $CD34^+$ cells from all sources including BM, peripheral blood (PB), and umbilical cord blood (UCB) have been used in clinical transplantation regimes for the last two decades (**10-15**). Use of $CD34^+$ cells in combination with various other hematopoietic stem cell transplantation (HSCT) strategies supports rapid engraftment kinetics with fewer chances of leukemia relapse and declined hospitalization time (**16**). These tempting results encouraged a number of people to attempt the development of efficient protocols for their ex-vivo expansion (17). In spite of enormous clinical utilities of CD34 little is known about its structure and function. It is merely reported to play critical role in cellular localization, HSCs differentiation and proliferation. Though, earlier reports indicated its pro-adhesive properties but recent findings acclaimed its more predominant anti-adhesive functions **(18-24**). The highly modified extracellular domain of CD34 is likely to facilitate cell trafficking during their circulation by avoiding non-specific adhesive interactions. Beside that CD34 expression is often linked with the active –proliferating states of HSCs (**24-27**). In contrast, CD34 expression could also be reported on quiescencent hematopoietic progenitors cells (HPCs) (**28-33**). In addition there are meager evidences of its role in HSCs differentiation (**34-35**) and attempts have been in progress to establish a correlation between CD34 expression and leukemia (**36**). Recent advancements in the techniques to achieve optimal clinical transplantation led to the finding of $CD34^-$ HPCs which are demonstrated to be equally capable of sustaining hematopoietic reconstitution (**37-38**). It is interesting to notice that $CD34^-$ cells could represent a more primitive stem cell state and these may express CD34 on their surface during various states of engraftment before returning back to their original $CD34^-$ state and remain dormant throughout steady-state (**39-42**). These findings are still in their infancy and concrete biological significance of CD34 expression in HSCs biology is still awaited. We review these findings to develop a consensus concept about the biological significance of CD34 in stem cell biology.

Discovery of $CD34^+$ cells

Discovery of the cell surface antigen CD34 was a milestone and was achieved due to a monoclonal antibody (My 10) specifically recognizing a highly glycosylated cell surface protein (CD34) on the myeloid leukemia cell line KG-1a **(1-3)**. The potential use of this and other related antibodies in the identification of CD34-expressing hematopoietic progenitors (HPCs) was demonstrated when their use led to successful hematopoietic reconstitution through their infusion, first in a lethally-irradiated baboon

and then in a breast cancer patient **(9-10).** The contemporary methods used for hematopoietic recovery involved determination and subsequent infusion of Granulocyte-Macrophage colony forming units (GM-CFUs) isolated from peripheral blood in cancer patients **(43)**. This was a time consuming and expensive method but was made easy by establishment of a positive correlationship between $CD34^+$ HPCs from patients' own peripheral blood following the chemotherapeutics/growth factors (rhGM-CSF) and GM-colony forming units derived from peripheral blood. The enumeration and isolation of HPCs ensuring hematopoietic recovery became possible by comparatively faster and cost effective flowcytometric methods **(44)**. Later on, several studies were performed by various research groups at Human Leukocyte Differentiation Antigen (HLDA) workshops introduced more than twenty different antibodies for the potential use in identifying and purifying $CD34^+$ HPCs for both clinical and research purposes (Table 1) **(45-48)**. The overwhelming utility of CD34 based reagents in identifying HPCs with the potential for long-term hematopoietic reconstitution assisted many clinicians in successfully selecting HPCs for transplantation **(16)**. The enormous potential of $CD34^+$ HPCs for clinical grafting raised the possibility of likely existence of many immature "true hematopoietic stem cells" in this population. It therefore remained a primary HSC selection marker for more than two decades.

Morphological and Immunological Characteristics of $CD34^+$ cells

$CD34^+$ cells are morphologically and immunologically heterogeneous population. Its expression is more dependent upon the stage of HSCs differentiation than lineage (**49**). There are several other concomitant surface expression markers such as Thy-1, CD38, HLA-DR, CD45-RA, CD71and lineage specific markers including T-lymphoid (TdT, CD10, CD7, CD5, CD2), B-lymphoid (TdT, CD10, CD19), Myeloid (CD33, CD13) and Megakaryocytic (CD61, CD41, CD42b) (**50**). There are peculiar morphological differences (May-Grimswald-Giemsa staining assays) in $CD34^+$ cells populations. Early $CD34^+$ progenitors ($CD33^-$, $HLA\text{-}DR^-$) are all lymphocyte like cells with more homogeneity in size, lacking cytoplasmic granules with a prominent nucleoli. These cells have low protein synthesis and proliferation activity with most cells in G_0 state. Whereas, more differentiated $CD34^+$ cells shown a large nucleus, eccentrically narrow rim of deep blue cytoplasmic granules (**51-54**). Apart from these immunologic markers there are various kinds of receptors expressed on the surface of these cells which can be largely defined into two subgroups,*viz.* (i) Tyrosine kinase receptors, e.g. Stem cell factor receptor (SCF-R), CD117; Macrophage Colony stimulating factor Receptor (MCSF-R), CD115 (ii) hematopoietic growth factor receptor lacking inherent tyrosine kinase domain, e.g. Granulocyte Macrophage-colony stimulating Factor receptor, CDw116 (**50, 54**). Recently, the human homologue of murine Flk-2/Flk-3 tyrosine kinase receptor namely stem cell tyrosine kinase receptor-1 (STK-1) has also been associated with the expression of CD34 (**55-57**). The estimation of reconstitution potential of $CD34^+$ population is often determined by clonogenic assays. More primitive long term culture initiating cells, CFU-Blast, CFU-T and CFU-B are commonly associated with $CD34^+$. $CD45RA^+$, low to variable expression level of HLA-DR. Whereas, $CD34^+$, $CD38^+$, $HLA\text{-}DR^+$ population is enriched of multipotent progenitors (CFU-GM, CFU-G, CFU-M, BFU-E, CFU-E,

BFU-Meg and CFU-Meg (**50**). The clonogenic capacity of all $CD34^+$ population ranges between 10-30% while rests of them do not proliferate in *in vitro* culture assays (**58-60**)**.**

Clinical utility of $CD34^+$ cells

Enriched $CD34^+$ cell content in the graft very well correlates with the increased rate of engraftment **(16)**. Infusion of higher doses of $CD34^+$ cells results in the significant reduction of time required for engraftment **(16)**. Therefore, $CD34^+$ cell enrichment has been proven to be of great importance in both the autologous and allogenic transplantation settings. In autologous transplantation, $CD34^+$ cells ($>5x10^6$cells/kg body weight) correlates well with engraftment kinetics which is measured by evaluating the time taken by patients to develop absolute neutrophil count (ANC) or platelet recovery count (PRC) in peripheral blood. Use of maximized $CD34^+$ cells dose (from $< 2.5x10^6$cells/kg to >12.5 $x10^6$cells/kg body weight) is shown to reduce the time taken to acquire ANC ($>0.5X10^9$ cells/L) from 11 to 8 days **(61)**. Further, $CD34^+$ cells are heterogeneous population and enrichment of specific $CD34^+$ subpopulation may have beneficial effect on the engraftment kinetics which is evident for the reduction in the platelet recovery time from 19 to 11 days on incubating $< 0.5 \times 10^6$ $CD34^+/CD41^+$ cells/kg of body weight **(62)**. Inclusion of such high number of $CD34^+$ cell dose often requires large bone marrow harvesting which could be a limiting factor due to technical complications. Harvesting of mobilized $CD34^+$ HSCs from peripheral blood (autologous/allogenic donors) has been a more favorable option in clinics **(63-67)**.

However, both autologous and allogenic grafts suffer from inherent risk of malignancy relapse, graft failure and/or Graft-vs-Host Disease (GVHD). Depletion of T-cells from peripheral mobilized stem cell graft has been suggested as a possible method to reduce the risk associated with these protocols of stem cell transplantation. But this is limited by increased events of graft failure and leukemia relapse **(68)**. The more advanced method combines unmanipulated marrow graft plus highly enriched $CD34^+$ mobilized peripheral blood cells which lack most of the T-cells (<1% of the graft) providing the beneficial effects of $CD34^+$ high cell dose while reducing associated risk of Graft-vs-Host Disease **(69)**. In addition, these approaches reduce the duration of hospitalization from 28 days to 14 days due to rapid engraftment kinetics **(69)**.

In clinical setting $CD34^+$ cells have been the best predictors of the number of HPCs for collection in the blood for both good and poor mobilizers **(70-74)**. Enumeration of $CD34^+$ cells in patients blood, (8-20 cell/µl giving 2-4 $x10^4$ cells/single leukapheresis), suggests both time and frequency of leukapheresis, (to determine when to start leukapheresis and how many times it should be done), to achieve sufficient number of HPCs for successful transplantation (6-8 $x10^6$ $CD34^+$ cells/ Kg body weight). To minimize different variables among different collection centers two commercial single tests, namely Procount (Beckton-Dickinson, Mt View, CA) and Stem kit (Beckman Coulter, Fullerton, CA) have been made available presently. Recently, alternative methods for HPCs enumeration in aphaeresis products are developed which are

suppose to be comparatively inexpensive and enables lesser time to collect sufficient number of HPCs for transplantation. The Food and Drug Administration (FDA) has approved the use of a HPCs window on an automated cell counter (Sysmex, Kobe, Japan) and this may be used to predict when to start aphaeresis **(75)**. To be noticed, the HPCs detected by this counter do not correlate well with the $CD34^+$cell numbers in the blood. The pluripotent HPCs are also identified on the basis of the levels of Aldehyde dehydrogenase (ALDH). HPCs identified on the basis this enzyme include both the $CD34^+$ and $CD34^-$ cells. A commercial assay has now been developed for this intracellular enzyme (Aldecount, Stemco Biomedical, Durham, NC) (**76-77**).

The structure of CD34 molecule

The type I cell surface protein CD34 is a member of CD34 family of proteins iincluding two other molecules namely Podocalyxin and Endoglycan (**78-80**). These three molecules share overall domain-structure and sequence homology (**Fig.1**) (**81-82**). The characteristic mucin like structure of all the three proteins consists of N-terminus carbohydrate rich region and cystine rich immunoglobulin like (Ig) region which remains anchored in cell membrane through a small transmembrane and C-terminus cytoplasmic tail region (**Fig.1**) (**49, 81-83**). The most N-terminus region of CD34 is enriched of Ser/ Thr residues (~ 35% of total protein sequence) that is essential for both O-linked and N-linked glycosylations playing crucial role in both stability and functional specificity of the proteins (**4, 84-89**). The specific interactions with poorly defined counter ligands and high negative charge provided by N/ O-linked moieties and glycans play central role in determining its function as an adhesion/ anti-adhesion molecule in different sites of expression and stage of development (**4, 84-89**). These attachments are also useful in classifying three different classes of clinically relevant epitopes (Type I-III) on CD34 depending on their sensitivity to neuraminidase from *Vibrio cholerae* and O-sialoglyco-protein endopeptidase (OSGE) from *Pasteurella haemolytic*a (**84,90-94**) (See Table 1). The cytoplasmic tail region of CD34 family members share maximal sequence similarity (33-58%) and high degree of sequence conservation (**83**). There is no catalytic domain/motif evident in any of the CD34 family members but various protein phosphorylation sites exist indicating its potential signaling capabilities (18, **95-96**). The Protein Kinase C mediated phosphorylation of CD34 cytoplasmic tail (Thr 356/ Ser 362 residues) is reported to up regulate its surface expression in hematopoietic cells. The SH2/ SH3 family member adapter protein Crk-L also interacts with juxtamembrane cytoplasmic tail region of CD34 (**97-98**). The interaction of CD34 with anti-CD34 monoclonal antibodies is reported to induce phosphorylation and relocalization of various cytoskeleton proteins including membrane associated Lyn and Syk Kinases and f-actin. A conspicuous signaling pathway and there functional consequences are yet to be defined.

The functional significance of CD34

Role in early hematopoiesis

CD34 plays an important role in early hematopoiesis, as evident from studies in mice, CD34 is also expressed in hematopoietic progenitors throughout embryogenesis and at diverse sites, including yolk sac islands, the aortic-gonadal-mesonepharose (AGM) region, fetal liver, and fetal BM (**99-100**). A $CD34^+$ fraction from the murine yolk sac and embryo at days 9 to 11 is reported to generate myeloid and erythroid colony forming units, suggesting that CD34 is relevant to the early onset of embryonic hematopoiesis through late embryonic hematopoietic development and adult hematopoiesis (**101**). An important role of this sialomucin in blood vessel formation is also expected, based on its expression on endothelial cells lining yolk sac blood islands (**4, 99-100, 102-103**). In fact, the interaction of endothelial cells with HPCs is likely to occur through CD34 and to regulate the growth and differentiation of HSCs. This is strongly evident from the demonstrated 60-fold expansion of $CD34^+$ yolk sac cells when cultured with $CD34^+$ endothelial cell lines derived from the transformation of yolk sac blood islands from 10 to 11-day-old mouse embryos (**101**). Interestingly, these $CD34^+$ yolk sac cells can be differentiated into myeloid and erythroid cells by the addition of erythropoietin to the same in vivo cultures. These studies further indicate that CD34 is likely to mediate the interaction between $CD34^+$ endothelial cells lining the yolk sac blood islands and $CD34^+$ yolk sac HPCs, inducing their growth, proliferation, and presumably self-renewal.

Role in adhesion

In addition to an important role of CD34 in early hematopoiesis, a distinct function that remains to be delineated is its role as an adhesion molecule (**19-20**). The extended N-terminal region bearing extensive O-linked/N-linked carbohydrate attachments has been proposed to function as an interacting junction for various adhesion molecules, such as selectins (**78**). The sulfated glycoform of human CD34 that is exclusively expressed on high endothelial venules (HEVs) is specifically shown to bind L-selectin-IgG chimeric protein (**104**). Lyn *et al.* demonstrated enhanced specific binding of human-$CD34^+/CD2^+$ (Hu-$CD34^+/CD2^+$) murine thymocytes to the human bone marrow stroma in a transgenic mouse model (**19**), whereas when murine thymocytes were co-cultured they did not bind to the human stroma. However, an enhanced adhesion of both Hu-$CD34^+/CD2^+$ murine thymocytes and normal murine cells was shown to occur with the prior incubation of these cells with anti-CD34 monoclonal antibodies, implying a signal-dependent adhesion (**19**). The cellular aggregation observed upon incubation of both KG-1 and KG-1a cells with type I and type II anti-CD34 monoclonal antibodies, which resulted in enhanced adhesion, tended to be signal-dependent (**18**). This aggregation event was demonstrated to be mediated by energy-dependent cytoskeletal rearrangement involving β_2-integrins such as CD11a, CD18, and CD54 or ICAM-1 and LFA-1 (**18**). These reports suggest that CD34 protein induces the active binding states of surface adhesion molecules, a process that is likely mediated by some unknown signaling pathway. The abrogation of CD34-mediated cellular aggregation on the deletion of its complete

cytoplasmic tail region suggests definitive involvement of CD34 in adhesion signaling (**20**). This effect is reversed by the expression of a truncated version of the CD34 protein consisting of only 16 residues juxtaposed with the membrane in the cytoplasmic region, suggesting that the induction of intracellular cues proceeds by the molecular engagement of class I and class II epitopes with anti-CD34 monoclonal antibodies (MoAbs) that assist CD34-mediated signaling. The MoAb-induced cellular adhesion is sensitive to prior treatment of HPCs with the protein tyrosine kinase inhibitor herbamycin A, implying that downstream CD34-induced signaling is mediated by protein tyrosine kinases (**18**). Although the potential protein tyrosine kinase phosphorylation site in the cytoplasmic tail region of the wild type CD34 protein (Tyr318) remains unphosphorylated (See Supplemental Data). Other protein tyrosine kinases, such as Lyn and Syk, are activated and recruited to the plasma membrane to form a cap-like structure upon interaction with CD34-Anti CD34 MoAbs (**105**). These interactions are followed by F-actin-mediated cytoskeletal rearrangement and have been shown to recruit a yet–to-be-defined cellular protein at the site of capping (**105**). The functional consequences of these interactions are not clear, but similar capping or uropod-like structures are well known to facilitate cellular locomotion, as shown in lymphocyte homing to inflammatory sites (**106**). CD34 surface expression is significantly upregulated upon protein kinase-mediated phosphorylation of CD34 at Thr 356 and Ser 362 in the cytoplasmic region **(95, 96**). The application of protein kinase C activators, such as 12-O-tetradecanoylphorbol-13-acetate (TPA), directly induces the surface expression of CD34 molecules via some unknown mechanism. The strongest evidence indicates that CD34 signaling is indirect and involves kinases, as shown by the existence of an SH2/SH3 binding site in its cytoplasmic tail (**98,107**).

Role in HSC differentiation and proliferation

Several preliminary reports have indicated an important role for CD34 in HSC terminal differentiation. Most multipotent progenitors express high levels of CD34 protein, while the expression is reduced in unipotent progenitors and terminally matured cells. The full length CD34 protein has been shown to inhibit IL-3 and Leukemia Inhibitory Factor-6 (LIF-6)-induced differentiation of a murine myeloid leukemia cell line (MI) into macrophages (**34**). When the CD34 gene was knocked down, erythroid differentiation was significantly reduced. In contrast, the differentiation of myeloid lineages was enhanced (35). Furthermore, the retroviral-mediated overexpression of CD34 was demonstrated to negatively regulate granulocytic and megakaryocytic differentiation, along with a significant enhancement of erythrocytic differentiation (35).

Role in cellular trafficking/migration

The HPCs/HSCs trafficking is regulated by sequential interactions among a large number of molecules including selectin-counter ligands, chemokine-chemokine receptors, integrin-counter ligands and components of bone marrow microenvironment (**108**). CD34 family members might be playing important

role in HPCs/HSCs trafficking by recognition of their carbohydrate rich extracellular domain that is good receptors for selectins (**78, 104**). In fact studies in CD34 knockout mice have revealed profound migratory impairments with minor hematopoietic defects (**109**). Doyonnas et al have reported > 20% reduction in the cellular migration of $CD34^{-/-}$ fetal liver HSCs in comparison to wild type by using short term homing assays (**110**). Accordingly knock down of podocalyxin in mice ($PodX^{-/-}$) exhibited >30% declined migration of HSCs in comparison to wild type (**110**). Knock down of both the CD34 family members ($CD34^{-/-}$ and $PodX^{-/-}$) resulted in >30% reduced HSCs migration (**110**). Similarly, $CD34^{-/-}$ cells engraft with a reduced (>20% reduction) efficiency in comparison to wild type HSCs in sublethally irradiated mice recipients (**21**). However, both the wild type and $CD34^{-/--}$ were shown to engraft equally in lethally irradiated mice (**21,111**). A possible explanation may for that may be the fact that lethal dose of irradiation produces breakages in the marrow endothelium and hence increases permeability, therefore reducing the need for specific interactions among HSCs and marrow endothelium during their migration from circulation into the BM (**112**).

The effect of CD34 expression in cellular migration is also evident from studies in asthmatic mice models showing profound impairments in mast cells and eosinophill migration in parenchyma (**21**). Dew et al demonstrated delayed repopulation kinetics of $CD34^{-/-}$ cells (**21**). Similarly, defects in $CD34^{-/-}$ mast cells/eosinophils migration to lung inflammatory sites were demonstrated (**113**). These migratory impairments in $CD34^{-/-}$ mast cells/eosinophils were also reported in mice experiments exhibiting resistance to the intestinal polyopsis and cancer due to lack of mast cells/eosinophil trafficking to these sites (114).

Role in cancer biology

CD34 family members of proteins have also been evaluated for their significance in various malignancies. There are several reports on the relationship between CD34 expression and leukemia (**36**). It is exclusively expressed in acute leukemia cells while chronic matured disorders are shown $CD34^{-}$(**36**). It has been used as a characteristic marker for discrimination between immature and mature leukemic cells (**36**). At the same time, expression of CD34 has been explored for the potential prognostic implications in acute leukemia (**36**). CD34 identification is a potential marker for monitoring minimal residual disease. Despite of variables (depending on various factors e.g. methods used: flowcytometric-vs-immunohistochemistry, sample BM-vs-peripheral blood, Frozen-vs-fresh, RECs lysed whole blood-vs-mononuclear cells, de novo-vs-secondary acute myeloid leukemia (AML), cut-off values for the detection of CD34) CD34 expression has been detected repeatedly on 25-64% AML patients (**115-116**). Expression of CD34 could also be taken as a worse prognostic marker influencing clinical outcomes when associated with some genetic lesions and chromosomal aberrations (**117-119**). Unlike AML the role of CD34 expression in acute lymphoblastic leukemia (ALL) is more clearly defined. CD34 is

detectable on most (approximately 70%) of B-($CD10^+$) cells in ALL patients (**118, 120-121**). Whereas it is not detected on >50% cases of phenotypically more immature pre pre B ALL ($CD10^-$) (B-I). In T-ALL, > 40% cases are $CD34^+$ independent of T-cell maturity (**118, 120-121**). Expression of CD34 in association with other surface markers such as CD19, CD45, CD10, CD38, and TdT is reported to be used as good marker for monitoring minimal residual disease in ALL (**122-123**). Similar results are demonstrated in ALL cases where CD34 expression is detected along with CD45, CD7, TdT and/or CyCD3 (**121, 124**). Expression of CD34 and CD10 is demonstrated as specific genotype in B-ALL. Translocation t(1:19/q23:p13) characterized by E2A-PBX-1 fusion protein is demonstrated to be $CD10^+CD34^-$ (or its derivative) (**125-126**). Similarly, CD34 is expressed in childhood B-ALL which is detected by TEL-AML-1 fusion protein, a characteristic of t(12:21) (p13:q22) translocation (**124**). Another member of CD34 family podocalyxin is highly expressed in several types of malignancies e.g. breast cancer, prostate cancer, embryonic carcinoma, leukemia and pancreatic cancer (**127-132**)

Discovery of $CD34^{-neg}$ HSCs and Their Relationship to $CD34^+$ Cells

With the advent of more sophisticated HSC selection methods, such as fluorescence-activated cell sorting (FACS) based on the efflux of certain dyes such as

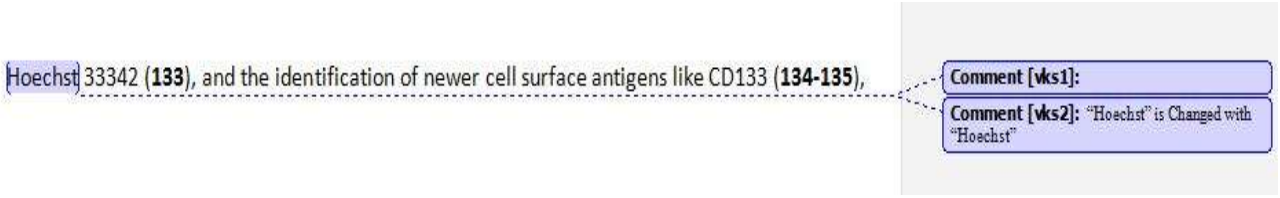

*The concept of existence of $CD34^-$ HSCs gained momentum among the research community. The strongest evidence for the regenerative potential of $CD34^-$ HSCs came from successful multilineage hematopoietic reconstitution by $CD34^-/c\ kit^+/Sca\text{-}1^+/Lin^-$ HPCs in murine models (**37**). This was followed by the demonstration of successful engraftment of $CD34^-\ CD38^-\ Lin^-$ cord blood (CB) cells in mice (**38**) and successful reconstitution by $CD34^-$ bone marrow (BM) cells in human/sheep competitive engraftment models (**39**). These findings led to the assumption that "true hematopoietic stem cells" may also be found in $CD34^-$ cell populations. More interestingly, $CD34^-$ HPCs/HSCs were found to become $CD34^+$ in ex vivo culture, and could return to the $CD34^-$ state after engraftment (while achieving a steady state) (**25**). Therefore, the expression of CD34 is believed to vary among mature, highly proliferating cells and quiescent stem cells (**40-42**). The variation in the expression of CD34 on HSCs has led to confusion among clinicians when selecting HSC*

populations for transplantation, which in turn raised the issue of its functional significance in hematopoiesis. These issues shall be discussed in detail in later sections.

Evidences from murine transplantation models

Firstly, Osawa and colleagues reported successful hematopoietic reconstitution using $CD34^-$ HSCs in lethally irradiated mice, challenging the concurrent concept of $CD34^+$ HSCs (**37**). In their studies, murine c-$Kit^+/Sca\text{-}1^+/Lin^-$ BM cells were fractionated into $CD34^+$ and $CD34^{-/low}$ populations using a novel 49E8 monoclonal antibody that was raised in rats immunized with Glutathione-S-Transferase-murine CD34 fusion protein. Greater colony-forming ability was observed in the murine $CD34^+$ ($mCD34^+$) population (approximately 20%/200 cells inoculated in IL-3-dependent colony forming unit cultures (CFU-C) and approximately 14.1%/200 cells in 12-day colony forming unit spleen (CFU-S) assays) in comparison to the $mCD34^{-/low}$ cells (~0.16, CFU-C and 1.6, CFU-S, respectively). However, studies like competitive long-term reconstitution assays (CLTR) revealed sustained long-term multilineage reconstitution by $mCD34^{-/low}$ cells in comparison to $mCD34^+$ cells, which provided an early but short-term multilineage reconstitution in lethally irradiated mice. Furthermore, the infusion of a single $CD34^{-/low}$ cell reconstituted approximately 85% of the lymphohematopoietic cells in the peripheral blood for more than 3 months in 21% of mice. To avoid the ambiguity of contamination with $CD34^+$ cells in these studies, the authors performed quantitative reverse transcription polymerase chain reaction (qRT-PCR) and established the lack of CD34 mRNA in $CD34^-/c\text{-}Kit^+/Sca\text{-}1^+/Lin^-$ cells. This was the first experimental evidence for the existence of $CD34^-$ HSCs in mice. In agreement with this finding, successful long-term reconstitution was also demonstrated in murine models through the use of Thy-1^{low} $Lin^{-neg/low}Sca\text{-}1^+$ (TLS) $CD34^{-neg}$ cells (**136**). The authors separated TLS BM cells into $CD34^+$ and $CD34^-$ subpopulations and demonstrated successful radioprotection by both cell types. Similar to the findings reported by Osawa's group, a larger number of CFU-S (93-95%), colony forming cells (CFCs), and cobblestone area forming cells (CAFCs) (one of every five $CD34^+$ TLS) were observed in the $CD34^+$ subpopulation. The distribution of these competitive long-term repopulating units (CRUs) between both subpopulations was shown to be equal by injecting a limited number of cells into lethally irradiated Ly-5 congenic mouse models. Similarly, successful hematopoietic reconstitution was again demonstrated using both $CD34^+$ Lin^- and $CD34^-$ Lin^- BM cells in syngeneic mouse models by Donelly et al (**137**). They observed a 100-fold higher repopulating activity of $CD34^+$ cells, which was assumed to be a manifestation of the different methods used for transplantation. In agreement with this direct experimental evidence, the reconstitution potential of $CD34^-$ HSCs was also confirmed by a newer method of HSC selection for transplantation. Goodell et al demonstrated a characteristic phenomenon in which HSCs efflux the DNA binding dye Hoechst 33342 in the flow cytometric determination, and termed these

cells as "side population" (**133**). This side population (later coined as *mesenchymal cells*)was demonstrated to be $CD34^-$ and had high reconstitution capabilities, as demonstrated in mouse reconstitution experiments. Altogether, these studies strengthened the belief that $CD34^-$ HSCs do exist, at least in mice.

$CD34^-$ cells in human

Following these explanatory studies, most of the existing information on human $CD34^-$ HSCs has been obtained from xenogeneic transplantation studies. Bhatia et al. *d*emonstrated the multilineage regenerative potential of human $CD34^-$ $CD38^-$ cells in NOD/SCID mice (**38**). In these studies, 13 of 16, 1 of 5, and 4 of 56 mice receiving more than 10^5 Lin^-CD34^- cells from human cord blood exhibited successful engraftment, with one SCID repopulating cell activity (SRC) out of 1.25 x 10^5 Lin^-CD34^- cord blood cells in limited serial dilution assays. Successful reconstitution by $CD34^-$ cells was demonstrated in human/sheep *in utero* engraftment models (**39**). It was reported that 4 of 9 fetuses had long-term multilineage human cell engraftment when more than 12 x 10^4 $CD34^-$ cells from human BM were transplanted. These observations were again confirmed by Verfaillie et al., who reported successful hematopoietic reconstitution in sheep fetuses by human Lin^-CD34^- cells from human BM and GM-CSF-mobilized peripheral blood (PB) (**138**). Infusion of 3.5 x 10^4 Lin^- $CD34^-$ cells from either BM or GM-CSF-mobilized PB resulted in reconstitution in 9 of 9 and 6 of 6 recipients, respectively. Thus, human $CD34^-$ HSCs from many different sources, such as bone marrow, peripheral blood, and cord blood demonstrated reconstitution potential.

Relationship between $CD34^+$ and $CD34^-$ cells

Several groups independently reported that $CD34^-$ cells first differentiate into $CD34^+$ cells and return to their $CD34^-$ state upon achieving homeostasis (**40-42**). $CD34^-$ $CD38^-$ Lin^- cells from human bone marrow and GM-CSF-mobilized peripheral blood were all observed to express CD34 when grown in a serum-free culture, and demonstrated high colony forming potential (**139-143**). Similarly, $CD34^-$ cells differentiate into $CD34^+$ cells with higher repopulating potential when grown in cytokine-supported short-term culture assays (2-4 days) (**38**). Along with their differentiation into $CD34^+$ cells exhibiting higher repopulating activity, $CD34^-$ cells rapidly proliferate and differentiate into erythrocytes, granulocytes, and megakaryocytes after 10 days of ex vivo culture (**25**). These studies indicate that $CD34^-$ cells are inferior to $CD34^+$ cells, as they show low colony forming ability. This assumption was supported by Nakamura et al, who demonstrated acquisition of both high colony forming ability and CD34 expression by human cord blood Lin^-CD34^- cells cultured for 7-days with murine bone marrow stromal cell line Hess-5 and thrombopoietin, Flt-3 ligand, SCF, G-CSF, IL-3, and IL-6 (**144**). These studies indicated a close relationship between $CD34^-$ and $CD34^+$ HSCs. As discussed by various groups, $CD34^-$ cells

seem to be more primitive, and can be activated upon stimulation with different cytokines, such as SCF, IL-6, and IL-11 (**144**). However, $CD34^+$ cells are also speculated to revert to their $CD34^-$ state under certain circumstances (**144**). This interchangeable distribution of $CD34^-$ $CD34^+$ HSCs into two pools has been termed as the "stem cell cycle" (**26-28**) (**Fig.2**). HSCs in this cycle may remain distributed in bone marrow and peripheral blood. Perhaps $CD34^-$ HSCs can be triggered to the $CD34^+$ state (active state), and can leave the bone marrow and circulate in the peripheral blood, proliferate, differentiate, and return to the bone marrow, and to their quiescent state (**26-27**). However, the mechanism by which specific factors regulate their transition from one state to another remains unclear. Primarily, cell-to-cell interactions and growth factors are major regulators of these events. One of the predominant growth factors to regulate the HSC fate is SCF, which is reported to induce CD34 expression and differentiation in *ex vivo* culture (**28**). SCF induces the expression of $p27^{kip-1}$ protein, which blocks proliferation during differentiation, whereas IL-6 promotes HSC proliferation while inhibiting the expression of $p27^{kip-1}$ in proliferating HSCs.

The expression of CD34 in HSCs is under the control of various factors, including the developmental stage and interactions with different environmental factors, such as cytokines and growth factors. The significance of its expression for only a transient period is not completely defined. The concept demonstrated by Sato et al. that expression of CD34 indicates a proliferatively active state remains ambiguous, because expression has also been demonstrated on quiescent stem cells (**29, 145**). $CD34^+$ cells lack Ki67 expression, which indicates cells in G_0 phase that cannot be readily induced to enter the cell cycle by the application of cytokines (**30-33**). This is also supported by the demonstration of an inverse relationship between CD34 expression and secondary colony forming ability (**146**). SCF, along with having an up regulating effect on CD34 expression in ex vivo cultures, also induces cyclin-dependent kinase $p27^{kip-1}$ to block cellular proliferation during differentiation (**27**). These contradictory reports raise confusion among researchers, and it is becoming more difficult to decide whether to select $CD34^+$ or $CD34^-$ cells for clinical use. In this regard, detailed knowledge of the structure and function of CD34 might be helpful in determining its exact role in different biological and clinical processes. The structure of CD34 has so far only been defined based on molecular biology and immunological analysis, and a functionally relevant critical analysis of its structure is yet to be de defined.

Current status of $CD34^+$ cells in regenerative medicine and future indications

Despite the confusion that whether CD34 is expressed or not on most immature true HSCs, it remains the major selection marker and $CD34^+$ progenitors are widely used in clinical HSCT settings. In addition, $CD34^+$ cells are demonstrated to acquire trans-differentiation markers such as endothelium markers on ex vivo culture expressing endothelial marker protein e.g.

von Williebrand factor (vWF) and DIL-acetylated LDL (1,1\'-dioctadecyl-3,3,3\',3\'-tetramethyl-indocarbocynanine perchlorate labeled acetylated Low density lipid) (**147-148)**. Initially, Asahara *et al*., reported neovascularization by injecting human peripheral blood derived $CD34^+$/ $CD34^-$ cells into a mice model of unilateral hind limb ischemia (147). The amount of human $CD34^+$ DIL acetylated LDL labeled cells were 8 times higher then $CD34^-$ cells (**147**). Similarly, acquisition of cardiogenic phenotype was demonstrated by bone marrow derived $CD34^+$ (**149-151**). Kocher et al., demonstrated marked capillary regeneration by G-CSF mobilized human peripheral blood $CD34^+$/ $CD133^+$ cells in nude rats (**152**). These findings extends the scope of $CD34^+$ cells in clinics beyond the hematopoietic system.

Beside this iconic use of $CD34^+$ HPCs/ HSCs in clinics they are vastly used in lab investigations. $CD34^+$ cells have been used for identification and cloning of human FLT-3 receptor and its ligand (**153-154**); cloning of a novel tyrosine kinase TNK-1 by using $CD34^+$ cells (155-156). Efforts have been made to delineate the molecular mechanism of hematopoiesis by studying the development of $CD34^+$ cells from human embryonic stem cells (**157**). Furthermore, $CD34^+$ $CD38^-$ Lin^- HSC enriched cells could be used as a model for microarray chip analysis to determine differentially expressed genes in HSCs (153). Together these findings indicate a much wider use of $CD34^+$ cells/ reagent in both clinics and lab investigations.

Acknow6ledgements

We are thankful to Director of the Institute of Nuclear Medicine & Allied Science (INMAS) Delhi-110054 for providing all essential support during this work. We sincerely acknowledge the Ministry of Defence (DRDO) for project support, and Dr. Vimal K. Singh particularly thanks the Council for Scientific and Industrial Research (CSIR) and the Dept. of Science and Technology (DST) for providing a fellowship and the young scientist award.

References

1. **Civin CI, LC Strauss, C Brovall, MJ Fackler, JF Schwartz and JH Shaper. (l984)**. Antigenic analysis of hematopoiesis III; A hematopoietic progenitor cell surface antigen defined by a monoclonal antibody raised against KG-1a cells. J Immunol 133:157–165.
2. **Tindle RW, RAB Nichols, L Chan, D Campara, D Calovsky and GD Birnie. (1985)**. A novel monoclonal antibody B1–3C5 recognizes myeloblasts and non-B non-Tlymphoblasts in acute leukemia and CGL blast crises andreact with immature cells in normal bone marrow. Leuk Res 9: 1–10.
3. **Katz F, RW Tindle, DR Sutherland and MD Greaves.(1985).** Identification of a membrane glycoprotein associatedwith

hemopoietic progenitor cells. LeukRes 9:191–198.

4. **Fina l, HV Molgaard, D Robertson, N Bradley, P Monaghan,D Delia, DR Sutherland, MA Baker and MF Greaves. (1990),** Expression of CD34 gene vascular endothelial cells. Blood 75:2417–2426.
5. **Beschorner WE, CL Civin, LC Strauss (1985).** Localization of hematopoietic progenitor cells in tissue with the anti-My-10 monolconal antibody. Am J Pathol 119:1-4.
6. **Brown J, MF Greaves, HV Molgaard (1991)** The gene encoding the stem cell antigen CD34 is conserved in mouse and expressed in haemopoietic progenitor cell lines, brain, and embryonic fibroblasts. Int Immunol 3:175-184.
7. **Suga H, D Matsumoto, H Eto,K Inoue, N Aoi, H Kato, J Araki, K Yoshimura (2009).** functional implications of cd34 expression in human adipose–derived stem/progenitor cells. Stem Cells and Dev 18: 1201-1210.
8. **Mosna F, L Sensebé, M Krampera (2010).** Human bone marrow and adipose tissue mesenchymal stem cells: a user's guide. Stem Cells and Dev 19 1449- 1470.
9. **Peister A, JA Mellad, BL Larson, BM Hall, LF Gibson, DJ Prockop (2004).** Adult stem cells from bone marrow (MSCs) isolated from different strains of inbred mice vary in surface epitopes, rates of proliferation, and differentiation potential. Blood 103:1662-1668.
10. **Berenson RJ, WI Bensinger, RS Hill, RG Andrews, J Garcia-Lopez, DF Kalamasz, BJ Still, B Spitzer, CD Buckner and ID Bernstein (1991).** Engraftment after infusion of CD34+ marrow cells in patients with breast cancer or neuroblastoma. Blood 77: 1717- 1722.
11. **Berenson RJ, RG Andrews, WI Bensinger. D Kalamasz, G Knitter (1988).** Antigen $CD34^+$ marrow cells can engraft lethally irradiated babbon. J Clin Invest 81: 951-955.
12. **Hogan CJ, EJ Shpall, O McNulty, I McNiece I, JE Dick, LD Shultz, G Keller (1997).** Engraftment and development of human CD34(+)-enriched cells from umbilical cord blood in NOD/LtSz-scid/scid mice. Blood 90:85-96.
13. **Lister J, JF Gryn, KL McQueen, DT Harris, JM Rossetti, RK Shadduck (2007).** Multiple unit HLA-unmatched sex-mismatched umbilical cord blood transplantation for advanced hematological malignancy. Stem Cells Dev. 16:177-186.
14. **Chan SL, M Choi, S Wnendt,M Kraus, E Teng, HF Leong, S Merchav (2007).** Enhanced in vivo homing of uncultured and selectively amplified cord blood CD34+ cells by cotransplantation with cord blood-derived unrestricted somatic stem cells. Stem Cells 25:529-536.
15. **Wu JY, C Liao, ZP Xu, JS Chen, SL Gu, YN Huang, Y Li, XW Tang, X Yang, PH Tang, KS Tsang (2000).** Banking and transplantation of

umbilical cord blood in Guangzhou, China. Cytotherapy. 8:488-497.

16. **Burt RK. (1999)**. Clinical utility of maximizing the CD34cell counts in stem cell grafts. Stem Cells 17:373–378.
17. **Piacibello W, F Sanavio, A Severino, L Garetto, A Danè, L Gammaitoni, M Aglietta (1998). E**x vivo expansion of cord blood progenitors. Vox Sang 74 Suppl 2:457-
18. **Majidic O, I Ohannes Stock and E Winfried. (1994).** Signaling and induction of enhenced cytoadhesiveness via thehematopoietic progenitor cell surface molecule CD34. Blood 83:1226–1234.
19. **Lyn H, M Gillian, G Karin, F Grosveld, M Greaves and T Enver. (1995).** The stem cell antigen CD34 functions as a regulator of hematopoietic cell adhesion. Proc Natl Acad Sci USA 92:12240–12244.
20. **Hu MC-T and SL Chien. (1998).** The cytoplasmic domain is essential for cytoadhesion signaling but not sufficient forproliferation signaling. Blood 91:1152–1162.
21. **Drew E, JS Merzaban, W Seo, HJ Ziltener, KM McNagny (2005).** CD34 and CD43 inhibit mast cell adhesion and are required for optimal mast cell reconstitution. Immunity 22 43-47.
22. **Furness SG, K McNagny (2006).** Beyond the mere markers: Functions for CD34 family of sialomucins in hematopoiesis. Immunol Res 34: 13-32
23. **McNagny K, JS Nielsen (2008).** Novel Functions of CD34 family. J Cell Sci 121: 3683-3692.
24. **McNagny K, JS Nielsen (2009).** CD34 is a Key Regulator of Hematopoietic Stem Cell Trafficking to Bone Marrow and Mast Cell Progenitor Trafficking in the Periphery. Microcirculation 16, 487-496.
25. **Fujisaki T,MG Berger, S Rose-John, CL Eaves (1999).** Rapid differentiation of a rare subset of adult human $Lin^-CD34^-CD38^-$ cells stimulated by multiple growth factors in vitro. Blood 94:1926-1932.
26. **Huss R (2000).** Perspectives on the morphology and biology of CD34 negative stem cells. J Hematother Stem Cell Res 9: 783-793.
27. **Huss R (1998).** $CD34^-$ stem cells as the earliest precursors of hematopoietic progeny. Exp Hematol 26: 1022-1023.
28. **Bonnet D (2001).** Normal and leukemic CD34 negative human hematopoietic stem cells. Rev Clin Exp Hematol 5: 42-61.
29. **Hao QL, FT Thiemann, D Petersen, EM Smogorzewska, GM Crooks (1996).** Extended long-term culture reveals a highly quiescent and primitive human hematopoietic progenitor population. Blood 88:3306-3313.
30. **Gothol A, R Pyatt, J McMahel**, S **Rice, and EF Srour (1997).** Functional hetrogeneity of human $CD34^+$ cells isolated in

subcompartments of the G0/G1 phase of cell cycle. Blood 90: 4384-4393.

31. **Landberg G, G Roos (1993).** Proliferating cell nuclear antigen expression in human hematopoietc stem cells during growth stimulation and differentiation. Cell Prolif 26:427-437.
32. **Jordan CT, G Yamasaki, D Minamolo (1990).** High resolution cell cycle analysis of defined phenotypic subset within primitive human hematopoietic stem cells population. Exp Hematol 24:1347-1355.
33. **Dao MA, N Taylor, JA Nolta (1998).** Reduction in the level of the cyclin-dependent kinase inhibitor p27 (Kip-1) coupled with transforming growth factor beta neutralization induces cell cycle entry and increases retroviral transduction of primitive human hematopoietic stem cells. Proc Natl Acad Sci USA 95:13006-13011.
34. **Fackler MJ, DS Krause. OM Smith, CL Civin, and WS May (1995).** Full-length but not truncated CD34 inhibits hematopoietic cell differentiation of MI cells. Blood 8S: 3040-3047.
35. **Salati S, Z Roberta, E Bianchi, A Testa, F Mavilio, R Manfredini, S Ferrari (2008)**. Role of CD34 antigen in myeloid differentiation of human hematopoietic progenitor cells. Stem Cells 26: 950-959.
36. **Basso G, F lanza, A Orphan, B Moretti, G Castoldi (2001).** Clinical and biological significance of CD34 expression in acute leukemia. J Biol Regul Homeost Agents15: 68-78.
37. **Osawa M, K Hanada, H Hamada, H Nakayuchi (1996).** Long-term lymphohematopoietic reconstitution by a single CD34-low/negative hematopoietic stem cell. Science 273: 242-245.
38. **Bhatia M, D Bonnet, B Murdoch, OI Gan, J Dick (1998).** A newly discovered class of human hematopoietic cells with SCID-repopulating activity. Nature Med 4: 1038-1045.
39. **Zanjani ED, G Almeida-Porada, AG Livingston, H Zeng, M Ogawa (2003).** Reversible expression of CD34 by adult human bone marrow long-term engrafting cells in vivo. Exp Hematol 31: 406-412.
40. **Sato T, JH Laver, M Ogawa (1999).** Reversible expression of CD34 by murine hematopoietic stem cells. Blood 94:2548-2554.
41. **Tajima F, T Sato, JH Laver and M Ogawa (2006).** CD34 expression by murine hematopoietic stem cells mobilized by granulocyte colony-stimulating factor. Blood 696:1989–1993.
42. **Matsuoka S, Y Ebihara, M Xu, T Ishii**, D **Sugiyama**, H **Yoshino**,T **Ueda**, A **Manabe**, R **Tanaka**,Y **Ikeda**, T **Nakahata**, **and K Tsuji (2001) .** CD34 expression on long-term repopulating hematopoietic stem cells changes during developmental stages. Blood 97: 419–425.
43. **Gianni AM, M Bregni, AC Stern, S Sienaa, C Tarellab, A Pilerib and G**

Bonadonnaa (1989). Granulocyte-macrophage colony-stimulating factor to harvest circulating haemopoietic stem cells for autotransplantation. Lancet 334: 580-585.

44. **Siena S, M Bregni, B Brando, N Belli, F Ravagnani, L Gandola, AC Stern, PM Lansdorp, G Bonadonna and AM Gianni (1991). F**low cytometry for clinical estimation of circulating hematopoietic progenitors for autologous transplantation in cancer patients. Blood 77: 400-409.
45. **Civin CI. (1989).** Report on the CD34 cluster workshop. In : Leukocyte Typing IV.T Trischman, MJ Fackler, T Trischmann, MJ Fackler, I Bernstein, J Brunning, L Campos, M Greaves, M Kamoun M, Katz D, Lansdorp P, Look A,Seed B, Sutherland D, Tindle R, Uchanska-Ziegler B, Knapp W, Dorken B, Gilk W, Rieber E,Stein H, Schmidt R, von den Borne A, eds, Oxford University, Oxford, UK,pp 818-825.
46. **Greaves MF. (**1995**)** MC7. CD34 workshop panel report. In: Leukocyte Typing V: White Cell Differentiation Antigens, **Titley I, Colman SM Greaves M, Titley I, Colman S, Buhring H-J, Campos L,Castoldi G, Garrdo F, Gaudnack G, Girard J-P, Ingles-Esteve J, Invemizzi R, Knapp W, Lansdorp P, Lanza F, Merle-Beral H, ParraviciniC, Razak K, Ruiz-Cabello F, Springer T, van der Schoot C,Sutherland D: M10** CD34 cluster workshop section, in Schlossman S, Boumsell L, Gilks W, Harlan J, Kishimoto T, Morimoto C, Ritz J, Shaw S, Silverstein R, Springer T, Tedder T, Todd R, eds, Oxford University Press, New York, pp 840-846.
47. **Nishio H. (**1997**)** White cell differentiation antigens. **In:** Leucocyte typing VI. Proceedings of the 6th International Workshop and Conference, **Tada J, Hashiyama M, Hirn J, Ingles-Esteve J, Suda T.**. In: Kishimoto T, Kikutani H,von dem Borne AEG, Goyert SM, Mason DY, Miyasaka M,eds, Garland Publishing Inc, Kobe, Japan. pp. 974-984, and pp. 1134.
48. **Lanza F, S Moretti, S Papa, F Malavasi, GL Castoldi (1994).** Report on the fifth International Workshop on human leukocyte differentiation antigens, Boston, November 3-7, 1993. Haematologica 79: 374-386.
49. **Andrews RG, JW Singer, ID Bernstein (1986).** Monoclonal antibody 12-8 recognizes a 115-kd molecule present on both unipotent and multipotent hematopoietic colony-forming cells and their precursors. Blood 67: 842-845.
50. **Civin CI, SD Gore (1993).** Antigenic analysis of hematopoiesis: a review. J Hematother 2:137-144.
51. **Lansdorp PM, HJ Sutherland, CJ Eaves (1990).** Selective expression of CD45 isoforms on functional subpopulations of CD34+ hematopoietic cells from human bone marrow. J Exp Med 172:363-366.
52. **Baum CM, IL Weissman, AS Tsukamoto, AM Buckle (**1992**).**

Isolation of a candidate human hematopoietic stem-cell population. Proc Natl Acad Sci USA89:2804-2808.

53. **Huang S, LWMM Terstappen (**1994**).** Lymphoid and myeloid differentiation of single human CD34+, HLA-DR–, CD38– hematopoietic stem cells. Blood 83:1515-1526.
54. **Gunji Y, M Nakamura, H Osawa, K Nagayoshi, H Nakauchi, Y Miura, M Yanagisawa and T Suda** (**1993).** Human primitive hematopoietic progenitor cells are more enriched in KITlow cells than in KIT high cells. Blood 82:3283-3289.
55. **Rosnet O, S Marchetto, O de Lapeyriere, D Birnbaum (**1991**).** Murine Flt3, a gene encoding a novel tyrosine kinase receptor of the PDGFR/CSF1R family. Oncogene6:1641-1650.
56. **Matthews W, CT Jordan, GW Wiegand, D Pardoll, IR Lemischka (**1991**).** A receptor tyrosine kinase specific to hematopoietic stem and progenitor cell-enriched populations. Cell 65: 1143- 1152.
57. **Small D, M Levenstein, E Kim, C Carow, S Samin, P Rockwell, L Wirre, C Burrow, MZ Ratajczakii, AM Gewirtzii, and Cl Civin (**1994**).** STK-1, the human homologue of Flk-2/Flt-3, is selectively expressed in CD34+ human bone marrow cells and is involved in the proliferation of early progenitor/stem cells. Proc Natl Acad Sci USA 91: 459- 463.
58. **Lyman SD, L James, L Johnson, K Brasel, P de Vries, SS Escobar, H Downey, RR Splett, MP Beckmann, HJ McKenna (1994).** Cloning of the human homologue of the murine flt3 ligand: a growth factor for early hematopoietic progenitor cells. Blood 83:2795-1801.
59. **Kmiecik TE, JE Keller, E Rosen, GF van de Woude (**1992**).** Hepatocyte growth factor is a synergistic factor for the growth of hematopoietic progenitor cells. Blood 80:2454-2457.
60. **Metcalf D (**1993**).** Hematopoietic regulators: redundancy or subtlety? Blood 82:3515-3523.
61. **Weaver CH, B Hazelton, R Birch, P Palmer, C Allen, L Schwartzberg and W West (**1995**).** An analysis of engraftment kinetics as a function of the CD34 content of peripheral blood progenitor cell collections in 692 patients after the administration of myeloablative chemotherapy. Blood 86: 3961-3969.
62. **Dercksen MW, S Rodenhuis, MK Dirkson, WP Schaasberg, JW Baars, E van der Wall, JC Slaper-Cortenbach, HM Pinedo, AE Von dem Borne and CE van der Schoot (**1995**).** Subsets of CD34+ cells and rapid hematopoietic recovery after peripheral blood stem cell transplantation. J Clin Oncol 13: 1922-1932.
63. **Aversa F, A Tabilio, A Velardi, I Cunningham, A Terenzi, F Falzetti, L Ruggeri, G Barbabietola, C**

Aristei, P Latini, Y Reisner, MF Martelli (1998**).** Treatment of high-riskleukemia with T-cell-depleted stem cells from related donors with one fully mismatched HLA haplotype. N Engl J Med 339: 1186-1193.

64. **Körbling M, N Mirza, P Thall, H Engel, K Vanbesien, S Giralt, B Andersson, HD Kleine, D Seong, AB Deisseroth, M Andreeff, R Champlin (**1997**).** 100 HLA-identical allogeneic blood stem cell transplantations: the M.D. Anderson Cancer Center experience. Bone Marrow Transplant 19: S72a.
65. **Schmitz N, P Dreger, M Suttorp, EB Rohwedder, T Haferlach, H Loffler, A Hunter, NH Russell (1995).** Primary transplantation of allogeneic peripheral blood progenitor cells mobilized by filgrastim (granulocyte colony-stimulating factor). Blood 85:1666-1672.
66. **Körbling M, D Przepiorka, YO Huh, H Engel, K van Besien, S Giralt, B Andersson, HD Kleine, D Seong and AB Deisseroth (1995).** Allogeneic blood stem cell transplantation for refractory leukemia and lymphoma: potential advantage of blood over marrow allografts. Blood 85: 1659-1665.
67. **Bensinger WI, CH Weaver, FR Appelbaum**, **S Rowley, T Demirer, J Sanders, R Storb, CD Buckner (1995).** Transplantation of allogeneic peripheral blood stem cells mobilized by recombinant human granulocyte colony-stimulating factor. Blood 85: 1655-1658.
68. **Mavroudis DA, EJ Read, J Molldrem, A Raptis, M Plante, CS Carter, S Phang, CE Dunbar, AJ Barrett (1998).** T cell-depleted granulocyte colony-stimulating factor (G-CSF) modified allogeneic bone marrow transplantation for hematological malignancy improves graft CD34+ cell content but is associated with delayed pancytopenia. Bone Marrow Transplant; 21: 431-440.
69. **Burt RK, TM Kuzel, M Fishman, M Brush, M Villa, C Welles, S Rosen, AE Traynor(1999).** Stem cell component therapy: supplementation of unmanipulated marrow with CD34 enriched peripheral blood stem cells. Bone Marrow Transplant 23: 381-386.
70. **Schots R, I Van Riet, S Damianos, J Flament, P Lacor, Y Staelens, L Steenssens, B Van Camp, M De Waele (1996).** The absolute number of circulating CD34+ cells predicts the number of hematopoietic stem cells that can be predicted by apheresis. Bone Marrow Transplant17: 509-515.
71. **Schwella N, J Beyer, I Schwaner, HG Heuft, O Rick, D Huhn, S Serke and W Siegert (1996).** Impact of preleukapheresis cell counts on collection results and correlation of progenitor cell dose with engraftment after high-dose chemotherapy in patients with germ-cell cancer. J Clin Oncol 14: 1114-1121.
72. **Mohle R, S Murea, M Pforsich, B Witt, R Haas (1996).** Estimation of the progenitor cell yield in a leukapheresis product by previous

measurement of CD34+ cells in the peripheral blood. Vox Sang 71: 90-96.

73. **Ford C, K Chan, WF Reilly, FB Petersen (2003).** An evaluation of predictive factors for CD34+ cell harvest yields from patients mobilized with chemotherapy and growth factors. Transfusion 43: 622-625.
74. **Moncada V, C Bolan, Y Yau, YY Yau, SF Leitman (2003).** Analysis of PBPC yields during large volume leukapheresis of subjects with a poor mobilization response to filgrastim. Transfusion 43: 495-501.
75. **Yu J, W Leisenring, W Fritschle, S Heimfeld, H Shulman, WI Bensinger, LA Holmberg and SD Rowley (2000).** Enumeration of HPC in mobilized peripheral blood with the Sysmex SE-9500 predicts final $CD34^+$ cell yield in the apheresis collection. Bone Marrow Transplant 25: 1157-1164.
76. **Storms R, A Trujillo, JB Springer, L Shah, OM Colvin, SM Ludeman, and C Smith (**1999**).** Isolation of primitive human hematopoietic progenitors on the basis of aldehyde dehydrogenase activity. Proc Natl Acad Sci USA 96: 9118-9123.
77. **Balber A, C Gentry, C Pritchard, C Baucom, E Deibert, C Smith (**2003**).** ABC-mediated efflux of ALDH reaction product: implications for enumeration and isolation of blood progenitor cells. Biol Blood Marrow Transplant 9: 231a.
78. **Lasky LA.** Sialomucin ligands for selectins: A new family of cell adhesion molecules. Princess Takamatsu Symp 1994; 24:81 –90.
79. **Kerjaschki D, DJ Sharkey, MG Farquhar (**1984**).** Identification and characterization of podocalyxin. The major sialoprotein of the renal glomerular epithelial cell. J Cell Biol; 98 1591–1596.
80. **Carey DJ (**1997**).** Syndecans: multifunctional cell-surface co-receptors. Biochem J 327: 1-16.
81. **Kershaw DB, SG Beck, BL Wharram, JE Wiggins, M Goyal, PE Thomas, RC Wiggins (**1997**).** Molecular cloning and characterization of human podocalyxin-like protein. orthologous relationship to rabbit pclp1 and rat podocalyxin. J Biol Chem 272: 15708-15714.
82. **Simmons DL, AB Satterthwaite, DG Tenen, B Seed (**1992**).** Molecular cloning of a cDNA encoding CD34, a sialomucin of human hematopoietic stem cells. J. Immunol 148: 267-271.
83. **Sassetti C, K Tangemann, MS Singer, DB Kershaw and SD Rosen (**1998**).** Identification of podocalyxin-like protein as a high endothelial venule ligand for L-selectin: Parallels to CD34. J Exp Med 187: 1965-1975.
84. Sutherland DR, SM Watt, G K Dowden K Karhi, MA Baker, MF Greaves and JE Smart. (1988). Structural and partial amino acid sequence analysis of the human hematopoietic progenitor cell antigen CD34. Leukemia 2:793–803
85. Pallant A, A Eskonzi and M Matter. (1989). Characterization of cDNA

encoding human leukosialin and localizationof the leukosialin gene to chromosome 16. Proc Natl Acad Sci USA 86:1328–1332.

86. Kitten N, AN Barcley, AC Willis and AF Willioms. (1987). The sequence of rat leukosialin (W3/13 antigen) reveals amolecule with O-linked glycosylation of one third of its extracellular amino acids. EMBO J 6:4029–4034.
87. Greaves MF, J Brown, HV Molgaard, NK Spurr, D Delia and DR Sutherland. (1992). Molecular features of CD34: a hematopoietic progenitor associated molecule. Leukemia 6:31–36.
88. Sutherland DR and A Keating. (1992). The CD34 antigen; structure, biology and potential clinical applications. Hematother 1:115–129.
89. Shimzu Y and S Shaw. (1993). Mucins in the mainstream. Nature 366:630–631.
90. **Watt SM, K Karhi, K Gatter, AJ Furley, FE Katz, LE Healy, LJ Altass, NJ Bradley, DR Sutherland, R Levinsky, M Greaves (**1987**).** Distribution and epitope analysis of the cell membrane glycoprotein (HPCA-1) associated with human haemopoietic progenitor cells. Leukemia 1: 417-426.
91. **Otulakowski GL, PE Shewen, AE Udoh, A Mellors,., and BN Wilki (1983),** Proteolysis of sialoglycoprotein by *Pasteurella haemolytica* cytotoxic culture supernatant. Infect Immun 42: 64-70.
92. **Prater C, J Plotkin, D Jayd (**1991**).** The properdin-like type I repeats of thrombospondin contain a self-attachment site. J Cell Biol 112:1031 –1040.
93. **Rich KA, FW George, J Law (**1993**).** Cell adhesive motif in region II of malarial circumsporozoite protein. Science 240:1574 –1577.
94. **Liesi P, A Narvanen, J Soos (**1989**).** Identification of neurite growth promoting domain of laminin using synthetic peptides. FEBS Lett 244: 141 –148.
95. **Cooper JA, FS Esch, SS Taylor, T Hunter (**1984 **).** Phosphorylation sites in enolase and lactate dehydrogenase utilized by tyrosine kinase in vivo and in vitro. J Biol Chem 259: 7835–7841.
96. **Fackler MJ, CL Civin, WS May (**1992**).** Up-regulation of surface CD34 is associated with protein kinase C mediated hyper-phosphorylation of CD34. J Biol Chem 267:17540–17546.
97. **Arai A, Y Nosaka, H6Kohsaka**, **N Miyasaka**, **and O Miura (**1999**).** Crk-L activates integrin mediated hematopoietic cell adhesion through the guanine nucleotide exchange factor C3G. Blood 93:3713 –3722.
98. **Gangenahalli GU, VK Singh, YK Verma, P Gupta, RK Sharma, R Chandra, S Gulati, and PM Luthra (**2005**).** Three-dimensional structure prediction of the interaction of CD34 with the SH3 domain of Crk-L. Stem Cells Dev 14:470–477.
99. **Young PE, S Baumhueter, LA Lasky (**1995**).** The sialomucin CD34

is expressed on hematopoietic cells and blood vessels during murine development. Blood 85: 96-105.

100. **Lin G, E Finger, JC Gutierrez-Ramos (**1995**).** Expression of CD34 in endothelial cells, hematopoietic progenitors and nervous cells in fetal and adult mouse tissues. Eur J Immunol 25:1508-1516.

101. **Fennie C, J Cheng, D Dowbenko, P Young, LA Lasky (**1995**).** $CD34^+$ endothelial cell lines derived from murine yolk sac induce the proliferation and differentiation of yolk sac CD34' hematopoietic progenitors. Blood 86: 4454-4467.

102. **Baumhueter S, C Kyle, N Dybdal, LA Lasky (**1994**).** Global vascular expression of murine CD34, a sialomucin-like ligand for L-selectin. Blood 84:2554- 2565.

103. **Kalaria RN, SN Kroon (**1992**).** Expression of leukocyte antigen CD34 by brain capillaries in Alzheimer's disease and neurologically normal subjects. Acta Neuropathol 84: 606-612.

104. **Baumhueter S, MS Singer, W Henzel S, Hemmerich, M Renz, SD Rosen**, **LA Lasky (**1993**).** Binding of L-selectin to the vascular sialomucin CD34. Science 262:436 – 438.

105. **Tada J, M Omine, T Suda, N Yamaguchi (**1999**).** A common signaling pathway via Syk and Lyn Tyrosine kinase generated from capping of the sialomuin CD34 and CD43 in immature hematopoietic cells. Blood 93:3723 – 3735.

106. **Heath JP, BF Holifield (**1991**).** Cell locomotion: new research rests old ideas on membrane and cytoskeletal flow. Cell Motil Cytoskel 18: 245 –257.

107. **Felschow DM, ML McVeigh, GT Hoehn, CI Civin and MJ Facklert (**2001**).** The adapter protein Crk-L associates with CD34. Blood 97: 3768–3775.

108. **Magnon C, and PS Frenette (2008)**, Hematopoietic stem cell trafficking. StemBook, ed. The Stem Cell Research Community, StemBook, doi/10.3824/stembook.1.8.1, http://www.stembook.org..

109. **Cheng J, S Baumhueter, G Cacalano, K Carver-Moore, H Thibodeaux, R Thomas, HE Broxmeyer, S Cooper, N Hague, M Moore, LA Lasky (**1996**).** Hematopoietic defects in mice lacking the sialomucin CD34. Blood 87 479-490.

110. **Doyonnas R, JS Nielsen, S Chelliah, E Drew, T Hara, A Miyajima, and KM McNagny (**2005**).** Podocalyxin is a CD34-related marker of murine hematopoietic stem cells and embryonic erythroid cells. Blood105: 4170-4178.

111. **Nielsen JS, ML Graves, S Chelliah, AW Vogl, CD Roskelley, KM McNagny (**2007**).** The CD34-related molecule podocalyxin is a potent inducer of microvillus formation. PLoS ONE **2**, e237.

112. **Mazo IB, EJ Quackenbush, JB Lowe, UH von Andrian (**2002**).**

Total body irradiation causes profound changes in endothelial traffic molecules for hematopoietic progenitor cell recruitment to bone marrow. Blood 99: 4182-4191.

113. **Blanchet MR, S Maltby, DJ Haddon, H Merkens, L Zbytnuik and KM McNagny (**2007**).** CD34 facilitates the development of allergic asthma. Blood; 110: 2005-2012.

114. **Gounaris E, SE Erdman, C Restaino, MF Gurish , DS Friend , F Gounari , DM Lee, G Zhang, JN Glickman, K Shin, VP Rao, T Poutahidis, R Weissleder, KM McNagny, and K Khazaie (**2007**).** Mast cells are an essential hematopoietic component for polyp development. Proc. Natl. Acad. Sci. USA 104: 19977-19982.

115. **Smith FO, B Lampkin, C Versteeg, DA Flowers, PA Dinndorf, JD Buckley, WG Woods, GD Hammond and ID Bernstein (**1992**).** Expression of lymphoid-associated cell surface antigens by childhood acute myeloid leukemia cells lacks prognostic significance. Blood 79: 2415-2422.

116. **Ciolli S, F Leoni, R Caporale, A Pascarella, F Salti, P Rossi-Ferrini (**1993**).** CD34+ expression fails to predict the outcome in adult acute myeloid leukemia. Haematologica 78: 151-155.

117. **Porwit-MacDonald A, G Janossy, K Ivory, D Swirsky, R Peters, K Wheatley, K Walker, A Turker, AH Goldstone, and A Burnettet (**1996**).** Leukemia associated changes identified by quantitative flow cytometry. CD34 overexpression in acute myelogeneous leukemia with M2 with t(8; 21) translocation. Blood 87: 1152-1159.

118. **Jennings D, K Foon (**1997**).** Recent advances in flow cytometry: Application to the diagnosis of hematologic malignancies. Blood 90: 2863-2892.

119. Legrand O, J Perrot, M Baudard, A Cordier, R Lautier, G Simonin, R Zittoun, N Casadevall, and J Marie (2000**).** The immunophenotype of 177 adults with acute myeloid leukemia: proposal of a prognostic score. Blood 96: 870-877.

120. **Terstappen L, M Safford, S Konemann (**1991**).** Flow cytometric characterization of acute myeloid leukemia. Part II. Phenotypic heterogeneity at diagnosis. Leukemia9:757-767.

121. **Pui C, ML Hancock, DR Head, GK Rivera, AT Look, JT Sandlund, and FG Behm (**1993**).** Clinical significance of CD34 expression in childhood acute lymphoblastic leukemia. Blood; 82: 889-894.

122. **Ciudad J, JF San Miguel, MC Lopez-Berges, MA García Marcos, M González, L Vázquez, MC del Cañizo, A López, JJ Van Dongen, A Orfao (**1999**).** Detection of abnormalities in B-cell differentiation pattern is a tool useful to predict relapse in precursor-BALL. Br J Haematol 104: 695-705.

123. **Campana D, E Coustan Smith (**1999**).** Detection of minimal residual disease in acute leukemia by flow cytometry. Cytometry; 38: 139-152.

124. **Porwit-MacDonald A, E Bjorklund, P Lucio, EG van Lochem, J Mazur, A Parreira, MW van den Beemd, ER van Wering, E Baars, G Gaipa, A Biondi, J Ciudad, JJ van Dongen, JF San Miguel, A Orfao (**2000**).** BIOMED – 1 concerted action report: Flow cytometric characterization of CD7+ cell subset in normal bone marrow as a basis for the diagnosis and follow-up of T cell acute lymphoblastic leukemia (T-ALL). Leukemia 14: 816-825.

125. **Pui CH, SC Raimondi, ML Hancock, GK Rivera, RC Ribeiro, HH Mahmoud, JT Sandlund, WM Crist and FG Behm (**1994**) .** Immunologic, cytogenetic and clinical characterization of childhood acute lymphoblastic leukemia with the t(1; 19) (q23; p13) or its derivative. J Clin Oncol 12: 2601-2606.

126. **Borowitz MJ, SP Hunger, AJ Carroll, JJ Shuster, DJ Pullen, CP Steuber and ML Cleary (**1993**) .** Predictability of the t(1; 19) (q23; p13) from surface antigen phenotype: Implications for screening cases of childhood acute lymphoblastic leukemia for molecular analysis: a Pediatric Group study. Blood 82: 1086-1091.

127. **Casey G, PJ Neville, X Liu, SJ Plummer, MS Cicek, LM Krumroy, AP Curran, MR McGreevy, WJ Catalona, EA Klein, JS Witte (**2006**).** Podocalyxin variants and risk of prostate cancer and tumor aggressiveness. Hum. Mol. Genet.; 15:735-741.

128. **Heukamp LC, HP Fischer, P Schirmacher, X Chen, K Breuhahn, C Nicolay, R Buttner and I Gutgemann (**2006**).** Podocalyxin-like protein 1 expression in primary hepatic tumours and tumour-like lesions. Histopathology 49: 242-247.

129. **Kelley TW, D Huntsman, KM McNagny , CD Roskelley and ED His (**2005**).** Podocalyxin: a marker of blasts in acute leukemia. Am J Clin Pathol 124: 134-142.

130. **Ney JT, H Zhou, B Sipos, R Buttner, X Chen, G Kloppel and I Gutgemann (**2007**).** Podocalyxin-like protein 1 expression is useful to differentiate pancreatic ductal adenocarcinomas from adenocarcinomas of the biliary and gastrointestinal tracts. Hum Pathol 38: 359-364.

131. **Schopperle WM, DB Kershaw and WC DeWolf (**2003**).** Human embryonal carcinoma tumor antigen, Gp200/GCTM-2, is podocalyxin. Biochem Biophys Res Commun 300: 285-290.

132. **Somasiri A, JS Nielsen, N Makretsov, ML McCoy, L Prentice, CB Gilks, SK Chia, KA Gelmon, DB Kershaw, DG Huntsman, KM McNagny, and CD Roskelley (**2004**).** Overexpression of the anti-adhesin podocalyxin is an independent

predictor of breast cancer progression. Cancer Res 64: 5068-5073.

133. Goodell MA, K Brose, G Paradis, AS Conner, RC Mulligan (1996**).** Isolation and functional properties of murine hematopoietic stem cells that are replicating in vivo. J Exp Med 183: 1797–1806.

134. **Yin AH, S Miraglia, ED Zanjani, G Almeida-Porada, M Ogawa, AG Leary, J Olweus, J Kearney, DW Buck (**1997**).** AC133, a novel marker for human hematopoietic stem and progenitor cells. Blood **90**:5002-5012.

135. **Miraglia S, W Godfrey, AH Yin, G Almeida-Porada, M Ogawa, AG Leary, J Olweus, J Kearney, DW Buck (**1997**).** A novel five-transmembrane hematopoietic stem cell antigen: isolation, characterization, and molecular cloning. Blood **90**: 5013-5021.

136. **Morel F, A Galy, B Chen, and SJ Szilvassy (**1998**).** Equal distribution of competitive long-term repopulating stem cells in the CD341 and CD342 fractions of Thy-1low Lin2/low Sca-11 bone marrow cells. Exp Hematol 26: 440-448.

137. **Donnelly DS, D Zelterman, S Sharkis, DS** Krause (1999)**.** Functional activity of murine $CD34^+$ and $CD34^-$ hematopoietic stem cell populations. Exp Hematol 27: 788–796.

138. **Verfaillie CM, Almeida-Porada, S Wissink, ED Zanjani (**2000**).** Kinetics of engraftment of $CD34^-$ and $CD34^+$ cells from umbilical cord blood differs from $CD34^-$ and $CD34^+$ cells from bone marrow. Exp Hematol 28:1071-1079.

139. **Sutherland HJ, CJ Eaves, AC Eaves, W Dragowska, and PM Lansdorp (**1989**).** Characterization and partial purification of human marrow cells capable of initiating long-term hematopoiesis in vitro. Blood 74:1563–1570.

140. **Sutherland HJ, PM Lansdorp, DH Henkelman, AC Eaves & CJ Eaves (**1990**).** Functional characterization of individual human hematopoietic stem cells cultured at limiting dilution on supportive marrow stromal layers. Proc Natl Acad Sci USA 87:3584 -3588.

141. **Petzer AL, DE Hogge, PM Landsdorp, DS Reid & CJ Eaves (**1996**).** Self-renewal of primitive human hematopoietic cells (long-term-culture-initiating cells) in vitro and their expansion in defined medium. Proc Natl Acad Sci USA 93: 1470–1474.

142. **Hao Q, F Thiemann, D Petersen, E Smogorzewska & G Crooks (**1996**).** Extended long-term culture reveals a highly quiescent and primitive human hematopoietic progenitor population. Blood 88:3306–3313.

143. **Engelhardt M, J Douville, D Behringer, A Jahne, A Smith, R Hens- chler, W Lange (**2001**).** Hematopoietic recovery of ex vivo perfusion culture expanded bone marrow and unexpanded peripheral

blood progenitors after myeloablative chemotherapy. Bone Marrow Transplant 27:249–259.

144. **Nakamura Y, AK Chargui, H Kawada, T Sato**, **T Tsuji**, **T Hotta**, **and S Kato (**1999**).** Ex vivo generation of $CD34^+$ cells from $CD34^-$ hematopoietic cells. Blood 94: 4053–4059.

145. **Shah AJ, EM Smogorzewaska, C Hannum, and GM Crooks (**1996**).** Flt-3 ligand induces proliferation of quiescent human bone marrow CD34 CD38 cells and maintains progenitor cells in vitro. Blood 87:3563 –3570.

146. **Gordon MY, SB Marley, RJ Davidson, FH Grand, JL Lewis, DX Nguyen, S Lloyd, JM Goldman (**2000**).** Contact-mediated inhibition of human haematopoietic progenitor cell proliferation may be conferred by stem cell antigen CD34. Hematol J 1:77-86.

147. **Asahara T**, **Murohara T, Sullivan A, Silver M, van der Zee R, Li T, Witzenbichler B, Schatteman G, Isner JM.** Isolation of putative progenitor endothelial cells for angiogenesis. Science 1997; 275: 964-967.

148. **Shi Q, S Rafii, Wu MH, ES Wijelath, C Yu, A Ishida, Y Fujita, S Kothari, R Mohle, LR Sauvage, MA Moore, RF Storb, WP Hammond (**1998**).** Evidence for circulating bone marrow derived endothelial cells. Blood 92: 362-367.

149. **Badroff C, RP Brandes, R Popp, S Rupp, C Urbich, A Aicher, I Fleming, R Busse, AM Zeiher, S Dimmeler (**2003**).** Transdifferentiation of blood derived human adult endothelial progenitor cells into functionally active cardiomyocytes. Circulation 107: 1024-1032.

150. **Condorelli G, U Borello, L De Angelis, M Latronico, D Sirabella, M Coletta, R Galli, G Balconi, A Follenzi, G Frati, MG Cusella De Angelis, L Gioglio, S Amuchastegui, L Adorini, L Naldini, A Vescovi, E Dejana, G Cossu (**2001**).** Cardiomyocytes inducedendothelial cells to transdifferentiate inot cardiac muscles: implication for myocardium regeneration. Proc Natl Acad Sci 98: 10733-10738.

151. **Yeh ET, S Zhang, HD Wu, M Körbling, JT Willerson, Z Estrov. (**2003**)** Transdifferentiation of human peripheral bloodderived $CD34^+$ enriched cells population into cardiomyocytes, endothelial cells and smooth muscle cells in vivo. Circulation 108: 2070-2073.

152. **Kocher AA, MD Schuster, MJ Szabolcs, S Takuma, D Burkhoff, J Wang, S Homma, NM Edwards, S Itescu (**2001**).** Neovascularization of ischemic myocardium by human bone marrow derived angioblast prevents cardiomyocytes apoptosis, reduces remodeling and improves cardiac functions. Nat Med 7:430-436.

153. **Hoehn GT, T Stokland, S Amin, M Ramirez, AL Hawkins, CA Griffin, D Small, CI**. **Civin (**1996**)** Tnk1: a novel intracellular tyrosine kinase gene isolated from human umbilical cord blood CD34+/Lin-/CD38- stem/progenitor cells. Oncogene12:903-913.

154. **Felschow DM, CI Civin, GT Hoehn (**2000**)**. Characterization of the tyrosine kinase Tnk1 and its binding with phospholipase C-gamma1. Biochem Biophys Res Commun 273:294- 301.

155. **Zambidis ET, B Peault, TS Park, F Bunz, CI Civin (**2005**).** Hematopoietic differentiation of human embryonic stem cells progresses through sequential hematoendothelial,primitive, and definitive stages resembling human yolk sac development. Blood 106:860-870.

156. **Georgantas RW 3rd, R Hildreth, S Morisot, J Alder, CG Liu, S Heimfeld, GA Calin, CM Croce, CI Civin** (2007 **).** CD34+ hematopoietic stem-progenitor cell microRNA expression and function: a circuit diagram of differentiation control. Proc Natl Acad Sci USA104:2750-2755.

157. **Alder JK, RW Georgantas 3rd, RL Hildreth, IM Kaplan, S Morisot, X Yu, M McDevitt, CI Civin (**2008**).** Kruppel-like factor 4 is essential for inflammatory monocyte differentiation in vivo. J Immunol 180:5645-5652.

Figures and their legends

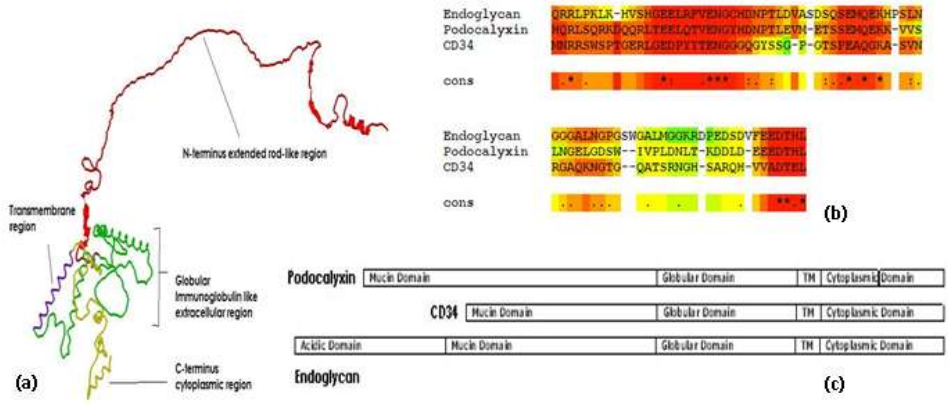

Figure 1. Structure of CD34 protein: (a) Predicted three-dimensional model of human CD34 protein showing different structural regions. The N-terminal region likely attains an extended rod-like structure protruding away from the cell surface, providing enough space for optimal interactions with various cellular adhesion molecules, followed by a cysteine-rich globular domain that likely supports the N-terminal rod-like structure like a scaffold. The molecule remains anchored through a small single transmembrane helix, and protrudes inside the cytoplasm through a comparatively small cytoplasmic region. The 3D model was generated manually by following comparative homology modeling protocols, and the picture was generated by Raswin version 6.0. (b) Multiple sequence alignment of the CD34 cytoplasmic domain with human Podocalyxin and human endoglycan cytoplasmic tail regions, revealing a high degree of sequence conservation (red). The human CD34 cytoplasmic tail sequence was obtained from amino acid nos. 301-373, human podocalyxin from amino acid no. 453, and human Endoglycan from amino acid no. 525. The sequence alignment was generated by T-COFFEE Version 6.07. Color indication: BAD AVG GOOD (c) structural domain similarities among the CD34 family of proteins. The endoglycan consists of one highly acidic region in the N-terminal region, which is absent in CD34 and podocalyxin.

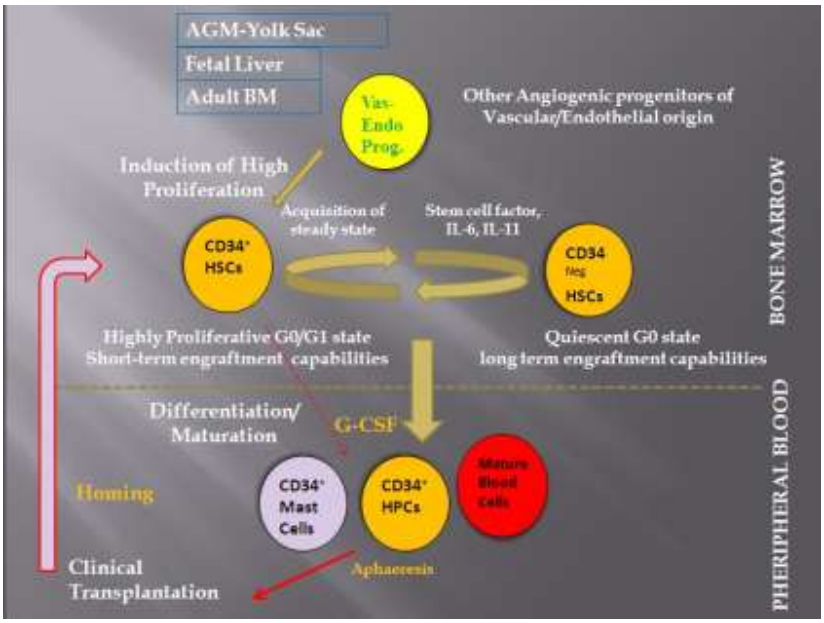

66

Figure 2. Schematic presentation of the distribution of hematopoietic stem cells in different states of activation: Expression of CD34 on hematopoietic stem cells is regulated by various factors, including cytokines, resulting in their altered proliferation and differentiation rates during different states of hematopoiesis. $CD34^{+}$ HPCs are believed to possess high proliferation rates in comparison to $CD34^{-neg}$ HPCs. On the other hand, $CD34^{-neg}$ HPCs are assumed to be more primitive, with higher long-term engraftment potential. The expression of CD34 on the surface of HPCs is assumed to be induced upon activation of cellular proliferation. It can be inhibited upon the achievement of homeostasis.

Epitope types	zyme sensitivity		Antibodies	Functional significance
	Neuraminidase From Vibrio cholera.	***O-Linked Glycoprotease from Pasteurella hae molytica.***		
Class I	Sensitive	Sensitive	12.8, BI.3C5, Immu409, B-G25, B-H21 My10, ICH3, Immu133, 14G3, ICO-115	Induction Of Adhesion Signaling
Class II	Resistant	Sensitive	QBEnd10, 43A1, MD34.3, MD34.1*, MD34.2, 4A1, 9044, 9049*, 45.28	Induction Of Adhesion Signaling
Class III	Resistant	Resistant	TUK3, 115.2, 8G12, CD34-9F2, 581, 553, 563, Birma-K3, BF23, 6A6, 7E10, 4H11	Not Defined

IOSR Journal of Electronics and Communication Engineering (IOSR-JECE)
ISSN: 2278-2834, ISBN: 2278-8735. Volume 3, Issue 4 (Sep-Oct. 2012), PP 06-11
www.iosrjournals.org

Patch Antenna Array Fault Modeling and Its Monitoring

Umesh Kumar[1], Rajiv Kapoor[2]
[1](Student, Delhi Technological University, India)
[2](Faculty, Delhi Technological University, India)

Abstract : The *On/Off faults are among the most prominent hazards observed in antenna arrays. They behave like a catalyst towards steady degradation of the circuit's performance. This paper is regarding fault monitoring in the microstrip patch antenna array [1][6]. The fault modeling, included here is single and double fault models of the patch antenna array of 8 elements. There is a marked deviation in the parametric properties of the array because of On/Off faults. By observation and analysis of these trends, the detection of fault in the array is simplified to a great extent. We aim at identification of On/Off faults in a faulty array structure by observation of its characteristic properties (like S- parameters and Radiation Pattern) and their analysis using Matrix Comparison Method and Scaled Conjugate Gradient Back Propagation Algorithm in Artificial Neural Network.*

Keywords: *Patch antenna, patch array antenna feed, S-parameter, radiation pattern, characteristic impedance, neural network.*

I. INTRODUCTION

Microstrip array [1],[2] is designed at 2.49 GHz used in IEEE 802.11b high-speed TCP/IP communications. It can be used as mass-produced, inexpensive equipment designed for FCC part 15 unlicensed uses. Microstrip antennas have been one of the most innovative topics in antenna theory and design in recent years, and are increasingly finding application in a wide range of modern microwave systems. The development of microstrip antennas has been driven by systems requirements for antennas with low-profile, low-weight, low-cost, easy integrability into arrays or with microwave integrated circuits, or polarization diversity. One of the best features of microstrip antennas is the ease with which they can be formed into arrays, and a wide variety of series-fed, corporate-fed, scanning, and polarization-agile arrays have been designed using microstrip elements. With the help of IE3D simulation tool, which is most versatile, easy to use, efficient and accurate electromagnetic simulation tool, the single patch as well as patch array has been simulated successfully. For modelling and simulation of Matrix Comparison Method [13] and Scaled Conjugate Gradient Back Propagation Algorithm in Artificial Neural Network [9], the MATLAB software is used.

II. Design Of Single Patch

The required specifications for the patch [9] are:
Resonant Frequency (f_0) = 2.49 GHz
Dielectric constant of Substrate=2.33
Height of the substrate =1.6mm
Matching Load=50Ω
Using the standard formulae and the standard design considerations we obtain a single patch with following parameters:
Width of the patch (W)=46.66 mm
Effective Dielectric (ϵ_{reff})=2.2248
Effective Length (Leff)=40.40 mm
Length extension (ΔL)=0.8175 mm
Length of the patch (L)=38.765 mm
Inset position (y)=13.665 mm
Inset width (W_0)=5.2578 mm

Fig. 1-schematic of single patch element with inset line feed

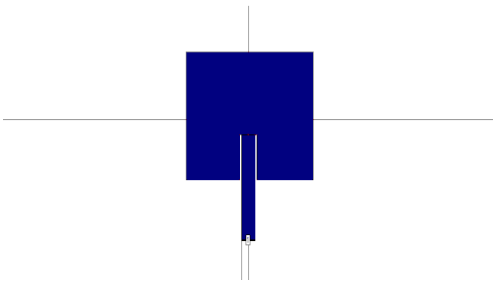

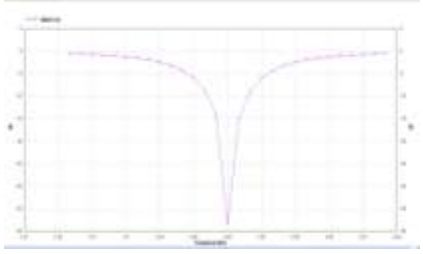

Fig. 2- The reflection loss is around -37.5 dB indicating effective coupling between port and element.

The microstrip inset feed line (figure 1) is a conducting strip, usually of much smaller width compared to the patch. It's easy to fabricate, simple to match by controlling the position of inset [3][4] and rather simple to model. But with increase in substrate thickness, spurious and surface radiation increase resulting in limiting the bandwidth.

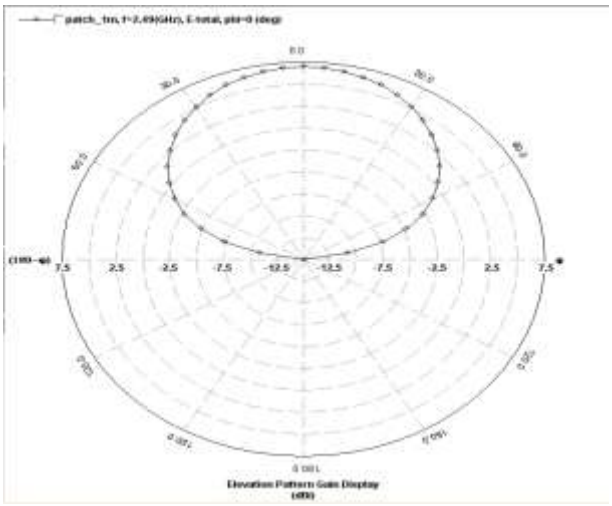

Fig. 3- This graph gives us the 2D view of radiation pattern in the azimuthal plane. The half power beamwidth is determined to be 74.42º.

We determine the physical spacing between the elements and the structure of the feed using the above information. To have zero grating lobes we kept the inter element spacing to be λ/2. Since any larger distance resulted in one or more grating lobes while smaller distances led to introduction of inherent asymmetries into the design.The feed length was taken to be approximately λ/4 for impedance transformation at the desired resonant frequency of 2.49GHz. The feed width was chosen on a hit-and-trial basis to obtain the required load matching of 50Ω. The initial width of the feed connecting the single element to the entire feed structure was taken to be the same as inset width (W_0).

III. Antenna Array Fault Modeling

The antenna array feed is based on parallel feed technique with improved beam shape [7]. The resonant frequency has changed from 2.49 GHz to 2.5 GHz (figure-2). This much of shift is tolerable since the maximum limit of tolerance is 2%. The shift in our case is 0.43%. As we can see that at resonant frequency we have a dip of -37.5 dB which gives very good antenna performance (figure 5). Here we have considered only the single and double fault modelling with different combinations of faults in the elements of the patch antenna array. The deviation in values of reflection coefficient and radiation pattern from those of fault-free case is valid. At the resonance frequency, these deviations are reduced. Hence, the patch array is very less prone to single fault errors. In case of double faults, these deviations are much higher than those of single fault cases. At resonance frequency, these deviations got reduced. Although the deviations are within tolerable limit, they are still traceable.

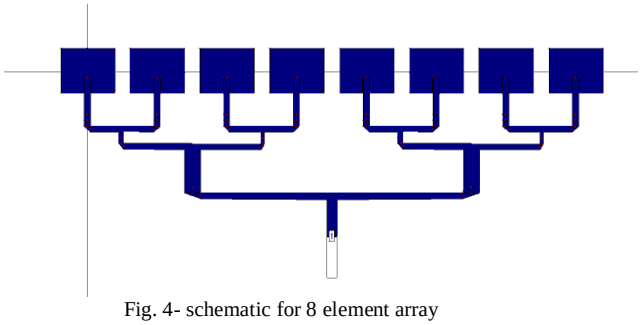

Fig. 4- schematic for 8 element array

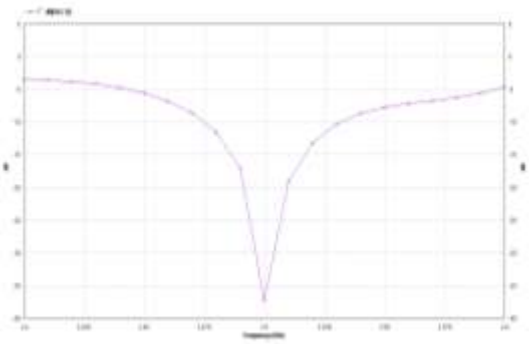

Fig. 5- Plot of S[1,1] in dB scale

The deviation in values of reflection coefficient and radiation pattern from those of fault-free case is valid. At the resonance frequency, these deviations are reduced. Hence, the patch array is very less prone to single fault errors. In case of double faults, these deviations are much higher than those of single fault cases. At resonance frequency, these deviations got reduced. Although the deviations are within tolerable limit, they are still traceable.

III a. The single fault

In the following figures, the fault model is shown with feed discontinuity fault in the first element and the antenna characteristics parameter.

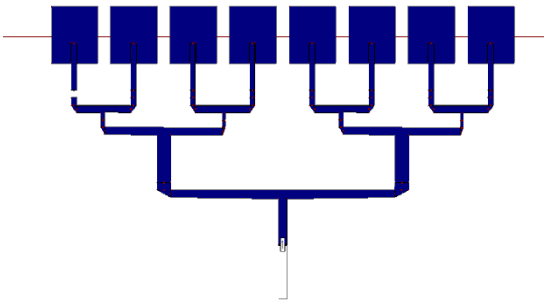

Fig. 6-discontinuity of feed in first patch element

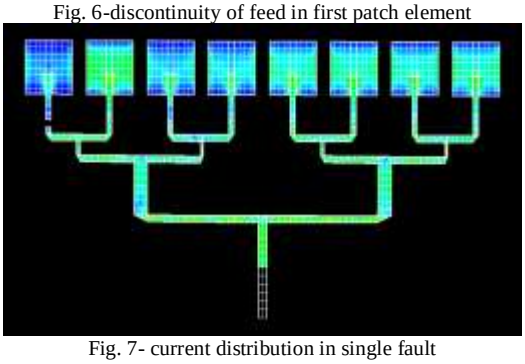

Fig. 7- current distribution in single fault

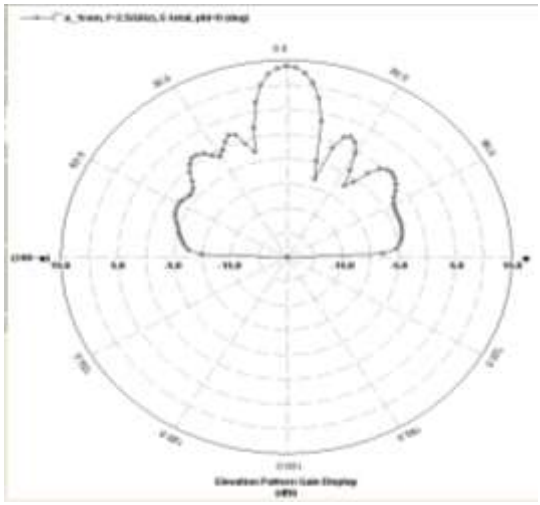

Fig. 8- 2D polar plot of gain pattern

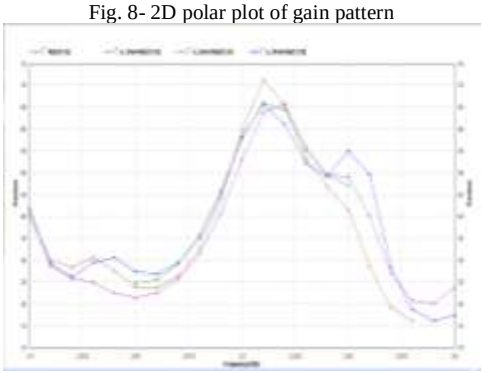

Fig. 9- *Re* Z[1,1] for all combinations of faulty cases

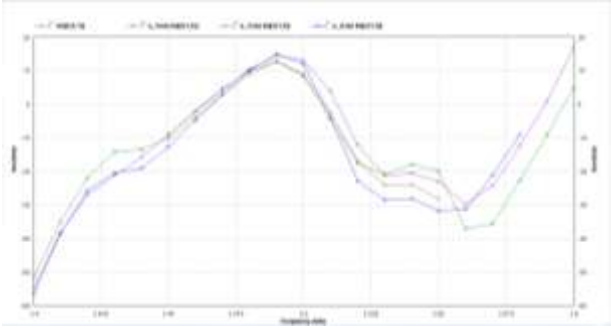

Fig. 10- *Im* Z[1,1] for all combinations of faulty cases

The point here is to be noted that patch with discontinued feeding is still showing current distribution, which is the parasitic effect [8] of the elements nearby.

III b. The double fault

In the following figures, the fault model is shown with feed discontinuity fault in the first and second element and the antenna characteristics parameter.

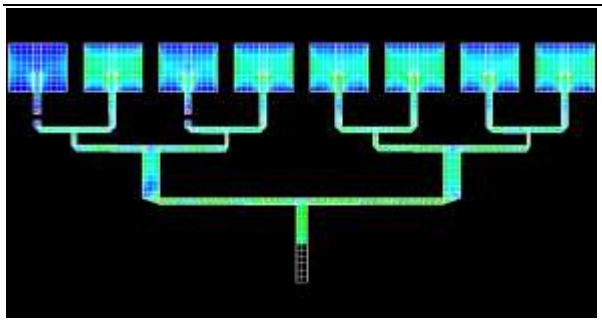

Fig. 11- current distribution in double fault

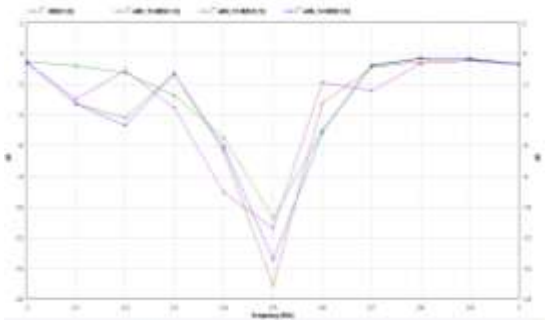

Figure12-dB S[1,1] characteristics of Double Faulty cases for combinations of (1,3), (1,4) and (1,5) faults

In the following figures antenna characteristics for the fault of combinations of (1, 3), (1, 4) and (1, 5) are only shown (figure 12,13). Rest of the cases can similarly be modelled.

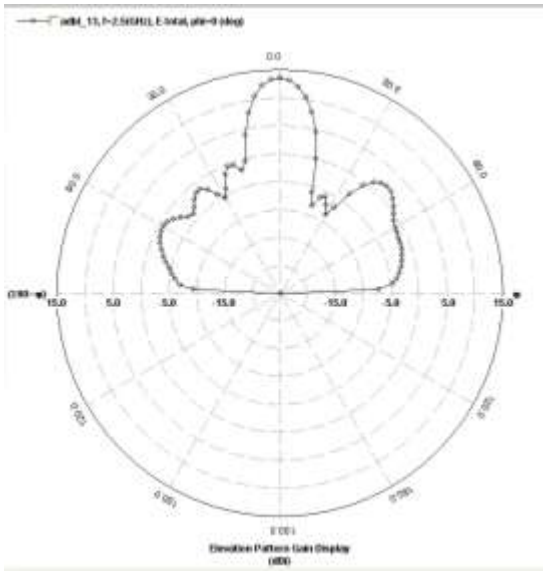

(a)

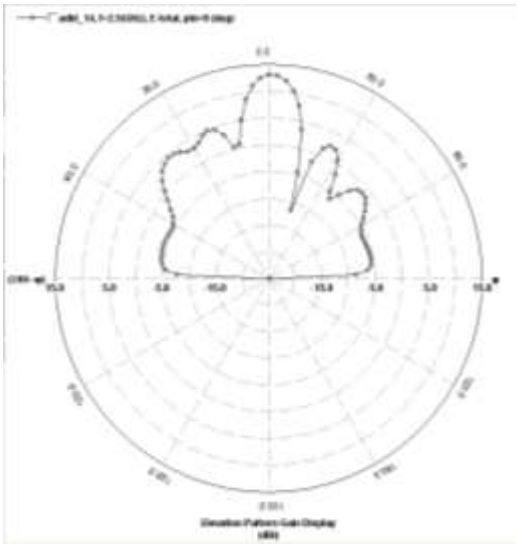

(b)

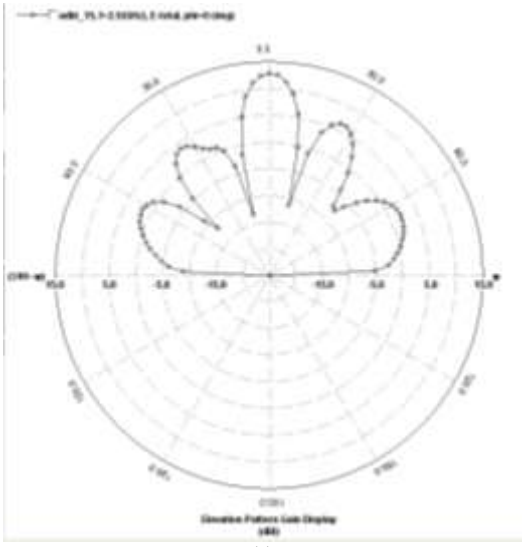

(c)

Figure 13-2D polar plot of Double Faulty cases for combinations of a(1,3),b (1,4) andc (1,5) faults

These are the 2D polar plots for each of the double faulty cases, which shows gain for double fault cases of 13.35 dBs.

IV. Antenna Array Fault Monitoring

IV a. Matrix Comparison Method

The efficiency of the matrix comparison method [13] for the fault identification is up to 85 % on an average for up to double fault in array.

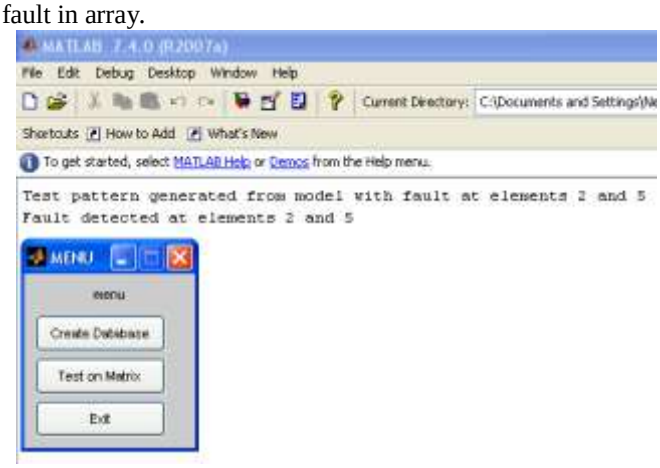

Fig.14- simulation of matrix comparison method with MATLAB

IV b. Artificial Neural Network Method

The ANN is based on Scaled Conjugate Gradient Back Propagation Algorithm in Artificial Neural Network [14][15], gives an accuracy of more than 95 % and more for most of the test cases.

Figure 15- simulation of performance characteristic of ANN method

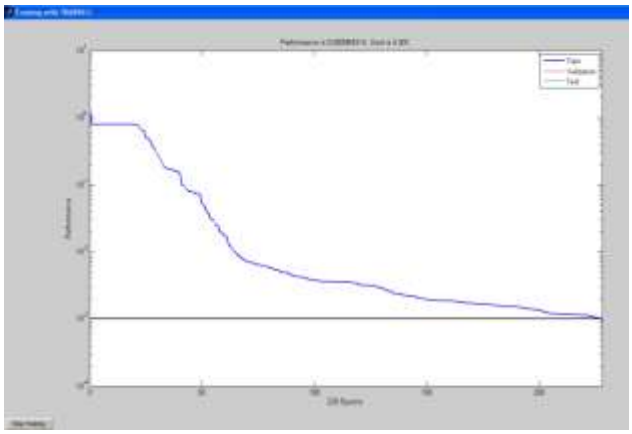

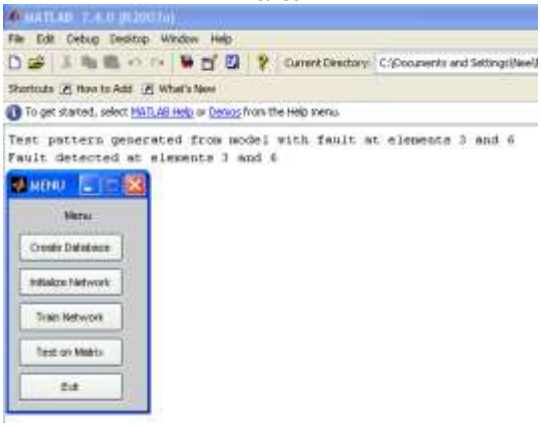

Figure 16- fault monitoring simulation

Monitoring these deviations using ANN(figure 15) we obtain the following Neural Network training statistics:
Epochs elapsed = 228
Time elapsed = 2 min 6 sec
Performance achieved = 0.000964314
Gradient at last = 0.0326946

V. Conclusion

The design of patch antenna for IEEE 802.11 has been successfully implemented at 2.49 GHz. The patch gives us very accurate results.

The 8 – element microstrip antenna array meets the requisite specifications. Although there is relative shift in resonant frequency (from 2.49 to 2.5 GHz), it is within tolerable limits (2%).

It is found out that on an average the Matrix Comparison Method gives an accuracy of 80 – 85 %. This method is also found to be susceptible to ambiguity decisions.

The ANN gives an accuracy of more than 95 % and more for most of the test cases. This method is free of any error generated because of ambiguity.

VI. Future Scope

Dipole antennas [12] can be used instead of microstrip patches. It is known that dipoles are more susceptible to flaws in array structures and hence errors can be easily traced. Circularly polarized patches can be used instead of linearly polarized ones. Cavity model analysis can be used instead of transmission line model.

The same analysis can be implemented for a larger array structure consisting of 32/64 elements. Higher degree of faults can be analysed in the array.

References

[1] H. Entschladen, U. Nagel ,"Microstrip patch array antenna",*IEEE Trans.*1984,PP. 931-933.

[2] K.A. Carver and J.A. Mink, "Microstrip antenna technology", *IEEE transactions on Antennas & Propagation*, VOL. 29, January 1981, PP. 2-24.

[3] Edward H. Newman, John E. Tehan, "Analysis of microstrip arrya and feed network" ,*IEEE Trans.* VOL. AP-33,1985.

[4] M. Ramesh AND Yip KB ," Desing formula for inset fed microstrip patch antenna *", journal of microwave and optoelectronics VOL. 3 N. Dec*-2003.

[5] N. Bayat, H. R. Hassani, S. Mohammad and Ali Nezhad, "Sidelobe reduction in microstrip patch antenna array", *IEEE Trans. NOV*-2011

[6] J.R. James, P.S. Hall, 'Handbook OF Microstrip Antennas' *VOL. 2, Peter Peregrinus ltd., London United Kingdom, 1989.*

[7] A. Mohd. Tarmizi, M.T. Mohd Wor, A.R. Tharek and R. Abdolee,"Reconfigurable Microstrip Patch Antenna Array with Beam Shaping" *IEEE TRANS.2007*

[8] Shuguang Chen and Ryuichi Iwata,"Mutual Coupling Effect in Microstrip Patch Array Antenna" *IEEE TRANS 1998.*

[9] Z. I. Dafalla, W.T.Y. Kuan, A.M. Abdel Rahman and S.C. Shudakar,"design of a Rectangular Microstrip Patch Antenna at 1 GHZ" *IEEE Trans, RF and microwave confrence oct. 2004.*

[10] QI-JUN Zhang, Kuldip C. Gupta,Vijay K. Devabhaktuni, "Artificial Neural Networks for RF and Microwave Design: From theory to practice".

[11] Abhilasha Mishra, A.B. Nand Gaonkar, V.D. Bhagile, S.C. Mehrotra, P.M. Patil," "Design OF Square AND Rectangular Microstrip antenna with the use of FFBP algorithm of artificial neural network" *IEEE TRANS.* 2009.

[12] Huiling Jiang; Fumio Kira; Keizo Cho. "Printed Dipole Antenna Comprising Partially Cylindrical Parasitic Element" *Microwave Conference proceedings, 2005. APMC 2005. Asia-pacific conference proceedings VOLUME: 3*.

[13] Ming-TE Liang, Chin-Ming Lin, and Chi-Jang Yeh," Comparison Matrix Method and its Applications to Damage Evaluation for Existing Reinforced Concrete Bridges" *journal of marine science and technology, VOL. 11, NO. 2, PP. 70-82 (2003).*

[14] Orlando De Jesús AND Martin T. Hagan, " backpropagation algorithms for a broad class of dynamic networks" *IEEE Trans, March 2006.*

[15] Xiao-Hu Yu, Guo-An Chen, Shi-Xin Cheng," Dynamic Learning Rate Optimization of the backpropagation algorithm" *IEEE Transactions on neural networks, vol. 6, no. 3, may 1995.*

Performance and Emission Studies of a Compression Ignition Engine on blends of Calophyllum Oil and Diesel.

Chinmay Mishra*, Naveen Kumar, Sidharth, B. S. Chauhan

Department of Mechanical Engineering, Delhi Technological University,

Shahabad Daulatpur, Delhi-110042

*Corresponding Author E-mail: chinmaya.pravatmishra@gmail.com

ABSTRACT:

In the present scenario of energy crisis and global warming, the use of eco-friendly renewable fuels is gaining worldwide attention. Amongst the variety of such fuels, bio-fuels from energy crops form an important solution. In this context, fuels derived from non-edible vegetable oil have a major role to provide energy security and mitigate environmental degradation. Despite extensive work carried out by large number of researchers, a huge number of non-edible vegetable oils are yet to be explored as a feed stock for small energy requirements. So there is an urgent need to assess the potential of such underutilized feed stocks. It has been found that chemical processing of vegetable oil should be carried to bring its properties similar to diesel fuel. However, the chemical processing requires capital investment and technical experience which is not feasible in rural areas. Therefore the vegetable oil in neat form without any chemical treatment presents a sustainable solution. The present study aims at evaluation of one such underutilized species "Calophyllum". This plant is abundantly available in coastal India, Bangladesh, South America, African coast and Australia. The oil in raw form and blended with diesel (10% and 20% by volume) were used to fuel a single cylinder diesel engine and the results compared with baseline data of diesel. The results suggest a reduction of 6.97% and 12.4% in brake thermal efficiency (BTE) on 10% and 20% blend respectively as compared to mineral diesel operation. Further brake specific energy consumption (BSEC) was found to increase by 7.35% for 10% blend and 14.03% for 20% blend. This reduction in BTE is compensated by the fact that CO emission is reduced by 25% at full load with 10% blend; and around 50% with 20% blend suggesting better combustion. The NOx emissions were found to be reduced by 13.48% at full load with 10% blend and by 25.24% for 20% blend. Un-burnt hydrocarbon (UBHC) emissions at peak load were increased by 9.1% at 10% blend as compared to baseline. At 20% blend, the UBHC emissions were found to be further increased by 18% compared to the neat diesel operation. UBHC emissions are lower at partial loads but tend to increase at higher loads for all fuels. This is due to the lack of oxygen, which is caused by engine operation at a higher equivalence ratio. On the basis of exhaustive experimental work, it can be concluded that 10% blend of Calophyllum oil with diesel in unmodified diesel engine may roughly decrease CO emissions by 12% and NOx by 25% whereas UBHC is increased by 9%, at the penalty of 5% reduction in BTE and 8% increase of BSEC.

Key words: Bio-fuels, Energy security, Performance, Vegetable oil, Single cylinder, Brake thermal efficiency, Brake specific energy consumption, Emission, Unburnt hydrocarbon etc.

1. INTRODUCTION

With rapid economic growth and large human population, the resurging economies like India and China are putting huge pressure on global energy supply and environmental sustainability. Globalization and rapid economic growth has resulted in exhaustive use of energy resources worldwide. This can be explained by certain trends exhibited by post reformed India and its energy intensive economy.

The total primary energy consumption of India was 524.2 mtoe in 2011 which has increased around 75% as compared to the base year 2000[1]. During the period 2000-2010, the Indian GDP growth rate was a robust 6.8% per annum [2], which shows that increasing energy consumption is an indicator of healthy economic growth [3].Per capita energy consumption in India was 560kgoe in 2009 which has increased significantly from 434 kgoe in 2000 with an average annual growth rate of 3.2% [4]. During the same period global average per capita energy consumption was found to increase from 1638.3kgoe in year 2000 to 1788.2kgoe in 2009 with an average annual growth rate of 1.01% [4]. Therefore Indian per capita energy consumption is found to be 3.19 times less than global average but its rate of growth is 3.16 times more than the global average during the period 2000 to 2009. Hence, it is very much expected that the energy requirements of India are supposed to increase many folds to reach the global average level in the years to come.

As highlighted above, countries like India need an abundant and sustainable energy supply for the foreseeable future to maintain the economic growth momentum and progressive social transformation without jeopardizing environment. However, the present energy sources and their sustainability as well as environmental effect are the factors of great concern. This can be explained by the heavy reliability of developing economies like India on exhaustible resources such as fossil fuels.

Out of the total primary energy requirement of India, 42.3% is met through coal, 23.6% through oil, 26.2% through renewables and rest through others [5]. Contribution of non-renewable sources like coal and oil towards total primary energy requirement in India has alarmingly increased [5] since last ten years partly due to installation of a large number of Mega thermal power projects running on coal, natural gas or oil and an exponential increase in terms of numbers as well as variations of automobile fleet that was made available for a billion plus market. India does not have large reserves of crude oil and imported 163.59 million tones (which is nearly 70% of its total oil requirement) of crude oil worth 4559 billion Indian rupees in 2010-11[6].

This heavy dependence of countries like India on non-renewable resources results in faster resource depletion, environmental degradation and a huge economic burden for import of expensive fossil fuels resulting in widening trade deficit [7]. Excessive use of perishable energy resources (mostly fossil fuels) has major local, regional and global environmental impact such as [8]:

1. Local - Air pollution.
2. Regional - Acid rain and airborne pathogens (i.e. infections, particles and chemicals).
3. Global - Greenhouse effect.

Projections for the 30-year period from 1990 to 2020 indicate that vehicle travel, and consequently fossil-fuel demand, will almost triple and the resulting emissions will pose a serious problem. The main reason for increased pollution levels, in spite of the stringent emission standards that have been enforced, is the increased demand for energy in all sectors and most significantly the increased use of internal combustion engines for mobility and power. [7,8]. Among them diesel engines have proven their utility in the transportation and power sectors due to higher efficiency and ruggedness. They are also potential sources of decentralized energy generation for small electrification plant [9]. However, concerns about long-term avail-ability of petroleum diesel, stringent environmental norms and environmental impacts due to extensive use in fast growing economies, have mandated the search for a renewable alternative of diesel fuel [10]. In this context, fuels derived from non-edible vegetable oil have a major role to provide energy security and mitigate environmental degradation. A large number of non-edible vegetable oils are yet to be explored as a feed stock for small energy needs. There is an urgent need to assess the potential suitability of such underutilized feed stocks. It has been found that chemical processing of vegetable oil should be carried to bring its properties similar to diesel fuel. However, the chemical processing requires capital investment and technical experience which is not feasible in rural areas. Therefore the vegetable oil in neat form without any chemical treatment presents a sustainable solution.

The present study deals with the evaluation of one such underutilized fuel species known as Calophyllum [11-13]. It is a medium-sized to large evergreen tree that averages 8–20 m (25–65 ft) in height with a broad spreading crown of irregular branches. The tree supports a dense canopy of glossy, elliptical leaves, fragrant white flowers, and large round nuts. It grows along coastal areas and adjacent lowland forests, although it occasionally occurs inland at higher elevations. It is native to East Africa, India, Southeast Asia, Australia, and the South Pacific. It has been widely planted throughout the tropics and is naturalized in the main Hawaiian Islands [11, 12]. The flowering and fruiting periods vary and in India, the flowers appear in May-June and sometimes again in November. It has been suggested that apomixis may occur in Calophyllum, resulting in polyembryony. Trees often bear fruit throughout the year [13].Its oil generating part is the seeds and one large brown seed of 2–4 cm (0.8–1.6 in) in diameter is found in each fruit. Seeds are prepared by cleaning off the skin and husk from the shell of the seed; there are 100–200 seeds/kg, with shells intact but husks removed [11, 12]. The bisexual flowers are pollinated by insects such as bees. This oil has been used as a lighting fuel for centuries. The use of this seed oil could be carried out by blending directly in mineral diesel without any substantial chemical treatment or conversion to biodiesel and subsequent application in a compression ignition engine to exhibit its potential as an eco-friendly fuel.

2. CALOPHYLLUM AS A POTENTIAL SOURCE

Calophyllum is a perennial angiosperm widely available in the costal belt of India. Its botanical name is “Calophyllum Innophyllum”. In India it is locally known as “Polanga” Some unique characteristics of the plant are [11-13]:

1. High transpiring plant thus its carbon absorption and Oxygen emission is higher.
2. It has no incubation in yielding i.e. seeds could be obtained throughout the year.
3. It is non-edible oil, hence would not create food inflation.
4. After yielding the oil from the seed, the residue can be used as organic fertilizer.

3. PHYSICO-CHEMICAL CHARACTERIZATION

Comparison of important physico-chemical properties of Calophyllum oil with respect to diesel fuel is essential for its evaluation as an engine fuel and subsequent analysis. Various properties of the seed oil like flash point, density, viscosity, calorific value, blend stability etc. were determined in accordance with ASTM/BIS standards as described below.

The diesel used in the present study was procured from a local refilling station. The properties of diesel procured was as per IS 1460 : 2005. The Calophyllum oil sample was taken from a local supplier and subsequently pressure filtered in laboratory. It was heated at 100^0C for 30 minutes with mild stirring and then kept in an air tight screw cap bottle for chemical analysis. Kinematic viscosity of liquid fuel samples were measured at 40^0C as per ASTM D-445. The equipment used was "Petrotest Viscometer". Specific gravity of the samples was measured at a temperature of 15^0C in accordance with ASTM D-4052. The equipment used was "Antan Par Density Meter, Model DMA 4500". Similarly calorific values of the fuel samples were measured as per ASTM D-240 standard with the help of "Parr 6100 Calorimeter". Flash point of liquid samples was measured using "Pensky Martin's Flash Point Apparatus" in accordance with ASTM D-93(2011). A comparison of various physico-chemical properties of diesel and Calophyllum oil is shown in Table-1.

Property	Diesel	Calophyllum
Specific gravity	0.827	0.922
Viscosity (dP)	3.972	14.83
Flash point (^{0}C)	66	210
Boiling Point (^{0}C)	385	514
Color	Pale Yellow	Blackish
Calorific value (kJ/Kg)	44100	39100

Table-1: Properties of Calophyllum Innophyllum oil in comparison with mineral diesel.

It can be seen that the properties like specific gravity and calorific value of both the fuels are comparable, but viscosity of Calophyllum oil is too high. The high viscosity of vegetable oils may contribute to the formation of carbon deposits in the engines, incomplete fuel combustion and results in reducing the life of an engine [17]. Therefore any direct blending of vegetable oil in unmodified diesel engines should be confined within 30% of volume wise substitution of diesel.

4. EXPERIMENTAL PROCEDURE

In the present investigation, pressure filtered Calophyllum oil was taken and heated up to 100^0C with mild stirring to remove any absorbed moisture. Stirring was done to prevent explosion of trapped moisture at the bottom of the oil carrying container. It was then cooled and kept in an airtight bottle. During the course of present study, two blends of diesel and Calophyllum oil were prepared.

While preparation of blend, 10% Calophyllum oil was blended with 90% diesel (v/v %) and called as D90/B10 and 20% Calophyllum oil was blended with 80% diesel (v/v %) which was termed as D80/B20.The nomenclature of neat diesel was D100.

The test set up (Fig.1) consists of the CI engine (Specification given in table-2), the fuel supply and measurement system, air supply and measurement system, load variation and measurement system along with emission measurement system. The engine trial was conducted as specified by IS: 10,000. The diesel engine used was a Kirloskar make 4 Stroke, single cylinder, 1500 rpm, vertical, water cooled, diesel engine with hydraulic dynamometer. For fuel supply, two separate tanks were used, one for neat diesel and the other for various blends. Fuel flow from the tanks to fuel meter was controlled by a valve. The fuel measurement unit consisted of a graduated tube of 100mL capacity.

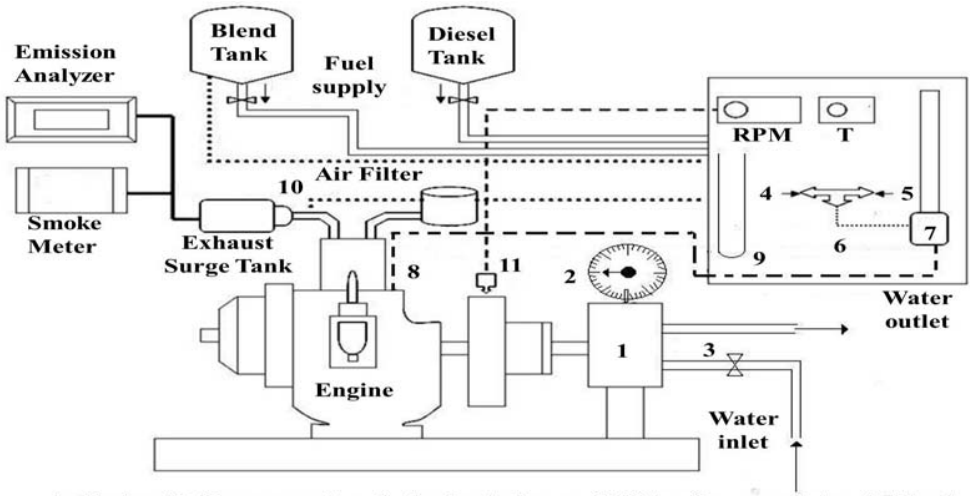

Fig.1: Schematic diagram of the experimental setup.

The fuel flow from tank was regulated by a stop valve. Flow rate was measured by measuring the time requirement by a stop watch for 20cc consumption of fuel through the graduated tube. Air flow measurement was done by the air box method. For applying different load, a hydraulic dynamometer was provided. For measurement of engine emission, an AVL 437 smoke meter and an AVL Di Gas Analyzer were used. The accuracy and reproducibility of the instrument was +/- 1% of full scale reading.

The detector used in the smoke meter was a Selenium photocell with diameter 45 mm. Its maximum sensitivity in light was within the frequency range of 550 to 570 nm. Below 430 nm and above 680 nm, the sensitivity of the instrument was less than 4% related to the maximum sensitivity. The measurement principle for CO, UBHC and CO_2 was infrared measurement and for NO_x and O_2 it was electrochemical measurement.

1	Make	Kirloskar Brothers Limited
2	BHP	05
3	Compression ratio	18:1
4	Stroke length (mm)	110
5	Brake drum arm length (mm)	335
6	Speed (rpm)	1500
7	Cylinder diameter (mm)	80
8	Orifice diameter. (mm)	20
9	Coefficient of discharge	0.6
10	Injection angle (degree BTDC)	23

Table-2: Engine specification.

5. RESULTS AND DISCUSSIONS

Exhaustive performance and emission test were carried out with D100, D90/B10 and D80/B20 as the fuel. For each blend, the results were obtained at 6 different loads i.e. at 0%, 20%, 40%, 60%, 80% and 100% load using the hydraulic dynamometer. The different performance parameters evaluated were brake thermal efficiency (BTE), brake specific energy consumption (BSEC) and brake mean effective pressure (BMEP). Various emissions determined were carbon monoxide (CO), un-burnt hydrocarbons (UBHC) and nitrogen oxides (NO_x).

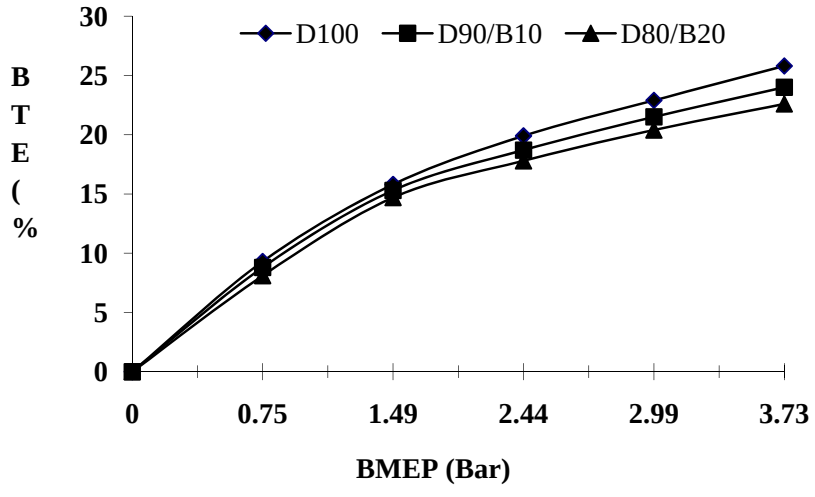

Fig. 2: Variation of BTE with BMEP

The variation of brake thermal efficiency (BTE) with brake mean effective pressure (BMEP) is shown in Fig. 2. BTE at full load is maximum for D100. With 10% blending, BTE is decreased by 6.97% and 12.4% for 20% blend in comparison to neat diesel at full load. The decrease in efficiency with blending may be attributed to the fact that with higher blend percentage, mass of fuel consumption increases faster than decline in calorific value to generate same amount of power [3,9,18,19]. However, at lower loads the variation in BTE for blends is less.

The results obtained are not consistent with the results of Pramnik as he has reported better thermal efficiency using Jatropha Oil. [17].

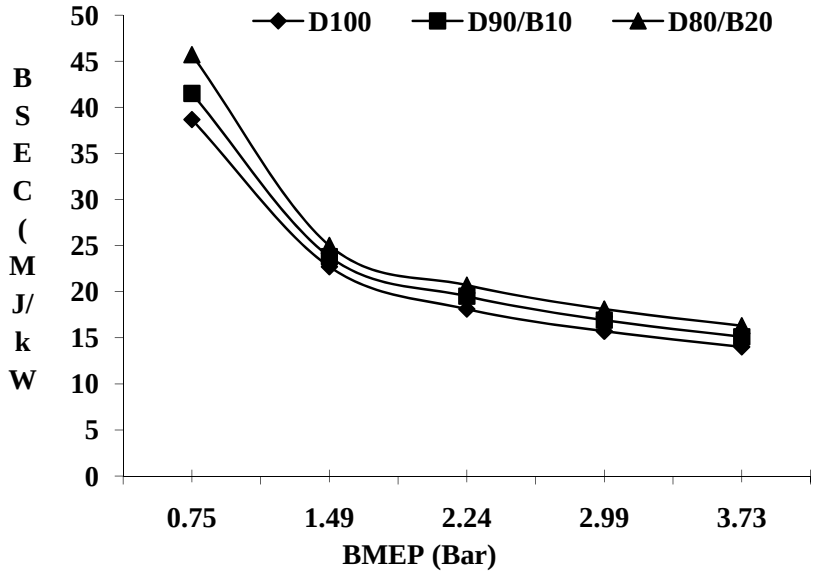

Fig.3: Variation of BSEC with BMEP.

Brake specific energy consumption (BSEC) is a parameter to compare the energy requirement for producing unit power [3].The variation of BSEC with BMEP is shown in the Fig. 3. It is clear that BSEC of Calophyllum-diesel blend is higher than neat diesel which may be due to high relative fuel density, viscosity and low calorific value of fuel blends [3, 17, 18]. The higher density of Calophyllum diesel blends led to more discharging of fuel for the same displacement of the plunger in the fuel injection pump, thereby increasing the specific fuel consumption and thus energy consumption for producing unit power [9]. For D90/B10 fuel, BSEC at full load is increased by 7.85% compared to pure diesel. Similarly for D80/B20 fuel the BSEC at full load is increased by 16.42% over neat diesel operation.

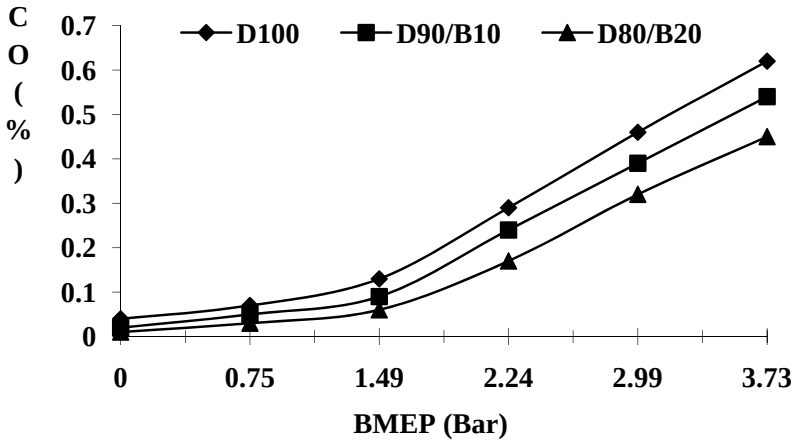

Fig.4: Variation of carbon mono oxide with BMEP

The variation of carbon monoxide with respect to BMEP is shown in Fig.4. Within the whole experimental range, the CO emission from the Calophyllum diesel blends is lower than neat diesel fuel. With increase in Calophyllum percentage in diesel, CO emission decreases, as Calophyllum is an oxygenated fuel and contains oxygen which helps in complete combustion. [15,16,18]. As evident from the figure, the variation of CO emission is insignificant at lower loads for different test fuels. At higher loads, the percentage differences are in two digits. [16].

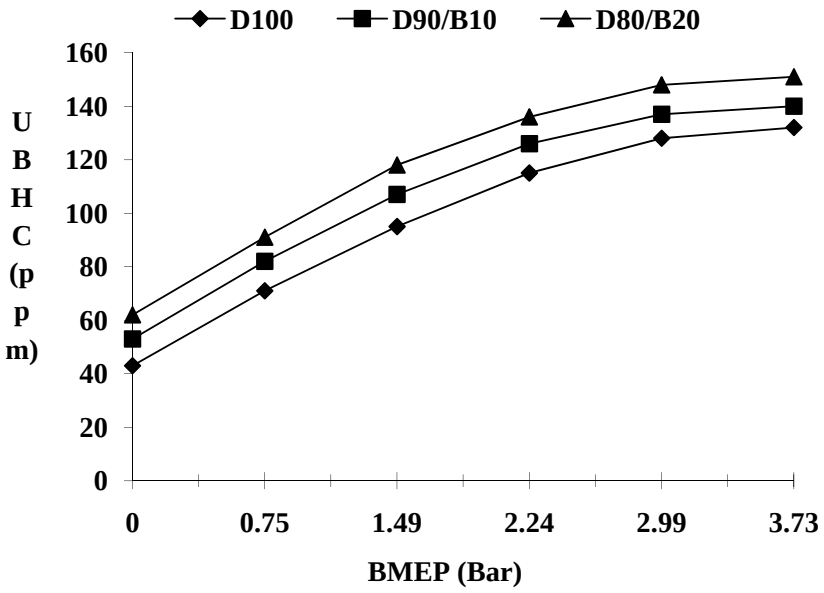

Fig. 5: Variation of unburned hydrocarbon with BMEP

The variation of emissions of un-burnt hydrocarbons (UBHC) with respect to BMEP is shown in Fig.5. The value of UBHC emission from the diesel engine in the case of Calophyllum diesel blend is higher than that of diesel fuel. UBHC emissions are lower at partial loads but tend to increase at higher loads for all fuels. This is due to the lack of oxygen, which is caused by engine operation at a higher equivalence ratio [3,9,16,19].

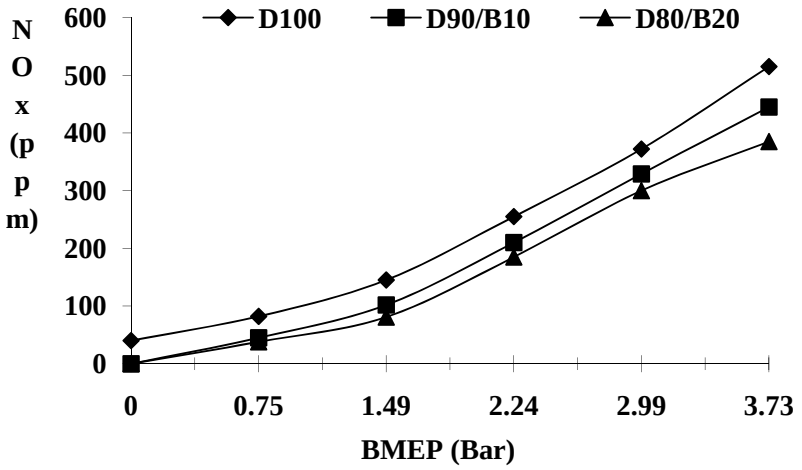

Fig. 6: Variation of NOx emissions with BMEP

Fig.6 shows the variation of NOx emission. It indicates that at full load, NO_x emission is reduced by 13.59% with D90/B10 fuel as compared D100 fuel. Similarly for D80/B20 fuel, the decrease of NO_x at full load is 25.24% [14,16]. The decline in NOx emission may be attributed to the fact that the peak engine temperature is reduced due to reduction in calorific value of fuels combusted which prohibits NO_x formation [15,13]. This is the most important emission characteristic of plant oil as the NO_x emission is the most harmful gaseous emission from engines; therefore, its reduction has always been the goal of engine researchers and makers. This typical emission characteristic of NO_x for plant oil is very useful in the application of plant oil in diesel engines. The results obtained from the experiment clearly show that using plant oil in diesel engine reduces NO_x emissions, which is in accordance to results obtained by Wang et al. [19, 13].

6. CONCLUSION

The following conclusion can be drawn from the series of exhaustive experiments and subsequent analysis carried in the present study.

1. The experimental results show that the engine performance with Calophyllum oil diesel blend is slightly inferior to the performance with neat diesel operation due to marginal reduction in brake thermal efficiency (BTE) and some tolerable increment in brake specific energy consumption (BSEC).
2. It is found that CO emissions are lower for Calophyllum oil diesel blend than diesel fuel and this reduction increases with increase of Calophyllum oil in Calophyllum oil diesel blend.
3. Emissions of nitrogen oxides (NO_x) are found to be reduced substantially with Calophyllum oil diesel blend.
4. However, un-burnt hydrocarbons (UBHC) emission is found to be marginally higher at higher percentage blend.
5. It could be concluded that Calophyllum oil when blended with diesel up to 20%, are promising alternative to fossil diesel and would not require any modification in engine design.

8. REFERENCES

1. BPSR-2011.

2. http://maninair.in/gdp-growth-rate-india.

3. Chauhan BS, Kumar N, Jun YD, Lee KB.(2010). Performance and emission study of preheated Jatropha oil on medium capacity diesel engine. Energy 35 (2010) 2484-2492.

4. http://data.worldbank.org.

5. International energy agency survey 2009.http://www.iea.org/stats/pdf_graphs/INTPESPI.pdf.

6. Petstat 2010-11.

7. Gill SS, A. Tsolakis, K.D. Dearn, J. Rodriguez Fernandez(2010.). Combustion characteristics and emissions of Fischer Tropsch diesel fuels in IC engines. Progress in Energy and Combustion Science 37 (2011) 503-523.
8. Agarwal AK. Bio-fuels (alcohols and biodiesel) applications as fuels for internal combustion engines. Prog Energ Combust 2007;33:233-71.

9. Chauhan BS, Kumar N, Cho H.MCho (2009). Performance and emission studies on an agriculture engine on neat Jatropha oil. Journal of Mechanical Science and Technology 24 (2) (2010) 529-535.

10. Chauhan BS, Kumar N, Pal SS, Jun YD. Experimental studies on fumigation of ethanol in a small capacity diesel engine. Energy 2011; 36:1030-8.

11. Species Profiles for Pacific Island Agro-forestry, April 2006, ver. 2.1.

12. www.traditionaltree.org.

13. http://www.worldagroforestrycentre.org.

14. LapuertaM, Armas .O, Hernández .J.J, Tsolakis A.(2010). Potential for reducing emissions in a diesel engine by fuelling with conventional biodiesel and Fischer–Tropsch diesel. Fuel 89 (2010) 3106–3113.

15. Canakci M., Ozsezen A.N., Arcaklioglu .E, Erdil .A (2009). Prediction of performance and exhaust emissions of a diesel engine fueled with biodiesel produced from waste frying palm oil. Expert Systems with Applications 36 (2009) 9268–9280.

16. Y. D. Wang, T. Al-Shemmeri, P. Eames, J. McMullan, N.Hewitt, Y. Huang and S. Rezvani, An experimental investigationof the performance and gaseous exhaust emissions of a diesel engine using blends of a vegetable oil, *Applied Thermal Engineering*, 26 (2006) 1684-1691.

17. Pramanik K, Properties and use of jatrophacurcas oil and diesel fuel blends in compression ignitionengine. Renewable energy, 2003, Vol 28, ISS 2, 239-248.

18. Chauhan BS, Kumar N, Cho H.MCho(2012). A study on the performance and emission of a diesel engine fueled with Jatropha biodiesel oil and its blends. Energy 37 (2012) 616-622.

19. Chauhan BS, Kumar N, Sidharth, Sinha S K. Performance and emission characteristics of thumbaoil in a

medium capacity diesel engine. 2011 2nd International Conference on Advances in Energy Engineering.(ICAEE2011)

Journal of Materials Chemistry B

Accepted Manuscript

This is an *Accepted Manuscript*, which has been through the RSC Publishing peer review process and has been accepted for publication.

Accepted Manuscripts are published online shortly after acceptance, which is prior to technical editing, formatting and proof reading. This free service from RSC Publishing allows authors to make their results available to the community, in citable form, before publication of the edited article. This *Accepted Manuscript* will be replaced by the edited and formatted *Advance Article* as soon as this is available.

To cite this manuscript please use its permanent Digital Object Identifier (DOI®), which is identical for all formats of publication.

More information about *Accepted Manuscripts* can be found in the **Information for Authors**.

Please note that technical editing may introduce minor changes to the text and/or graphics contained in the manuscript submitted by the author(s) which may alter content, and that the standard **Terms & Conditions** and the **ethical guidelines** that apply to the journal are still applicable. In no event shall the RSC be held responsible for any errors or omissions in these *Accepted Manuscript* manuscripts or any consequences arising from the use of any information contained in them.

Phase Control of Nanostructured Iron Oxide for Application to Biosensor

Rachna Sharma[1,3], Ved Varun Agrawal[1,*], A. K. Srivastava[1], Govind[1], Lata Nain[2], Imran Chaudhary[1], Soumya Ranjan Kabi[2], R. K. Sinha[3], and Bansi D. Malhotra[4,*]

[1]National Physical Laboratory, New Delhi-110012, India

[2]Division of Microbiology, Indian Agricultural Research Institute, New Delhi-110012, India

[3]Department of Applied Physics, Delhi Technological University, New Delhi- 110042, India

[4]Department of Biotechnology, Delhi Technological University, New Delhi- 110042, India

Abstract

We report results of the studies relating to phase transformation of bare Fe_3O_4 nanoparticles (NPs) to α-Fe_2O_3 NPs obtained during electrophoretic film deposition onto indium-tin oxide coated glass plate. The *in-situ* oxidation of NPs during electrophoretic deposition can be circumvented using surface passivation of the Fe_3O_4 NPs with organic shell (carbon) as well as inorganic shell (silica) while retaining biocompatibility of Fe_3O_4 NPs. XRD and XPS studies reveal the transformation of Fe_3O_4 NPs to α-Fe_2O_3 NPs on electrophoretic deposition and retention of phase of Fe_3O_4 NPs on encapsulation with carbon and silica, respectively. The results of SEM studies indicate decreased agglomeration of Fe_3O_4 NPs on encapsulation during film deposition. Attempts have been made to compare the characteristics of cholesterol biosensors fabricated using Fe_3O_4@C and α-Fe_2O_3 NPs, respectively. The Fe_3O_4@C NPs based cholesterol biosensor shows response time as 60 s, linearity range as 25-500 $mgdl^{-1}$, sensitivity as 193 $nAmg^{-1}dlcm^{-2}$ and Michaelis-Menten constant as 1.44 $mgdl^{-1}$.

Keywords: nanostructured iron oxide, phase transformation, *in-situ* oxidation, surface passivation, biocompatibility

Phone: +91-11-45609489,

E-mail: agrawalvv@nplindia.org; bansi.malhotra@gmail.com

Introduction

Nanostructured iron oxides (Fe_3O_4, γ-Fe_2O_3 and α-Fe_2O_3) owing to their multifunctional properties such as small size, superparamagnetism, low toxicity etc. are being widely investigated for applications in high-density information storage[1], electronic devices[2], ferrofluid technology[3], catalysis[4], pharmaceuticals[5] and biotechnology[6]. Among these, applications of nanostructured iron oxides in clinical diagnostics and biomedicine have aroused much interest because of their biocompatibility and stability in physiological conditions[7, 8]. They can also be used as contrast agents in magnetic resonance imaging[9, 10], as mediators in hyperthermia[11], as carriers for guided drug delivery[12-14] and as immobilization support for desired biomolecules for diagnosis of various pathogens, diseases and estimation of various biochemical analytes such as glucose, urea etc[15-17]. Besides this, particle size of the nanostructured iron oxide can be controlled to a similar size as that of a biomolecule (protein 5-50 nm; virus 20-450 nm; cell 10-100 μm)[18].

Despite several advantages, susceptibility of Fe_3O_4 NPs towards oxidation and the tendency to agglomerate due to the strong dipole-dipole attraction between particles, have limited their applications till date[19]. It is anticipated that encasing colloids in a shell of a different material may perhaps protect the core from extraneous chemical and physical changes. And core-shell nanostructures are known to exhibit improved physical and chemical properties over the single-component counterparts, and hence are potentially useful for a range of applications. To

improve stability of the deposited NPs, many molecules such as carbon and silica have been considered as interesting encapsulants[20-22]. Compared to polymer and inorganic shells, carbon shells exhibit much higher stability in various chemical and physical environments such as acid or base media, as well as at high temperatures and pressures[23]. Thus, carbon coated Fe_3O_4 NPs may perhaps ensure prolonged activity of the biomolecules and enhanced stability of the biosensors.

Among the various methods, formation of nanocrystalline films using electrophoretic deposition has recently gained much interest since it is cost effective[24] and can be used to obtain uniform thin films by optimizing parameters such as solution concentration, applied potential, pH of the solution etc[25,24]. The fabrication of nanostructured iron oxide films using electrophoretic deposition and its characterization may perhaps yield important information relating to phase change of nanostructured iron oxide. Also, the utilization of nanostructured iron oxide films for fabrication of biosensors may perhaps result in enhanced electrocatalytic activity of the given biomolecule and improved sensitivity for detection of the desired analyte.

We report a novel method of controlling phase of iron oxide NPs obtained during electrophoretic deposition. It is shown that phase of the nanostructured iron oxide during electrophoretic deposition can be tuned to desired requirement by using bare Fe_3O_4 NPs or capped Fe_3O_4 NPs as the starting material. The nanocrystalline films of Fe_3O_4@C and α-Fe_2O_3 NPs have been employed for the fabrication of a biosensor using cholesterol oxidase as a model enzyme and biosensing characteristics have been investigated using electrochemical techniques such as cyclic voltammetry and electrochemical impedance spectroscopy. To the best of our knowledge, there is as yet no report on the phase transformation of Fe_3O_4 NPs during electrophoretic deposition, its prevention and further application in biosensing.

Experimental Methods

Materials and Methods

Ferrous sulphate heptahydrate ($FeSO_4.\ 7H_2O$), ferric chloride ($FeCl_3$), sodium hydroxide (NaOH), fructose ($C_6H_{12}OH$) powder and tetraethyl orthosilicate ($Si(OC_2H_5)_4$) have been purchased from Sigma-Aldrich. All reagents are of analytical grade and have been used without further purification. De-ionized water (Milli Q 10 TS) with resistivity >18.2 MΩ-cm has been used for preparing all aqueous solutions. Indium-tin-oxide (ITO) coated glass plates have been obtained from Balzers, UK, (Baltracom 247 ITO, 1.1 mm thick) with a sheet resistance and transmittance of 25 Ωsq^{-1} and 90%, respectively. Cholesterol powder and cholesterol oxidase (EC 1.1.36 from Pseudomonas fluorescens) with specific activity of 26 Umg^{-1} have been purchased from Sigma–Aldrich (USA). The stock solution of cholesterol has been prepared in 10% triton X-100 and stored at 4°C.

a) Preparation of Fe_3O_4, Fe_3O_4@C and Fe_3O_4@SiO_2 NPs

i) Fe_3O_4 NPs

The Fe_3O_4 NPs have been prepared via hydrolytic reaction based on chemical co-precipitation of metal salts with an alkali as reported earlier[26]. Briefly, 0.32 M $FeSO_4.7H_2O$ and 0.64 M $FeCl_3$ are added to 10 ml of deoxygenated water (containing 12.1 N HCl) with continuous stirring at 30 °C. Solution containing iron salts is dropwise added to 100 ml of NaOH solution (1.5 M) with vigorous stirring at 30 °C. Mixture is then stirred for additional 30 mins resulting in appearance of a black precipitate. The particles are washed by centrifugation at 3500 rpm for 30 mins and supernatant is removed by decantation. Particles are then redispersed in 200 ml of deoxygenated water and are stabilized by making pH of the sol 3.5 using HCl.

Further, Fe_3O_4 NPs are subjected to high temperature and pressure using autoclaves. 30 ml of above synthesized NPs are autoclaved at 180 °C for 4 h[27].

ii) Fe_3O_4@C NPs

Carbon capped Fe_3O_4 NPs have been prepared via hydrothermal carbonization reaction. For this purpose, 10 mmol of fructose powder is added to 30 mL of Fe_3O_4 NPs sol[23, 28, 29] and the mixture is autoclaved at 180 °C for 4 h. At this temperature, fructose melts and carbonization of fructose occurs, resulting in the carbon shell over Fe_3O_4 NPs[30]. The reaction mixture is cooled under ambient conditions. The synthesized product is washed by centrifugation at 3500 min^{-1} and the supernatant is removed by decantation. No change in color of the sol is observed and pH of the NPs redispersed in water is recorded as 8.0.

iii) Fe_3O_4@SiO_2 NPs

To 10 mL of Fe_3O_4 NPs sol (diluted with 40 mL of iso-propanol) are added 1 mL of ammonia and 1 mL of tetraethyl orthosilicate (TEOS)[31]. The mixture is stirred at 30 °C for 4 h and change in colour from dark brown to light brown is observed on completion of the reaction. The synthesized NPs are collected by centrifugation at 3500 min^{-1} and pH of the NPs redispersed in water is recorded as 9.6.

b) Preparation of Nanostructured Iron Oxide Films

The nanocrystalline films of iron oxide are deposited onto ITO coated glass plates using a two-electrode system with platinum as the auxillary electrode and ITO coated glass plate as the deposition electrode. The electrophoretic deposition involves charged particles in a suspension being deposited onto an electrode under the influence of applied electric field. Thus, use of

surfactant is avoided and charge on the surface of NPs is introduced by adjusting pH of the suspension to obtain stable sol. Fe_3O_4 NPs carry positive charge at pH 3.5 since isoelectric point of Fe_3O_4 is 6-7[32-34]. Cationic NPs are deposited onto ITO coated glass plate at the cathode terminal. Application of even a small voltage leads to electrolysis of water producing hydrogen and oxygen gas that hinder continuous flow of the NPs and affect the film uniformity[25]. Thus, mixture of methanol-water (2:1) is utilized for deposition of the desired nanocrystalline film. Conditions for obtaining uniform films have been optimized for various parameters such as applied potential, concentration, deposition time etc and uniform films of Fe_3O_4 NPs and Fe_3O_4 NPs (autoclaved) are obtained on application of 5V potential for 30 s.

The Fe_3O_4@C and Fe_3O_4@SiO_2 NPs have been deposited in methanol-water (2:1) mixture. Although Fe_3O_4@C NPs are stable at 8.0 pH but no deposition occurs indicating that NPs carry negligible charge. Positive charge on NPs is then introduced by adjusting pH to 3.5 and nanocrystalline film is deposited onto ITO coated glass plate at the cathode terminal by applying optimized potential of 10 V for 60 s. Interestingly, Fe_3O_4@SiO_2 NPs carry negative charge at pH 9.6 (as iso-electric point of SiO_2 NPs is ~2)[35], thus nanocrystalline film is deposited onto ITO coated glass plates at the anode terminal on application of 10 V potential for 60 s.

c) Fabrication of Nanostructured Iron Oxide Films based Bioelectrodes

ChOx is physiosorbed onto the nanostructured iron oxide films. For this purpose, 20 µL of freshly prepared ChOx solution (1 mg/mL) is spread onto the α-Fe_2O_3 and Fe_3O_4@C nanocrystalline films. ChOx immobilized iron oxide films are incubated at 27 °C for 2 h and at 4 °C for 12 h[36]. Later weakly bound ChOx are removed by washing these films with 100 mM PBS buffer containing 0.05% Tween-20[37]. These films are stored at 4°C when not in use. The

fabricated ChOx/Fe_3O_4@C film/ITO and ChOx/α-Fe_2O_3 film/ITO bioelectrodes have been characterized via SEM, CV and EIS studies and the enzyme activity measurements for the fabricated bioelectrodes have been carried out using CV and EIS techniques.

d) Characterization

TEM micrographs have been recorded using a high-resolution transmission electron microscope (HR-TEM, Tecnaii-G2F30 STWIN). Samples for TEM are prepared on 200 mesh carbon coated copper grids. A drop of iron oxide NPs sol is carefully placed on the copper grid surface and is then dried under ambient conditions. The structure of the powder samples and nanostructured iron oxide films have been analyzed using X-ray powder diffraction (XRD, Cu-Kα radiation, Rigaku) over the 2□ range from 25°-70° using monochromatized X-ray beam with Cu-Kα radiations (λ = 1.54 Å). XPS measurements have been carried out in a Perkin Elmer XPS chamber (PHI 1257) with a base pressure of 5×10^{-9} torr. The chamber is equipped with a dual anode Mg-K_α (energy 1253.6 eV) and Al-K_α (energy 1486.6 eV) X-ray source and a high-resolution hemispherical energy analyzer for energy resolved electron detection. The Mg-K_α X-ray source has been used for this study. The samples are sputtered with 4 keV argon ions to remove surface contamination prior to XPS studies. The absorption studies of the bare and encapsulated NPs have been conducted on Phoenix – 2200 DPCV UV-Vis Spectrophotometer in the wavelength range of 200-900 nm. The transmission studies of nanostructured iron oxide films in the infrared region have been carried out on Perkin Elmer, Spectrum BX II spectrophotometer in the wavenumber range of 400-4000 cm^{-1}. The morphological changes of nanocrystalline films on enzyme immobilization have been studied using SEM, LEO 440 scanning electron microscope.

The electrochemical experiments have been conducted on Autolab PGSTAT 302N System (Ecochemie, The Netherlands) in a three electrodes system. All electrochemical experiments have been carried out in a cell containing 15 ml of 100 mM Phosphate Buffer Solution (PBS) containing 0.9% NaCl and 5 mM $K_3/K_4[Fe(CN)_6]$ as a redox probe and using a platinum wire as auxiliary, a Ag/AgCl wire as reference, and the nanostructured iron oxide films on ITO as the working electrode.

Results and Discussion

a) TEM Studies of Iron Oxide NPs

Fig. 1(a) shows TEM micrograph of Fe_3O_4 NPs indicating formation of nearly monodispersed nanocrystals with average diameter of 10 nm. The lattice spacing of ~ 2.56 Å obtained from fringe pattern [Inset Fig. 1(a)], match with the d-value (2.56 Å), corresponding to (311) hkl plane of the Fe_3O_4 nanocrystals [JCPDS file – 890951]. However, after hydrothermal treatment, the average size of NPs increases by about two nm [Fig. 1(b)]. Increase in average particle size of autoclaved NPs and decrease in the number of smaller NPs indicates growth of NPs at the expense of smaller NPs, suggesting Ostwald ripening[38] of NPs. Also, the edges and roughness observed on NPs surfaces are reduced on hydrothermal treatment and the NPs assume spherical shape. Thus, size and soomthness of the NPs can be tailored using hydrothermal treatment.

On capping of Fe_3O_4 NPs with carbon and silica, the average particle size of Fe_3O_4 NPs increased to 14 nm and 20 nm [Fig. 1(c), 1(d)] suggesting the formation of carbon and silica shell, respectively, over Fe_3O_4 NPs. Due to the formation of the thick shell of silica, the Fe_3O_4 NPs are well separated and uniform [Inset Fig. 1(d)] while some agglomeration has been observed in case of Fe_3O_4@C NPs [Inset Fig. 1(c)].

b) UV-visible Studies of Fe_3O_4, Fe_3O_4 (autoclaved), Fe_3O_4@C and Fe_3O_4@SiO_2 NPs

Fig. 2 shows absorption spectra of the Fe_3O_4 NPs, Fe_3O_4 NPs (autoclaved), Fe_3O_4 NPs capped with carbon and Fe_3O_4 NPs capped with silica in the UV-Vis wavelength range. The absorption onset of Fe_3O_4 NPs is at ~ 600 nm [Fig. 2(a)]. Because of the quantam size effect, this onset value is blue-shifted by 100 nm as compared to that of the bulk Fe_3O_4[39]. The band near 300 nm corresponds to ligand field transitions of Fe^{3+} and shoulder peak around 480 nm corresponds to excitation of Fe-Fe pair[40]. Similar spectrum is observed for the autoclaved Fe_3O_4 NPs [Fig. 2(b)]. The higher absorption for autoclaved NPs for the same concentration may be due to increase in particle size of the NPs on hydrothermal treatment.

On encapsulation of the Fe_3O_4 NPs with carbon and silica shells, the scattering from the NPs increases due to increase in particle size[41]. Importantly, this increase in scattering is specific to wavelength range of 500-900 nm. On contrary, the absorption at lower wavelengths suppresses due to capping of the Fe_3O_4 NPs. Such crossover in absorption spectra for the same concentration suggests surface modification of Fe_3O_4 NPs. For carbon capped Fe_3O_4 NPs, the characteristic spectrum from Fe_3O_4 NPs is retained [Fig. 2(c)] but the partial suppression of the absorption intensity suggests capping of the Fe_3O_4 NPs with thin layer of carbon. On capping of Fe_3O_4 NPs with silica, absence of characteristic absorption from Fe_3O_4 NPs (200-450 nm) can be seen[42, 43] [Fig. 2(d)]. This suggests complete coverage of Fe_3O_4 NPs with thick shell of silica, which increases over all scattering from the NPs while on contrary it completely suppresses the absorption from Fe_3O_4 NPs.

c) X-ray Diffraction Studies of Fe_3O_4 NPs and Nanostructured Iron Oxide Films

Fig. 3(a) shows XRD pattern of bare Fe_3O_4 NPs. The diffraction peaks obtained correspond to cubic spinel structure of Fe_3O_4[44, 45]. The average particle diameter of 10.6 nm calculated using Debye-Scherrer formula (from the most intense peak at 2□ = 35.57°) is in agreement with the particle size determined by statistical analysis of the TEM images, indicating that each individual particle is a single crystal[46].

Fig. 3(b) and 3(c) show XRD spectra of iron oxide films prepared from Fe_3O_4 NPs and Fe_3O_4 NPs (autoclaved), respectively. The diffraction peaks of films match with the α-Fe_2O_3 [JCPDS file - 890599-96]. Inspite of Fe_3O_4 NPs being starting material for the film deposition, the XRD spectra obtained from the deposited film corresponds to that of α-Fe_2O_3. This change of phase can be ascribed to oxidation of NPs during electrophoretic deposition in water-methanol mixture. The hydroxyl (OH) groups resulting from the dissociation of water and methanol molecules get adsorbed on the surface of magnetite NPs and catalyze their oxidation process[47]. In addition, the application of potential above the oxidation potential of Fe^{2+} (i.e. 0.77 V) results in the modified nucleation rate (kinetics), enhanced diffusion of species and gradient of the lattice constant, which drive the nucleation of α-Fe_2O_3 NPs[47, 48]. Also, as we have mentioned in the manuscript that uncapped Fe_3O_4 NPs undergo rapid agglomeration during deposition and their large size favor the oxidation to hematite over magnetite[49]. To the best of our knowledge, change in phase of Fe_3O_4 NPs obtained during electrophoretic deposition occurring in such short span of time (30 s) has not been reported in literature.

To control this oxidation step, Fe_3O_4 NPs have been encapsulated with organic carbon shell and inorganic silica shell as mentioned in the preceding section. Fig. 3(d) and 3(e) show XRD spectra of films obtained from Fe_3O_4@C NPs and Fe_3O_4@SiO_2 NPs, respectively. Diffraction peaks obtained from the films of encapsulated NPs match with Fe_3O_4 (with slight

shift), indicating that no oxidation occurs during deposition of films on capping Fe_3O_4 NPs with organic and inorganic shell. After capping, the surface of Fe_3O_4 NPs has been passivated which circumvent the adsorption of hydroxyl groups onto their surface and thus prevent their phase change. Thus, an additional oxidation step during electrophoretic deposition of Fe_3O_4 NPs can be circumvented using surface passivation.

d) X-ray Photoelectron Studies of α-Fe_2O_3 and Fe_3O_4@C films

To further confirm the phase of NPs before and after electrophoretic deposition, XPS core level spectra of α-Fe_2O_3 and Fe_3O_4@C films have been acquired for Fe 2p and the deconvoluted Fe 2p3/2 spectra are shown in Fig. 4. Background subtraction and peak fitting of the spectra have been done using Shirley function and Gaussian function, respectively and the spectra have been referenced to C 1s main peak at 284.6 eV. Considerable difference can be seen in the two spectra for α-Fe_2O_3 and Fe_3O_4@C films.

Fig. 4(a) shows the deconvoluted XPS Fe $2p_{3/2}$ spectra of α-Fe_2O_3 film. The peak fitting of spectra reveals that Fe^{2+} and Fe^{3+} ions are present in the ratio of 1:6.7. This shows that the film majorly contains Fe_2O_3 with traces of Fe_3O_4, which suggests *in-situ* oxidation of uncapped Fe_3O_4 NPs during electrophoretic deposition. However, the deconvolution and peak fitting of Fe $2p_{3/2}$ spectra obtained for Fe_3O_4@C film reveals that the ratio of Fe^{2+} and Fe^{3+} ions is 1:2 [Fig. 4(b)]. This shows that Fe_3O_4 NPs retain their phase on encapsulation with carbon and the film consists of Fe_3O_4 NPs. Thus, surface passivation restricts the *in-situ* oxidation of Fe_3O_4 NPs during electrophoretic deposition. Presence of metal Fe has also been noticed in Fe_3O_4@C film while hydrated Fe is present in both the films as expected[50, 51].

e) FTIR Studies of Nanostructured Iron Oxide Films

Fig. 5 shows the transmittance spectra of nanostructured iron oxide films. In case of α-Fe_2O_3 NPs film [Fig. 5(a), 5(b)] (obtained from Fe_3O_4 NPs and Fe_3O_4 NPs (autoclaved), respectively), the peak seen at 566 cm^{-1} corresponds to the vibrations of Fe-O[19]. However, on capping of Fe_3O_4 NPs with carbon and silica, the Fe-O vibration peak at 566 cm^{-1} disappears and two additional peaks at 649 cm^{-1} and 465 cm^{-1} [Fig. 5(c), 5(d)] have been obtained.

In case of carbon capped Fe_3O_4 NPs [Fig. 5(c)], peak at 2934 cm^{-1} refers to the C-H stretching vibrations, peak at 1416 cm^{-1} refers to the C-H bending vibrations and peak at 1066 cm^{-1} refers to the C-O stretching vibrations. All these peaks indicate the presence of aliquots of fructose, since fructose molecules present in hydrated state are unlikely to decompose completely[52-54] but as a convention adopted by previous reports, we label these nanoparticles as carbon capped Fe_3O_4 NPs[23, 29].

In case of silica capped Fe_3O_4 NPs [Fig. 5(d)], sharp peak at 1118 cm^{-1} corresponds to characteristic Si-O vibrations, revealing capping of the Fe_3O_4 NPs with silica[55, 56]. The broad band found at 3300-3400 cm^{-1} and peak at 1602 cm^{-1} present in all the films correspond to the O-H stretching mode and H-O-H bending mode, respectively, indicating presence of the interstitial water molecules in the films[44].

f) Morphological Studies of Nanostructured Iron Oxide Films and Bioelectrodes

Fig. 6 shows the SEM micrographs of the nanostructured iron oxide films. It can be seen that the α-Fe_2O_3 films obtained from Fe_3O_4 NPs and Fe_3O_4 NPs (autoclaved) has an average particle size of 300 nm and 200 nm, respectively [Fig. 6(a), 6(b)]. The observed increase in particle size and deformation in shape indicate agglomeration of the uncapped NPs on deposition. The agglomeration is more prominent for the as-prepared Fe_3O_4 NPs owing to their surface

roughness. The electrical double layer gradient is maximum at the edges of the NPs which result in the electrostatic attraction of the NPs and the growth in their size[57]. However, due to removal of edges and surface smoothening of the NPs on hydrothermal treatment, autoclaved NPs undergo reduced aggregation.

On capping of Fe_3O_4 NPs with carbon and silica, the agglomeration has been further restricted. The radical decrease of average particle size to 100 nm [Fig. 6(c)] and 160 nm [Fig. 6(d)] is observed in case of carbon capped NPs and silica capped NPs, respectively. Also, the capped NPs retain their initial spherical shape on deposition as compared to the film of uncapped NPs. The reduction in size and retention of spherical shape indicate considerable decrease in agglomeration of NPs on capping. Further, the immobilization of the cholesterol oxidase onto nanostructured iron oxide films has been confirmed using SEM [Figure S1, supplementary information]. The change in morphology from dense uniform distribution of NPs in the nanoscale to the globular structure of ChOx in the micron scale is attributed to physical adsorption of ChOx molecules onto nanostructured iron oxide films[58].

g) Biocompatibility of Fe_3O_4@C and α-Fe_2O_3 Films

The biocompatibility of Fe_3O_4@C and α-Fe_2O_3 films have been investigated using bacterial system i.e. gram positive (Bacillus sp.) and gram negative (Providencia sp.) bacteria. Two methods have been utilized to examine the biocompatibility of nanostructured iron oxide films. Firstly, cultures of gram positive and gram negative bacteria are spread on nutrient agar plates and Fe_3O_4@C and α-Fe_2O_3 films are kept on these plates under optimum growth conditions (28 °C & 150 rpm). No zone of inhibition is observed for nanostructured iron oxide films. Secondly, the side arm flasks are prepared with nutrient broth and both the bacteria are inoculated. Films

are kept in the nutrient broth and grown under optimum conditions (28 °C & 150 rpm). Colorimetric readings recorded at interval of 2 h are summarized in Table I, which clearly indicates the biocompatibility of Fe_3O_4@C and α-Fe_2O_3 films as the optical density of gram positive and gram negative bacteria increases with time in presence of nanostructured iron oxide films.

h) Electrochemical Characterization of ChOx Immobilized Iron Oxide Electrodes

i) ChOx/Fe_3O_4@C film/ITO Bioelectrode

Fig. 7(a) shows the cyclic voltammograms of ITO electrode, Fe_3O_4@C film/ITO electrode and ChOx/Fe_3O_4@C film/ITO bioelectrode in the potential range of -0.7 V to +0.7 V at scan rate of 30 mV/s. The decrease in anodic peak current obtained for Fe_3O_4@C film/ITO electrode [Fig. 7(a) (ii)] compared to that of the ITO electrode [Fig. 7(a) (i)] reveals formation of the layer of Fe_3O_4@C NPs on the ITO surface. Further, increase in oxidation current obtained for ChOx/Fe_3O_4@C film/ITO bioelectrode [Fig. 7(a) (iii)] compared to that of the Fe_3O_4@C film/ITO electrode [Fig. 7(a) (ii)] is attributed to the electron transfer facilitated by redox moieties at the active sites (FAD centres) of the enzyme at the electrode surface.

Fig. 7(b) shows the Nyquist plots obtained for ITO electrode, Fe_3O_4@C film/ITO electrode and ChOx/Fe_3O_4@C film/ITO bioelectrode. The increased R_{ct} value of 1.35 kΩ for Fe_3O_4@C film/ITO electrode [Fig. 7(b) (ii)] compared to the R_{ct} value of 0.28 kΩ for ITO electrode [Fig. 7(b) (i)] indicates formation of the Fe_3O_4@C NPs layer on the ITO surface. The presence of Fe_3O_4@C NPs layer impedes the flow of electrons resulting in an increased value of R_{ct}. Further, decrease in R_{ct} value from 1.35 kΩ for Fe_3O_4@C film/ITO electrode to 1.18 kΩ for ChOx/Fe_3O_4@C film/ITO bioelectrode [Fig. 7(b) (iii)] reveals the ChOx immobilization onto

Fe_3O_4@C film/ITO electrode. This decrease in R_{ct} value is ascribed to the facile electron transfer aided by the redox moieties of the enzyme at the electrode surface.

According to Laviron's theory, the slope of the linear curve between the anodic peak potential and the logarithm of scan rate represents RT/αnF (α- transfer coefficient). This can be used to calculate the surface concentration of the ionic species of the bioelectrodes using the following equation:

$$i_p = n^2F^2\nu CA\,(4RT)^{-1} \quad \ldots \text{Eq.1}$$

where, i_p/ν can be calculated from the i_p Vs. ν plot[58] (i_p- anodic peak current; ν- scan rate).

The slope of the linear plot of anodic peak potential vs. logarithm of scan rate for ChOx/Fe_3O_4@C film/ITO bioelectrode gives RT/αnF = 0.23. Using Eq.1, the surface concentration on the ChOx/Fe_3O_4@C film/ITO bioelectrode has been found to be as 2.52×10^{-11} molcm^{-2}.

ii) ChOx/α-Fe_2O_3 film/ITO Bioelectrode

Fig. 7(c) shows the cyclic voltammograms obtained for ITO electrode, α-Fe_2O_3 film/ITO electrode and ChOx/α-Fe_2O_3 film/ITO bioelectrode in the potential range of -0.7 V to +0.7 V at scan rate of 30 mVs^{-1}. The oxidation peak seen at 0.38 V is attributed to the oxidation of the redox couple, $K_3/K_4[Fe(CN)_6]$ present in the buffer[58]. The decrease in the oxidation current obtained for α-Fe_2O_3 film/ITO electrode [Fig. 7(c) (ii)] compared to that of the ITO electrode [Fig. 7(c) (i)] indicates formation of the layer of α-Fe_2O_3 NPs onto the ITO surface. Further, increase in oxidation current obtained for ChOx/α-Fe_2O_3 film/ITO bioelectrode [Fig. 7(c) (iii)] compared to that of the α-Fe_2O_3 film/ITO electrode [Fig. 7(c) (ii)] is attributed to the presence of redox moieties at active sites (FAD centres) of the enzyme leading to fast electron transfer between the enzyme and the electrode surface[37].

Fig. 7(d) shows the Nyquist plots obtained for ITO electrode, α-Fe_2O_3 film/ITO electrode and ChOx/α-Fe_2O_3 film/ITO bioelectrode. The increased R_{ct} (charge transfer resistance) value of 1.14 kΩ obtained for α-Fe_2O_3 film/ITO electrode [Fig. 7(d) (ii)] compared to the R_{ct} value of 0.28 kΩ for ITO electrode [Fig. 7(d) (i)] is attributed to the formation of layer of α-Fe_2O_3 NPs on the ITO surface. Formation of α-Fe_2O_3 NPs layer results in decreased interfacial electron transfer, thereby causing increase in the R_{ct} value. Further, observed decrease in R_{ct} value from 1.14 kΩ for α-Fe_2O_3 film/ITO electrode [Fig. 7(d) (ii)] to 0.82 kΩ for ChOx/α-Fe_2O_3 film/ITO bioelectrode [Fig. 7(d) (iii)] is attributed to facile electron transfer mediated by the redox centres of the enzyme.

The surface concentration of the ionic species on the ChOx/α-Fe_2O_3 film/ITO bioelectrode has been found to be as 1.81×10^{-11} molcm^{-2} (using RT/αnF = 0.16). The higher concentration of ionic species on ChOx/Fe_3O_4@C film/ITO bioelectrode compared to the ChOx/α-Fe_2O_3 film/ITO bioelectrode is attributed to that of the larger surface area provided by the Fe_3O_4@C nanocrystalline film owing to the smaller particle size of NPs as compared to α-Fe_2O_3 nanocrystalline film for enzyme immobilization.

i) Electrochemical Response of ChOx Immobilized Iron Oxide Electrodes

i) ChOx/ Fe_3O_4@C film/ITO Bioelectrode

Fig. 8(a) shows response of the ChOx/Fe_3O_4@C film/ITO bioelectrode obtained as a function of cholesterol concentration using cyclic voltammetry. The bioelectrode exhibits the response time of 60 s [Figure S4(a)]. The anodic peak current of ChOx/Fe_3O_4@C film/ITO bioelectrode plotted as a function of cholesterol concentration [Fig. 9(a)] reveals the linearity range as 25-500 mgdl^{-1} with standard deviation and correlation coefficient of 4.82 μA and 0.99, respectively. The

sensitivity of the ChOx/Fe_3O_4@C film/ITO bioelectrode exhibited by the slope of linear regression curve is 193 $nAmg^{-1}dlcm^{-2}$. The value of Michaelis-Menten constant of ChOx immobilized Fe_3O_4@C film has been found to be as 1.44 $mgdl^{-1}$.

The Nyquist plots for the ChOx/Fe_3O_4@C film/ITO bioelectrode as a function of cholesterol concentration have been investigated to obtain impedimetric response of the biosensor [Fig. 8(b)]. The linear calibration curve obtained by plotting the R_{ct} value for ChOx/Fe_3O_4@C film/ITO bioelectrode as a function of cholesterol concentration [Fig. 10(a)] reveals linearity range of 25-500 $mgdl^{-1}$ with standard deviation and regression coefficient of 0.02 kΩ and 0.99, respectively. The sensitivity of 0.90 $\Omega mg^{-1}dlcm^{-2}$ is obtained from the slope of the linear regression curve of ChOx/Fe_3O_4@C film/ITO bioelectrode.

The shelf life and reproducibility of the ChOx/Fe_3O_4@C film/ITO bioelectrode have been investigated using cyclic voltammetry. The activity of the bioelectrode is monitored at regular interval of seven days. The bioelectrode exhibits only 6% reduction in peak current after 10 weeks for 100 $mgdl^{-1}$ cholesterol concentration when stored at 4°C [Fig. S2(a)]. The reproducibility of the sensing parameters of the bioelectrode has been studied with cholesterol concentration of 25 $mgdl^{-1}$ and it has been found that the bioelectrode can be used upto 25 times without significant decrease (40 μA) of the response signal [Fig. S3(a)].

ii) ChOx/α-Fe_2O_3 film/ITO Bioelectrode

Fig. 8(c) shows the response of the ChOx/α-Fe_2O_3 film/ITO bioelectrode obtained as a function of cholesterol concentration using cyclic voltammetric technique. The response time of this electrode is found to be 60 s [Fig. S4(b)]. The magnitude of amperometric current of ChOx/α-Fe_2O_3 film/ITO bioelectrode plotted as a function of cholesterol concentration [Fig. 9(b)] shows linearity in the range 25-500 $mgdl^{-1}$ with standard deviation and correlation coefficient of 4.52

μA and 0.99, respectively. The sensitivity of the ChOx/α-Fe_2O_3 film/ITO bioelectrode exhibited by the slope of linear calibration curve is found to be as 218 $nAmg^{-1}dlcm^{-2}$. The value of Michaelis-Menten constant of ChOx immobilized α-Fe_2O_3 film has been found to be as 1.46 $mgdl^{-1}$.

The electrochemical impedimetric response of the ChOx/α-Fe_2O_3 film/ITO bioelectrode has been investigated as a function of cholesterol concentration using Nyquist plots [Fig. 8(d)]. The linear calibration curve obtained by plotting the R_{ct} values for ChOx/α-Fe_2O_3 film/ITO bioelectrode as a function of cholesterol concentration [Fig. 10(b)] reveals the linearity range of 50-500 $mgdl^{-1}$ with standard deviation and regression coefficient of 0.02 kΩ and 0.97, respectively. The value of sensitivity exhibited by the slope of the linear regression curve for ChOx/α-Fe_2O_3 film/ITO bioelectrode is 0.42 $\Omega mg^{-1}dlcm^{-2}$.

The shelf-life of the ChOx/α-Fe_2O_3 film/ITO bioelectrode has been investigated for 100 $mgdl^{-1}$ cholesterol concentration using cyclic voltammetry. The bioelectrode exhibits 6% decrease in the peak current for first 8 weeks but sudden decrease in the signal has been observed afterwards and the current reduced by 11.5% after 10 weeks [Fig. S2(b)]. The ChOx/α-Fe_2O_3 film/ITO bioelectrode can be used upto 20 times with insignificant loss (66 μA) of the signal [Fig. S3(b)].

Table II Comparison table summarizing characteristics of the cholesterol biosensors based on nanostructured metal oxide films.

Conclusions

The nanocrystals of Fe_3O_4 with average particle diameter of 10 nm have been synthesized. The electrophoretic deposition of bare Fe_3O_4 NPs in methanol-water mixture results in oxidation and phase transformation of NPs and film of α-Fe_2O_3 NPs has been obtained. The phase transformation of Fe_3O_4 NPs can be circumvented using surface passivation of Fe_3O_4 NPs with organic carbon shell and inorganic silica shell. Encapsulation of Fe_3O_4 NPs restricts agglomeration of NPs during film deposition and retains high surface to volume ratio for enzyme loading. Due to the non-conducting nature of silica, Fe_3O_4@SiO_2 NPs shows poor electrochemical response. However, these can be utilized for applications in drug delivery[21], biocatalysis and bioseparations[20, 59], magnetic resonance imaging[60], determination of metal ion concentration[61] etc. Growth of gram positive and gram negative bacteria in contact with Fe_3O_4@C and α-Fe_2O_3 films reveals biocompatible nature of nanostructures that is suitable for prolonged activity of enzymes and thus stability of biosensors. The fabricated cholesterol biosensors employing Fe_3O_4@C and α-Fe_2O_3 nanocrystalline films show sensitivities of 193 $nAmg^{-1}dlcm^{-2}$ and 218 $nAmg^{-1}dlcm^{-2}$, respectively, from cyclic voltammetric studies and sensitivities of 0.42 $\Omega mg^{-1}dlcm^{-}2$ and 0.90 $\Omega mg^{-1}dlcm^{-2}$, respectively, from electrochemical impedance spectroscopic studies. The low values of Michaelis-Menten constant reveal the enhanced enzymatic activity of ChOx onto nanostructured iron oxide films. The comparable sensitivities for biosensors obtained using Fe_3O_4@C and α-Fe_2O_3 NPs suggest that encapsulation of Fe_3O_4 NPs with carbon do not significantly affect electrocatalytic activity of Fe_3O_4 NPs while adds to the stability of the NPs. However, encapsulation of Fe_3O_4 NPs with conjugated carbon molecules, conducting polymers like polypyrrole, polyaniline etc may result in improved sensitivity of the biosensor.

Supplementary Information

SEM studies showing the immobilization of cholesterol oxidase onto nanostructured iron oxide films, shelf life, reproducibility and response time studies of the fabricated cholesterol biosensors.

Acknowledgment

We thank Prof. R. C. Budhani, Director, National Physical Laboratory, New Delhi, India for providing facilities. R. S. is thankful to the UGC-CSIR for award of Junior Research Fellowship. Authors thank Dr. K. N. Sood, NPL for SEM measurements, Dr. S. M. Shivprasad, JNCASR for XPS measurements and Dr. Kavita Arora, JNU for TEM studies. Financial support received from the Department of Science and Technology (DST) centre on biomolecular electronics and CSIR Empower projects is sincerely acknowledged. Thanks are due to Dr. Pratima Solanki, C. M. Pandey, Manoj Patel and all the members of the Biomedical Instrumentation Section, NPL, for discussions.

References

1. S. Chou, *J. Appl. Phys.*, 1994, **76**, 6673.
2. D. Schaadt, *J. Vac. Sci. Technol. A*, 2000, **18**, 1834.
3. K. Mosbach and L. Andersson, *Nature*, 1977, **270**, 259-261.
4. D. K. Yi, S. S. Lee and J. Y. Ying, *Chem. Mater.*, 2006, **18**, 2459-2461.
5. C. B. Catherine and S. G. C. Adam, *J. Phys. D: Appl. Phys.*, 2003, **36**, R198.
6. E. Amstad, M. Textor and E. Reimhult, *Nanoscale*, **3**, 2819-2843.
7. S. Laurent, D. Forge, M. Port, A. Roch, C. Robic, L. Vander Elst and R. N. Muller, *Chem. Rev.*, 2008, **108**, 2064-2110.
8. T. Osaka, T. Matsunaga, T. Nakanishi, A. Arakaki, D. Niwa and H. Iida, *Anal. Bioanal. Chem.*, 2006, **384**, 593-600.
9. R. Weissleder, H.-C. Cheng, A. Bogdanova and A. Bogdanov, *J. Magn. Reson. Imaging*, 1997, **7**, 258-263.
10. F. Cengelli, D. Maysinger, F. Tschudi-Monnet, X. Montet, C. Corot, A. Petri-Fink, H. Hofmann and L. Juillerat-Jeanneret, *J. Pharmacol. Exp. Ther.*, 2006, **318**, 108-116.

11. F. Sonvico, S. p. Mornet, S. b. Vasseur, C. Dubernet, D. Jaillard, J. Degrouard, J. Hoebeke, E. Duguet, P. Colombo and P. Couvreur, *Bioconjugate Chem.*, 2005, **16**, 1181-1188.
12. M. Mahmoudi, A. Simchi, M. Imani and U. O. Halfeli, *J. Phys. Chem. C*, 2009, **113**, 8124-8131.
13. A. Petri-Fink, M. Chastellain, L. Juillerat-Jeanneret, A. Ferrari and H. Hofmann, *Biomaterials*, 2005, **26**, 2685-2694.
14. A. K. Gupta and S. Wells, *IEEE T. Nanobiosci.*, 2004, **3**.
15. J. Li, R. Yuan and Y. Chai, *Microchim. Acta*, **173**, 369-374.
16. J. Wang, Z. Zhu, A. Munir and H. S. Zhou, *Talanta*, **84**, 783-788.
17. H. Li, Q. Wei, J. He, T. Li, Y. Zhao, Y. Cai, B. Du, Z. Qian and M. Yang, *Biosens. Bioelectron.*, **26**, 3590-3595.
18. I. M. Hsing, Y. Xu and W. Zhao, *Electroanalysis*, 2007, **19**, 755-768.
19. G. Zhao, J. J. Feng, Q. L. Zhang, S. P. Li and H. Y. Chen, *Chem. Mater.*, 2005, **17**, 3154-3159.
20. H.-H. Yang, S.-Q. Zhang, X.-L. Chen, Z.-X. Zhuang, J.-G. Xu and X.-R. Wang, *Anal. Chem.*, 2004, **76**, 1316-1321.
21. K. Souza, J. Ardisson and E. Sousa, *J. Mater. Sci.- Mater. M.*, 2009, **20**, 507-512.
22. T. Sen, A. Sebastianelli and I. J. Bruce, *J. Am. Chem. Soc.*, 2006, **128**, 7130-7131.
23. W. Xian-Wen, Z. Guo-Xing, X. Chuan-Jun and Y. Yin, *Nanotechnology*, 2006, **17**, 4307.
24. I. Zhitomirsky, *J. Mater. Sci.*, 2006, **41**, 8186-8195.
25. L. Besra and M. Liu, *Prog. Mater Sci.*, 2007, **52**, 1-61.
26. Y. S. Kang, S. Risbud, J. F. Rabolt and P. Stroeve, *Chem. Mater.*, 1996, **8**, 2209-2211.
27. T. J. Daou, G. Pourroy, S. Begin-Colin, J. M. Greneche, C. Ulhaq-Bouillet, P. Legare, P. Bernhardt, C. Leuvrey and G. Rogez, *Chem. Mater.*, 2006, **18**, 4399-4404.
28. Y. Li, T. Leng, H. Lin, C. Deng, X. Xu, N. Yao, P. Yang and X. Zhang, *J. Proteome Res.*, 2007, **6**, 4498-4510.
29. X. Shouhu, H. Lingyun, J. Wanquan, G. Xinglong, H. Yuan and C. Zuyao, *Nanotechnology*, 2007, **18**, 035602.
30. J. Li and C.-y. Liu, *New J. Chem.*, 2009, **33**, 1474-1477.
31. Y. Lu, Y. Yin, B. T. Mayers and Y. Xia, *Nano Lett.*, 2002, **2**, 183-186.

32. Z. X. Sun, F. W. Su, W. Forsling and P. O. Samskog, *J. Colloid Interface Sci.*, 1998, **197**, 151-159.
33. M. Jarlbring, L. Gunneriusson, B. Hussmann and W. Forsling, *J. Colloid Interface Sci.*, 2005, **285**, 212-217.
34. T. J. Daou, G. Pourroy, J. M. Greneche, A. Bertin, D. Felder-Flesch and S. Begin-Colin, *Dalton T.*, 2009, 4442-4449.
35. M. L. Fisher, M. Colic, M. P. Rao and F. F. Lange, *J. Am. Ceram. Soc.*, 2001, **84**, 713-718.
36. P. R. Solanki, S. K. Arya, S. P. Singh, M. K. Pandey and B. D. Malhotra, *Sensor Actuat. B- Chem.*, 2007, **123**, 829-839.
37. Z. Matharu, G. Sumana, S. K. Arya, S. P. Singh, V. Gupta and B. D. Malhotra, *Langmuir*, 2007, **23**, 13188-13192.
38. L. Yonglan, *Mater. Lett.*, 2007, **61**, 1039-1041.
39. L. Huo, W. Li, L. Lu, H. Cui, S. Xi, J. Wang, B. Zhao, Y. Shen and Z. Lu, *Chem. Mater.*, 2000, **12**, 790-794.
40. T. D. W. David M. Sherman, *Am. Mineral.*, 1985, **70**, 1262-1269.
41. T. A. Egerton and I. R. Tooley, *Int. J. Cosmetic Sci.*, **34**, 117-122.
42. S. L. Westcott, S. J. Oldenburg, T. R. Lee and N. J. Halas, *Langmuir*, 1998, **14**, 5396-5401.
43. Y. Kobayashi, V. Salgueirino-Maceira and L. M. Liz-Marzan, *Chem. Mater.*, 2001, **13**, 1630-1633.
44. K. Tao, H. Dou and K. Sun, *Chem. Mater.*, 2006, **18**, 5273-5278.
45. W. Cai and J. Wan, *J. Colloid Interface Sci.*, 2007, **305**, 366-370.
46. J. Sun, S. Zhou, P. Hou, Y. Yang, J. Weng, X. Li and M. Li, *J. Biomed. Mater. Res. A*, 2007, **80A**, 333-341.
47. O. N. Shebanova and P. Lazor, *Journal of Raman Spectroscopy*, 2003, **34**, 845-852.
48. J. Tang, M. Myers, K. A. Bosnick and L. E. Brus, *The Journal of Physical Chemistry B*, 2003, **107**, 7501-7506.
49. W. Feitknecht and K. J. Gallagher, *Nature*, 1970, **228**, 548-549.
50. J. Morales, L. Sanchez, F. Martin, F. Berry and X. L. Ren, *J. Electrochem. Soc.*, 2005, **152**, A1748-A1754.

51. P. Guardia, J. Perez-Juste, A. Labarta, X. Batlle and L. M. Liz-Marzan, *Chem. Commun.*, **46**, 6108-6110.
52. B. M. Kabyemela, T. Adschiri, R. M. Malaluan and K. Arai, *Ind. Eng. Chem. Res.*, 1999, **38**, 2888-2895.
53. Q. Wang, H. Li, L. Chen and X. Huang, *Carbon*, 2001, **39**, 2211-2214.
54. C. Adina, F. Florinela, T. Abdelmoumen and S. Carmen, *Rom. Biotech. Lett.*, 2010, **15**.
55. A. Azioune, A. Ben Slimane, L. Ait Hamou, A. Pleuvy, M. M. Chehimi, C. Perruchot and S. P. Armes, *Langmuir*, 2004, **20**, 3350-3356.
56. D. Kandpal, S. Kalele and S. Kulkarni, *Pramana*, 2007, **69**, 277-283.
57. P. Pramod, S. T. S. Joseph and K. G. Thomas, *J. Am. Chem. Soc.*, 2007, **129**, 6712-6713.
58. Z. Matharu, P. Pandey, M. K. Pandey, V. Gupta and B. D. Malhotra, *Electroanalysis*, 2009, **21**, 1587-1596.
59. T. Sen, A. Sebastianelli and I. J. Bruce, *J. Am. Chem. Soc.*, 2006, **128**, 7130-7131.
60. J. L. Campbell, J. Arora, S. F. Cowell, A. Garg, P. Eu, S. K. Bhargava and V. Bansal, *PLoS ONE*, **6**, e21857.
61. L. L. Vatta, J. Kramer and K. R. Koch, *Sep. Sci. Technol.*, 2007, **42**, 1985-2002.
62. A. A. Ansari, A. Kaushik, P. R. Solanki and B. D. Malhotra, *Electrochem. Commun.*, 2008, **10**, 1246-1249.
63. A. A. Ansari, A. Kaushik, P. R. Solanki and B. D. Malhotra, *Electroanalysis*, 2009, **21**, 965-972.
64. S. P. Singh, S. K. Arya, P. Pandey, B. D. Malhotra, S. Saha, K. Sreenivas and V. Gupta, *Appl. Phys. Lett.*, 2007, **91**, 063901-063903.
65. P. R. Solanki, A. Kaushik, A. A. Ansari and B. D. Malhotra, *Appl. Phys. Lett.*, 2009, **94**, 143901-143903.
66. G. Kouassi, J. Irudayaraj and G. McCarty, *Journal of Nanobiotechnology*, 2005, **3**, 1.

Tables

Table I Optical density of gram positive (providencia sp.) and gram negative (bacillus sp.) bacteria as a function of time in presence of Fe_3O_4@C and α-Fe_2O_3 films.

Nanostructured film	**Bacteria**	**Optical Density**						
		0 hrs	2 hrs	4 hrs	6 hrs	8 hrs	10 hrs	12 hrs
Fe_3O_4@C film	Providencia sp.	0.01	0.03	0.07	0.15	0.28	0.43	0.56
Fe_3O_4@C film	Bacillus sp.	0.02	0.09	0.24	0.57	0.68	0.73	0.89
α-Fe_2O_3 film	Providencia sp.	0.03	0.06	0.09	0.14	0.19	0.54	0.63
α-Fe_2O_3 film	Bacillus sp.	0.02	0.08	0.26	0.58	0.65	0.82	0.85

Table II Comparison table summarizing characteristics of the cholesterol biosensors based on nanostructured metal oxide films.

Electrode	**Transducer**	**Linear Range ($mgdL^{-1}$)**	**Sensitivity**	**K_m value**	**Response time (s)**	**Reproducibility**	**Shelf life (days)**	**Ref.**
CeO_2/ ITO	Cyclic Voltammetry	10-400	----	2.08 mM	15	----	----	[62]
Chitosan-SnO_2/ ITO	Cyclic Voltammetry	5-400	34.7 $\mu Amg^{-1}dlcm^{-2}$	3.8 mM	5	----	80	[63]
ZnO/ Au	Cyclic Voltammetry	25-400	45.7 $nAmg^{-1}dlcm^{-2}$	2.1 mM	15	----	70	[64]
ZnO/ ITO	Cyclic Voltammetry	5-400	59.0 $nAmg^{-1}dlcm^{-2}$	0.03 mM	10	20	85	[65]
Fe_3O_4 NPs	Spectroscopy	50-200	----	0.45 mM	---	----	10	[66]
Fe_3O_4@C/ ITO	Cyclic Voltammetry Impedance Spectroscopy	25-400	193 $nAmg^{-1}dlcm^{-2}$ 0.90 $\Omega mg^{-1}dlcm^{-2}$	0.03 mM	60	25	70	**Present Work**
α-Fe_2O_3/ ITO	Cyclic Voltammetry Impedance Spectroscopy	50-400	218 $nAmg^{-1}dlcm^{-2}$ 0.42 $\Omega mg^{-1}dlcm^{-2}$	0.04 mM	60	20	56	

Scheme

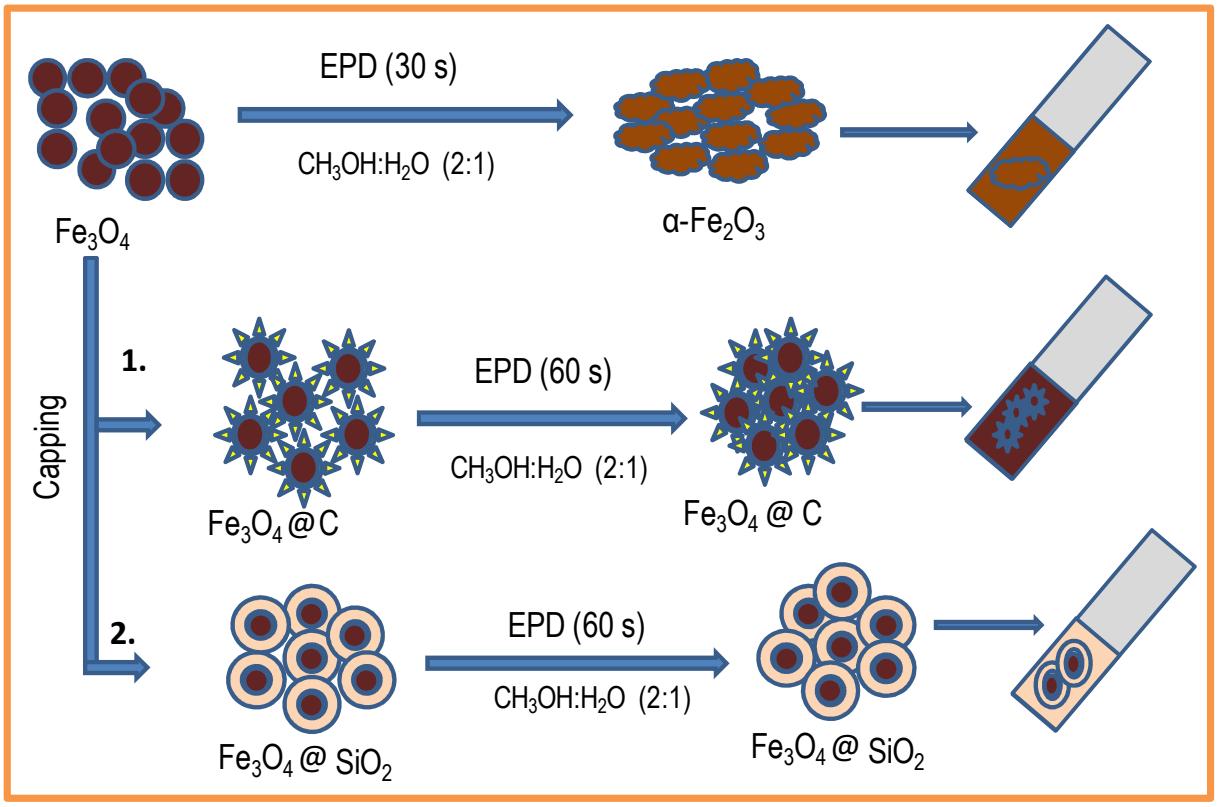

Figure Captions

Fig. 1 TEM micrographs of: (a) Fe_3O_4 NPs; Inset: High-resolution image of a single particle, and; (b) Fe_3O_4 NPs (autoclaved).

Fig. 2 UV-vis absorption spectra of : (a) Fe_3O_4 NPs; (b) Fe_3O_4 NPs (autoclaved); (c) Fe_3O_4@C NPs; (d) Fe_3O_4@SiO_2 NPs.

Fig. 3 XRD spectra of: (a) Fe_3O_4 NPs; (b) film obtained from Fe_3O_4 NPs; (c) film obtained from Fe_3O_4 NPs (autoclaved); (d) film obtained from Fe_3O_4@C NPs; (e) film obtained from Fe_3O_4@ SiO_2 NPs.

Fig. 4 Deconvoluted XPS spectra of Fe $2p_{3/2}$ acquired for: (a) α-Fe_2O_3 film, and; (b) Fe_3O_4@C film.

Fig. 5 FTIR spectra of: (a) α-Fe_2O_3 NPs film obtained from Fe_3O_4 NPs; (b) α-Fe_2O_3 NPs film obtained from Fe_3O_4 NPs (autoclaved); (c) film of Fe_3O_4@C NPs; (d) film of Fe_3O_4@SiO_2 NPs.

Fig. 6 SEM micrograph of: (a) α-Fe_2O_3 NPs film obtained from Fe_3O_4 NPs; (b) α-Fe_2O_3 NPs film obtained from Fe_3O_4 NPs (autoclaved); (c) film of Fe_3O_4@C NPs; (d) film of Fe_3O_4@SiO_2 NPs.

Fig. 7 (a) CV curves for the ITO electrode (i), Fe_3O_4@C film/ITO electrode (ii) and ChOx/ Fe_3O_4@C film/ITO bioelectrode (iii); (b) Nyquist plots for the ITO electrode (i), Fe_3O_4@C film/ITO electrode (ii) and ChOx/Fe_3O_4@C film/ITO bioelectrode (iii); (c) CV curves for the ITO electrode (i), α-Fe_2O_3 film/ITO electrode (ii) and ChOx/α-Fe_2O_3 film/ITO bioelectrode (iii); (d) Nyquist plots for the ITO electrode (i), α-Fe_2O_3 film/ITO electrode (ii) and ChOx/α-Fe_2O_3 film/ITO bioelectrode (iii).

Fig. 8 (a) CV response studies of ChOx/Fe_3O_4@C film/ITO bioelectrode; (b) EIS response studies of ChOx/Fe_3O_4@C film/ITO bioelectrode; (c) CV response studies of ChOx/α-Fe_2O_3 film/ITO bioelectrode and; (d) EIS response studies of ChOx/α-Fe_2O_3 film/ITO bioelectrode with different cholesterol concentrations ($mgdl^{-1}$): (i) 10; (ii) 25; (iii) 50; (iv) 100; (v) 200; (vi) 300; (vii) 400 and (viii) 500.

Fig. 9 Linear calibration plots obtained using CV data for: (a) ChOx/Fe_3O_4@C film/ITO bioelectrode and; (b) ChOx/α-Fe_2O_3 film/ITO bioelectrode.

Fig. 10 Linear calibration plots obtained using EIS data for: (a) ChOx/Fe_3O_4@C film/ITO bioelectrode and; (b) ChOx/α-Fe_2O_3 film/ITO bioelectrode.

Figures

Figure 1

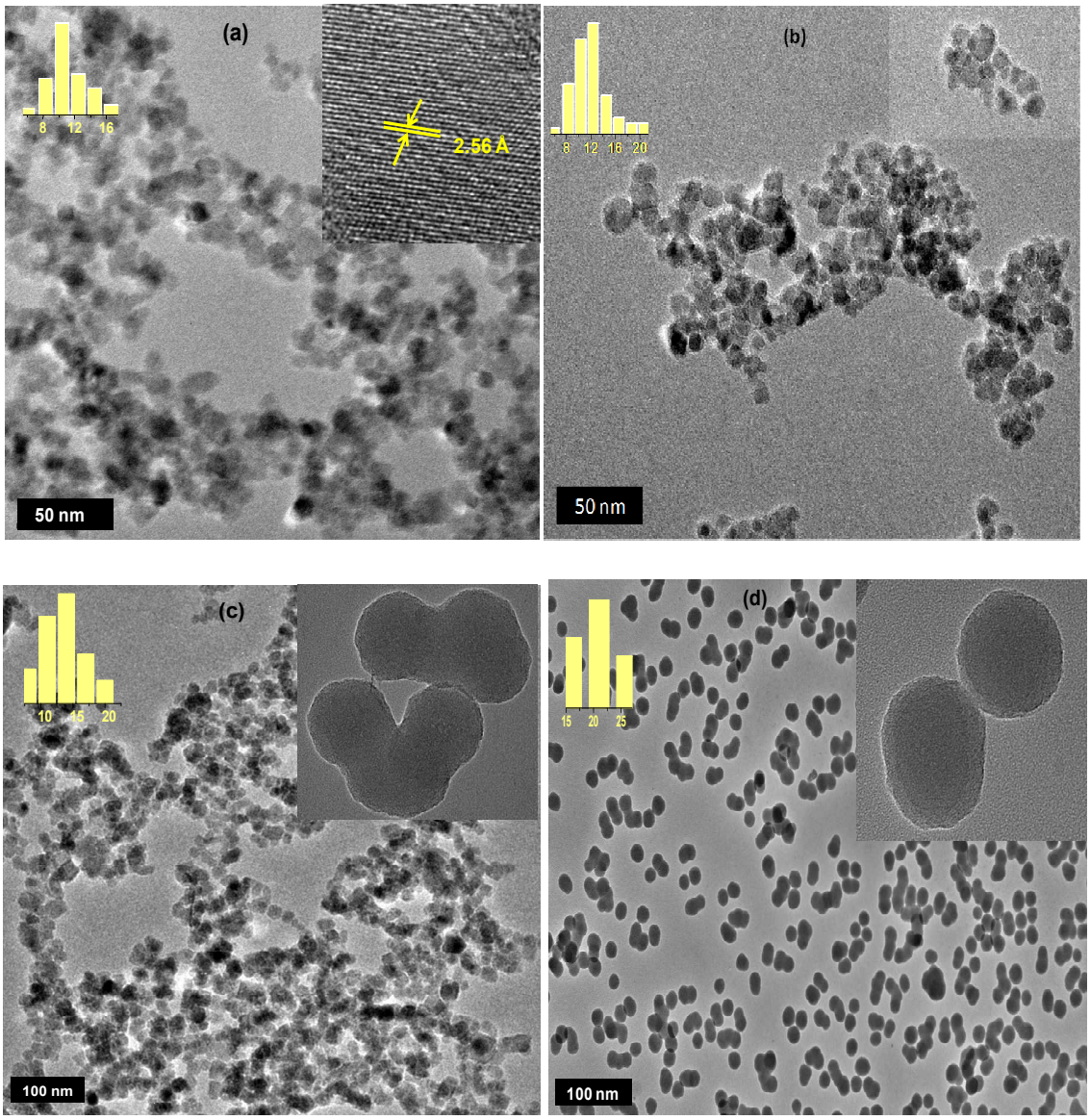

Figure 2

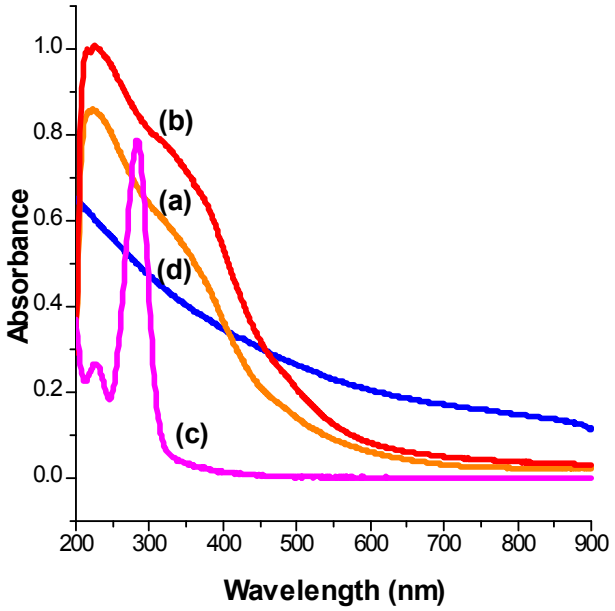

Figure 3

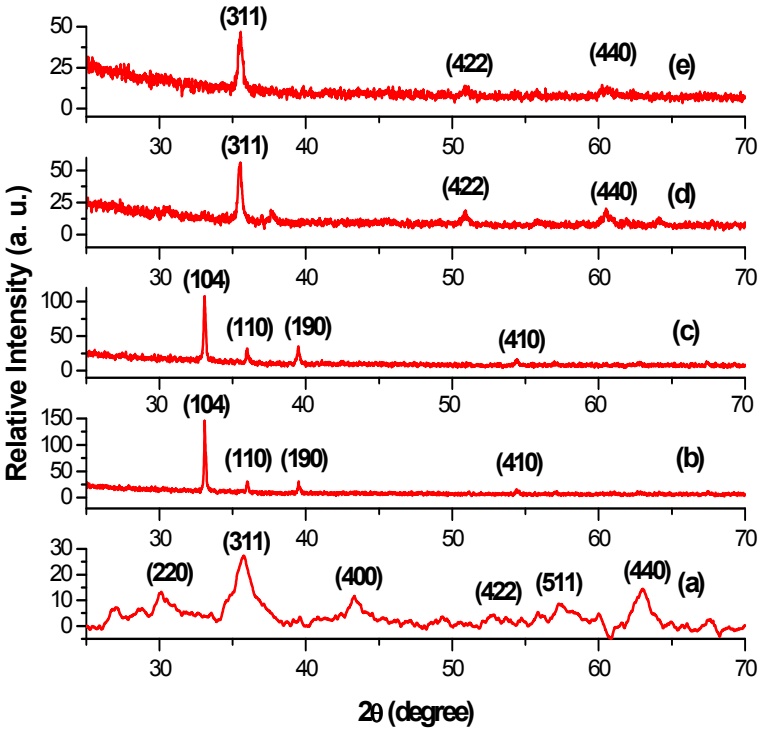

Figure 4

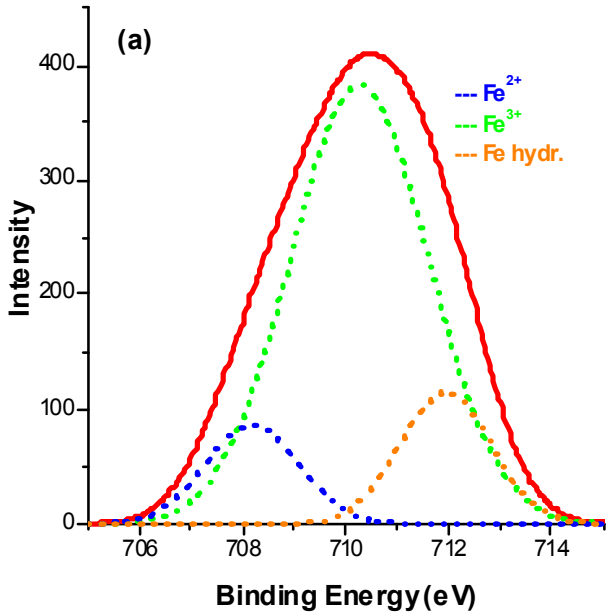

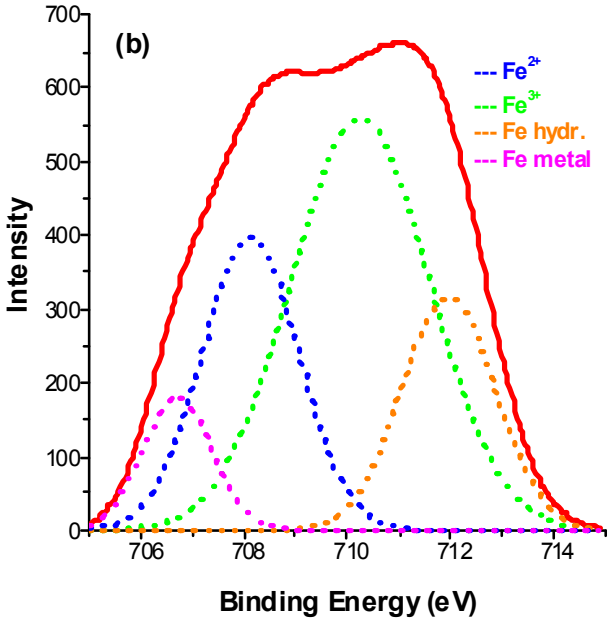

Figure 5

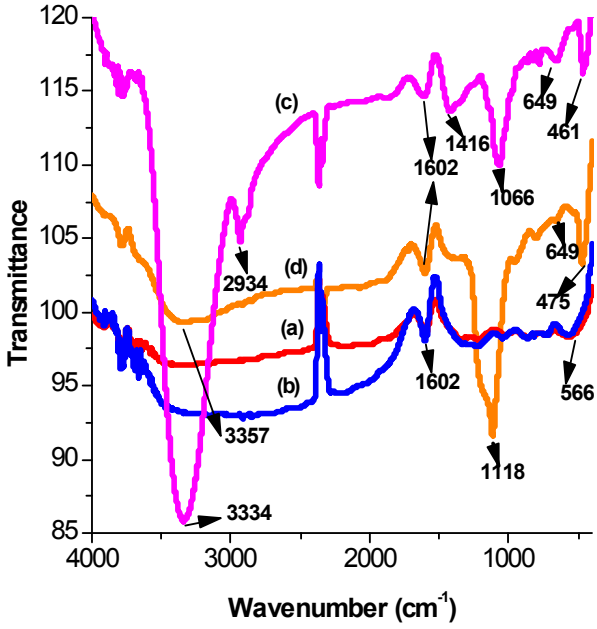

Figure 6

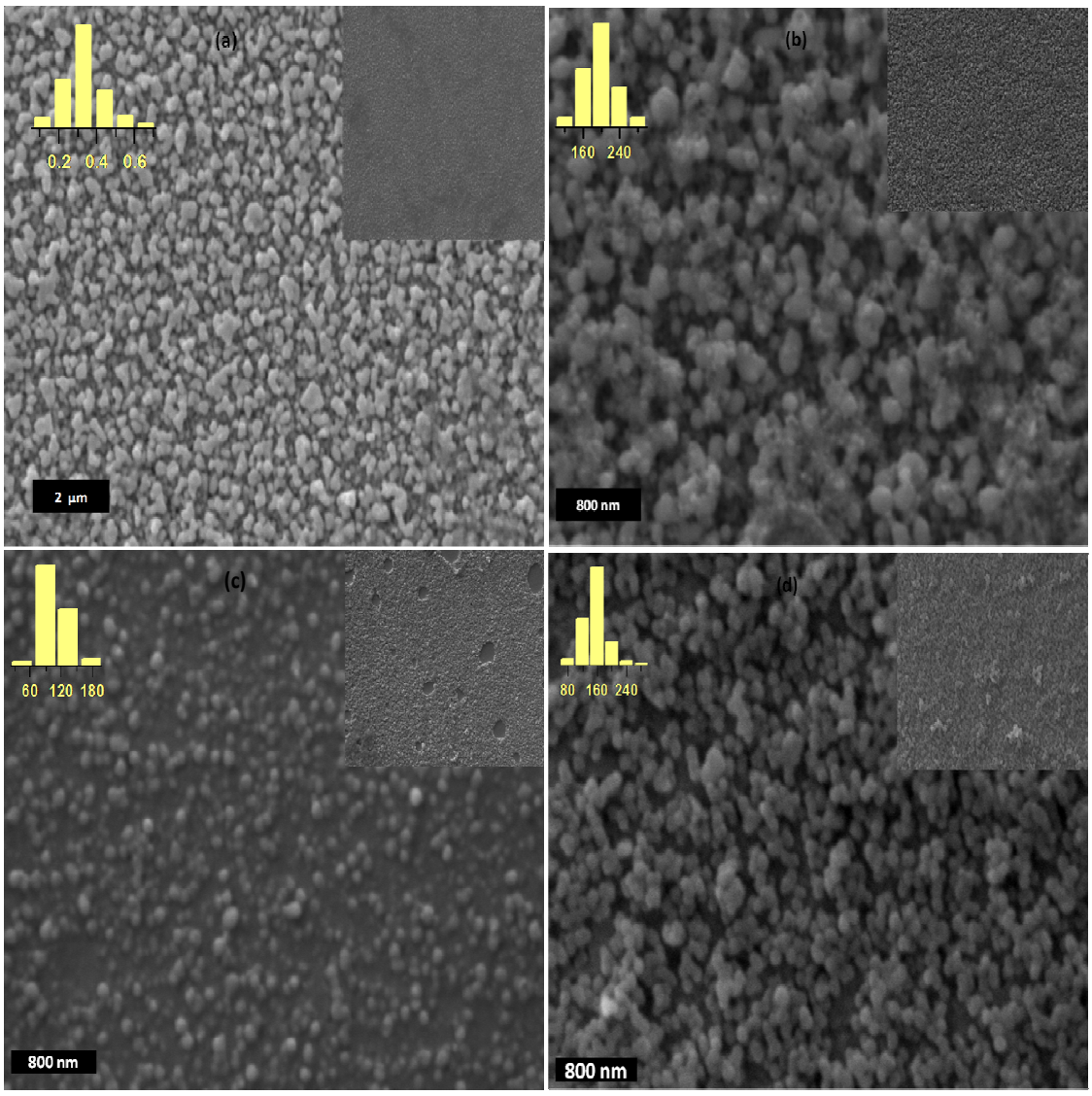

Figure 7

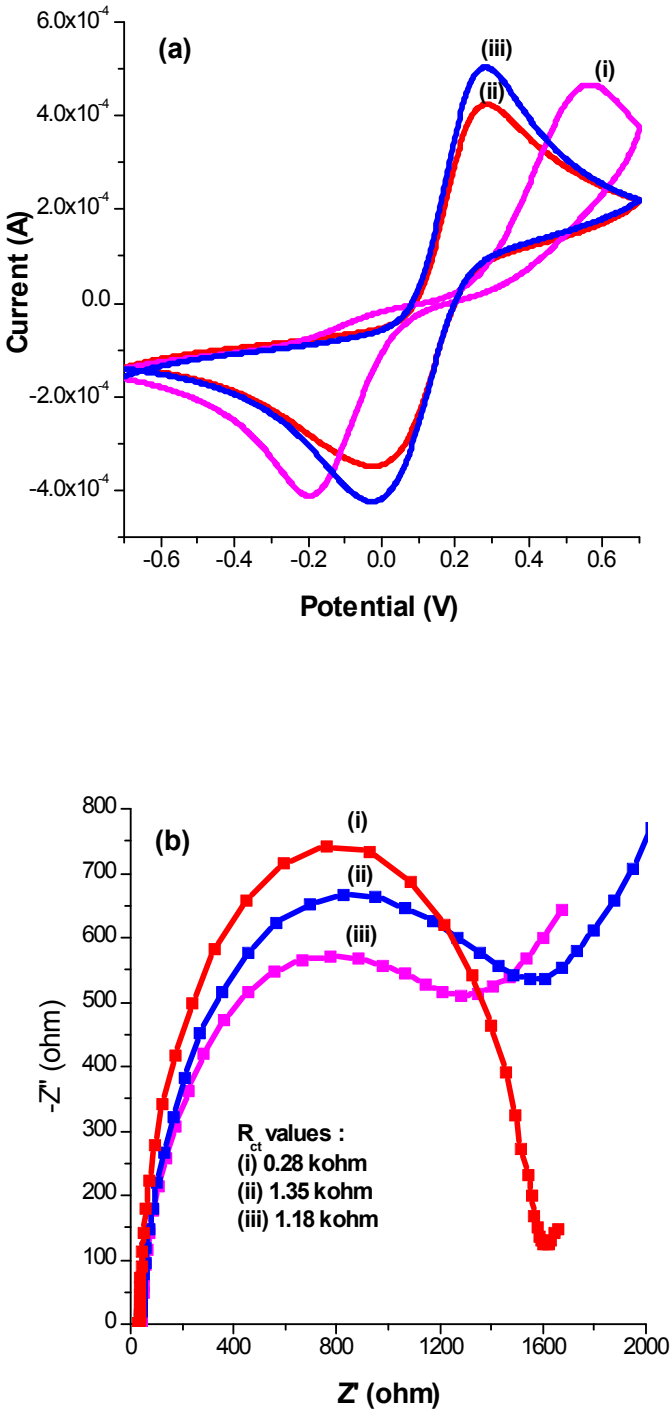

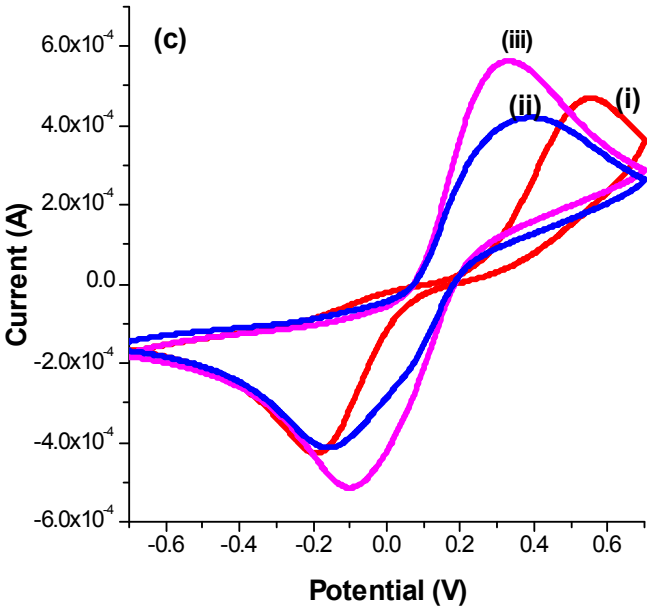

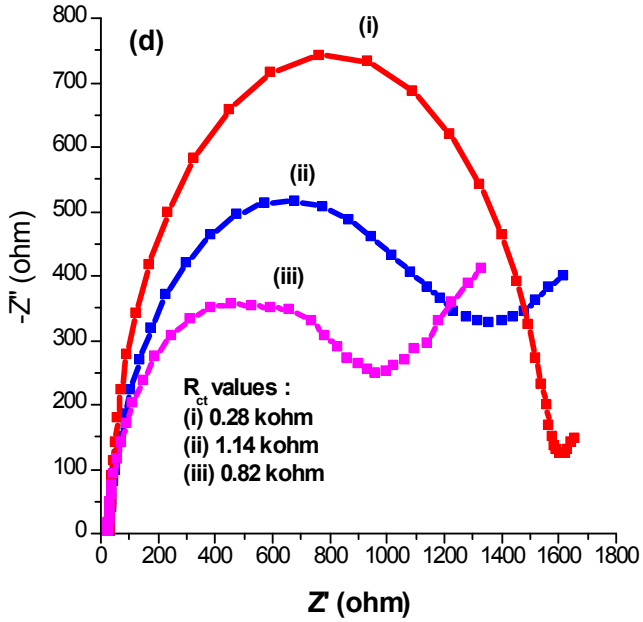

Figure 8

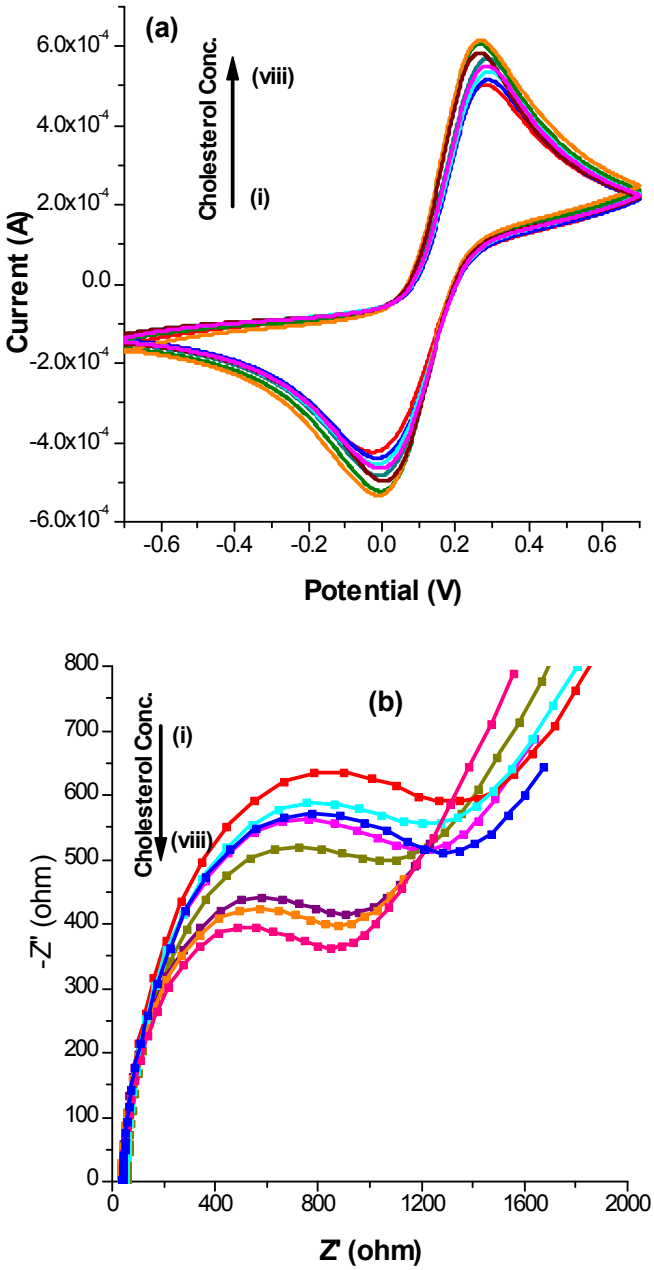

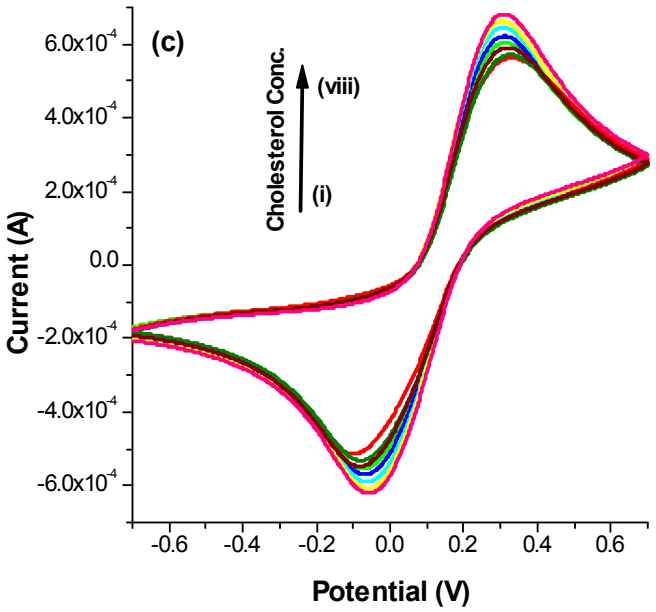

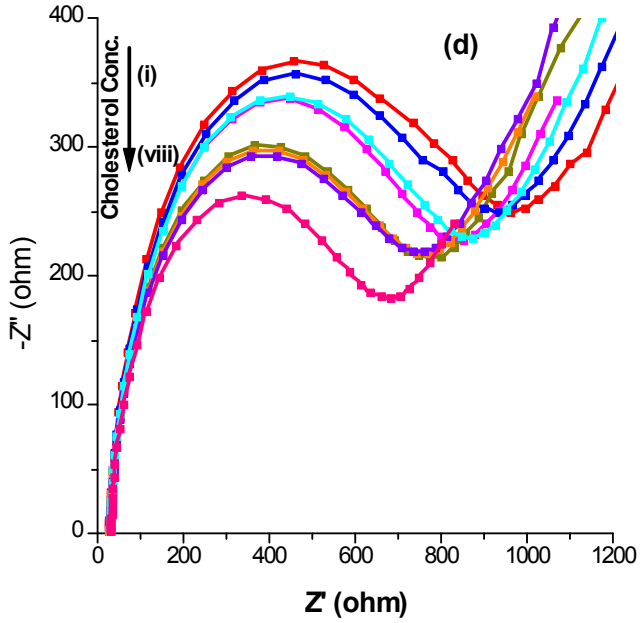

Figure 9

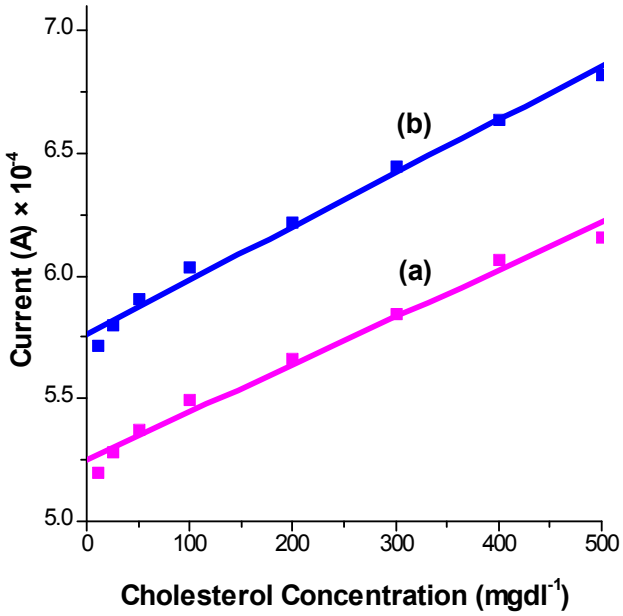

Figure 10

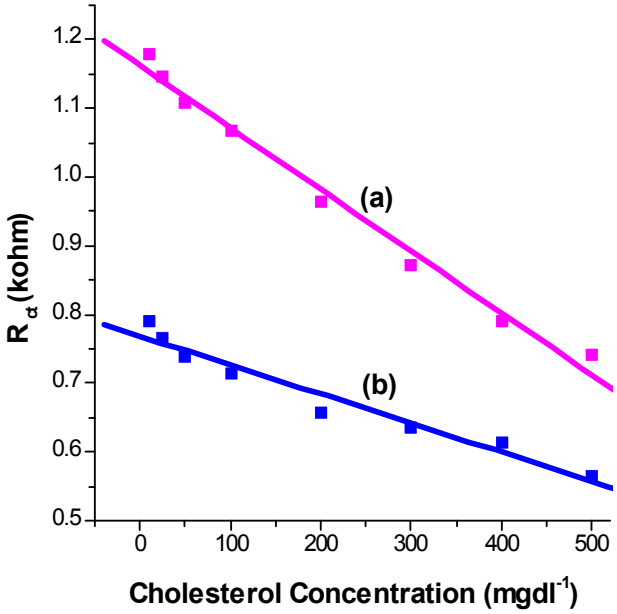

Table of Contents Graphic

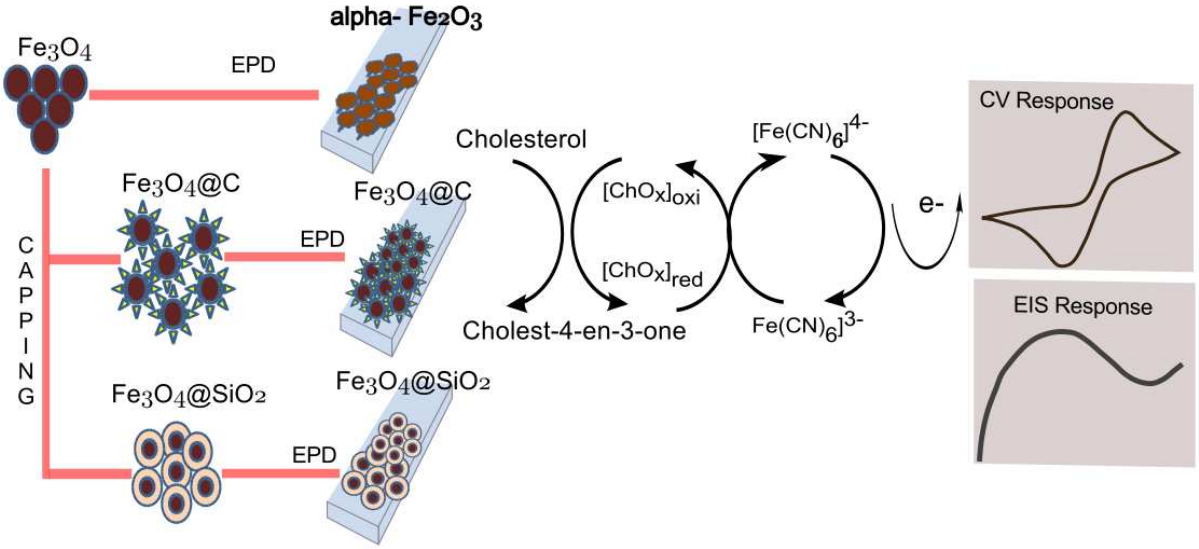

Rapid phase transformation of Fe_3O_4 NPs to α-Fe_2O_3 NPs during electrophoretic deposition and its phase control via organic and inorganic encapsulants. Fabrication of highly sensitive electrochemical cholesterol biosensor employing different phases of nanostructured iron oxide.

Journal of Materials Chemistry B

Accepted Manuscript

This is an *Accepted Manuscript*, which has been through the RSC Publishing peer review process and has been accepted for publication.

Accepted Manuscripts are published online shortly after acceptance, which is prior to technical editing, formatting and proof reading. This free service from RSC Publishing allows authors to make their results available to the community, in citable form, before publication of the edited article. This *Accepted Manuscript* will be replaced by the edited and formatted *Advance Article* as soon as this is available.

To cite this manuscript please use its permanent Digital Object Identifier (DOI®), which is identical for all formats of publication.

More information about *Accepted Manuscripts* can be found in the **Information for Authors**.

Please note that technical editing may introduce minor changes to the text and/or graphics contained in the manuscript submitted by the author(s) which may alter content, and that the standard **Terms & Conditions** and the **ethical guidelines** that apply to the journal are still applicable. In no event shall the RSC be held responsible for any errors or omissions in these *Accepted Manuscript* manuscripts or any consequences arising from the use of any information contained in them.

Phase Control of Nanostructured Iron Oxide for Application to Biosensor

Rachna Sharma[1,3], Ved Varun Agrawal[1,*], A. K. Srivastava[1], Govind[1], Lata Nain[2], Imran Chaudhary[1], Soumya Ranjan Kabi[2], R. K. Sinha[3], and Bansi D. Malhotra[4,*]

[1]National Physical Laboratory, New Delhi-110012, India

[2]Division of Microbiology, Indian Agricultural Research Institute, New Delhi-110012, India

[3]Department of Applied Physics, Delhi Technological University, New Delhi- 110042, India

[4]Department of Biotechnology, Delhi Technological University, New Delhi- 110042, India

Abstract

We report results of the studies relating to phase transformation of bare Fe_3O_4 nanoparticles (NPs) to α-Fe_2O_3 NPs obtained during electrophoretic film deposition onto indium-tin oxide coated glass plate. The *in-situ* oxidation of NPs during electrophoretic deposition can be circumvented using surface passivation of the Fe_3O_4 NPs with organic shell (carbon) as well as inorganic shell (silica) while retaining biocompatibility of Fe_3O_4 NPs. XRD and XPS studies reveal the transformation of Fe_3O_4 NPs to α-Fe_2O_3 NPs on electrophoretic deposition and retention of phase of Fe_3O_4 NPs on encapsulation with carbon and silica, respectively. The results of SEM studies indicate decreased agglomeration of Fe_3O_4 NPs on encapsulation during film deposition. Attempts have been made to compare the characteristics of cholesterol biosensors fabricated using Fe_3O_4@C and α-Fe_2O_3 NPs, respectively. The Fe_3O_4@C NPs based cholesterol biosensor shows response time as 60 s, linearity range as 25-500 $mgdl^{-1}$, sensitivity as 193 $nAmg^{-1}dlcm^{-2}$ and Michaelis-Menten constant as 1.44 $mgdl^{-1}$.

Keywords: nanostructured iron oxide, phase transformation, *in-situ* oxidation, surface passivation, biocompatibility

Phone: +91-11-45609489,

E-mail: agrawalvv@nplindia.org; bansi.malhotra@gmail.com

Introduction

Nanostructured iron oxides (Fe_3O_4, γ-Fe_2O_3 and α-Fe_2O_3) owing to their multifunctional properties such as small size, superparamagnetism, low toxicity etc. are being widely investigated for applications in high-density information storage[1], electronic devices[2], ferrofluid technology[3], catalysis[4], pharmaceuticals[5] and biotechnology[6]. Among these, applications of nanostructured iron oxides in clinical diagnostics and biomedicine have aroused much interest because of their biocompatibility and stability in physiological conditions[7, 8]. They can also be used as contrast agents in magnetic resonance imaging[9, 10], as mediators in hyperthermia[11], as carriers for guided drug delivery[12-14] and as immobilization support for desired biomolecules for diagnosis of various pathogens, diseases and estimation of various biochemical analytes such as glucose, urea etc[15-17]. Besides this, particle size of the nanostructured iron oxide can be controlled to a similar size as that of a biomolecule (protein 5-50 nm; virus 20-450 nm; cell 10-100 μm)[18].

Despite several advantages, susceptibility of Fe_3O_4 NPs towards oxidation and the tendency to agglomerate due to the strong dipole-dipole attraction between particles, have limited their applications till date[19]. It is anticipated that encasing colloids in a shell of a different material may perhaps protect the core from extraneous chemical and physical changes. And core-shell nanostructures are known to exhibit improved physical and chemical properties over the single-component counterparts, and hence are potentially useful for a range of applications. To

improve stability of the deposited NPs, many molecules such as carbon and silica have been considered as interesting encapsulants[20-22]. Compared to polymer and inorganic shells, carbon shells exhibit much higher stability in various chemical and physical environments such as acid or base media, as well as at high temperatures and pressures[23]. Thus, carbon coated Fe_3O_4 NPs may perhaps ensure prolonged activity of the biomolecules and enhanced stability of the biosensors.

Among the various methods, formation of nanocrystalline films using electrophoretic deposition has recently gained much interest since it is cost effective[24] and can be used to obtain uniform thin films by optimizing parameters such as solution concentration, applied potential, pH of the solution etc[25,24]. The fabrication of nanostructured iron oxide films using electrophoretic deposition and its characterization may perhaps yield important information relating to phase change of nanostructured iron oxide. Also, the utilization of nanostructured iron oxide films for fabrication of biosensors may perhaps result in enhanced electrocatalytic activity of the given biomolecule and improved sensitivity for detection of the desired analyte.

We report a novel method of controlling phase of iron oxide NPs obtained during electrophoretic deposition. It is shown that phase of the nanostructured iron oxide during electrophoretic deposition can be tuned to desired requirement by using bare Fe_3O_4 NPs or capped Fe_3O_4 NPs as the starting material. The nanocrystalline films of Fe_3O_4@C and α-Fe_2O_3 NPs have been employed for the fabrication of a biosensor using cholesterol oxidase as a model enzyme and biosensing characteristics have been investigated using electrochemical techniques such as cyclic voltammetry and electrochemical impedance spectroscopy. To the best of our knowledge, there is as yet no report on the phase transformation of Fe_3O_4 NPs during electrophoretic deposition, its prevention and further application in biosensing.

Experimental Methods

Materials and Methods

Ferrous sulphate heptahydrate ($FeSO_4.\ 7H_2O$), ferric chloride ($FeCl_3$), sodium hydroxide (NaOH), fructose ($C_6H_{12}OH$) powder and tetraethyl orthosilicate ($Si(OC_2H_5)_4$) have been purchased from Sigma-Aldrich. All reagents are of analytical grade and have been used without further purification. De-ionized water (Milli Q 10 TS) with resistivity >18.2 MΩ-cm has been used for preparing all aqueous solutions. Indium-tin-oxide (ITO) coated glass plates have been obtained from Balzers, UK, (Baltracom 247 ITO, 1.1 mm thick) with a sheet resistance and transmittance of 25 Ωsq^{-1} and 90%, respectively. Cholesterol powder and cholesterol oxidase (EC 1.1.36 from Pseudomonas fluorescens) with specific activity of 26 Umg^{-1} have been purchased from Sigma–Aldrich (USA). The stock solution of cholesterol has been prepared in 10% triton X-100 and stored at 4°C.

a) Preparation of Fe_3O_4, Fe_3O_4@C and Fe_3O_4@SiO_2 NPs

i) Fe_3O_4 NPs

The Fe_3O_4 NPs have been prepared via hydrolytic reaction based on chemical co-precipitation of metal salts with an alkali as reported earlier[26]. Briefly, 0.32 M $FeSO_4.7H_2O$ and 0.64 M $FeCl_3$ are added to 10 ml of deoxygenated water (containing 12.1 N HCl) with continuous stirring at 30 °C. Solution containing iron salts is dropwise added to 100 ml of NaOH solution (1.5 M) with vigorous stirring at 30 °C. Mixture is then stirred for additional 30 mins resulting in appearance of a black precipitate. The particles are washed by centrifugation at 3500 rpm for 30 mins and supernatant is removed by decantation. Particles are then redispersed in 200 ml of deoxygenated water and are stabilized by making pH of the sol 3.5 using HCl.

Further, Fe_3O_4 NPs are subjected to high temperature and pressure using autoclaves. 30 ml of above synthesized NPs are autoclaved at 180 °C for 4 h[27].

ii) Fe_3O_4@C NPs

Carbon capped Fe_3O_4 NPs have been prepared via hydrothermal carbonization reaction. For this purpose, 10 mmol of fructose powder is added to 30 mL of Fe_3O_4 NPs sol[23, 28, 29] and the mixture is autoclaved at 180 °C for 4 h. At this temperature, fructose melts and carbonization of fructose occurs, resulting in the carbon shell over Fe_3O_4 NPs[30]. The reaction mixture is cooled under ambient conditions. The synthesized product is washed by centrifugation at 3500 min^{-1} and the supernatant is removed by decantation. No change in color of the sol is observed and pH of the NPs redispersed in water is recorded as 8.0.

iii) Fe_3O_4@SiO_2 NPs

To 10 mL of Fe_3O_4 NPs sol (diluted with 40 mL of iso-propanol) are added 1 mL of ammonia and 1 mL of tetraethyl orthosilicate (TEOS)[31]. The mixture is stirred at 30 °C for 4 h and change in colour from dark brown to light brown is observed on completion of the reaction. The synthesized NPs are collected by centrifugation at 3500 min^{-1} and pH of the NPs redispersed in water is recorded as 9.6.

b) Preparation of Nanostructured Iron Oxide Films

The nanocrystalline films of iron oxide are deposited onto ITO coated glass plates using a two-electrode system with platinum as the auxillary electrode and ITO coated glass plate as the deposition electrode. The electrophoretic deposition involves charged particles in a suspension being deposited onto an electrode under the influence of applied electric field. Thus, use of

surfactant is avoided and charge on the surface of NPs is introduced by adjusting pH of the suspension to obtain stable sol. Fe_3O_4 NPs carry positive charge at pH 3.5 since isoelectric point of Fe_3O_4 is 6-7[32-34]. Cationic NPs are deposited onto ITO coated glass plate at the cathode terminal. Application of even a small voltage leads to electrolysis of water producing hydrogen and oxygen gas that hinder continuous flow of the NPs and affect the film uniformity[25]. Thus, mixture of methanol-water (2:1) is utilized for deposition of the desired nanocrystalline film. Conditions for obtaining uniform films have been optimized for various parameters such as applied potential, concentration, deposition time etc and uniform films of Fe_3O_4 NPs and Fe_3O_4 NPs (autoclaved) are obtained on application of 5V potential for 30 s.

The Fe_3O_4@C and Fe_3O_4@SiO_2 NPs have been deposited in methanol-water (2:1) mixture. Although Fe_3O_4@C NPs are stable at 8.0 pH but no deposition occurs indicating that NPs carry negligible charge. Positive charge on NPs is then introduced by adjusting pH to 3.5 and nanocrystalline film is deposited onto ITO coated glass plate at the cathode terminal by applying optimized potential of 10 V for 60 s. Interestingly, Fe_3O_4@SiO_2 NPs carry negative charge at pH 9.6 (as iso-electric point of SiO_2 NPs is ~2)[35], thus nanocrystalline film is deposited onto ITO coated glass plates at the anode terminal on application of 10 V potential for 60 s.

c) Fabrication of Nanostructured Iron Oxide Films based Bioelectrodes

ChOx is physiosorbed onto the nanostructured iron oxide films. For this purpose, 20 µL of freshly prepared ChOx solution (1 mg/mL) is spread onto the α-Fe_2O_3 and Fe_3O_4@C nanocrystalline films. ChOx immobilized iron oxide films are incubated at 27 °C for 2 h and at 4 °C for 12 h[36]. Later weakly bound ChOx are removed by washing these films with 100 mM PBS buffer containing 0.05% Tween-20[37]. These films are stored at 4°C when not in use. The

fabricated ChOx/Fe_3O_4@C film/ITO and ChOx/α-Fe_2O_3 film/ITO bioelectrodes have been characterized via SEM, CV and EIS studies and the enzyme activity measurements for the fabricated bioelectrodes have been carried out using CV and EIS techniques.

d) Characterization

TEM micrographs have been recorded using a high-resolution transmission electron microscope (HR-TEM, Tecnaii-G2F30 STWIN). Samples for TEM are prepared on 200 mesh carbon coated copper grids. A drop of iron oxide NPs sol is carefully placed on the copper grid surface and is then dried under ambient conditions. The structure of the powder samples and nanostructured iron oxide films have been analyzed using X-ray powder diffraction (XRD, Cu-Kα radiation, Rigaku) over the 2□ range from 25°-70° using monochromatized X-ray beam with Cu-Kα radiations (λ = 1.54 Å). XPS measurements have been carried out in a Perkin Elmer XPS chamber (PHI 1257) with a base pressure of 5×10^{-9} torr. The chamber is equipped with a dual anode Mg-K_α (energy 1253.6 eV) and Al-K_α (energy 1486.6 eV) X-ray source and a high-resolution hemispherical energy analyzer for energy resolved electron detection. The Mg-K_α X-ray source has been used for this study. The samples are sputtered with 4 keV argon ions to remove surface contamination prior to XPS studies. The absorption studies of the bare and encapsulated NPs have been conducted on Phoenix – 2200 DPCV UV-Vis Spectrophotometer in the wavelength range of 200-900 nm. The transmission studies of nanostructured iron oxide films in the infrared region have been carried out on Perkin Elmer, Spectrum BX II spectrophotometer in the wavenumber range of 400-4000 cm^{-1}. The morphological changes of nanocrystalline films on enzyme immobilization have been studied using SEM, LEO 440 scanning electron microscope.

The electrochemical experiments have been conducted on Autolab PGSTAT 302N System (Ecochemie, The Netherlands) in a three electrodes system. All electrochemical experiments have been carried out in a cell containing 15 ml of 100 mM Phosphate Buffer Solution (PBS) containing 0.9% NaCl and 5 mM $K_3/K_4[Fe(CN)_6]$ as a redox probe and using a platinum wire as auxiliary, a Ag/AgCl wire as reference, and the nanostructured iron oxide films on ITO as the working electrode.

Results and Discussion

a) TEM Studies of Iron Oxide NPs

Fig. 1(a) shows TEM micrograph of Fe_3O_4 NPs indicating formation of nearly monodispersed nanocrystals with average diameter of 10 nm. The lattice spacing of ~ 2.56 Å obtained from fringe pattern [Inset Fig. 1(a)], match with the d-value (2.56 Å), corresponding to (311) hkl plane of the Fe_3O_4 nanocrystals [JCPDS file – 890951]. However, after hydrothermal treatment, the average size of NPs increases by about two nm [Fig. 1(b)]. Increase in average particle size of autoclaved NPs and decrease in the number of smaller NPs indicates growth of NPs at the expense of smaller NPs, suggesting Ostwald ripening[38] of NPs. Also, the edges and roughness observed on NPs surfaces are reduced on hydrothermal treatment and the NPs assume spherical shape. Thus, size and soomthness of the NPs can be tailored using hydrothermal treatment.

On capping of Fe_3O_4 NPs with carbon and silica, the average particle size of Fe_3O_4 NPs increased to 14 nm and 20 nm [Fig. 1(c), 1(d)] suggesting the formation of carbon and silica shell, respectively, over Fe_3O_4 NPs. Due to the formation of the thick shell of silica, the Fe_3O_4 NPs are well separated and uniform [Inset Fig. 1(d)] while some agglomeration has been observed in case of Fe_3O_4@C NPs [Inset Fig. 1(c)].

b) UV-visible Studies of Fe_3O_4, Fe_3O_4 (autoclaved), Fe_3O_4@C and Fe_3O_4@SiO_2 NPs

Fig. 2 shows absorption spectra of the Fe_3O_4 NPs, Fe_3O_4 NPs (autoclaved), Fe_3O_4 NPs capped with carbon and Fe_3O_4 NPs capped with silica in the UV-Vis wavelength range. The absorption onset of Fe_3O_4 NPs is at ~ 600 nm [Fig. 2(a)]. Because of the quantam size effect, this onset value is blue-shifted by 100 nm as compared to that of the bulk Fe_3O_4[39]. The band near 300 nm corresponds to ligand field transitions of Fe^{3+} and shoulder peak around 480 nm corresponds to excitation of Fe-Fe pair[40]. Similar spectrum is observed for the autoclaved Fe_3O_4 NPs [Fig. 2(b)]. The higher absorption for autoclaved NPs for the same concentration may be due to increase in particle size of the NPs on hydrothermal treatment.

On encapsulation of the Fe_3O_4 NPs with carbon and silica shells, the scattering from the NPs increases due to increase in particle size[41]. Importantly, this increase in scattering is specific to wavelength range of 500-900 nm. On contrary, the absorption at lower wavelengths suppresses due to capping of the Fe_3O_4 NPs. Such crossover in absorption spectra for the same concentration suggests surface modification of Fe_3O_4 NPs. For carbon capped Fe_3O_4 NPs, the characteristic spectrum from Fe_3O_4 NPs is retained [Fig. 2(c)] but the partial suppression of the absorption intensity suggests capping of the Fe_3O_4 NPs with thin layer of carbon. On capping of Fe_3O_4 NPs with silica, absence of characteristic absorption from Fe_3O_4 NPs (200-450 nm) can be seen[42, 43] [Fig. 2(d)]. This suggests complete coverage of Fe_3O_4 NPs with thick shell of silica, which increases over all scattering from the NPs while on contrary it completely suppresses the absorption from Fe_3O_4 NPs.

c) X-ray Diffraction Studies of Fe_3O_4 NPs and Nanostructured Iron Oxide Films

Fig. 3(a) shows XRD pattern of bare Fe_3O_4 NPs. The diffraction peaks obtained correspond to cubic spinel structure of Fe_3O_4[44, 45]. The average particle diameter of 10.6 nm calculated using Debye-Scherrer formula (from the most intense peak at 2□ = 35.57°) is in agreement with the particle size determined by statistical analysis of the TEM images, indicating that each individual particle is a single crystal[46].

Fig. 3(b) and 3(c) show XRD spectra of iron oxide films prepared from Fe_3O_4 NPs and Fe_3O_4 NPs (autoclaved), respectively. The diffraction peaks of films match with the α-Fe_2O_3 [JCPDS file - 890599-96]. Inspite of Fe_3O_4 NPs being starting material for the film deposition, the XRD spectra obtained from the deposited film corresponds to that of α-Fe_2O_3. This change of phase can be ascribed to oxidation of NPs during electrophoretic deposition in water-methanol mixture. The hydroxyl (OH) groups resulting from the dissociation of water and methanol molecules get adsorbed on the surface of magnetite NPs and catalyze their oxidation process[47]. In addition, the application of potential above the oxidation potential of Fe^{2+} (i.e. 0.77 V) results in the modified nucleation rate (kinetics), enhanced diffusion of species and gradient of the lattice constant, which drive the nucleation of α-Fe_2O_3 NPs[47, 48]. Also, as we have mentioned in the manuscript that uncapped Fe_3O_4 NPs undergo rapid agglomeration during deposition and their large size favor the oxidation to hematite over magnetite[49]. To the best of our knowledge, change in phase of Fe_3O_4 NPs obtained during electrophoretic deposition occurring in such short span of time (30 s) has not been reported in literature.

To control this oxidation step, Fe_3O_4 NPs have been encapsulated with organic carbon shell and inorganic silica shell as mentioned in the preceding section. Fig. 3(d) and 3(e) show XRD spectra of films obtained from Fe_3O_4@C NPs and Fe_3O_4@SiO_2 NPs, respectively. Diffraction peaks obtained from the films of encapsulated NPs match with Fe_3O_4 (with slight

shift), indicating that no oxidation occurs during deposition of films on capping Fe_3O_4 NPs with organic and inorganic shell. After capping, the surface of Fe_3O_4 NPs has been passivated which circumvent the adsorption of hydroxyl groups onto their surface and thus prevent their phase change. Thus, an additional oxidation step during electrophoretic deposition of Fe_3O_4 NPs can be circumvented using surface passivation.

d) X-ray Photoelectron Studies of α-Fe_2O_3 and Fe_3O_4@C films

To further confirm the phase of NPs before and after electrophoretic deposition, XPS core level spectra of α-Fe_2O_3 and Fe_3O_4@C films have been acquired for Fe 2p and the deconvoluted Fe 2p3/2 spectra are shown in Fig. 4. Background subtraction and peak fitting of the spectra have been done using Shirley function and Gaussian function, respectively and the spectra have been referenced to C 1s main peak at 284.6 eV. Considerable difference can be seen in the two spectra for α-Fe_2O_3 and Fe_3O_4@C films.

Fig. 4(a) shows the deconvoluted XPS Fe $2p_{3/2}$ spectra of α-Fe_2O_3 film. The peak fitting of spectra reveals that Fe^{2+} and Fe^{3+} ions are present in the ratio of 1:6.7. This shows that the film majorly contains Fe_2O_3 with traces of Fe_3O_4, which suggests *in-situ* oxidation of uncapped Fe_3O_4 NPs during electrophoretic deposition. However, the deconvolution and peak fitting of Fe $2p_{3/2}$ spectra obtained for Fe_3O_4@C film reveals that the ratio of Fe^{2+} and Fe^{3+} ions is 1:2 [Fig. 4(b)]. This shows that Fe_3O_4 NPs retain their phase on encapsulation with carbon and the film consists of Fe_3O_4 NPs. Thus, surface passivation restricts the *in-situ* oxidation of Fe_3O_4 NPs during electrophoretic deposition. Presence of metal Fe has also been noticed in Fe_3O_4@C film while hydrated Fe is present in both the films as expected[50, 51].

e) FTIR Studies of Nanostructured Iron Oxide Films

Fig. 5 shows the transmittance spectra of nanostructured iron oxide films. In case of α-Fe_2O_3 NPs film [Fig. 5(a), 5(b)] (obtained from Fe_3O_4 NPs and Fe_3O_4 NPs (autoclaved), respectively), the peak seen at 566 cm^{-1} corresponds to the vibrations of Fe-O[19]. However, on capping of Fe_3O_4 NPs with carbon and silica, the Fe-O vibration peak at 566 cm^{-1} disappears and two additional peaks at 649 cm^{-1} and 465 cm^{-1} [Fig. 5(c), 5(d)] have been obtained.

In case of carbon capped Fe_3O_4 NPs [Fig. 5(c)], peak at 2934 cm^{-1} refers to the C-H stretching vibrations, peak at 1416 cm^{-1} refers to the C-H bending vibrations and peak at 1066 cm^{-1} refers to the C-O stretching vibrations. All these peaks indicate the presence of aliquots of fructose, since fructose molecules present in hydrated state are unlikely to decompose completely[52-54] but as a convention adopted by previous reports, we label these nanoparticles as carbon capped Fe_3O_4 NPs[23, 29].

In case of silica capped Fe_3O_4 NPs [Fig. 5(d)], sharp peak at 1118 cm^{-1} corresponds to characteristic Si-O vibrations, revealing capping of the Fe_3O_4 NPs with silica[55, 56]. The broad band found at 3300-3400 cm^{-1} and peak at 1602 cm^{-1} present in all the films correspond to the O-H stretching mode and H-O-H bending mode, respectively, indicating presence of the interstitial water molecules in the films[44].

f) Morphological Studies of Nanostructured Iron Oxide Films and Bioelectrodes

Fig. 6 shows the SEM micrographs of the nanostructured iron oxide films. It can be seen that the α-Fe_2O_3 films obtained from Fe_3O_4 NPs and Fe_3O_4 NPs (autoclaved) has an average particle size of 300 nm and 200 nm, respectively [Fig. 6(a), 6(b)]. The observed increase in particle size and deformation in shape indicate agglomeration of the uncapped NPs on deposition. The agglomeration is more prominent for the as-prepared Fe_3O_4 NPs owing to their surface

roughness. The electrical double layer gradient is maximum at the edges of the NPs which result in the electrostatic attraction of the NPs and the growth in their size[57]. However, due to removal of edges and surface smoothening of the NPs on hydrothermal treatment, autoclaved NPs undergo reduced aggregation.

On capping of Fe_3O_4 NPs with carbon and silica, the agglomeration has been further restricted. The radical decrease of average particle size to 100 nm [Fig. 6(c)] and 160 nm [Fig. 6(d)] is observed in case of carbon capped NPs and silica capped NPs, respectively. Also, the capped NPs retain their initial spherical shape on deposition as compared to the film of uncapped NPs. The reduction in size and retention of spherical shape indicate considerable decrease in agglomeration of NPs on capping. Further, the immobilization of the cholesterol oxidase onto nanostructured iron oxide films has been confirmed using SEM [Figure S1, supplementary information]. The change in morphology from dense uniform distribution of NPs in the nanoscale to the globular structure of ChOx in the micron scale is attributed to physical adsorption of ChOx molecules onto nanostructured iron oxide films[58].

g) Biocompatibility of Fe_3O_4@C and α-Fe_2O_3 Films

The biocompatibility of Fe_3O_4@C and α-Fe_2O_3 films have been investigated using bacterial system i.e. gram positive (Bacillus sp.) and gram negative (Providencia sp.) bacteria. Two methods have been utilized to examine the biocompatibility of nanostructured iron oxide films. Firstly, cultures of gram positive and gram negative bacteria are spread on nutrient agar plates and Fe_3O_4@C and α-Fe_2O_3 films are kept on these plates under optimum growth conditions (28 °C & 150 rpm). No zone of inhibition is observed for nanostructured iron oxide films. Secondly, the side arm flasks are prepared with nutrient broth and both the bacteria are inoculated. Films

are kept in the nutrient broth and grown under optimum conditions (28 °C & 150 rpm). Colorimetric readings recorded at interval of 2 h are summarized in Table I, which clearly indicates the biocompatibility of Fe_3O_4@C and α-Fe_2O_3 films as the optical density of gram positive and gram negative bacteria increases with time in presence of nanostructured iron oxide films.

h) Electrochemical Characterization of ChOx Immobilized Iron Oxide Electrodes

i) ChOx/Fe_3O_4@C film/ITO Bioelectrode

Fig. 7(a) shows the cyclic voltammograms of ITO electrode, Fe_3O_4@C film/ITO electrode and ChOx/Fe_3O_4@C film/ITO bioelectrode in the potential range of -0.7 V to +0.7 V at scan rate of 30 mV/s. The decrease in anodic peak current obtained for Fe_3O_4@C film/ITO electrode [Fig. 7(a) (ii)] compared to that of the ITO electrode [Fig. 7(a) (i)] reveals formation of the layer of Fe_3O_4@C NPs on the ITO surface. Further, increase in oxidation current obtained for ChOx/Fe_3O_4@C film/ITO bioelectrode [Fig. 7(a) (iii)] compared to that of the Fe_3O_4@C film/ITO electrode [Fig. 7(a) (ii)] is attributed to the electron transfer facilitated by redox moieties at the active sites (FAD centres) of the enzyme at the electrode surface.

Fig. 7(b) shows the Nyquist plots obtained for ITO electrode, Fe_3O_4@C film/ITO electrode and ChOx/Fe_3O_4@C film/ITO bioelectrode. The increased R_{ct} value of 1.35 kΩ for Fe_3O_4@C film/ITO electrode [Fig. 7(b) (ii)] compared to the R_{ct} value of 0.28 kΩ for ITO electrode [Fig. 7(b) (i)] indicates formation of the Fe_3O_4@C NPs layer on the ITO surface. The presence of Fe_3O_4@C NPs layer impedes the flow of electrons resulting in an increased value of R_{ct}. Further, decrease in R_{ct} value from 1.35 kΩ for Fe_3O_4@C film/ITO electrode to 1.18 kΩ for ChOx/Fe_3O_4@C film/ITO bioelectrode [Fig. 7(b) (iii)] reveals the ChOx immobilization onto

Fe_3O_4@C film/ITO electrode. This decrease in R_{ct} value is ascribed to the facile electron transfer aided by the redox moieties of the enzyme at the electrode surface.

According to Laviron's theory, the slope of the linear curve between the anodic peak potential and the logarithm of scan rate represents RT/αnF (α- transfer coefficient). This can be used to calculate the surface concentration of the ionic species of the bioelectrodes using the following equation:

$$i_p = n^2F^2\nu CA\,(4RT)^{-1} \quad \ldots \text{Eq.1}$$

where, i_p/ν can be calculated from the i_p Vs. ν plot[58] (i_p- anodic peak current; ν- scan rate).

The slope of the linear plot of anodic peak potential vs. logarithm of scan rate for ChOx/Fe_3O_4@C film/ITO bioelectrode gives RT/αnF = 0.23. Using Eq.1, the surface concentration on the ChOx/Fe_3O_4@C film/ITO bioelectrode has been found to be as 2.52×10^{-11} molcm^{-2}.

ii) ChOx/α-Fe_2O_3 film/ITO Bioelectrode

Fig. 7(c) shows the cyclic voltammograms obtained for ITO electrode, α-Fe_2O_3 film/ITO electrode and ChOx/α-Fe_2O_3 film/ITO bioelectrode in the potential range of -0.7 V to +0.7 V at scan rate of 30 mVs^{-1}. The oxidation peak seen at 0.38 V is attributed to the oxidation of the redox couple, $K_3/K_4[Fe(CN)_6]$ present in the buffer[58]. The decrease in the oxidation current obtained for α-Fe_2O_3 film/ITO electrode [Fig. 7(c) (ii)] compared to that of the ITO electrode [Fig. 7(c) (i)] indicates formation of the layer of α-Fe_2O_3 NPs onto the ITO surface. Further, increase in oxidation current obtained for ChOx/α-Fe_2O_3 film/ITO bioelectrode [Fig. 7(c) (iii)] compared to that of the α-Fe_2O_3 film/ITO electrode [Fig. 7(c) (ii)] is attributed to the presence of redox moieties at active sites (FAD centres) of the enzyme leading to fast electron transfer between the enzyme and the electrode surface[37].

Fig. 7(d) shows the Nyquist plots obtained for ITO electrode, α-Fe_2O_3 film/ITO electrode and ChOx/α-Fe_2O_3 film/ITO bioelectrode. The increased R_{ct} (charge transfer resistance) value of 1.14 kΩ obtained for α-Fe_2O_3 film/ITO electrode [Fig. 7(d) (ii)] compared to the R_{ct} value of 0.28 kΩ for ITO electrode [Fig. 7(d) (i)] is attributed to the formation of layer of α-Fe_2O_3 NPs on the ITO surface. Formation of α-Fe_2O_3 NPs layer results in decreased interfacial electron transfer, thereby causing increase in the R_{ct} value. Further, observed decrease in R_{ct} value from 1.14 kΩ for α-Fe_2O_3 film/ITO electrode [Fig. 7(d) (ii)] to 0.82 kΩ for ChOx/α-Fe_2O_3 film/ITO bioelectrode [Fig. 7(d) (iii)] is attributed to facile electron transfer mediated by the redox centres of the enzyme.

The surface concentration of the ionic species on the ChOx/α-Fe_2O_3 film/ITO bioelectrode has been found to be as 1.81×10^{-11} molcm^{-2} (using RT/αnF = 0.16). The higher concentration of ionic species on ChOx/Fe_3O_4@C film/ITO bioelectrode compared to the ChOx/α-Fe_2O_3 film/ITO bioelectrode is attributed to that of the larger surface area provided by the Fe_3O_4@C nanocrystalline film owing to the smaller particle size of NPs as compared to α-Fe_2O_3 nanocrystalline film for enzyme immobilization.

i) Electrochemical Response of ChOx Immobilized Iron Oxide Electrodes

i) ChOx/ Fe_3O_4@C film/ITO Bioelectrode

Fig. 8(a) shows response of the ChOx/Fe_3O_4@C film/ITO bioelectrode obtained as a function of cholesterol concentration using cyclic voltammetry. The bioelectrode exhibits the response time of 60 s [Figure S4(a)]. The anodic peak current of ChOx/Fe_3O_4@C film/ITO bioelectrode plotted as a function of cholesterol concentration [Fig. 9(a)] reveals the linearity range as 25-500 mgdl^{-1} with standard deviation and correlation coefficient of 4.82 μA and 0.99, respectively. The

sensitivity of the ChOx/Fe_3O_4@C film/ITO bioelectrode exhibited by the slope of linear regression curve is 193 $nAmg^{-1}dlcm^{-2}$. The value of Michaelis-Menten constant of ChOx immobilized Fe_3O_4@C film has been found to be as 1.44 $mgdl^{-1}$.

The Nyquist plots for the ChOx/Fe_3O_4@C film/ITO bioelectrode as a function of cholesterol concentration have been investigated to obtain impedimetric response of the biosensor [Fig. 8(b)]. The linear calibration curve obtained by plotting the R_{ct} value for ChOx/Fe_3O_4@C film/ITO bioelectrode as a function of cholesterol concentration [Fig. 10(a)] reveals linearity range of 25-500 $mgdl^{-1}$ with standard deviation and regression coefficient of 0.02 kΩ and 0.99, respectively. The sensitivity of 0.90 $\Omega mg^{-1}dlcm^{-2}$ is obtained from the slope of the linear regression curve of ChOx/Fe_3O_4@C film/ITO bioelectrode.

The shelf life and reproducibility of the ChOx/Fe_3O_4@C film/ITO bioelectrode have been investigated using cyclic voltammetry. The activity of the bioelectrode is monitored at regular interval of seven days. The bioelectrode exhibits only 6% reduction in peak current after 10 weeks for 100 $mgdl^{-1}$ cholesterol concentration when stored at 4°C [Fig. S2(a)]. The reproducibility of the sensing parameters of the bioelectrode has been studied with cholesterol concentration of 25 $mgdl^{-1}$ and it has been found that the bioelectrode can be used upto 25 times without significant decrease (40 μA) of the response signal [Fig. S3(a)].

ii) ChOx/α-Fe_2O_3 film/ITO Bioelectrode

Fig. 8(c) shows the response of the ChOx/α-Fe_2O_3 film/ITO bioelectrode obtained as a function of cholesterol concentration using cyclic voltammetric technique. The response time of this electrode is found to be 60 s [Fig. S4(b)]. The magnitude of amperometric current of ChOx/α-Fe_2O_3 film/ITO bioelectrode plotted as a function of cholesterol concentration [Fig. 9(b)] shows linearity in the range 25-500 $mgdl^{-1}$ with standard deviation and correlation coefficient of 4.52

μA and 0.99, respectively. The sensitivity of the ChOx/α-Fe_2O_3 film/ITO bioelectrode exhibited by the slope of linear calibration curve is found to be as 218 $nAmg^{-1}dlcm^{-2}$. The value of Michaelis-Menten constant of ChOx immobilized α-Fe_2O_3 film has been found to be as 1.46 $mgdl^{-1}$.

The electrochemical impedimetric response of the ChOx/α-Fe_2O_3 film/ITO bioelectrode has been investigated as a function of cholesterol concentration using Nyquist plots [Fig. 8(d)]. The linear calibration curve obtained by plotting the R_{ct} values for ChOx/α-Fe_2O_3 film/ITO bioelectrode as a function of cholesterol concentration [Fig. 10(b)] reveals the linearity range of 50-500 $mgdl^{-1}$ with standard deviation and regression coefficient of 0.02 kΩ and 0.97, respectively. The value of sensitivity exhibited by the slope of the linear regression curve for ChOx/α-Fe_2O_3 film/ITO bioelectrode is 0.42 $\Omega mg^{-1}dlcm^{-2}$.

The shelf-life of the ChOx/α-Fe_2O_3 film/ITO bioelectrode has been investigated for 100 $mgdl^{-1}$ cholesterol concentration using cyclic voltammetry. The bioelectrode exhibits 6% decrease in the peak current for first 8 weeks but sudden decrease in the signal has been observed afterwards and the current reduced by 11.5% after 10 weeks [Fig. S2(b)]. The ChOx/α-Fe_2O_3 film/ITO bioelectrode can be used upto 20 times with insignificant loss (66 μA) of the signal [Fig. S3(b)].

Table II Comparison table summarizing characteristics of the cholesterol biosensors based on nanostructured metal oxide films.

Conclusions

The nanocrystals of Fe_3O_4 with average particle diameter of 10 nm have been synthesized. The electrophoretic deposition of bare Fe_3O_4 NPs in methanol-water mixture results in oxidation and phase transformation of NPs and film of α-Fe_2O_3 NPs has been obtained. The phase transformation of Fe_3O_4 NPs can be circumvented using surface passivation of Fe_3O_4 NPs with organic carbon shell and inorganic silica shell. Encapsulation of Fe_3O_4 NPs restricts agglomeration of NPs during film deposition and retains high surface to volume ratio for enzyme loading. Due to the non-conducting nature of silica, Fe_3O_4@SiO_2 NPs shows poor electrochemical response. However, these can be utilized for applications in drug delivery[21], biocatalysis and bioseparations[20, 59], magnetic resonance imaging[60], determination of metal ion concentration[61] etc. Growth of gram positive and gram negative bacteria in contact with Fe_3O_4@C and α-Fe_2O_3 films reveals biocompatible nature of nanostructures that is suitable for prolonged activity of enzymes and thus stability of biosensors. The fabricated cholesterol biosensors employing Fe_3O_4@C and α-Fe_2O_3 nanocrystalline films show sensitivities of 193 $nAmg^{-1}dlcm^{-2}$ and 218 $nAmg^{-1}dlcm^{-2}$, respectively, from cyclic voltammetric studies and sensitivities of 0.42 $\Omega mg^{-1}dlcm^{-}2$ and 0.90 $\Omega mg^{-1}dlcm^{-2}$, respectively, from electrochemical impedance spectroscopic studies. The low values of Michaelis-Menten constant reveal the enhanced enzymatic activity of ChOx onto nanostructured iron oxide films. The comparable sensitivities for biosensors obtained using Fe_3O_4@C and α-Fe_2O_3 NPs suggest that encapsulation of Fe_3O_4 NPs with carbon do not significantly affect electrocatalytic activity of Fe_3O_4 NPs while adds to the stability of the NPs. However, encapsulation of Fe_3O_4 NPs with conjugated carbon molecules, conducting polymers like polypyrrole, polyaniline etc may result in improved sensitivity of the biosensor.

Supplementary Information

SEM studies showing the immobilization of cholesterol oxidase onto nanostructured iron oxide films, shelf life, reproducibility and response time studies of the fabricated cholesterol biosensors.

Acknowledgment

We thank Prof. R. C. Budhani, Director, National Physical Laboratory, New Delhi, India for providing facilities. R. S. is thankful to the UGC-CSIR for award of Junior Research Fellowship. Authors thank Dr. K. N. Sood, NPL for SEM measurements, Dr. S. M. Shivprasad, JNCASR for XPS measurements and Dr. Kavita Arora, JNU for TEM studies. Financial support received from the Department of Science and Technology (DST) centre on biomolecular electronics and CSIR Empower projects is sincerely acknowledged. Thanks are due to Dr. Pratima Solanki, C. M. Pandey, Manoj Patel and all the members of the Biomedical Instrumentation Section, NPL, for discussions.

References

1. S. Chou, *J. Appl. Phys.*, 1994, **76**, 6673.
2. D. Schaadt, *J. Vac. Sci. Technol. A*, 2000, **18**, 1834.
3. K. Mosbach and L. Andersson, *Nature*, 1977, **270**, 259-261.
4. D. K. Yi, S. S. Lee and J. Y. Ying, *Chem. Mater.*, 2006, **18**, 2459-2461.
5. C. B. Catherine and S. G. C. Adam, *J. Phys. D: Appl. Phys.*, 2003, **36**, R198.
6. E. Amstad, M. Textor and E. Reimhult, *Nanoscale*, **3**, 2819-2843.
7. S. Laurent, D. Forge, M. Port, A. Roch, C. Robic, L. Vander Elst and R. N. Muller, *Chem. Rev.*, 2008, **108**, 2064-2110.
8. T. Osaka, T. Matsunaga, T. Nakanishi, A. Arakaki, D. Niwa and H. Iida, *Anal. Bioanal. Chem.*, 2006, **384**, 593-600.
9. R. Weissleder, H.-C. Cheng, A. Bogdanova and A. Bogdanov, *J. Magn. Reson. Imaging*, 1997, **7**, 258-263.
10. F. Cengelli, D. Maysinger, F. Tschudi-Monnet, X. Montet, C. Corot, A. Petri-Fink, H. Hofmann and L. Juillerat-Jeanneret, *J. Pharmacol. Exp. Ther.*, 2006, **318**, 108-116.

11. F. Sonvico, S. p. Mornet, S. b. Vasseur, C. Dubernet, D. Jaillard, J. Degrouard, J. Hoebeke, E. Duguet, P. Colombo and P. Couvreur, *Bioconjugate Chem.*, 2005, **16**, 1181-1188.
12. M. Mahmoudi, A. Simchi, M. Imani and U. O. Halfeli, *J. Phys. Chem. C*, 2009, **113**, 8124-8131.
13. A. Petri-Fink, M. Chastellain, L. Juillerat-Jeanneret, A. Ferrari and H. Hofmann, *Biomaterials*, 2005, **26**, 2685-2694.
14. A. K. Gupta and S. Wells, *IEEE T. Nanobiosci.*, 2004, **3**.
15. J. Li, R. Yuan and Y. Chai, *Microchim. Acta*, **173**, 369-374.
16. J. Wang, Z. Zhu, A. Munir and H. S. Zhou, *Talanta*, **84**, 783-788.
17. H. Li, Q. Wei, J. He, T. Li, Y. Zhao, Y. Cai, B. Du, Z. Qian and M. Yang, *Biosens. Bioelectron.*, **26**, 3590-3595.
18. I. M. Hsing, Y. Xu and W. Zhao, *Electroanalysis*, 2007, **19**, 755-768.
19. G. Zhao, J. J. Feng, Q. L. Zhang, S. P. Li and H. Y. Chen, *Chem. Mater.*, 2005, **17**, 3154-3159.
20. H.-H. Yang, S.-Q. Zhang, X.-L. Chen, Z.-X. Zhuang, J.-G. Xu and X.-R. Wang, *Anal. Chem.*, 2004, **76**, 1316-1321.
21. K. Souza, J. Ardisson and E. Sousa, *J. Mater. Sci.- Mater. M.*, 2009, **20**, 507-512.
22. T. Sen, A. Sebastianelli and I. J. Bruce, *J. Am. Chem. Soc.*, 2006, **128**, 7130-7131.
23. W. Xian-Wen, Z. Guo-Xing, X. Chuan-Jun and Y. Yin, *Nanotechnology*, 2006, **17**, 4307.
24. I. Zhitomirsky, *J. Mater. Sci.*, 2006, **41**, 8186-8195.
25. L. Besra and M. Liu, *Prog. Mater Sci.*, 2007, **52**, 1-61.
26. Y. S. Kang, S. Risbud, J. F. Rabolt and P. Stroeve, *Chem. Mater.*, 1996, **8**, 2209-2211.
27. T. J. Daou, G. Pourroy, S. Begin-Colin, J. M. Greneche, C. Ulhaq-Bouillet, P. Legare, P. Bernhardt, C. Leuvrey and G. Rogez, *Chem. Mater.*, 2006, **18**, 4399-4404.
28. Y. Li, T. Leng, H. Lin, C. Deng, X. Xu, N. Yao, P. Yang and X. Zhang, *J. Proteome Res.*, 2007, **6**, 4498-4510.
29. X. Shouhu, H. Lingyun, J. Wanquan, G. Xinglong, H. Yuan and C. Zuyao, *Nanotechnology*, 2007, **18**, 035602.
30. J. Li and C.-y. Liu, *New J. Chem.*, 2009, **33**, 1474-1477.
31. Y. Lu, Y. Yin, B. T. Mayers and Y. Xia, *Nano Lett.*, 2002, **2**, 183-186.

32. Z. X. Sun, F. W. Su, W. Forsling and P. O. Samskog, *J. Colloid Interface Sci.*, 1998, **197**, 151-159.
33. M. Jarlbring, L. Gunneriusson, B. Hussmann and W. Forsling, *J. Colloid Interface Sci.*, 2005, **285**, 212-217.
34. T. J. Daou, G. Pourroy, J. M. Greneche, A. Bertin, D. Felder-Flesch and S. Begin-Colin, *Dalton T.*, 2009, 4442-4449.
35. M. L. Fisher, M. Colic, M. P. Rao and F. F. Lange, *J. Am. Ceram. Soc.*, 2001, **84**, 713-718.
36. P. R. Solanki, S. K. Arya, S. P. Singh, M. K. Pandey and B. D. Malhotra, *Sensor Actuat. B- Chem.*, 2007, **123**, 829-839.
37. Z. Matharu, G. Sumana, S. K. Arya, S. P. Singh, V. Gupta and B. D. Malhotra, *Langmuir*, 2007, **23**, 13188-13192.
38. L. Yonglan, *Mater. Lett.*, 2007, **61**, 1039-1041.
39. L. Huo, W. Li, L. Lu, H. Cui, S. Xi, J. Wang, B. Zhao, Y. Shen and Z. Lu, *Chem. Mater.*, 2000, **12**, 790-794.
40. T. D. W. David M. Sherman, *Am. Mineral.*, 1985, **70**, 1262-1269.
41. T. A. Egerton and I. R. Tooley, *Int. J. Cosmetic Sci.*, **34**, 117-122.
42. S. L. Westcott, S. J. Oldenburg, T. R. Lee and N. J. Halas, *Langmuir*, 1998, **14**, 5396-5401.
43. Y. Kobayashi, V. Salgueirino-Maceira and L. M. Liz-Marzan, *Chem. Mater.*, 2001, **13**, 1630-1633.
44. K. Tao, H. Dou and K. Sun, *Chem. Mater.*, 2006, **18**, 5273-5278.
45. W. Cai and J. Wan, *J. Colloid Interface Sci.*, 2007, **305**, 366-370.
46. J. Sun, S. Zhou, P. Hou, Y. Yang, J. Weng, X. Li and M. Li, *J. Biomed. Mater. Res. A*, 2007, **80A**, 333-341.
47. O. N. Shebanova and P. Lazor, *Journal of Raman Spectroscopy*, 2003, **34**, 845-852.
48. J. Tang, M. Myers, K. A. Bosnick and L. E. Brus, *The Journal of Physical Chemistry B*, 2003, **107**, 7501-7506.
49. W. Feitknecht and K. J. Gallagher, *Nature*, 1970, **228**, 548-549.
50. J. Morales, L. Sanchez, F. Martin, F. Berry and X. L. Ren, *J. Electrochem. Soc.*, 2005, **152**, A1748-A1754.

51. P. Guardia, J. Perez-Juste, A. Labarta, X. Batlle and L. M. Liz-Marzan, *Chem. Commun.*, **46**, 6108-6110.
52. B. M. Kabyemela, T. Adschiri, R. M. Malaluan and K. Arai, *Ind. Eng. Chem. Res.*, 1999, **38**, 2888-2895.
53. Q. Wang, H. Li, L. Chen and X. Huang, *Carbon*, 2001, **39**, 2211-2214.
54. C. Adina, F. Florinela, T. Abdelmoumen and S. Carmen, *Rom. Biotech. Lett.*, 2010, **15**.
55. A. Azioune, A. Ben Slimane, L. Ait Hamou, A. Pleuvy, M. M. Chehimi, C. Perruchot and S. P. Armes, *Langmuir*, 2004, **20**, 3350-3356.
56. D. Kandpal, S. Kalele and S. Kulkarni, *Pramana*, 2007, **69**, 277-283.
57. P. Pramod, S. T. S. Joseph and K. G. Thomas, *J. Am. Chem. Soc.*, 2007, **129**, 6712-6713.
58. Z. Matharu, P. Pandey, M. K. Pandey, V. Gupta and B. D. Malhotra, *Electroanalysis*, 2009, **21**, 1587-1596.
59. T. Sen, A. Sebastianelli and I. J. Bruce, *J. Am. Chem. Soc.*, 2006, **128**, 7130-7131.
60. J. L. Campbell, J. Arora, S. F. Cowell, A. Garg, P. Eu, S. K. Bhargava and V. Bansal, *PLoS ONE*, **6**, e21857.
61. L. L. Vatta, J. Kramer and K. R. Koch, *Sep. Sci. Technol.*, 2007, **42**, 1985-2002.
62. A. A. Ansari, A. Kaushik, P. R. Solanki and B. D. Malhotra, *Electrochem. Commun.*, 2008, **10**, 1246-1249.
63. A. A. Ansari, A. Kaushik, P. R. Solanki and B. D. Malhotra, *Electroanalysis*, 2009, **21**, 965-972.
64. S. P. Singh, S. K. Arya, P. Pandey, B. D. Malhotra, S. Saha, K. Sreenivas and V. Gupta, *Appl. Phys. Lett.*, 2007, **91**, 063901-063903.
65. P. R. Solanki, A. Kaushik, A. A. Ansari and B. D. Malhotra, *Appl. Phys. Lett.*, 2009, **94**, 143901-143903.
66. G. Kouassi, J. Irudayaraj and G. McCarty, *Journal of Nanobiotechnology*, 2005, **3**, 1.

Tables

Table I Optical density of gram positive (providencia sp.) and gram negative (bacillus sp.) bacteria as a function of time in presence of Fe_3O_4@C and α-Fe_2O_3 films.

Nanostructured film	**Bacteria**	**Optical Density**						
		0 hrs	2 hrs	4 hrs	6 hrs	8 hrs	10 hrs	12 hrs
Fe_3O_4@C film	Providencia sp.	0.01	0.03	0.07	0.15	0.28	0.43	0.56
Fe_3O_4@C film	Bacillus sp.	0.02	0.09	0.24	0.57	0.68	0.73	0.89
α-Fe_2O_3 film	Providencia sp.	0.03	0.06	0.09	0.14	0.19	0.54	0.63
α-Fe_2O_3 film	Bacillus sp.	0.02	0.08	0.26	0.58	0.65	0.82	0.85

Table II Comparison table summarizing characteristics of the cholesterol biosensors based on nanostructured metal oxide films.

Electrode	**Transducer**	**Linear Range ($mgdL^{-1}$)**	**Sensitivity**	**K_m value**	**Response time (s)**	**Reproducibility**	**Shelf life (days)**	**Ref.**
CeO_2/ ITO	Cyclic Voltammetry	10-400	----	2.08 mM	15	----	----	[62]
Chitosan-SnO_2/ ITO	Cyclic Voltammetry	5-400	34.7 $\mu Amg^{-1}dlcm^{-2}$	3.8 mM	5	----	80	[63]
ZnO/ Au	Cyclic Voltammetry	25-400	45.7 $nAmg^{-1}dlcm^{-2}$	2.1 mM	15	----	70	[64]
ZnO/ ITO	Cyclic Voltammetry	5-400	59.0 $nAmg^{-1}dlcm^{-2}$	0.03 mM	10	20	85	[65]
Fe_3O_4 NPs	Spectroscopy	50-200	----	0.45 mM	---	----	10	[66]
Fe_3O_4@C/ ITO	Cyclic Voltammetry Impedance Spectroscopy	25-400	193 $nAmg^{-1}dlcm^{-2}$ 0.90 $\Omega mg^{-1}dlcm^{-2}$	0.03 mM	60	25	70	**Present Work**
α-Fe_2O_3/ ITO	Cyclic Voltammetry Impedance Spectroscopy	50-400	218 $nAmg^{-1}dlcm^{-2}$ 0.42 $\Omega mg^{-1}dlcm^{-2}$	0.04 mM	60	20	56	

Scheme

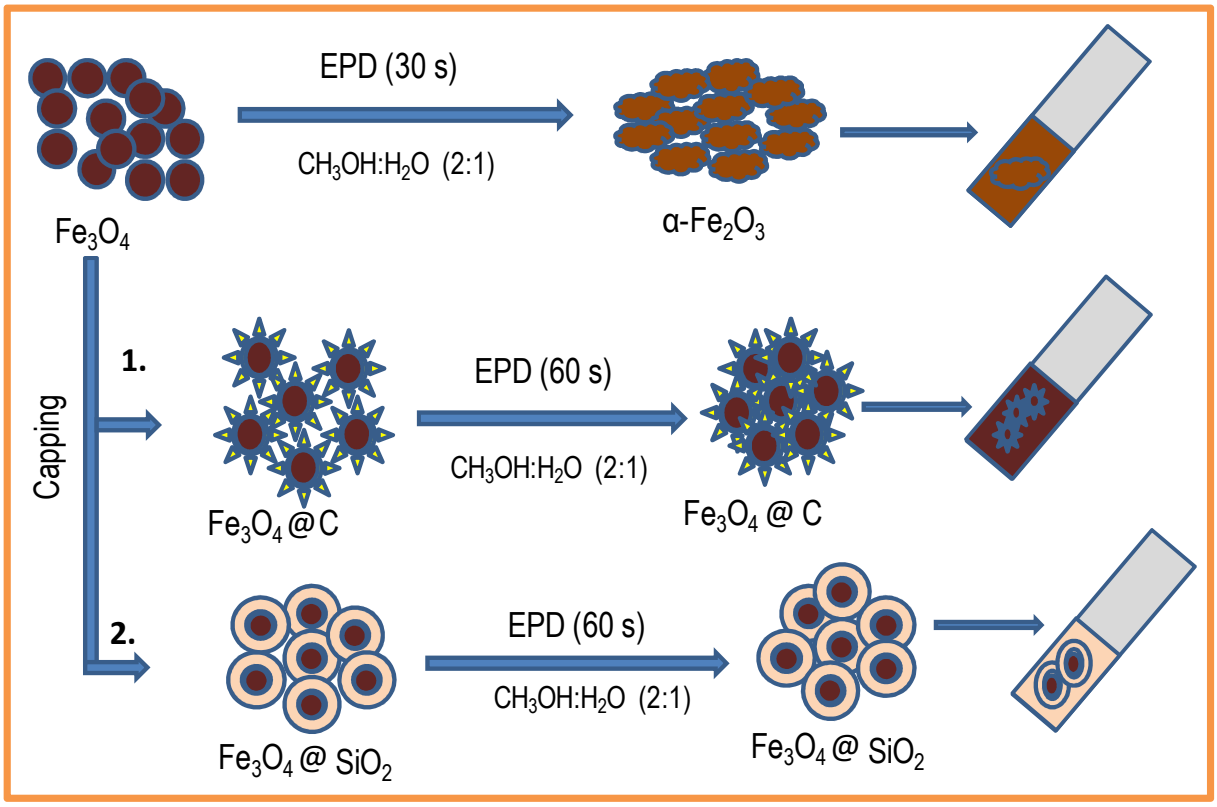

Figure Captions

Fig. 1 TEM micrographs of: (a) Fe_3O_4 NPs; Inset: High-resolution image of a single particle, and; (b) Fe_3O_4 NPs (autoclaved).

Fig. 2 UV-vis absorption spectra of : (a) Fe_3O_4 NPs; (b) Fe_3O_4 NPs (autoclaved); (c) Fe_3O_4@C NPs; (d) Fe_3O_4@SiO_2 NPs.

Fig. 3 XRD spectra of: (a) Fe_3O_4 NPs; (b) film obtained from Fe_3O_4 NPs; (c) film obtained from Fe_3O_4 NPs (autoclaved); (d) film obtained from Fe_3O_4@C NPs; (e) film obtained from Fe_3O_4@ SiO_2 NPs.

Fig. 4 Deconvoluted XPS spectra of Fe $2p_{3/2}$ acquired for: (a) α-Fe_2O_3 film, and; (b) Fe_3O_4@C film.

Fig. 5 FTIR spectra of: (a) α-Fe_2O_3 NPs film obtained from Fe_3O_4 NPs; (b) α-Fe_2O_3 NPs film obtained from Fe_3O_4 NPs (autoclaved); (c) film of Fe_3O_4@C NPs; (d) film of Fe_3O_4@SiO_2 NPs.

Fig. 6 SEM micrograph of: (a) α-Fe_2O_3 NPs film obtained from Fe_3O_4 NPs; (b) α-Fe_2O_3 NPs film obtained from Fe_3O_4 NPs (autoclaved); (c) film of Fe_3O_4@C NPs; (d) film of Fe_3O_4@SiO_2 NPs.

Fig. 7 (a) CV curves for the ITO electrode (i), Fe_3O_4@C film/ITO electrode (ii) and ChOx/ Fe_3O_4@C film/ITO bioelectrode (iii); (b) Nyquist plots for the ITO electrode (i), Fe_3O_4@C film/ITO electrode (ii) and ChOx/Fe_3O_4@C film/ITO bioelectrode (iii); (c) CV curves for the ITO electrode (i), α-Fe_2O_3 film/ITO electrode (ii) and ChOx/α-Fe_2O_3 film/ITO bioelectrode (iii); (d) Nyquist plots for the ITO electrode (i), α-Fe_2O_3 film/ITO electrode (ii) and ChOx/α-Fe_2O_3 film/ITO bioelectrode (iii).

Fig. 8 (a) CV response studies of ChOx/Fe_3O_4@C film/ITO bioelectrode; (b) EIS response studies of ChOx/Fe_3O_4@C film/ITO bioelectrode; (c) CV response studies of ChOx/α-Fe_2O_3 film/ITO bioelectrode and; (d) EIS response studies of ChOx/α-Fe_2O_3 film/ITO bioelectrode with different cholesterol concentrations ($mgdl^{-1}$): (i) 10; (ii) 25; (iii) 50; (iv) 100; (v) 200; (vi) 300; (vii) 400 and (viii) 500.

Fig. 9 Linear calibration plots obtained using CV data for: (a) ChOx/Fe_3O_4@C film/ITO bioelectrode and; (b) ChOx/α-Fe_2O_3 film/ITO bioelectrode.

Fig. 10 Linear calibration plots obtained using EIS data for: (a) ChOx/Fe_3O_4@C film/ITO bioelectrode and; (b) ChOx/α-Fe_2O_3 film/ITO bioelectrode.

Figures

Figure 1

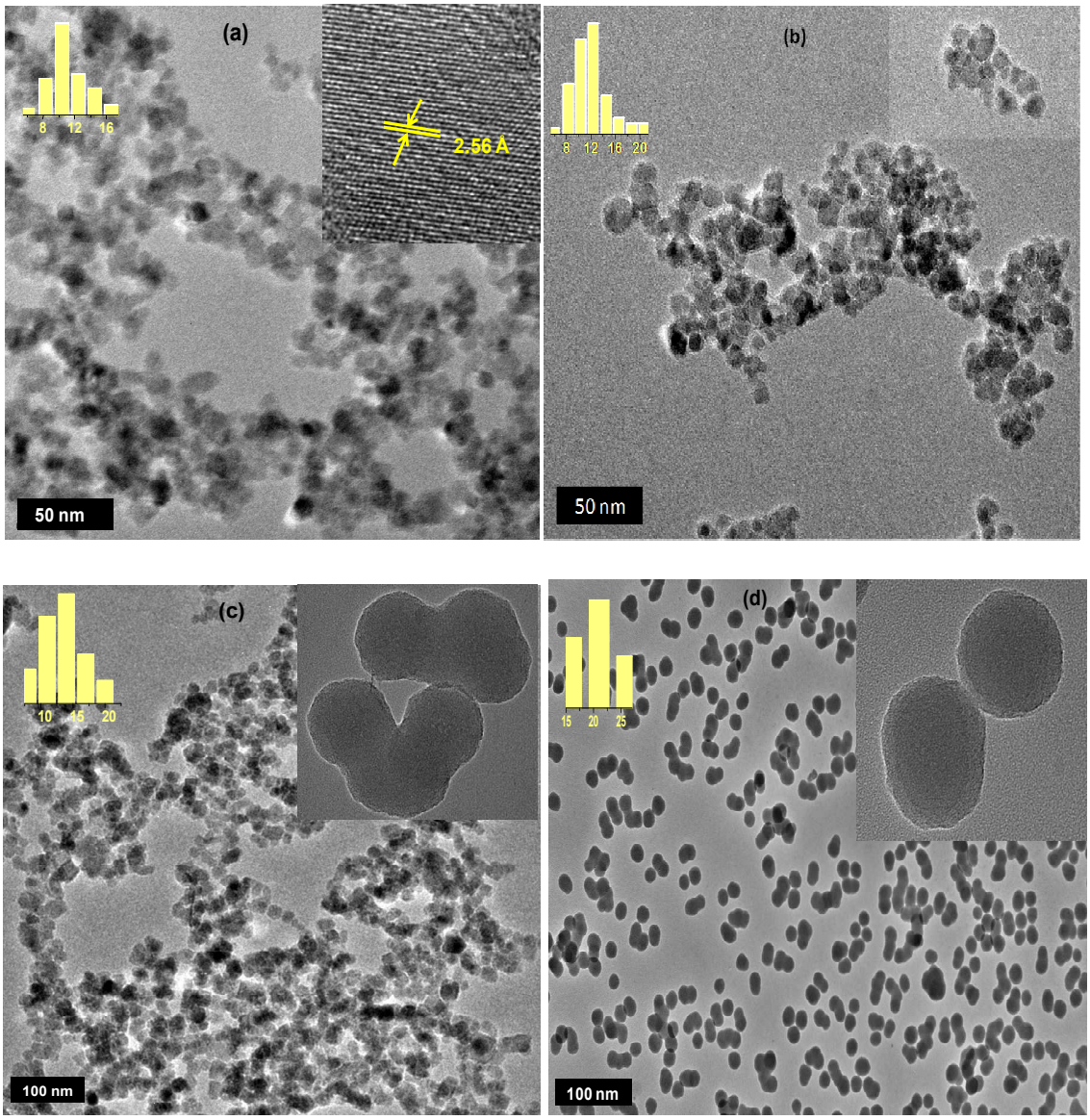

Figure 2

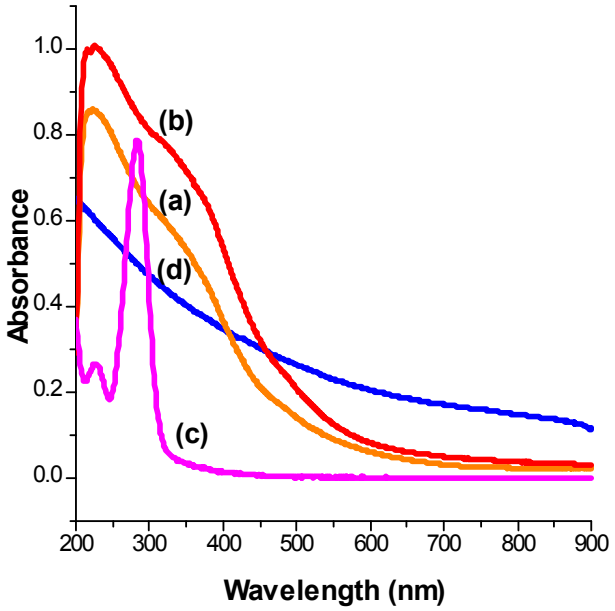

Figure 3

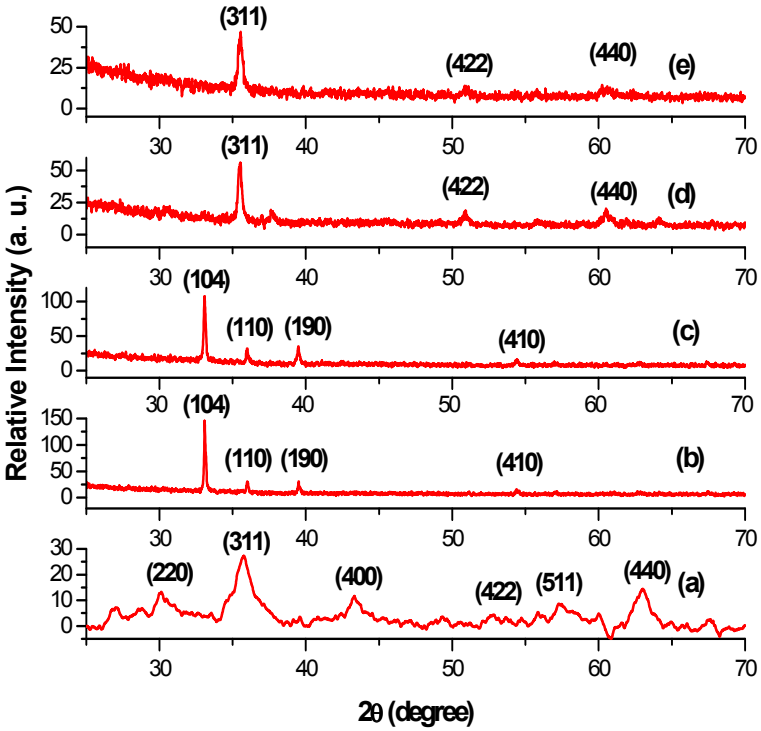

Figure 4

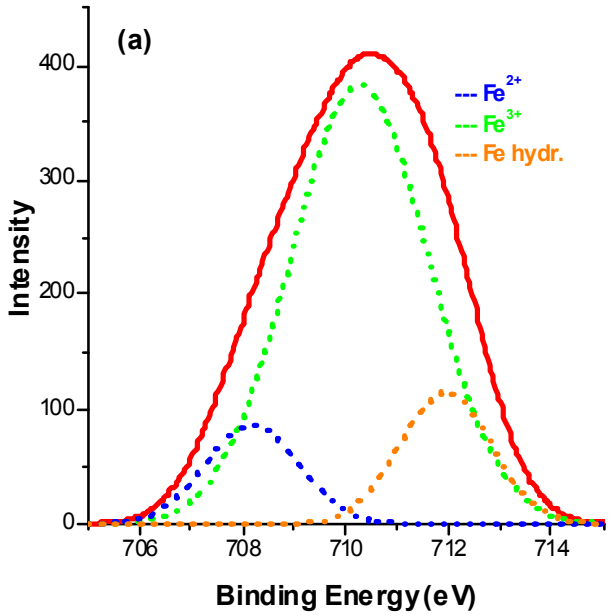

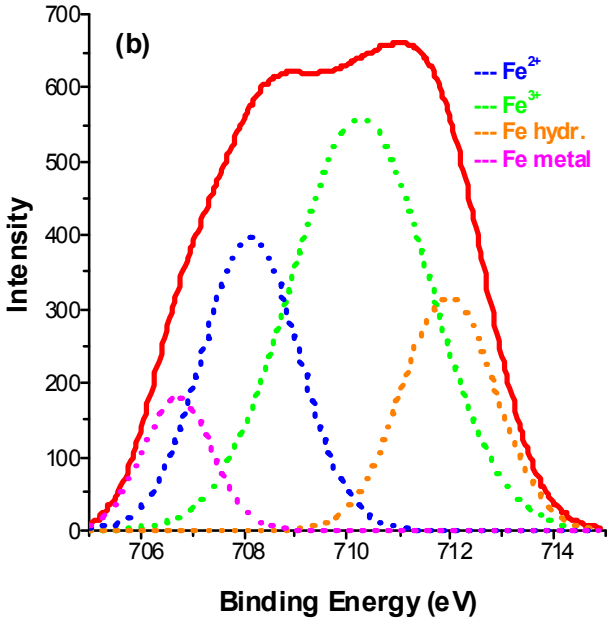

Figure 5

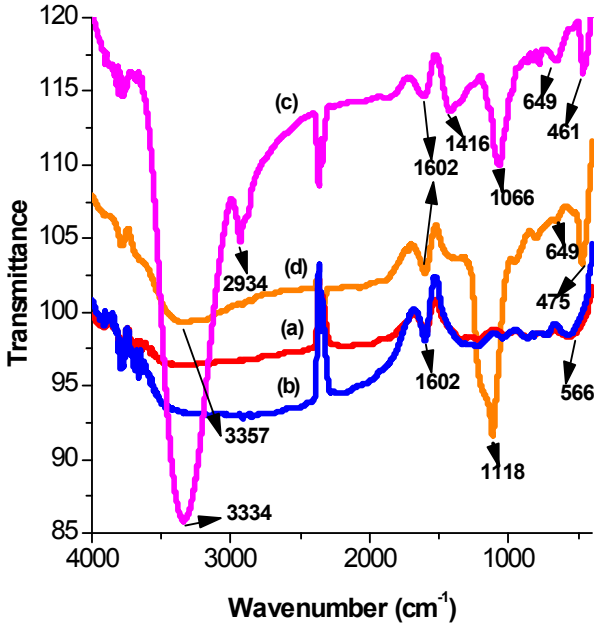

Figure 6

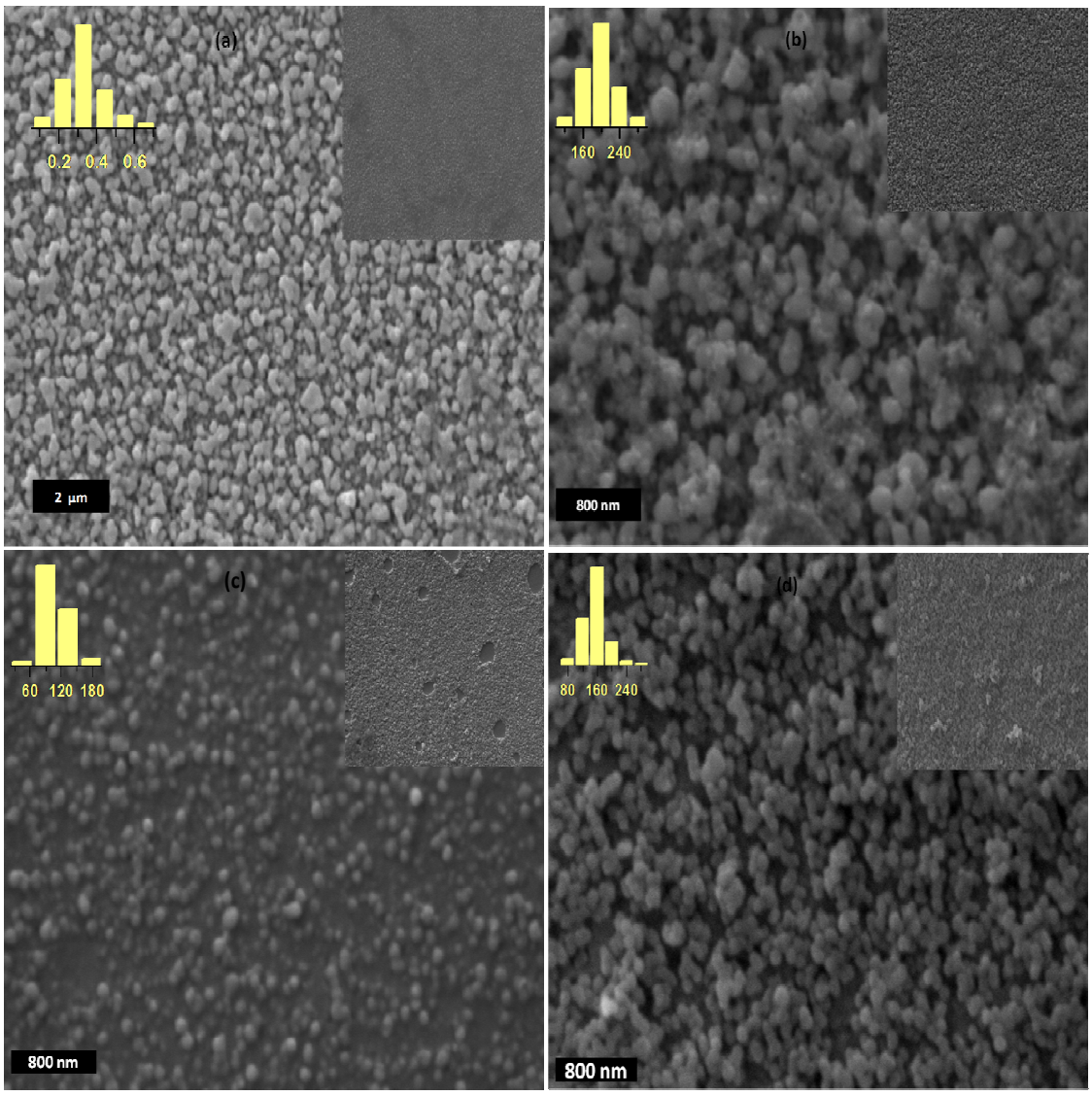

Figure 7

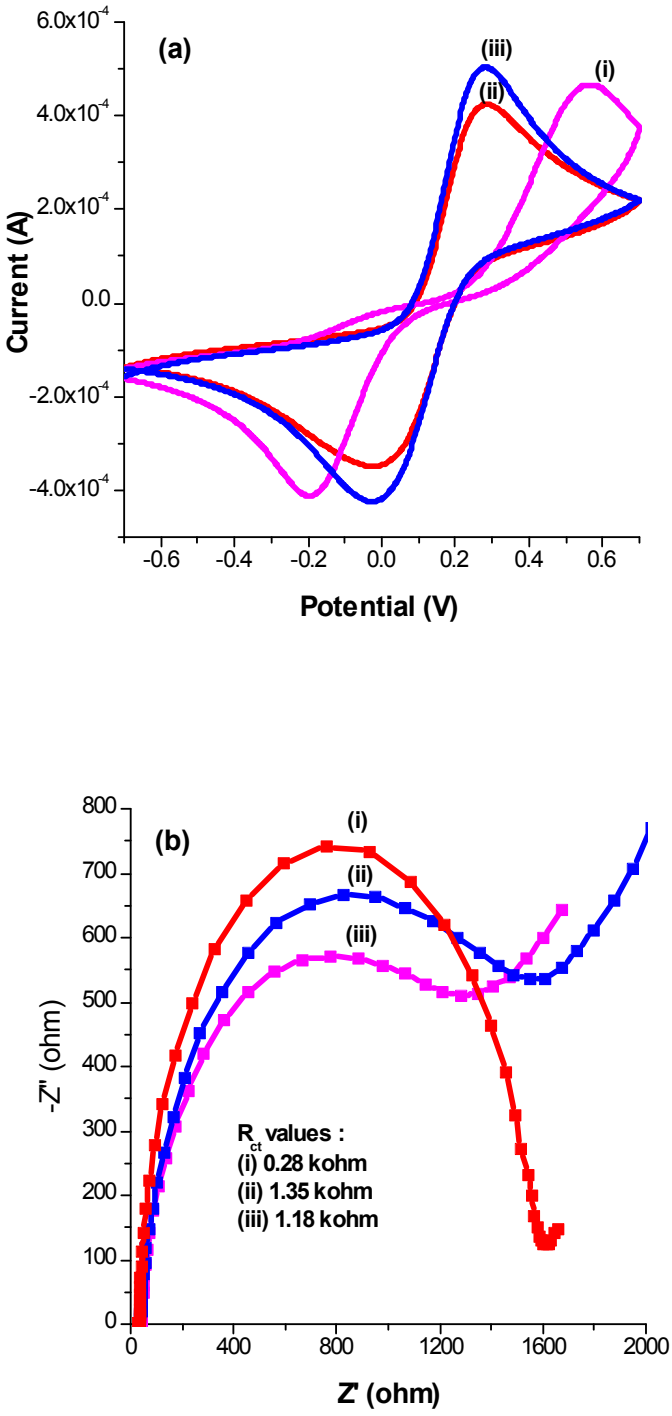

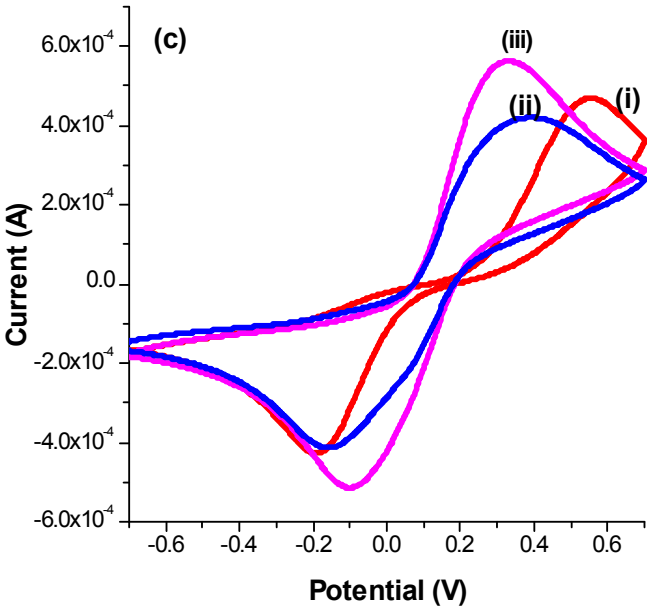

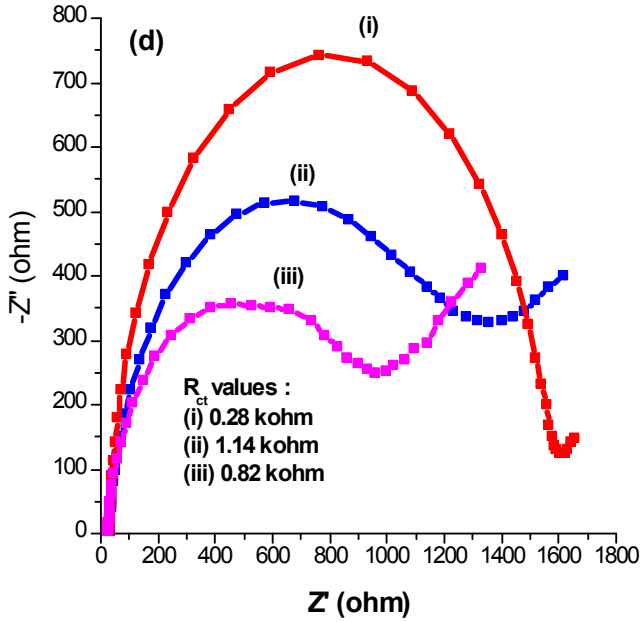

Figure 8

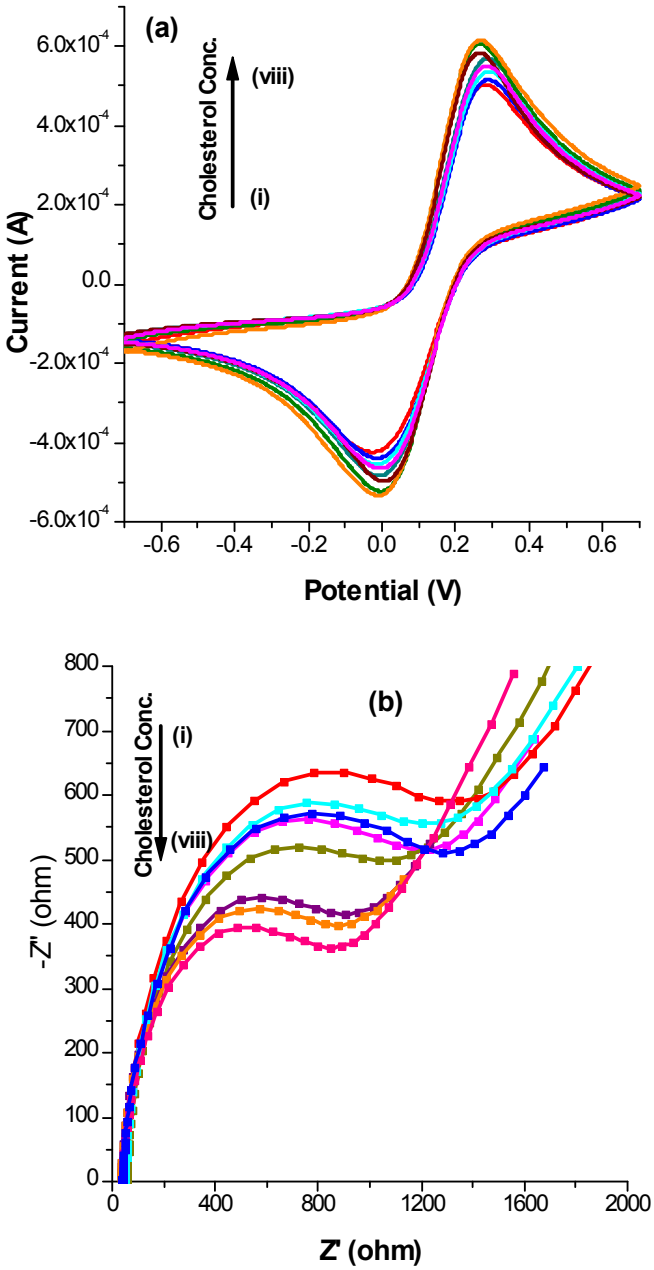

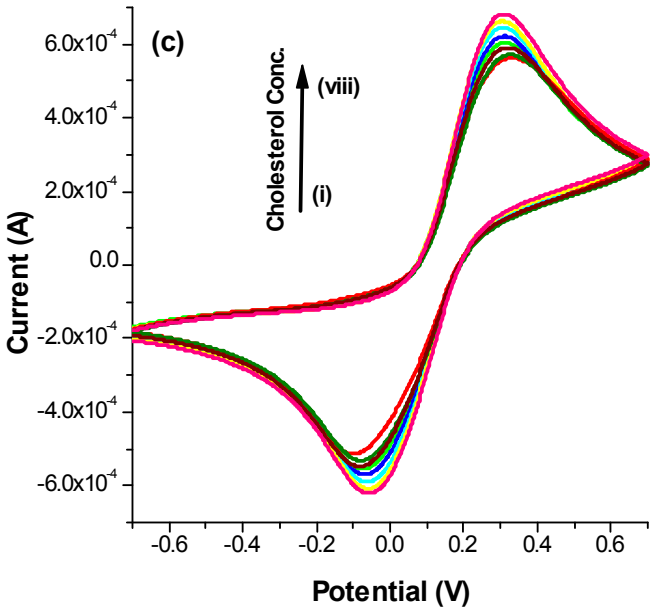

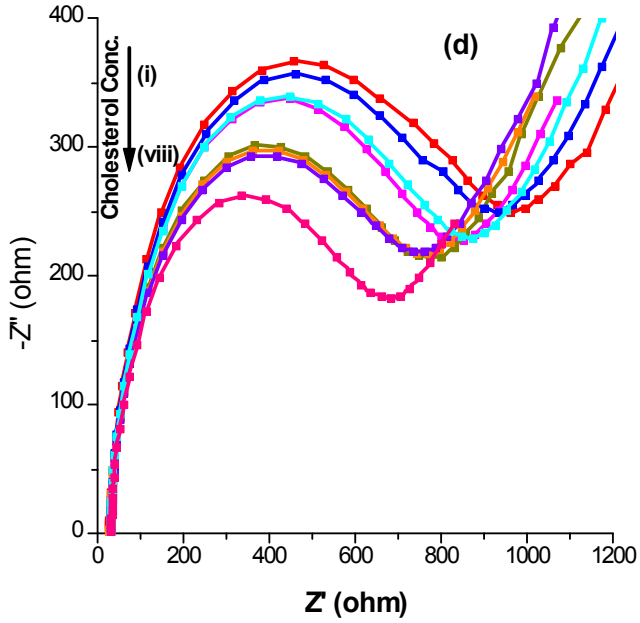

Figure 9

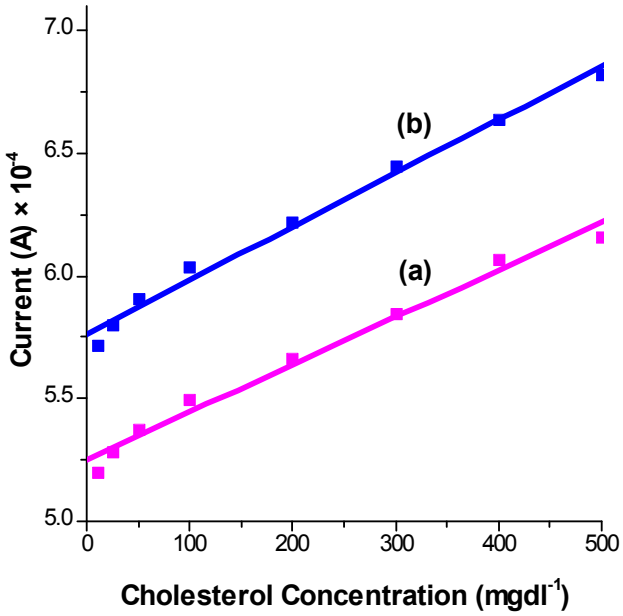

Figure 10

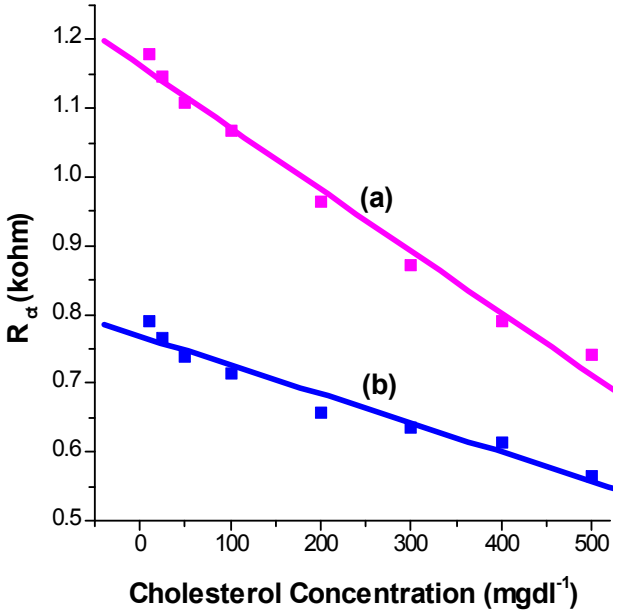

Table of Contents Graphic

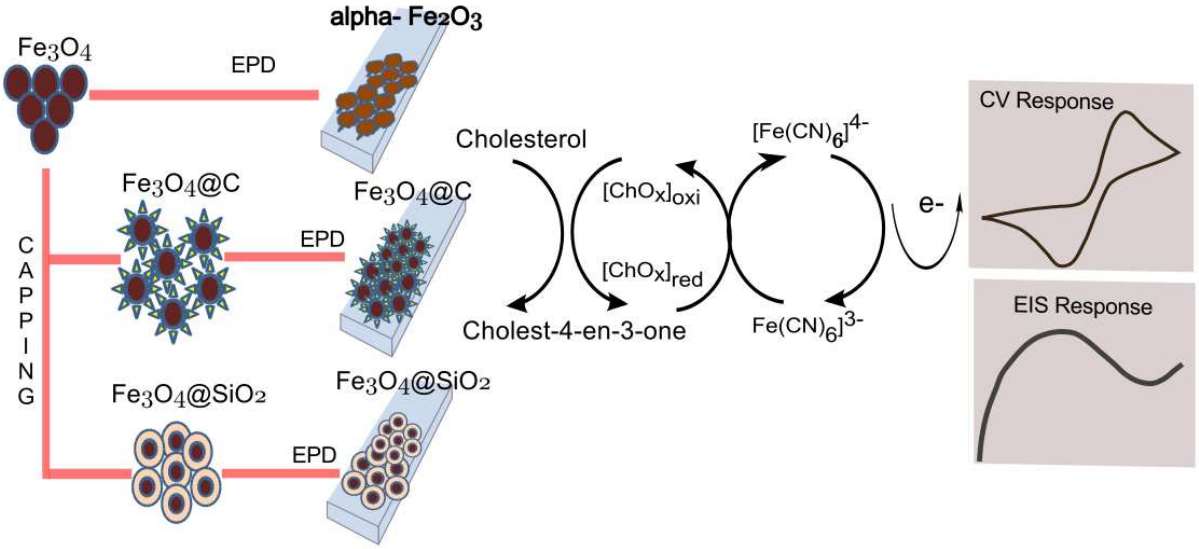

Rapid phase transformation of Fe_3O_4 NPs to α-Fe_2O_3 NPs during electrophoretic deposition and its phase control via organic and inorganic encapsulants. Fabrication of highly sensitive electrochemical cholesterol biosensor employing different phases of nanostructured iron oxide.

Some Exact Solutions of Magnetized viscous model in String Cosmology

C.P. Singh [a], **Vijay Singh**[b]

Department of Applied Mathematics,
Delhi Technological University (Formerly Delhi College of Engineering)
Bawana Road, Delhi-110 042, India.
[a] E-mail: cpsphd@rediffmail.com
[b] E-mail: gtrcosmo@gmail.com

Abstract In this paper we study anisotropic Bianchi-V universe with magnetic field and bulk viscous fluid in string cosmology. Exact solutions of the field equations are obtained by using the equation of state for a cloud of strings and a relationship between bulk viscous coefficient and expansion scalar. The bulk viscous coefficient is assumed to be inversely proportional to the expansion scalar. It is interesting to examine the effects of magnetized bulk viscous string model in early and late stages of the evolution of the universe. This paper investigates the different string models like geometrical(Nambu string), Takabayashi (p-string) and Reddy string models by taking certain physical conditions. The introduction of magnetic field or bulk viscosity or both results in rapid change in scale factors as well as in the classical potential. The presence of viscosity prevents the universe to be empty in its future evolution. The physical and geometrical aspects of each string model are discussed in detail.

Keywords: String cosmology; Magnetic field; Cosmological models; Bulk Viscosity.

PACS number(s): 98.80-k, 98.80-cq, 04.20-q.

1. Introduction

Recently the string cosmology has received considerable attention into the framework of general relativity mainly because of its possible role in the early universe. The concept of string cosmology was developed to describe the events at the very early stages of the evolution of the universe. The presence of the strings during the early universe can be explained using grand unified theories [1-3]. In the early stages of the evolution of the universe it is expected that topological defects could have formed naturally during the phase transitions followed by spontaneous broken symmetries. Cosmic strings are linear topological defects, have very interesting properties and might play an important role in the structure formation. These cosmic strings have stress energy and couple to the gravitational field. The gravitational effect of string in general relativity have been studied by Letelier [4] and Stachel [5]. Letelier [6] studied relativistic cosmological solutions of cloud formed by massive strings in Bianchi type-I and Kantowski-Sachs space-times. In these models each massive string is formed by a geometric string with particles attached along its extension. In principle the string can be eliminated and be ended up with the cloud of particles. This is a desirable property of a model of a string cloud to be used in cosmology. Matraverse [7] presented a class of exact solutions of Einstein field equations with a two parameter family of classical strings as the source of the gravitational field. Exact solutions of string cosmology in Bianchi type II, VI_0, VIII and IX space-times have been studied by Krori et al. [8]. Yavuz and Tarhan [9], Bali and Dave [10, 11], Bali and Upadhaya [12], Bali and Singh [13], Bali and Anjali [14], Bali and Pradhan [15], Pradhan and Chouhan [16], Mahanto et al.[17] are some of the authors who have investigated Bianchi type string cosmological models in general relativity.

The study of magnetic field provides an effective way to understand the initial phases of the cosmic evolution. Primordial magnetic field of cosmological origin have been discussed by Asseo and Sol [18], and Madsen[19]. Wolfe et al.[20], Kulsrud et al.[21], Barrow [22] are some of the authors who have studied the cosmological models with magnetic field and have pointed out its important in the early evolution of the universe. Matravers and Tsagas [23] have found that the interaction of the cosmological magnetic field with the space-time geometry could affect the expansion of the universe. Banerjee et al.[24], Chakraborty [25], Tikekar and Patel [26, 27] have studied Bianchi type I and III string cosmological models with and without source-free magnetic field. ShriRam and Singh [28] have obtained some new exact solutions of string cosmology with and without a source-free magnetic field in Bianchi type I space-time in different basic form. Patel and Maharaj [29] and Singh and Singh [30] have studied string cosmology with magnetic field in anisotropic models. Singh and ShriRam [31] have presented a technique to generate new exact Bianchi type III string cosmological solutions with magnetic field. Kilinç and Yavuz [32], Pradhan et al.[33], Pradhan [34], Bali and Jain [35], Saha and Visinescu [36], Pradhan et al.[37, 38], Saha et al.[39], Pradhan et al.[40], Amirhashchi et al.[41] and Rikhvitsky et al.[42] have investigated string cosmological models in the presence and absence of magnetic field. Recently, Singh and Singh [43] have studied anisotropic Bianchi V magnetized string model in general relativity and have discussed the effect of magnetic field in different string models.

The observations indicate that the media is not a perfect fluid and the viscosity is concerned in the evolution of the universe [44]. Bulk viscosity is of essential importance in

early universe. In order to study the evolution of the universe, many authors [45-53] have investigated cosmological models with a fluid containing viscosity. Yadav [54], Mohanty and Gauranga [55], Tripathy and Behara [56] are some of the authors who have studied string cosmological models with viscous fluid.

Bianchi type-V space-times are interesting to study the evolution of universe because of their richer structure both physically and geometrically than standard Freidmann-Roberson-Walker (FRW) models. These models represent the open FRW cosmological model. Coley [57], Singh et al.[58-60], Singh and Beesham [61], Singh [62] have studied Bianchi V models in general relativity in many physical contexts. Chakraborty and Chakraborty [63], and Bali [64] have studied string cosmology with magnetic field in Bianchi V space-time model for different directions of the magnetic field and string. Some authors [65, 66] have investigated anisotropic models with magnetic field and bulk viscosity in string cosmology. Recently, Sharif and Waheed [67], and Singh [68] have studied Bianchi I magnetized viscous fluid model in string cosmology and have discussed the effect of viscous fluid and magnetic field on the classical potential. Therefore, the study of magnetized cosmic strings with bulk viscosity leads to a better understanding of the dynamics of the universe during early and late stages of the evolution in a more generalized cosmological models.

The aim of this paper is to extend our earlier work [43] to find some exact solutions for Bianchi V model with magnetized viscous fluid in string cosmology. The equation of state for a cloud of strings and the inverse relation between expansion scalar and bulk viscous coefficient are used to solve the field equations exactly. The paper is organized as follows.

In section 2 the field equations for Bianchi V model with bulk viscosity and magnetic field in string cosmology are presented. Section 3 deals with the solution of field equations where a general quadrature form of volume scale factor of the model is given. Three different exact string models are presented in subsections 4.1, 4.2 and 4.3 of section 4. We discuss the various physical parameters in each case. Lastly, we present a summary of the results in section 5.

2. Model and Basic Equations

We consider the homogenous and anisotropic Bianchi -V metric in the form

$$ds^2 = -dt^2 + A^2dx^2 + e^{2x}\left(B^2dy^2 + C^2dz^2\right), \tag{1}$$

where A, B, and C are functions of cosmic time t only and are the scale factors in anisotropic background.

The energy-momentum tensor for bulk viscous string dust with magnetic field is given by [6, 69]

$$T_i^j = \rho u_i u^{\,j} - \lambda x_i x^j - \xi u^l{}_{;l}\left(g_i^j + u_i u^j\right) + E_i{}^j, \tag{2}$$

where ρ is the proper energy density for a cloud of strings with particles attached to them and λ is the string tensor density and is related by $\rho = \rho_p + \lambda$, where ρ_p is the particle energy density. The unit time-like vector u^i describes the particle's four velocity and unit space-like vector x^i denotes the direction of the string which can be taken along any of the three directions x, y and z axes. Thus, without loss of generality let us choose $x-$ direction

as the direction of the string along which the magnetic field is assumed to be present, i.e.,

$$x^i = (A^{-1}, 0, 0, 0) \tag{3}$$

In a co-moving coordinate system, we have

$$u^i = (0, 0, 0, 1) \tag{4}$$

Therefore, we have

$$u_i u^i = -x_i x^i = -1, \;\; u_i x^i = 0. \tag{5}$$

In Eq. (2), ξ is the coefficient of bulk viscosity, $u^l_{;l} = \theta$ is the expansion scalar and $E_i^{\;j}$ is the electromagnetic field tensor which is given by (see, ref.[70])

$$E_i^{\;j} = \bar{\mu}\left[|h|^2\left(u_i u^j + \frac{1}{2}g_i^{\;j}\right) - h_i h^j\right], \tag{6}$$

where $\bar{\mu}$ is the magnetic permeability, and h_i, the magnetic flux vector defined by

$$h_i = \frac{1}{\bar{\mu}}\bar{F}_{ij}u^j. \tag{7}$$

The dual electromagnetic field tensor $\bar{F}_{ij}$ is defined as

$$\bar{F}_{ij} = \frac{\sqrt{-g}}{2}\epsilon_{ijkl}F^{kl} \tag{8}$$

where F_{ij} is the electromagnetic field tensor and ϵ_{ijkl} is the Levi-Civita tensor density.

We assume that the magnetic field is generated in yz plane as its source is the electric current that flows in $x-$ direction. Therefore, the magnetic flux vector has only one non-zero component h_1, i.e., $h_1 \neq 0$, $h_2 = 0 = h_3 = h_4$. Moreover, the assumption of infinitely electrical conductivity [71] along with finite current leads to $F_{14} = 0 = F_{24} = F_{34}$.

Using Maxwell's equations

$$F_{ij;k} + F_{jk;i} + F_{ki;j} = 0, \;\; \text{and} \;\; F^{ij}_{\;\;;k} = 0, \tag{9}$$

we find

$$F_{23} == I, \quad \text{a constant.} \tag{10}$$

Hence, the non-zero component of magnetic flux vector is

$$h_1 = \frac{AI}{\bar{\mu}BC}. \tag{11}$$

Since $|h|^2 = h_l h^l = h_1 h^1 = g^{11}(h_1)^2$, therefore,

$$|h|^2 = \frac{I^2}{\bar{\mu}^2 B^2 C^2}\,. \tag{12}$$

Using Eqs. (11) and (12) into (6), the components of E_i^j are given by

$$E^1_{\ 1} = -\frac{I^2}{2\bar{\mu}^2 B^2 C^2} = -E^2_{\ 2} = -E^3_{\ 3} = E^4_{\ 4}. \tag{13}$$

The Einstein's field equations (in gravitational units $c = 8\pi G = 1$) read as

$$R_i^{\ j} - \frac{1}{2} g_i^{\ j} R = -T_i^{\ j}. \tag{14}$$

where R_i^j is the Ricci tensor and $R = g^{ij} R_{ij}$ is the Ricci scalar.

The field equations (14) with (1) and (2) subsequently lead to the following system of equations

$$\frac{\dot{A}\dot{B}}{AB} + \frac{\dot{B}\dot{C}}{BC} + \frac{\dot{C}\dot{A}}{CA} - \frac{3}{A^{\,2}} = \rho + \frac{I^2}{2\bar{\mu}B^{\,2}C^{\,2}}, \tag{15}$$

$$\frac{\ddot{A}}{A} + \frac{\ddot{C}}{C} + \frac{\dot{A}\dot{C}}{AC} - \frac{1}{A^2} = -\frac{I^2}{2\bar{\mu}B^{\,2}C^{\,2}} + \xi\theta, \tag{16}$$

$$\frac{\ddot{A}}{A} + \frac{\ddot{B}}{B} + \frac{\dot{A}\dot{B}}{AB} - \frac{1}{A^2} = -\frac{I^2}{2\bar{\mu}B^{\,2}C^{\,2}} + \xi\theta, \tag{17}$$

$$\frac{\ddot{B}}{B} + \frac{\ddot{C}}{C} + \frac{\dot{B}\dot{C}}{BC} - \frac{1}{A^2} = \lambda + \frac{I^2}{2\bar{\mu}B^{\,2}C^{\,2}} + \xi\theta, \tag{18}$$

$$2\frac{\dot{A}}{A} - \frac{\dot{B}}{B} - \frac{\dot{C}}{C} = 0, \tag{19}$$

where the overdots indicate ordinary differentiation with respect to t.

Let us define the volume scale factor τ as

$$\tau = ABC. \tag{20}$$

Let us consider the various important physical quantities such as expansion scalar θ, anisotropy parameter Δ and shear scalar σ^2, which are defined as

$$\theta = u^l_{;l} = \frac{\dot{A}}{A} + \frac{\dot{B}}{B} + \frac{\dot{C}}{C} = \frac{\dot{\tau}}{\tau}, \tag{21}$$

$$\Delta = \frac{1}{3}\sum_{i=1}^{3}\left(\frac{H_i - H}{H}\right)^2, \tag{22}$$

$$\sigma^2 = \frac{1}{2}\,\sigma_{ij}\sigma^{ij} = \frac{1}{3}\Delta H^2. \tag{23}$$

Here, $H = \frac{\theta}{3}$ is the mean Hubble parameter and $H_1 = \frac{\dot{A}}{A}$, $H_1 = \frac{\dot{B}}{B}$ and $H_1 = \frac{\dot{C}}{C}$ are the directional Hubble parameters in the directions of x, y and z axes, respectively.
The energy conservation equation $T^j_{i;j} = 0$ takes the form

$$\dot{\rho} + \frac{\dot{\tau}}{\tau}\rho - \frac{\dot{A}}{A}\lambda = \xi\frac{\dot{\tau}^2}{\tau^2}, \tag{24}$$

which is a consequence of field equations (15) -(19).

3. Solution of the field equations

To solve the field equations (15)-(19), we follow the method recently used by Saha and Visinescu [36]. From (16) and (17) we get

$$\frac{d}{dt}\left(\frac{\dot{C}}{C}-\frac{\dot{B}}{B}\right)+\left(\frac{\dot{C}}{C}-\frac{\dot{B}}{B}\right)\left(\frac{\dot{A}}{A}+\frac{\dot{B}}{B}+\frac{\dot{C}}{C}\right)=0. \tag{25}$$

Using (20) into (25), we get

$$\frac{d}{dt}\left(\frac{\dot{C}}{C}-\frac{\dot{B}}{B}\right)+\left(\frac{\dot{C}}{C}-\frac{\dot{B}}{B}\right)\frac{\dot{\tau}}{\tau}=0, \tag{26}$$

which on integration it gives

$$C=d_1B\exp\left(k_1\int\frac{dt}{\tau}\right), \tag{27}$$

where d_1 and k_1 are constants of integration.

From (19) we get

$$A^2=d_2BC, \tag{28}$$

where d_2 is a constants of integration, which has been taken unity without loss of generality.

From (15)-(18) and (28), we obtain

$$\frac{\ddot{\tau}}{\tau}=\frac{1}{2}\left[(3\rho+\lambda)+\frac{A^2I^2}{\bar{\mu}\tau^2}\right]+\frac{3}{2}\xi\theta+\frac{6}{\tau^{2/3}}. \tag{29}$$

From Eqs. (20), (27) and (28), we find the following form of metric functions in terms of τ as

$$A=\tau^{\frac{1}{3}}, \tag{30}$$

$$B=\frac{1}{\sqrt{d_1}}\,\tau^{\frac{1}{3}}\exp\left[-\frac{k_1}{2}\int\frac{dt}{\tau}\right], \tag{31}$$

$$C=\sqrt{d_1}\,\tau^{\frac{1}{3}}\exp\left[\frac{k_1}{2}\int\frac{dt}{\tau}\right]. \tag{32}$$

Now, Eqs. (24) and (29) take the forms

$$\dot{\rho}+\left(\rho-\frac{\lambda}{3}\right)\frac{\dot{\tau}}{\tau}=\xi\frac{\dot{\tau}^2}{\tau^2}, \tag{33}$$

and

$$\ddot{\tau}=\frac{1}{2}(3\rho+\lambda)\tau+\frac{k}{2}\,\tau^{-\frac{1}{3}}+6\tau^{\frac{1}{3}}+\frac{3}{2}\xi\theta\tau, \tag{34}$$

where $k = \frac{I^2}{\bar{\mu}}$.

Consider the equation of state for a cloud of string models[6]

$$\rho = \alpha\lambda, \tag{35}$$

where the constant α is defined by

$$\begin{aligned} \alpha &= 1 \quad (geometric\ or\ Nambu\ string), \\ &= (1+\omega) \quad (p-\ string\ or\ Takabayasi\ string), \\ &= -1 \quad (Reddy\ string), \end{aligned} \tag{36}$$

where ω is a constant such that $\omega > 0$. We further assume that the bulk viscosity is inversely proportional to the expansion scalar [72],i.e.,

$$\xi\theta = k_2, \tag{37}$$

where k_2 is a positive constant. From (33) and (35), we get

$$\frac{\dot{\rho}}{\left(1-\frac{1}{3\alpha}\right)\rho - k_2} = -\frac{\dot{\tau}}{\tau}, \tag{38}$$

which on integration, it gives

$$\rho = \frac{3\alpha}{(3\alpha-1)}\left[k_2 + k_3\tau^{-\left(\frac{3\alpha-1}{3\alpha}\right)}\right], \tag{39}$$

where k_3 is a constant of integration. For $\rho > 0$, it must have either $\alpha > 1/3$ or $\alpha < 0$. It means that all the above three string models (36) may be described by assuming the relation (37). Further, inserting ρ from (39) into (34) one finds

$$\ddot{\tau} = \frac{3\left(3\alpha+1\right)k_3}{2\left(3\alpha-1\right)}\tau^{\frac{1}{3\alpha}} + \frac{k}{2}\tau^{-\frac{1}{3}} + 6\tau^{\frac{1}{3}} + \frac{1}{2}\left(\frac{18\alpha}{3\alpha-1}\right)k_2\tau, \tag{40}$$

whose solution is

$$\dot{\tau}^2 = \left(\frac{9\alpha k_3}{3\alpha-1}\right)\tau^{\frac{3\alpha+1}{3\alpha}} + \frac{3}{2}k\tau^{\frac{2}{3}} + 9\tau^{\frac{4}{3}} + \left(\frac{9\alpha k_2}{3\alpha-1}\right)\tau^2 + k_4, \tag{41}$$

where k_4 is a constant of integration. Eq.(41) can be rewritten as

$$\dot{\tau} = \sqrt{\left(\frac{9\alpha k_3}{3\alpha-1}\right)\tau^{\frac{3\alpha+1}{3\alpha}} + \frac{3}{2}k\tau^{\frac{2}{3}} + 9\tau^{\frac{4}{3}} + \left(\frac{9\alpha k_2}{3\alpha-1}\right)\tau^2 + k_4}. \tag{42}$$

Taking into account that the energy density and string tension density obey equation of state (35), we conclude that ρ and λ, i.e., the right hand side of Eq.(34) is a function of τ only, i.e.,

$$\ddot{\tau} = F(\tau). \tag{43}$$

From the mechanical point of view, Eq. (43) can be interpreted as equation of motion of a single particle with unit mass under the force $F(\tau)$. Then the following first integral exists

$$\dot{\tau} = \sqrt{2[\epsilon - u(\tau)]}, \tag{44}$$

where ϵ can be viewed as energy level and $u(\tau)$ is the potential of the force F. A comprehensive description concerning potential can be found in ref.[73]. Comparing (42) and (44), we find $\epsilon = k_4/2$ and

$$u(\tau) = -\frac{1}{2}\left[\left(\frac{9\alpha k_3}{3\alpha - 1}\right)\tau^{\frac{3\alpha+1}{3\alpha}} + \frac{3}{2}k\tau^{\frac{2}{3}} + 9\tau^{\frac{4}{3}} + \left(\frac{9\alpha k_2}{3\alpha - 1}\right)\tau^2\right]. \tag{45}$$

Finally, we write Eq. (42) in a general quadrature form as

$$\int \frac{d\tau}{\sqrt{\left(\frac{9\alpha k_3}{3\alpha-1}\right)\tau^{\frac{3\alpha+1}{3\alpha}} + \frac{3}{2}k\tau^{\frac{2}{3}} + 9\tau^{\frac{4}{3}} + \left(\frac{9\alpha k_2}{3\alpha-1}\right)\tau^2 + k_4}} = t + t_0, \tag{46}$$

where the integration constant t_0 can be taken as zero for simplicity.

4. Solution of various string models

We observe that it is too difficult to solve (46), in general. Therefore, we present the following three string models depending on the values of α as defined in (36).

4.1 Geometric string model ($\alpha = 1$)

For $k_4 = 0$, Eq. (46) reduces to

$$\int \frac{d\tau}{\sqrt{\frac{9}{2}(k_3+2)\tau^{\frac{4}{3}} + \frac{3}{2}k\tau^{\frac{2}{3}} + \frac{9}{2}k_2\tau^2}} = t. \tag{47}$$

When $3(k_3+2)^2 > 4kk_2$, Eq.(47) gives

$$\tau = \left[\frac{1}{2k_2}\sqrt{\frac{3(k_3+2)^2 - 4kk_2}{3}}\,\cosh\left(\sqrt{2k_2}\,t\right) - \frac{k_3+2}{2k_2}\right]^{\frac{3}{2}}, \qquad k_2 \neq 0, \tag{48}$$

and for $3(k_3+2)^2 < 4kk_2$, we get

$$\tau = \left[\frac{1}{2k_2}\sqrt{\frac{4kk_2 - 3(k_3+2)^2}{3}}\,\sinh\left(\sqrt{2k_2}\,t\right) - \frac{k_3+2}{2k_2}\right]^{\frac{3}{2}}, \qquad k_2 \neq 0, \tag{49}$$

For small t (i.e., near t=0), we have $\cosh\left(\sqrt{2k_2}\,t\right) \approx \sqrt{2k_2}\,t$ and $\sinh\left(\sqrt{2k_2}\,t\right) \approx \sqrt{2k_2}\,t$. Therefore, (48) and (49) together can be written as

$$\tau = (P_1 t - Q_1)^{3/2}, \tag{50}$$

where $P_1 = \sqrt{\frac{|3(k_3+2)^2-4kk_2|}{6k_2}}$ and $Q_1 = \frac{k_3+2}{2k_2}$. At $t = 0$, τ becomes imaginary. For reality of the model, t must satisfy $t > \frac{Q_1}{P_1}$.

Using (50), Eqs.(30)-(32) take the forms

$$A = \sqrt{P_1 t - Q_1}, \tag{51}$$

$$B = \frac{1}{\sqrt{d_1}}\sqrt{P_1 t - Q_1}\ \exp\left[\frac{k_1}{P_1\sqrt{P_1 t - Q_1}}\right], \tag{52}$$

$$C = \sqrt{d_1}\sqrt{P_1 t - Q_1}\ \exp\left[-\frac{k_1}{P_1\sqrt{P_1 t - Q_1}}\right]. \tag{53}$$

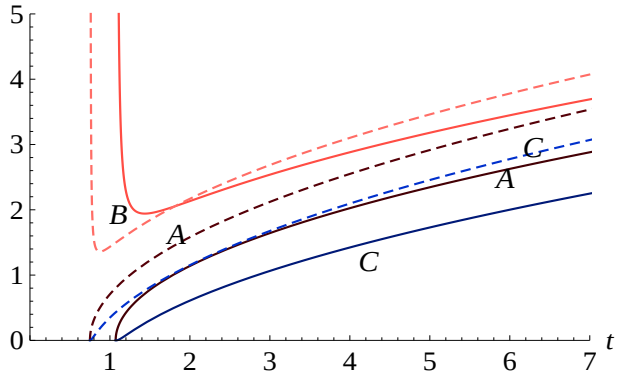

Fig. 1 Evolution of the universe with viscous fluid and magnetic field (bold lines) and with viscous fluid only (dashed lines).

Figure 1 illustrates the graph of the scale factors with respect to time in the presence of viscous fluid and magnetic field for $k_1 = 1 = k_2 = k_3 = d_1$, $I = 2$ and $\bar{\mu} = 1.00001$. The model starts expanding rapidly with time for $t > \frac{Q_1}{P_1}$, which tends to ∞ as $t \to \infty$. At $t = \frac{Q_1}{P_1}$, A and C become zero but B decreases from infinite value to a certain constant and then starts expanding with time. This expansion happens in both the cases, i.e., the presence of viscous fluid and magnetic field, and in the presence of viscous fluid only. In case of viscous model, t must satisfy $t > \frac{1}{\sqrt{2k_2}}$ for the expansion of the universe. The expansion of scale factors with respect to time in the presence of viscous fluid are shown by dotted lines in figure 1. We observe that the evolution starts earlier and goes faster than the magnetized viscous fluid model as shown by bold lines or magnetized field only (see, ref. Singh and Singh [43] for detail). Therefore, we may say that the bulk viscosity plays an important role in the expansion history of the universe.

The directional Hubble parameters along x, y and z axes are respectively given by

$$H_1 = \frac{P_1}{2(P_1 t - Q_1)}, \tag{54}$$

$$H_2 = \frac{P_1}{2(P_1 t - Q_1)} - \frac{k_1}{2(P_1 t - Q_1)^{\frac{3}{2}}}, \tag{55}$$

$$H_3 = \frac{P_1}{2(P_1t - Q_1)} + \frac{k_1}{2(P_1t - Q_1)^{\frac{3}{2}}}. \tag{56}$$

The average Hubble parameter in terms of cosmic time t is

$$H = \frac{P_1}{2(P_1t - Q_1)}. \tag{57}$$

The anisotropic parameter and shear scalar, respectively have the following expressions

$$\Delta = \frac{2k_1^2}{3P_1^2(P_1t - Q_1)}, \tag{58}$$

$$\sigma^2 = \frac{k_1^2}{4(P_1t - Q_1)^3}. \tag{59}$$

The above physical parameters (54) - (59) diverse at $t = \frac{Q_1}{P_1}$ and tend to zero as $\to \infty$. From (57) and (59), we get

$$\frac{\sigma}{\theta} = \frac{k_1}{3P_1\sqrt{(P_1t - Q_1)}}, \tag{60}$$

which is zero as $t \to \infty$. This shows that the model becomes isotropic in late time. The deceleration parameter becomes $q = 1$, which is a positive constant. Therefore, the present model expands with the decelerated rate throughout the evolution.

The energy density and string tension density are given by

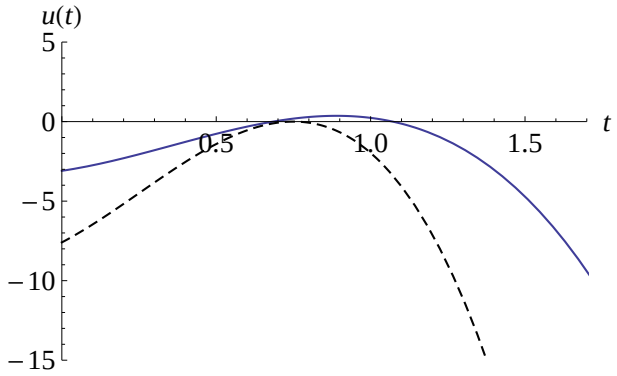

Fig. 2 Potential versus time with viscous fluid and magnetic field (bold lines) and with viscous fluid only (dashed lines).

$$\rho = \lambda = \frac{3}{2}\left(k_2 + \frac{k_3}{P_1t - Q_1}\right), \tag{61}$$

which shows that the matter behaves as a cloud of geometric strings. The particle density, ρ_p remains zero throughout the evolution. We observe that ρ and λ remains positive through out the evolution and become infinite at the initial epoch at $t = \frac{Q_1}{P_1}$. However, ρ and λ

decrease with time for $t > \frac{Q_1}{P_1}$ and these approach to a constant value, $\frac{3}{2}k_2$ as $t \to \infty$. The constant value of ρ is due to the the viscous term, k_2. It means that the viscosity parameter prevents the universe to be empty at late times of its evolution. The classical potential (45) in terms of t takes the form

$$u(t) = -\frac{3}{4}\left[3k_2(P_1t - Q_1)^3 + 3(k_3+2)(P_1t - Q_1)^2 + k(P_1t - Q_1)\right]. \tag{62}$$

Figure 2. plots the potential with respect to time in the presence of viscous fluid and magnetic field (bold line) and with viscous fluid only (dashed line) for $k_2 = 1 = k_3$, $I = 2$ and $\bar{\mu} = 1.00001$. We observe that $\mu(t)$ shows negative and positive nature with respect to time t in magnetized viscous fluid. However, it has negative in the presence of viscous fluid only. It is also found that there is much variation between theses two cases.

4.2. Reddy string model($\alpha = -1$)

For $k_4 = 0$, Eq. (46) becomes

$$\int \frac{d\tau}{\sqrt{9\tau^{\frac{4}{3}} + \frac{3}{4}(3k_3 + 2k)\tau^{\frac{2}{3}} + \frac{9}{4}k_2\tau^2}} = t. \tag{63}$$

When $k_2\,(3k_3 + 2k) > 12$, Eq.(63) gives

$$\tau = \left[\frac{1}{k_2}\sqrt{\frac{k_2(3k_2+2k) - 12}{3}}\,\sinh\left(\sqrt{k_2}\,t\right) - \frac{2}{k_2}\right]^{\frac{3}{2}}, \tag{64}$$

and for $k_2\,(3k_3 + 2k) < 12$, we get

$$\tau = \left[\frac{1}{k_2}\sqrt{\frac{12 - k_2(3k_2+2k)}{3}}\,\cosh\left(\sqrt{k_2}\,t\right) - \frac{2}{k_2}\right]^{\frac{3}{2}}, \tag{65}$$

For small t (i.e., near t=0), we have $\sinh\left(\sqrt{k_2}\,t\right) \approx \sqrt{k_2}\,t$ and $\cosh\left(\sqrt{k_2}\,t\right) \approx \sqrt{k_2}\,t$. Therefore, (64) and (65) together can be written as

$$\tau = (P_2t - Q_2)^{3/2}, \tag{66}$$

where $P_2 = \sqrt{\frac{1}{3k_2}|12 - k_2(3k_2+2k)|}$ and $Q_2 = \frac{2}{k_2}$.

At $t = 0$, τ becomes imaginary. For reality of the model, t must satisfy $t > \frac{Q_2}{P_2}$. From Eqs.(30)-(32) and (66), we find

$$A = \sqrt{P_2t - Q_2}, \tag{67}$$

$$B = \frac{1}{\sqrt{d_1}}\sqrt{P_2t - Q_2}\,\exp\left[\frac{k_1}{P_2\sqrt{P_2t - Q_2}}\right], \tag{68}$$

$$C = \sqrt{d_1}\sqrt{P_2t - Q_2}\,\exp\left[-\frac{k_1}{P_2\sqrt{P_2t - Q_2}}\right]. \tag{69}$$

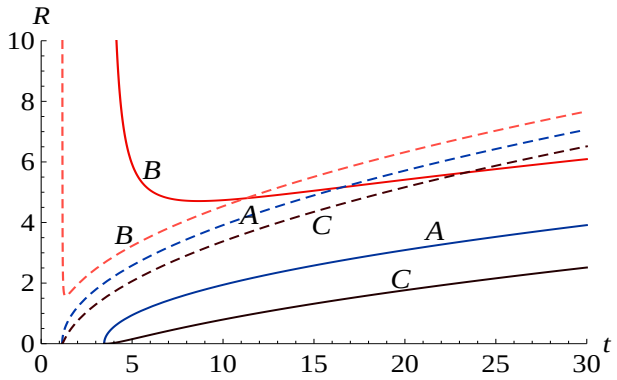

Fig. 3 Evolution of the universe with viscous fluid and magnetic field (bold lines) and with viscous fluid only (dashed lines).

Figure 3 plots the graph of scale factors with respect to t in the presence of magnetized viscous fluid (bold lines) and in the presence of viscous only (dashed lines) for $k_1 = 1 = k_2 = k_3 = d_1$, $I = 2$ and $\bar{\mu} = 1.00001$. We observe that all the scale factors expand with the passage of time in both cases. The interpretations can be made as the previous discussion in the case of geometric string model. The scale factors A and C start expansion from zero for $t > Q_2/P_2$ whereas the scale factor B evolves expansion from some finite value in both the cases. The viscous fluid increases the rate of expansion as shown by dashed lines.

The directional Hubble parameters along x, y and z axes are respectively given by

$$H_1 = \frac{P_2}{2(P_2t - Q_2)}, \tag{70}$$

$$H_2 = \frac{P_2}{2(P_2t - Q_2)} - \frac{k_1}{2(P_2t - Q_2)^{\frac{3}{2}}}, \tag{71}$$

$$H_3 = \frac{P_2}{2(P_2t - Q_)} + \frac{k_1}{2(P_2t - Q_2)^{\frac{3}{2}}}. \tag{72}$$

The average Hubble parameter in terms of cosmic time t is

$$H = \frac{P_2}{2(P_2t - Q_2)}. \tag{73}$$

The anisotropic parameter and shear scalar, respectively take the forms

$$\Delta = \frac{2k_1^2}{3P_2^2(P_2t - Q_2)}, \tag{74}$$

$$\sigma^2 = \frac{k_1^2}{4(P_2t - Q_2)^3}. \tag{75}$$

The above physical parameters in Eqs.(70) - (75) diverge at $t = \frac{Q_2}{P_2}$ and asymptotically tend to zero as $t \to \infty$. From (73) and (75), we get

$$\frac{\sigma}{\theta} = \frac{k_1}{3P_2\sqrt{(P_2t - Q_2)}}. \tag{76}$$

We find that (76) tends to zero as $t \to \infty$. Therefore, this string model also becomes isotropic for large t. The energy density, string tension density and particle density are respectively given by

$$\rho = \frac{3}{4}\left[k_2 + \frac{k_3}{(P_2t - Q_2)^2}\right], \tag{77}$$

$$\lambda = -\frac{3}{4}\left[k_2 + \frac{k_3}{(P_2t - Q_2)^2}\right], \tag{78}$$

$$\rho_p = \frac{3}{2}\left[k_2 + \frac{k_3}{(P_2t - Q_2)^2}\right]. \tag{79}$$

Figure 4 plots the graph of energy density, energy tension density and particle density with

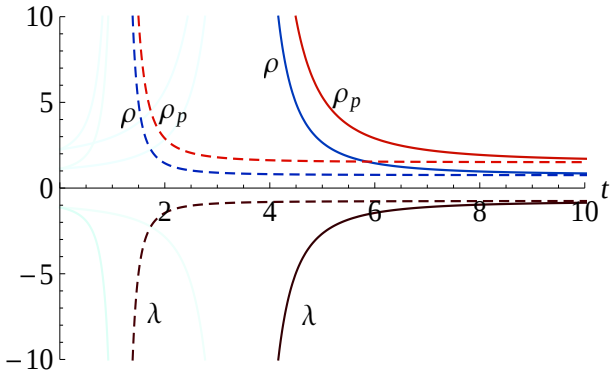

Fig. 4 Energy density, string tension density and particle density versus time with viscous fluid and magnetic field (bold lines) and with viscous fluid only (dashed lines)

respect to time in presence of magnetized viscous fluid (bold lines) and in presence of viscous only (dashed lines) for $k_2 = 1 = k_3$, $I = 2$ and $\bar{\mu} = 1.00001$. The figure shows that the energy density and particle density are positive through out the evolution and decrease with time. At $t = \frac{Q_2}{P_2}$, ρ and ρ_p are infinite and tend to a constant values, $\frac{3k_2}{4}$ and $\frac{3k_2}{2}$, repsectively as $t \to \infty$. The constant values of ρ and ρ_p in the later stages of evolution are due to the bulk viscosity.

The string tension density λ is negative and gradually increases with time, and finally it approaches to a constant value as $t \to \infty$.
The potential in terms of t is written as

$$u(t) = -\frac{3}{8}\left[3k_2(P_2t - Q_2)^3 + 12(P_2t - Q_2)^2 + (3k_3 + 2k)(P_2t - Q_2)\right]. \tag{80}$$

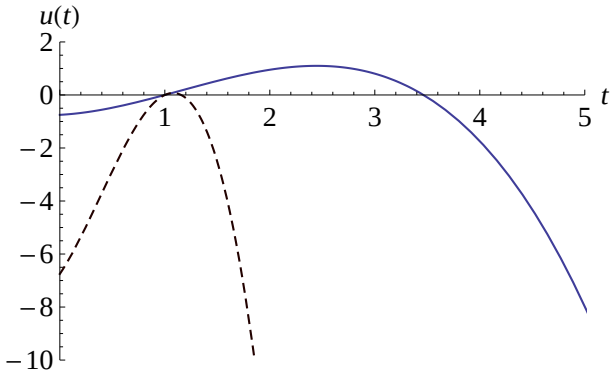

Fig. 5 Potential versus time with viscous fluid and magnetic field (bold lines) and with viscous fluid only (dashed lines).

The behavior of classical potential with time in both cases is shown in fig. 5. The figure shows that $\mu(t)$ is negative and positive in nature in the presence of magnetized viscous fluid whereas it remains negative due to the viscous fluid only. It is again find that there is much variation in these two forms of the fluid.

4.3 Takabayashi string model ($\alpha = 1 + \omega$)

For $k_4 = 0$, Eq.(46) reduces to

$$\int \frac{d\tau}{\sqrt{\frac{9(1+\omega)k_3}{3\omega+2}\tau^{\frac{3\omega+4}{3\omega+3}} + \frac{3k}{2}\tau^{\frac{2}{3}} + 9\tau^{\frac{4}{3}} + \frac{9(1+\omega)k_2}{3\omega+2}\tau^2}} = t. \tag{81}$$

One can observe that it is too difficult to find a general solution of τ in terms of t. Therefore, we express ρ, λ and ρ_p in terms of τ as

$$\rho = \frac{3(1+\omega)}{3\omega+2}\left[k_2 + k_3\tau^{-\frac{2+3\omega}{3(1+\omega)}}\right], \tag{82}$$

$$\lambda = \frac{3}{3\omega+2}\left[k_2 + k_3\tau^{-\frac{2+3\omega}{3(1+\omega)}}\right], \tag{83}$$

$$\rho_p = \frac{3\omega}{3\omega+2}\left[k_2 + k_3\tau^{-\frac{2+3\omega}{3(1+\omega)}}\right], \tag{84}$$

As $\omega > 0$, we find that ρ, λ and ρ_p remain positive through out the evolution of the universe. These physical parameters are decreasing function of τ and become constant for large t due to the bulk viscosity. The geometrical string model may be recovered for $\omega = 0$ as discussed in Sect. 4.1. The classical potential in this is given by

$$u(\tau) = -\frac{3}{2}\left[\frac{3k_3(1+\omega)}{3\omega+2}\tau^{\frac{4+3\omega}{3(1+\omega)}} + \frac{k}{2}\tau^{\frac{2}{3}} + 3\tau^{\frac{4}{3}} + \frac{3k_2(1+\omega)}{3\omega+2}\tau^2\right]. \tag{85}$$

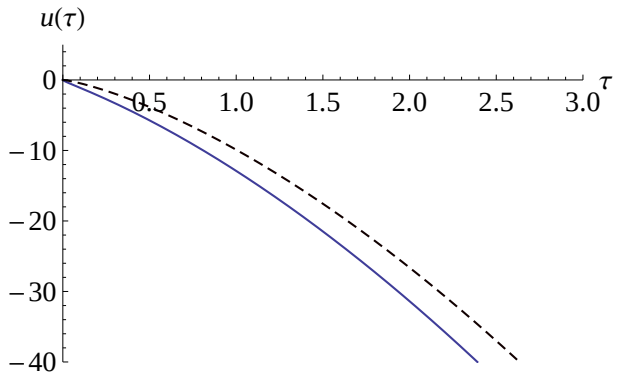

Fig. 6 Potential versus time with viscous fluid and magnetic field (bold lines) and with viscous fluid only (dashed lines).

Fig. 6 illustrates the behavior of potential $\mu(t)$ with respect to τ for $k_2 = 1 = k_3$, $I = 2$, $\bar{\mu} = 1.00001$ and $\omega = 1$. It is clear that potential remains negative and decreases rapidly throughout the evolution of the universe.

5. Conclusion

We have studied anisotropic Bianchi V string cosmological model with viscous fluid and magnetic field in general relativity by taking certain physical assumptions. Since viscous fluid and magnetic field have cosmological origin, it it interesting to discuss the viscous and magnetic field effects on the expansion history of the universe in early and late stages of evolution in string cosmology. The Einstein's field equations have been solved exactly for geometrical and Reddy string models whereas a general quadrature form of average scale factor has been found in Takabayashi string model. The solutions present interesting features in the presence of viscous fluid and magnetic field and in the presence of viscous fluid only. The effect of viscous term has more important for the expansion of the universe as we have already discussed in different string models. We have also plotted the graphs of various physical parameters to show the effects of magnetized viscous fluid and bulk viscous fluid only. We have observed that proper energy density, string tension density and particle density in geometrical string model remain positive through out the evolution. However, the string tension density is negative for Reddy string model and increases with time, and turns out to be finite for later time. At initial epoch, these physical parameters are infinite while they attain to be finite for later time due to bulk viscous effects. Hence, the presence of viscous term prevents to be empty in its future evolution. The different physical and kinematical parameters such as the respective directional Hubble parameters H_1, H_2 and H_3 along x, y and z directions, anisotropic parameter Δ, and shear scalar σ are infinite at initial epoch $t = P_1/Q_1$ or $t = P_2/Q_2$ as depend on the model and approach to zero asymptotically. The models approach isotropic at later stages of the evolution of the universe. The deceleration parameter turns out to be a positive constant in each string model. In Takabayashi model we have found a general quadrature form of average volume and correspondingly the solution for

the proper energy density, string tension density and particle energy density. These physical parameters approach to a constant value asymptotically as $t \to \infty$ due to the bulk viscosity.

We have also discussed the classical potential with respect to time in each string model and have observed that the classical potential changes its behavior rapidly due to the bulk viscous term. In our earlier work [43] we have discussed the role of magnetic field in Bianchi V string cosmological model in general relativity. We conclude that the role of bulk viscous fluid plays an important role in the evolution of the universe.

References

1. T.W.B. Kibble, J. Phys. A **9**, 1387 (1976)
2. A.E. Everett, Phys. Rev. D **24**, 858 (1981)
3. A. Vilenkin, Phys. Rev. D **24**, 2082 (1981)
4. P.S. Letelier, Phys. Rev. D **20**, 1294 (1979)
5. J. Stachel, Phys. Rev. D **21**, 2171 (1980)
6. P.S. Letelier, Phys. Rev. D **28**, 2414 (1983)
7. D.R. Matraverse, Gen. Relativ. Grav. **20**, 279 (1988)
8. K.D. Krori, T. Chaudhury, C.R. Mahanta, A. Mazumdar, Gen. Relativ. Grav. **22**, 123 (1990)
9. I. Yavuz, I. Tarhan, Astrophys. Space Sci. **240**, 45 (1996)
10. R. Bali, S. Dave, Pramana J. Phys. **56**, 513 (2001)
11. R. Bali, S. Dave, Astrophys. Space Sci. **288**, 503 (2003)
12. R. Bali, R.D. Upadhaya, Astrophys. Space Sci. **283**, 97 (2003)
13. R. Bali, D.K. Singh, Astrophys. Space Sci. **300**, 387 (2005)
14. R. Bali, Anjali, Astrophys. Space Sci. **302**, 201 (2006)
15. R. Bali, A. Pradhan, Chin. Phys. Lett. **24**, 585 (2007)
16. A. Pradhan, D.S. Chouhan, Astrophys. Space Sci. **331**, 697 (2011)
17. K.L. Mahanto, S.K. Biswal, S.K. Sahoo, M.C. Adhikary, Int. J. Theor. Phys. **51**, 1538 (2012)
18. E. Asseo, H. Sol, Phys. Rep. **6**, 148 (1987)
19. M.S. Madsen, MNRAS **237**, 109 (1989)
20. A.M. Wolfe, K. Lanzetta, A.L. Oren, Astrophys. J. **388**, 17 (1992)
21. R. Kulsrud, R. Cen, J.P. Ostriker, D. Ryu, Astrophys. J. **380**, 481 (1997)
22. J.D. Barrow, Phys. Rev. D **55**,7451 (1997)
23. D.R. Matravers, C.G. Tsagas, Phys. Rev. D **62**, 103519 (2000)
24. A. Banerjee, A.K. Sanyal, S. Chakraborty, Pramana-J. Phys. **34**, 1 1990
25. S. Chakraborty, Ind. J. Pure Appl. Phys. **29**, 31 (1991)
26. R. Tikekar, L.K. Patel, Gen. Relativ. Grav. **24**, 397, (1992)
27. R. Tikekar, L.K. Patel, Pramana J. Phys. **42**, 483 (1994)
28. ShriRam, J. K. Singh, Gen. Relativ. Grav. **27**, 1207 (1995)
29. L.K. Patel, S.D. Maharaj, Pramana J. Phys. **47**, 1 (1996)
30. G.P. Singh, T. Singh, Gen. Relativ. Grav. **31**, 371 (1999)
31. J.K. Singh, ShriRam, Astrophys. Sapce Sci. **246**, 65 (1997)
32. C. B. Kilinç, I. Yavuz, Astrophys. Space Sci **271**, 11 (2000)

33. A. Pradhan, A. Rai, S.K. Singh, Astrophys. Space Sci. **312**, 261 (2007)
34. A. Pradhan, Fizika B **16**, 205 (2007)
35. R. Bali, S. Jain, Int. J. Mod. Phys. D **16**, 1769 (2007)
36. B. Saha, M. Visinescu, Astrophys. Space Sci. **315**, 99 (2008)
37. A. Pradhan, K. Jatonia, A. Singh, Braz. J. Phys. **38**, 167 (2008)
38. A. Pradhan, V. Rai, K. Jatonia, Commun. Theor. Phys. **50**, 279 (2008)
39. B. Saha, V. Rikhvitsky, M. Visinescu, Cent. Eur. J. Phys. **8**, 113 (2010)
40. A. Pradhan, H. Amirhashchi, H. Zainuddin, Int. J. Thoer. Phys. **50**, 56 (2011)
41. H. Amirhashchi, H. Zainuddin, A. Pradhan, Int. J. Thoer. Phys. **50**, 2531 (2011)
42. V. Rikhvitsky, B. Saha, M. Visinescu, Astrophys. Sapce. Sci. **339**, 371, (2012)
43. C.P. Singh, V. Singh, arXiv:gr-qc/1209.5847 (2012)
44. M. Cataldo, N. Cruz, S. Lepe, Phys. Lett. B **619**, 5 (2005)
45. G.L. Murphy, Phys. Rev. D **8**, 4231 (1973)
46. V.A. Belinskii, I.M. Khalatrikov, Soviet Phys. JETP **42**, 205 (1976)
47. W.H. Huang, Phys. Lett. A **129**, 429 (1988)
48. W. Zimdahl, Phys. Rev. D **53**, 5483 (1996)
49. W. Zimdahl, Phys. Rev. D **61**, 083511 (2000)
50. L.P. Chimento, A.S. Jakubi, V. Méndez, R. Maartens, Class. Quantum Grav. **14**, 3363 (1997)
51. M.D. Mak, T. Harko, J. Math. Phys. **39**, 5458 (1998)
52. R. Maartens, Class. Quantum Grav. **12**, 1455 (1995)
53. C.P. Singh, Pramana J. Phys.**71**, 33 (2008)
54. M.K. Yadav, A. Rai, A. Pradhan, Int. J. Theor. Phys. **46**, 2677 (2007)
55. G. Mohanty, C.S. Gauranga, Tur. J. Phys **32**, 251 (2008)
56. S.K. Tripathy, D. Behera, Astrophys. Space Sci. **330**, 191 (2010)
57. A.A. Coley, Gen. Relativ. Grav. **22**, 3 (1990)
58. C.P. Singh, M. Zeyauddin, ShriRam, Astrophys. Space Sci. **315**, 181 (2008)
59. C.P. Singh, M. Zeyauddin, ShriRam, Int. J. Mod. Phys. A **23**, 2719 (2008)
60. C.P. Singh, M. Zeyauddin, ShriRam, Int. J. Theor. Phys. **47**, 3162 (2008)
61. C.P. Singh, A. Beesham, Int. J. Mod. Phys. A **25**, 3825 (2010)
62. C.P. Singh, Braz. J. Phys. **41**, 323 (2011)
63. N.C. Chakraborty, S. Chakraborty, Int. J. Mod. Phys. D **10**, 723 (2001)
64. R. Bali, Eur. J. Theor. Phys. **5**, 105 (2008)
65. R. Bali, U.K. Parrek, A. Pradhan, Chin. Phys. Lett. **24**, 2455 (2007)
66. R. Bali, R. Banerjee, S.K. Banerjee, Astrophys. Space Sci. **317**, 21 (2008)
67. M. Sharif, S. Waheed, Int. J. Mod. Phys. D **55**, 21500 (2012)
68. C.P.Singh, Astrophys. Space Sci. in press, (2012)
69. L.D. Landuam, E.M. Lifshitz, Fluid Mechanics, Pergamon Press, Oxford,p.505. (1936)
70. A. Linchnerowicz, Relativistic Hydrodynamics and Magneto Hydrodynam ics, Benjamin, New York, p.13 (1967)
71. R. Maartens, Pramana J. phys. **55**, 575 (2000)
72. B. Saha, Mod. Phys. Lett. A **20**, 2127 (2005)
73. B. Saha, T. Boyadjiev, Phys. Rev. D **69**, 124010 (2004)

String Cosmology with Magnetic field in Anisotropic Space-time

C. P. Singh[1] and Vijay Singh[2]

Department of Applied Mathematics,
Delhi Technological University (Formerly Delhi College of Engineering)
Bawana Road, Delhi-110 042, India.
cpsphd@rediffmail.com[1]
gtrcosmo@gmail.com[2]

Abstract In this paper we study the effect of the magnetic field in string cosmology for a spatially homogenous and anisotropic Bianchi type -V space-time model. In order to study the effect of magnetic field, the standard form of the energy momentum tensor for cosmic strings is modified by including an additional term for magnetic field. The magnetic field is due to an electric current produced along the x-axis with infinite electrical conductivity. The field equations are solved for different string models such as geometric string (Nambu string), Takabayashi string (p-string) and Reddy string using string equation of state. We also find the solution for string models with uniform energy density. The physical and geometrical properties of each string model with and without magnetic field are discussed in detail.

Keywords: Cosmology; Anisotropic models; Massive string cosmology; Magnetic field.

PACS number(s): 98.80-k, 98.80-cq, 04.20-q.

1. Introduction

The search for cosmological models that do not suffer from the problems inflicting the standard big bang model of cosmology has intensified since the advent of string theory. String theory is particularly relevant to the initial singularity problem whose solution has long been thought to require a quantum theory of gravity, for which string theory seems to be the most promising candidate. It is generally believed that the very early universe underwent phase transitions, which gave rise to topological stable structures. Among the various topological defects that occurred during the phase transition and before the creation of particles in the early universe, strings have interesting cosmological consequences and have been studied in more details [1]. It is thought that cosmic strings cause density perturbations leading to the formation of galaxies [2]. These cosmic strings have stress-energy and couple with the gravitational field. The pioneering work in the formulation of the energy momentum tensor for the classical massive strings was done by Letelier [3], who considered the massive strings to be formed by geometric strings with particles attached along its extension. Stachel [4] developed a classical theory of the geometric strings. Letelier [5] first used this idea in obtaining some cosmological solutions of massive strings in Bianchi type-I and Kantowski - Sachs space-times. The gravitational effects of cosmic strings have been obtained by Vilenkin [6], Gott [7] and Garfinkle [8]. As the gravitational is the only long range force binding the contents of the universe and Einstein's theory of gravitation is the sole theory for understanding the nature and evolution of the large scale structure of the universe, so it may be interesting to study the gravitational effects which arise from strings within the framework of Einstein gravity. In literature, homogeneous and anisotropic cosmological models have been widely studied in string cosmology in different contexts (Ref. [9-21]).

On the other hand, the occurrence of magnetic field on galactic scale is well established fact today, and their importance for a variety of astrophysical phenomena is generally acknowledged. Several authors [22-28] have pointed out the importance of magnetic field in different context. The importance of the magnetic field for various astrophysical phenomenon has been studied in many papers. The string cosmological models with magnetic field have also been discussed by Banerjee et al. [9], Chakraborty [29], Tikekar and Patel [30, 31], Patel and Maharaj [32], Singh and Singh [33], Pradhan and Bali [34], and Bali [35]. Bali and Anjali [36] have investigated Bianchi Type-I magnetized string dust cosmological model. Bali et al. [37] have studied Bianchi-I massive string cosmological models with magnetic field. Wang [38], Pradhan et al.[39, 40], Pradhan [41, 42], Amirhashchi et al. [43], and Saha and Visinescu [44] have investigated the string cosmology with an incident magnetic field. Saha et al.[45] and Rikhvitsky et al. [46] have studied Bianchi-I string cosmological model in the presence of magnetic field and have examined the quantum effects in framework of loop quantum cosmology. Recently Singh [47] has generalized the work of Saha and Visinescu [44] to include the viscous term and has discussed the effect of viscous fluid with and without magnetic field in different string models for Bianchi I space -time.

Bianchi V universes are the natural generalization of Friedmann -Robertson- Walker (FRW) models with negative curvature. Bianchi V cosmological model where the matter moves orthogonally to the hypersurface of homogeneity, has been studied by Heckmann and Schucking [48]. Roy and Singh [49] have investigated Bianchi V model with stiff matter and a source free electromagnetic field. Banerjee and Sanyal [50] have studied Bianchi V model with viscosity and heat flow. Coley [51] has investigated Bianchi V imperfect fluid cosmological models in general relativity. Bali and

Meena [52] have discussed Bianchi V titled model for stiff matter. Chakraborty and Chakraborty [53], Bali and Singh [53], and Bali [54] have studied Bianchi V models with magnetic field in string cosmology. Singh et al.[54-58], Singh and Beesham [59] and Singh [60] have studied Bainchi V space time in general relativity with different contexts.

The purpose of this paper is to investigate a Bianchi type-V string cosmological model in the presence of magnetic field. The inclusion of the magnetic field is motivated by the observational cosmology and astrophysics indicating that many subsystems of the universe possess magnetic fields. We examine geometric string (Nambu string), Takabayashi string (p-string) and Reddy string models using the string equation of state. We also discuss the string models with uniform energy density. Exact analytic solutions are obtained in each case except for Takabayashi string model. The behavior of each model with and without magnetic field together with geometrical and physical aspects are discussed in detail.

The paper is organized as follows: In Sect.2 the general features of string theory and the corresponding field equations with the magnetic field are presented. A general soultion is given in Sect.3. In Sect. 4 we present the exact solutions for different string models. A solution with uniform energy density is presented in Sect.5. Finally, In Sect.6 we summarize our results.

2. Model and Basic Equations

We consider the homogenous and anisotropic Bianchi type -V spacetime whose metric is given by

$$ds^2 = -dt^2 + R_1^2 dx^2 + R_2^2 e^{-2x} dy^2 + R_3^2 e^{-2x} dz^2, \tag{1}$$

where R_1, R_2, and R_3 are the functions of cosmic time t only and are the scale factors in anisotropic background.

The energy momentum tensor for a cloud string with a magnetic field is taken into the form (Bali,[54])

$$T_i^j = \rho u_i u^j - \lambda x_i x^j + E_i^{\ j}, \tag{2}$$

where ρ is the rest energy density for a cloud of strings with massive particles attached to them and is related to the strings tension density λ by the relation (Letelier, [3])

$$\rho = \rho_p + \lambda. \tag{3}$$

Here ρ_p is the rest energy density of the particles attached to the strings. The energy conditions [9](Strong, weak and dominant) demand $\rho \geq 0$, $\rho_p \geq 0$, while λ is unrestricted; it may be positive, negative or zero as well. Also u_i is the four velocity for the cloud of particles and x^i is the four vector representing the string's direction, i.e., the direction of anisotropy and we have

$$u_i u^i = -x_i x^i = -1, \;\; u_i x^i = 0 \;\; and \;\; x^i = \left(R_1^{-1}, 0, 0, 0\right). \tag{4}$$

In Eq. (2), E_{ij} is the electromagnetic field given by (Linchnerowicz [61])

$$E_i^{\ j} = \bar{\mu}\left[|h|^2\left(u_i u^j + \frac{1}{2} g_i^{\ j}\right) - h_i h^j\right], \tag{5}$$

where $\bar{\mu}$ is the magnetic permeability, and h_i the magnetic flux vector defined by

$$h_i = \frac{\sqrt{-g}}{2\bar{\mu}}\,\epsilon_{ijkl}F^{kl}u^j, \tag{6}$$

In the above F_{kl} is the electro-magnetic field tensor and ϵ_{ijkl} is the totally anti-symmetric Levi-Civita tensor density with $\epsilon_{0123} = 1$. Let us assume the coordinates to be comoving, so that $u^1 = 0 = u^2 = u^3$ and $u^4 = 1$. The incidental magnetic field is taken along x-axis, so that $h_1 \neq 0$, $h_2 = 0 = h_3 = h_4$. This leads to $F_{12} = 0 = F_{13}$ by virtue of (6). Also, $F_{14} = 0 = F_{24} = F_{34}$ due to the assumption of the infinite conductivity of the field (Maartens [62]). Hence the only non vanishing components of F_{ij} is F_{23}. Therefore, the first set of Maxwell's equations

$$F_{ij;k} + F_{jk;i} + F_{ki;j} = 0. \tag{7}$$

leads to

$$F_{23} = \text{constant} = I(say). \tag{8}$$

In Eq. (7) the semicolon stands for covariant differentiation. From (6), we get

$$h_1 = \frac{R_1 I}{\bar{\mu}R_2R_3}. \tag{9}$$

Since

$$|h|^2 = h_l h^l = h_1 h^1 = g^{11}(h_1)^2,$$

Therefore,

$$|h|^2 = \frac{I^2}{\bar{\mu}^2 R_2^2 R_3^2}\ . \tag{10}$$

Finally, one finds the following non-trivial components for $E_i^{\ j}$

$$E^0_{\ 0} = -\frac{I^2}{2\bar{\mu}R_2^2R_3^2} = E^1_{\ 1} = -E^2_{\ 2} = -E^3_{\ 3}, \tag{11}$$

and for the components of the string's energy momentum tensor, we have

$$T^0_{\ 0} = -\rho,\ T^1_{\ 1} = -\lambda,\ T^2_{\ 2} = T^3_{\ 3} = 0 = T^i_{\ j},\ \ (i \neq j) \tag{12}$$

The Einstein's field equations (in gravitational units $8\pi G/c^4 = 1$) read as

$$R_i^{\ j} - \frac{1}{2}Rg_i^{\ j} = -T_i^{\ j}. \tag{13}$$

The field equation (13) with (2) for line element (1) subsequently lead to the following system of equations

$$\frac{\dot{R}_1\dot{R}_2}{R_1R_2} + \frac{\dot{R}_2\dot{R}_3}{R_2R_3} + \frac{\dot{R}_3\dot{R}_1}{R_3R_1} - \frac{3}{R_1^2} = \rho + \frac{I^2}{2\bar{\mu}R_2^2R_3^2}, \tag{14}$$

$$\frac{\ddot{R}_1}{R_1} + \frac{\ddot{R}_3}{R_3} + \frac{\dot{R}_1\dot{R}_3}{R_1R_3} - \frac{1}{R_1^2} = -\frac{I^2}{2\bar{\mu}R_2^2R_3^2}, \tag{15}$$

$$\frac{\ddot{R}_1}{R_1}+\frac{\ddot{R}_2}{R_2}+\frac{\dot{R}_1\dot{R}_2}{R_1R_2}-\frac{1}{R_1^2}=-\frac{I^2}{2\bar{\mu}R_2^2R_3^2}, \tag{16}$$

$$\frac{\ddot{R}_2}{R_2}+\frac{\ddot{R}_3}{R_3}+\frac{\dot{R}_2\dot{R}_3}{R_2R_3}-\frac{1}{R_1^2}=\lambda+\frac{I^2}{2\bar{\mu}R_2^2R_3^2}, \tag{17}$$

$$2\frac{\dot{R}_1}{R_1}-\frac{\dot{R}_2}{R_2}-\frac{\dot{R}_3}{R_3}=0, \tag{18}$$

where a dot denotes ordinary derivative with respect to cosmic time t.

We define the various physical parameters such as the mean Hubble parameter H, anisotropy parameter A and shear scalar σ as

$$H=\frac{1}{3}\left(H_1+H_2+H_3\right), \tag{19}$$

$$A=\frac{1}{3}\sum_{i=1}^{3}\left(\frac{H_i-H}{H}\right)^2, \tag{20}$$

$$\sigma^2=\frac{1}{2}\,\sigma_{ij}\sigma^{ij}=\frac{1}{3}\theta^2-\left(\frac{\dot{R}_1\dot{R}_2}{R_1R_2}+\frac{\dot{R}_2\dot{R}_3}{R_2R_3}+\frac{\dot{R}_3\dot{R}_1}{R_3R_1}\right). \tag{21}$$

where $H_1=\frac{\dot{R}_1}{R_1}$, $H_2=\frac{\dot{R}_2}{R_2}$ and $H_3=\frac{\dot{R}_3}{R_3}$ are the directional Hubble parameters in directions of x, y and z axes, respectively and the scalar expansion is defined by $\theta=3H$. Also, $\sigma_{ij}=u_{i;j}+\frac{1}{2}\left(u_{i;k}u^ku_j+u_{j;k}u^ku_i\right)+\frac{1}{3}\theta\left(g_{ij}+u_iuj\right)$.

3. Solution of the field equations

We follow the method used by Saha and Visineseu [44] to solve the field equations (14)-(18). From (15) and (16), we get

$$\frac{d}{dt}\left(\frac{\dot{R}_3}{R_3}-\frac{\dot{R}_2}{R_2}\right)+\left(\frac{\dot{R}_3}{R_3}-\frac{\dot{R}_2}{R_2}\right)\left(\frac{\dot{R}_1}{R_1}+\frac{\dot{R}_2}{R_2}+\frac{\dot{R}_2}{R_2}\right)=0. \tag{22}$$

Let us define a new time-dependent function $\tau(t)$ as

$$\tau=R_1R_2R_3=\sqrt{-g}\,, \tag{23}$$

which is indeed the volume scale factor of the Bianchi V space-time. Using (23) into (22) and simplifies, we get

$$R_3=d_1R_2\exp\left[k_1\int\frac{dt}{\tau}\right], \tag{24}$$

where d_1 and k_1 are constants of integration. Eq.(18) gives

$$R_1^2=k_2R_2R_3, \tag{25}$$

where k_2 is a constants of integration without loss of generality we can take unity. Now from Eqs. (14)-(17) and (25), we get

$$\frac{\ddot{\tau}}{\tau} = \frac{1}{2}\left[(3\rho + \lambda) + \frac{R_1^2 I^2}{\bar{\mu}\tau^2}\right] + \frac{6}{\tau^{2/3}}. \tag{26}$$

On the other, the energy conservation law $T^j_{i\ ;j} = 0$ gives

$$\dot{\rho} + \frac{\dot{\tau}}{\tau}\rho - \frac{\dot{R}_1}{R_1}\lambda = 0. \tag{27}$$

From (23) - (25), we find the following forms of metric functions in terms of τ (Ref. [55])

$$R_1 = \tau^{\frac{1}{3}} \tag{28}$$

$$R_2 = \frac{1}{\sqrt{d_1}}\,\tau^{\frac{1}{3}} \exp\left[-\frac{k_1}{2}\int \frac{dt}{\tau}\right] \tag{29}$$

$$R_3 = \sqrt{d_1}\,\tau^{\frac{1}{3}} \exp\left[\frac{k_1}{2}\int \frac{dt}{\tau}\right] \tag{30}$$

It is to be noted that if the integration constant k_1 is taken to be zero, then anisotropic character of the model is lost and it reduces to a FRW model. Using (28)- (30), Eqs. (26) and (27) take the form

$$\ddot{\tau} = \frac{1}{2}(3\rho + \lambda)\tau + \frac{k}{2}\,\tau^{-\frac{1}{3}} + 6\tau^{\frac{1}{3}}, \tag{31}$$

$$\dot{\rho} + \left(\rho - \frac{1}{3}\lambda\right)\frac{\dot{\tau}}{\tau} = 0, \tag{32}$$

where $k = \frac{I^2}{\bar{\mu}}$.
To find the value of τ in terms of t, let us consider the equation of state for a cloud of string models[6]

$$\rho = \alpha\lambda, \tag{33}$$

where the constant α is defined by

$$\begin{aligned} \alpha &= 1 \quad (geometric\ or\ Nambu\ string), \\ &= (1+\omega) \quad (p-\ string\ or\ Takabayasi\ string), \\ &= -1 \quad (Reddy\ string), \end{aligned} \tag{34}$$

where ω is a constant such that $\omega > 0$. Using (33) into (32), we get

$$\frac{\dot{\rho}}{\rho} = \left(\frac{1-3\alpha}{3\alpha}\right)\frac{\dot{\tau}}{\tau}, \tag{35}$$

which is integrated to give the solution

$$\rho = \rho_0 \tau^{\frac{1}{3\alpha}-1}, \tag{36}$$

where ρ_0 is a positive constant of integration.

Now, Eq. (31) takes the form

$$\ddot{\tau} = \frac{1}{2}\left(\frac{3\alpha+1}{\alpha}\right)\rho_0\tau^{\frac{1}{3\alpha}} + \frac{k}{2}\tau^{-\frac{1}{3}} + 6\tau^{\frac{1}{3}}, \tag{37}$$

whose first integral is given by

$$\dot{\tau}^2 = 3\rho_0\tau^{\frac{3\alpha+1}{3\alpha}} + \frac{3}{2}k\tau^{\frac{2}{3}} + 9\tau^{\frac{4}{3}} + c_0, \tag{38}$$

which may be rewritten as

$$\dot{\tau} = \sqrt{3\rho_0\tau^{\frac{3\alpha+1}{3\alpha}} + \frac{3}{2}k\tau^{\frac{2}{3}} + 9\tau^{\frac{4}{3}} + c_0}, \tag{39}$$

where c_0 is a constant of integration. It is to be mentioned that τ is non-negative due to the expansion of the universe. At the points where $\tau = 0$, there occurs space-time singularity. On the other hand, the radical in (39) should be positive. Taking into account the energy density and string tension density obeying equation of state (33), we conclude that ρ and λ, and hence the right hand side of Eq. (31) is a function of τ only, i.e.,

$$\ddot{\tau} = F(\tau). \tag{40}$$

From the mechanical point of view, Eq. (40) can be interpreted as equation of motion of a single particle with unit mass under the force $F(\tau)$. Then the following first integral exists

$$\dot{\tau} = \sqrt{2[\epsilon - u(\tau)]}, \tag{41}$$

where ϵ can be viewed as energy level and $u(\tau)$ is the potential of the force F. Comparing Eqs. (39) and (41), we find $\epsilon = c_0/2$ and

$$u(\tau) = -\frac{1}{2}\left[3\rho_0\tau^{\frac{3\alpha+1}{3\alpha}} + \frac{3}{2}k\tau^{\frac{2}{3}} + 9\tau^{\frac{4}{3}}\right]. \tag{42}$$

Finally, we write the solution to Eq. (39) in a general quadrature form as

$$\int \frac{d\tau}{\sqrt{3\rho_0\tau^{\frac{3\alpha+1}{3\alpha}} + \frac{3}{2}k\tau^{\frac{2}{3}} + 9\tau^{\frac{4}{3}} + c_0}} = t + t_0, \tag{43}$$

where the integration constant t_0 can be taken to be zero.

It is too difficult to integrate (43) to find the exact value of τ in terms of t. Therefore, we look the solutions for different string models viz. geometrical, Takabayashi and Reddy strings using string equation of state (34) and the solution with uniform energy density in Sections 4 and 5.

4. Solution with equation of state

Let us solve the system of equations for the following string models to discuss the nature of solutions with and without magnetic field.

4.1 Geometric string model($\alpha = 1$)

For $\alpha = 1$ and $c_0 = 0$, Eq. (43) reduces to

$$\int \frac{d\tau}{\sqrt{3(\rho_0+3)\tau^{\frac{4}{3}} + \frac{3}{2}k\tau^{\frac{2}{3}}}} = t, \tag{44}$$

which on integration it gives

$$\tau = (c_1 t^2 - c_2)^{3/2}, \tag{45}$$

where $c_1 = (1 + \frac{\rho_0}{3})$ and $c_2 = \frac{k}{2(\rho_0+3)} = \frac{I^2}{2\bar{\mu}(\rho_0+3)}$.

At $t = 0$, τ becomes imaginary. For reality of the model, t must satisfy $t > \sqrt{\frac{3k}{2(\rho_0+3)^2}}$. From (28)-(30) and (45), we get the following form of the scale factors in terms of t.

$$R_1 = \sqrt{c_1 t^2 - c_2}, \tag{46}$$

$$R_2 = \frac{1}{\sqrt{d_1}}\sqrt{c_1 t^2 - c_2}\ \exp\left[\frac{k_1 t}{2c_2\sqrt{c_1 t^2 - c_2}}\right], \tag{47}$$

$$R_3 = \sqrt{d_1}\sqrt{c_1 t^2 - c_2}\ \exp\left[-\frac{k_1 t}{2c_2\sqrt{c_1 t^2 - c_2}}\right]. \tag{48}$$

We observe that R_1 and R_3 tend to zero but R_2 becomes indeterminate at $c_1 t^2 - c_2 = 0$. It is to be noted here that c_2 is the term which contains the magnetic field. Figure 1. shows that R_1 and R_3 always increase with time whereas R_2 decreases first then gradually increases with time in the presence of magnetic field. As $t \to \infty$, R_1 and R_2 tend to infinity whereas R_3 tends to zero. In fig. 1 we have assumed $\rho_0 = 3$, $I = 1$, $\bar{\mu} = 1.00001$, $d_1 = 10^4$, $c_1 = 2$ and $k_1 = 1$. In the absence of magnetic field, i.e., $c_2 = 0 = I$, we find that R_1 varies linearly where as R_2 and R_3 become indeterminate forms.

The directional Hubble parameters along x, y and z axes are respectively given by

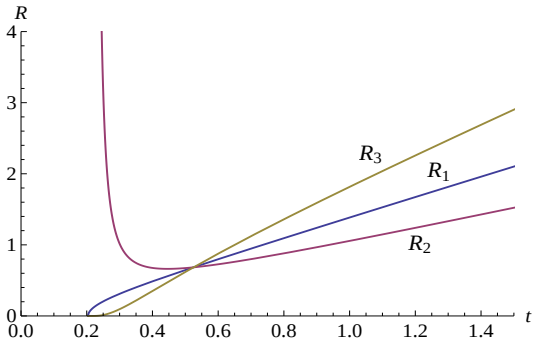

Fig. 1 Evolution of the universe in the presence of magnetic field

$$H_1 = \frac{c_1 t}{c_1 t^2 - c_2}, \tag{49}$$

$$H_2 = \frac{c_1 t}{c_1 t^2 - c_2} - \frac{k_1}{2(c_1 t^2 - c_2)^{\frac{3}{2}}}, \tag{50}$$

$$H_3 = \frac{c_1 t}{c_1 t^2 - c_2} + \frac{k_1}{2(c_1 t^2 - c_2)^{\frac{3}{2}}}. \tag{51}$$

The average Hubble parameter in terms of cosmic time t is

$$H = \frac{c_1 t}{c_1 t^2 - c_2}. \tag{52}$$

The anisotropic parameter and shear scalar, respectively have the following expressions

$$A = \frac{k_1^2}{6c_1^2 t^2 (c_1 t^2 - c_2)}, \tag{53}$$

$$\sigma^2 = \frac{k_1^2}{4(c_1 t^2 - c_2)^3}. \tag{54}$$

The deceleration parameter is given by

$$q = \frac{c_2}{c_1 t^2}. \tag{55}$$

One can observe that as $t \to \infty$, $q \to 0$, which shows the marginal inflation (Coasting cosmology) in late time evolution of the universe. The anisotropy parameter and shear scalar also tend to zero as $t \to \infty$. The expression for the ratio $\frac{\sigma}{\theta}$ gives

$$\frac{\sigma}{\theta} = \frac{k_1}{6c_1 t\sqrt{(c_1 t^2 - c_2)}}. \tag{56}$$

We find that as $t \to \infty$, (56) tends to zero, which shows that the model tends to be isotropic for large t. The energy density and string tension density are respectively calculated as

$$\rho = \lambda = \rho_0 (c_1 t^2 - c_2)^{-1}. \tag{57}$$

We observe that ρ and λ are decreasing function of time. As t increases, both the parameters gradually decrease and approach to zero as $t \to \infty$. Thus, the string tension density disappears in late times. In this case the particle density, ρ_p is zero. The potential in terms of t is written as

$$u(t) = -\frac{3}{4}\left[k(c_1 t^2 - c_2) + 2(3 + \rho_0)(c_1 t^2 - c_2)^2\right]. \tag{58}$$

Figure 2. illustrates the potential graph with and without magnetic field for $\rho_0 = 3$, $c_1 = 2$ and $\bar{\mu} = 1.00001$. One may observe that the potential starts from zero and goes to positive for some finite time of interval and then becomes negative in the presence of magnetic field whereas it starts from zero and remains negative through out the evolution in the absence of magnetic field.

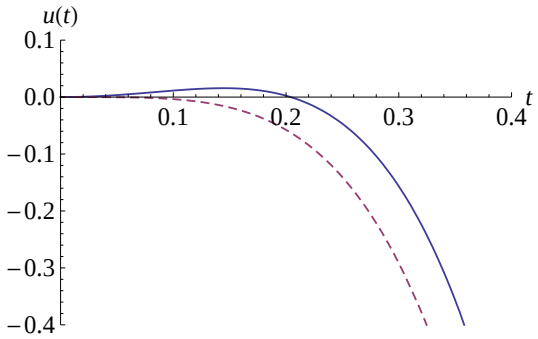

Fig. 2 Potential versus time in presence (bold line) and in absence (dashed line) magnetic field.

4.2. Reddy string model ($\alpha = -1$)

For $\alpha = -1$ and $c_0 = 0$, Eq. (43) reduces to

$$\int \frac{d\tau}{9\tau^{\frac{4}{3}} + 3\left(\rho_0 + \frac{k}{2}\right)\tau^{\frac{2}{3}}} = t, \tag{59}$$

The integral of (59) gives

$$\tau = (t^2 - c)^{3/2}, \tag{60}$$

where $c = \frac{k+2\rho_0}{6}$. At $t = 0$, τ becomes imaginary. For realty of the model, t must satisfy $t > \sqrt{\frac{k+2\rho_0}{6}}$. From (28)-(30) and (60), we get

$$R_1 = \sqrt{t^2 - c}, \tag{61}$$

$$R_2 = \frac{1}{\sqrt{d_1}}\sqrt{t^2 - c}\ \exp\left[\frac{k_1 t}{2c\sqrt{t^2 - c}}\right], \tag{62}$$

$$R_3 = \sqrt{d_1}\sqrt{t^2 - c}\ \exp\left[-\frac{k_1 t}{2c\sqrt{t^2 - c}}\right]. \tag{63}$$

The directional Hubble parameters are given by

$$H_1 = \frac{t}{t^2 - c}, \tag{64}$$

$$H_2 = \frac{t}{t^2 - c} - \frac{k_1}{2(t^2 - c)^{\frac{3}{2}}}, \tag{65}$$

$$H_3 = \frac{t}{t^2 - c} + \frac{k_1}{2(t^2 - c)^{\frac{3}{2}}}, \tag{66}$$

where as the average Hubble parameter has the form

$$H = \frac{t}{t^2 - c}. \tag{67}$$

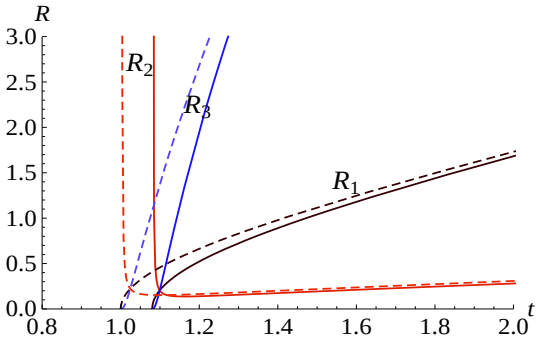

Fig. 3 Evolution of the universe in presence (bold lines) and in absence (dashed lines)of magnetic field.

The anisotropic parameter, shear scalar and deceleration parameter have the following expressions, respectively.

$$A = \frac{k_1^2}{6t^2(t^2-c)}, \tag{68}$$

$$\sigma^2 = \frac{k_1^2}{4(t^2-c)^3}, \tag{69}$$

$$q = \frac{c}{t^2}. \tag{70}$$

The expression for the ratio $\frac{\sigma}{\theta}$ gives

$$\frac{\sigma}{\theta} = \frac{k_1}{6t\sqrt{(t^2-c)}}. \tag{71}$$

The energy density, string tension density and particle density have the following expressions, respectively.

$$\rho = \rho_0(t^2-c)^{-2}, \tag{72}$$

$$\lambda = -\rho_0(t^2-c)^{-2}, \tag{73}$$

$$\rho_p = 2\rho_0(t^2-c)^{-2}. \tag{74}$$

The potential in terms of t is given by

$$u(t) = -\frac{3}{4}\left[k(t^2-c) + 6(t^2-c)^2 + 2\rho_0(t^2-c)^{-1}\right]. \tag{75}$$

We observe from figure 3 that the scale factors have the same behaviors in the presence of magnetic field as illustrated in fig.1. In the absence of magnetic field as shown by dashed lines in fig.3, the scale factors start expanding with different time of evolution. We have used $\rho_0 = 3$, $I = 1$, $\bar{\mu} = 1.00001$ and $d_1 = 100$ in fig.3. The other physical parameters such as deceleration parameter, anisotropy parameter, shear scalar also have the similar behaviors as discussed in section 4.1. For large t, all these parameters tend to zero. Therefore, the model approaches isotropic in later stage of the evolution of the universe. The energy density and particle density remain positive

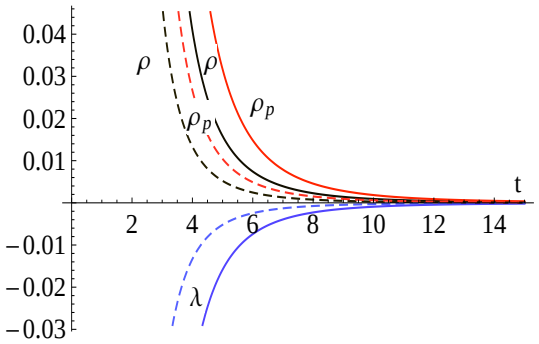

Fig. 4 Energy density, string tension density and particle density versus time in presence (bold lines) and in absence (dashed lines) of magnetic field.

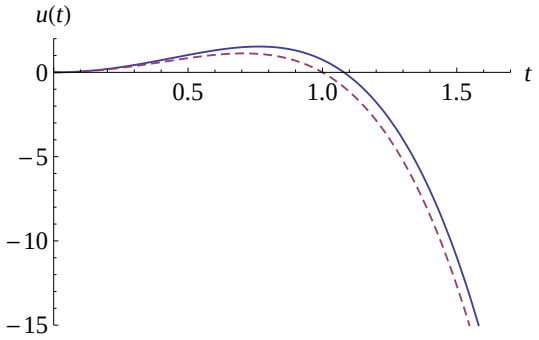

Fig. 5 Potential versus time in presence (bold line) and in absence (dashed line) magnetic field.

and decrease with time, and tend to zero for large t. The string tension density λ is negative and gradually increases with time, and finally it approaches to zero as $t \to \infty$. It is also observed that $\rho_p > |\lambda|$, i.e., the particle density remains larger than the string tension density during the cosmic expansion, especially in the early universe. The behaviors of these three parameters and potential with and without magnetic field are shown in figures 4 and 5, respectively with $\rho_0 = 3$, $I = 1$ or 0 and $\bar{\mu} = 1.00001$. The potential shows both positive and negative characters with and without magnetic field in this string model.

4.3 Takabayashi string model ($\alpha = 1 + \omega$)

For $\alpha = 1 + \omega$ and $c_0 = 0$, Eq. (43) reduces to

$$\int \frac{d\tau}{\sqrt{3\rho_0 \tau^{\frac{4+3\omega}{3(1+\omega)}} + \frac{3}{2}k\tau^{\frac{2}{3}} + 9\tau^{\frac{4}{3}}}} = t, \tag{76}$$

One can observe that it is too difficult to find the general solution of τ in terms of t. Therefore, we express the energy density, string tension density, particle density and potential in terms of τ as

$$\rho = \rho_0 \tau^{-\frac{2+3\omega}{3(1+\omega)}}, \tag{77}$$

$$\lambda = \frac{\rho_0}{(1+\omega)}\tau^{-\frac{2+3\omega}{3(1+\omega)}}, \qquad (\omega > 0) \tag{78}$$

$$\rho_p = \frac{\omega}{1+\omega}\rho_0\tau^{-\frac{2+3\omega}{3(1+\omega)}}, \tag{79}$$

$$u(\tau) = -\frac{3}{2}\left[\rho_0\tau^{\frac{3\omega+4}{3(1+\omega)}} + \frac{3}{2}k\tau^{\frac{2}{3}} + 9\tau^{\frac{4}{3}}\right]. \tag{80}$$

We observe that the physical parameters ρ, λ and ρ_p are decreasing functions of time and tend

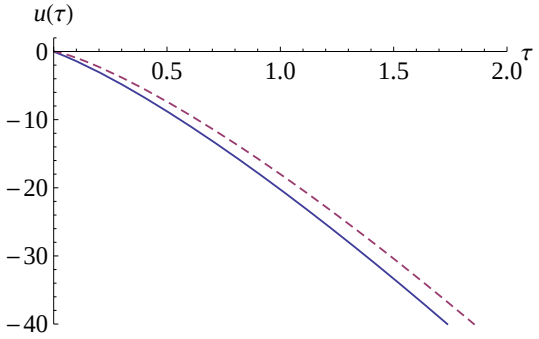

Fig. 6 Potential versus time in presence (bold line) and in absence (dashed line) magnetic field.

to zero as $t \to \infty$. Fig.6 shows the potential corresponding to Takabayashi string model with and without magnetic field for $\omega = 1$, $\rho_0 = 3$, and $\bar{\mu} = 1.00001$. It is always negative through out the evolution of the universe with and without magnetic field and decreases fast in the presence of magnetic field.

5. Solution with uniform energy density

Now we consider the rest energy density of the cloud of strings is uniform (i.e., $\rho = \rho_1$). From (32), we have $\tau = \tau_0$=constant. Eq.(31) gives

$$\lambda = -(3\rho_1 + k\tau_0^{-4/3} + 12\tau_0^{-2/3}). \tag{81}$$

Using the relation (4), we get

$$\rho_p = 4\rho_1 + k\tau_0^{-4/3} + 12\tau_0^{-2/3}. \tag{82}$$

The scale factors have the following expressions

$$R_1 = \tau_0^{1/3}, \tag{83}$$

$$R_2 = \frac{1}{\sqrt{d_1}}\,\tau_0^{1/3}\exp\left[-\frac{k_1}{2\tau_0}t\right], \tag{84}$$

$$R_3 = \sqrt{d_1}\,\tau_0^{1/3}\exp\left[\frac{k_1}{2\tau_0}t\right]. \tag{85}$$

We observe that the model is non-singular with the uniform density as R_1 is constant through out the evolution. The other two metric coefficients R_2 and R_3 are in exponential form. R_2 decreases to zero and R_3 exponentially grows with time. As λ is negative, therefore, the geometric string and Takabayashi string models are not possible due to negativity of the string tension density. The solution describes Reddy string model. During evolution of the universe the energy is getting transfer from string tension to particle density and their sum is always equal to ρ_1 and $\rho_p \geq 0$.

6. Conclusion

We have studied the anisotropic Bianchi type -V string cosmological model in the presence of magnetic field. The field equations have been solved exactly for the geometrical and Reddy string models. In both models we have found that the physical parameters have the same type of behaviors such as the scale factors along x and z axes increase with time but the scale factor along y axis decreases first and then increases with time, the energy density, particle density, anisotropy parameter and shear scalar all are decreasing functions of time and tend to zero as $t \to \infty$. In geometrical string model the string tension density decreases with time whereas it gradually increases with time and tends to zero for large t in Reddy string model as it is negative. It is also negative in the model with uniform energy density. All the string models tend to isotropic for large t. We have illustrated the scale factors, energy density, particle density, string tension density and potential with time for these models with and without magnetic field in figures 1-5.

In case of Takabayashi string model we observe that it is very difficult to find the solution due to complicated quadrature form of τ. Therefore, we have shown the potential versus τ graphically for this model the presence of magnetic field in fig.6. The reason to illustrate figures with and without magnetic field is to show the role of magnetic field in different string models. We have also discussed the string models with uniform energy density and have found a non-singular solution. In this model the geometric string and Takabayashi string models are not possible due to negativity of the string tension density.

References

1. Kibble, T.W.B.: J. Phys. A: Math. Gen. **9**, 1378 (1976).
2. Zel'dovich, Ya. B.: Mon. Not. R. Astron. Soc. **192**, 663 (1980).
3. Letelier, P.S.: Phys. Rev. D **20**, 1294 (1979).
4. Stachel, J.: Phys. Rev. D **21**, 2171 (1980).
5. Letelier, P.S.: Phys. Rev. D **28**, 2414 (1983).
6. Vilenkin, A.: Phys. Rep. **121**, 263 (1985).
7. Gott, J.R.: Astrophys. J. **288**, 422 (1985).
8. Garfinkle, D.: Phys. Rev. D **32**, 1323 (1985).
9. Banerjee, A., Sanyal, A.K., Chakraborty, S.: Pramana-J. Phys. **34**, 1 1990.
10. Chakraborty, S.: Ind. J. Pure Appl. Phys. **29**, 31 1991.
11. Ilhami , Y., Tarhan, I.: Astrophys. Space sci. **240**, 45 (1996).
12. Wang, X.X.: Chin. Phys. Lett. **20**, 615 (2003).
13. Pradhan, A., Yadav, A.K., Singh, R.P., Yadav, V.K.: Astrophys. Space Sci. **312**, 145

(2007).
14. Bali, R., Pradhan, A.: Chin. Phys. Lett. **24** 585 (2007).
15. Reddy, D.R.K., Naidu, R.L., Rao, V.U.M.: Int. J. Theor. Phys. **46**, 1443 (2007).
16. Rao, V.U.M., Vinutha, T., Shanthi, M.V.: Astrophys. Space Sci. **314**, 213 (2008).
17. Pradhan, A.: Commun. Theor. Phys. **51**, 367 (2009).
18. Pradhan, A., Amirhashchi, H., Yadav, M.K.: Fizika B **18**, 35 (2009).
19. Rao, V.U.M., Vinutha, T.: Astrophys. Space Sci. **325**, 59 (2010).
20. Pradhan, A., Chouhan, D.S.: Astrophys. Space Sci. **331**, 697 (2011).
21. Mahanto, K.L., Biswal, S.K., Sahoo, P.K., Adhikary, M.C.: Int. J. Theor. Phys. **51**, 1538, (2012).
22. Harrison, E.R.: Phys. Rev. Lett. **30**, 188 1973.
23. Melvin, M.A.: Ann. New York Acad. Sci. **262**, 253 1975.
24. Asseo, E., Sol, H.: Phys. Rep. **6**, 148 1987.
25. Parley, R., Taylor, G.: Astrophys. J. **101**, 1623 1991.
26. Wolfe, A.M., Lanzetta, K., Oren, A.L.: Astrophys. J. **388**, 17 (1992).
27. Kulstrud, R., Cen, R., Ostriker, J.P., Ryu, D.: Astrophys. J. **380** , 481 (1997).
28. Barrow, J.D.: Phys. Rev. D **55**, 7451, (1997).
29. Chakraborty, S.: Int. J. Pure Appl. Phys. **29**, 31, (1980).
30. Tikekar, R., Patel, L.K.: Gen. Relativ. Grav. **24**, 397, (1992).
31. Tikekar, R., Patel, L.K.: Pramana J. Phys. **42**, 482, (1994).
32. Patel, L.K., Maharaj, S.D.: Pramana J. Phys. **47**, 1, (1996).
33. Singh, G.P., Singh, T.: Gen. Relativ. Grav. **31**, 371, (1999).
34. Pradhan, A., Bali, R.: Euro. J. Theor. Phys. **5**, 91 (2008).
35. Bali, R.: Euro. J. Theor. Phys. **5**, 105, (2008).
36. Bali, R., Anjali: Astrophys. Space Sci. **302**, 901 (2006).
37. Bali, R., Pareek, U.K., Pradhan, A.: Chin. Phys. Lett. **24**, 2455, (2007).
38. Wang, X.X.: Chin. Phys. Lett. **23**, 1702, (2006).
39. Pradhan, A., Otarod, S., Singh, S.K.: Chin. J. Phys. **45**, 504, (2007).
40. Pradhan, A., Amirhashchi, H., Zainuddin, H.: Chin. J. Theor. Phys. **50**, 56, (2011).
41. Pradhan, A.: Fizika B **16**, 205, (2007).
42. Pradhan, A.: Commun. Theor. Phys. **51**, 367, (2009).
43. Amirhashchi, H., Zainuddin, H., Pradhan, A.: Int. J. Theor. Phys. **50**, 2531, (2011).
44. Saha, B., Visinescu, M.: Astrophys. Sapce. Sci. **315**, 99, (2008).
45. Saha, B., Rikhvitsky, V., Visinescu, M.: Cent. Eur. J. Phys. **8**, 113 (2010).
46. Rikhvitsky, V., Saha, B., Visinescu, M.: Astrophys. Sapce. Sci. **339**, 371, (2012).
47. Singh, C.P.: Astrophys. Space Sci. in press, (2012).
48. Heckmann, O., Schucking, E.: In Gravitation: An Introduction to Current Research ed. Witten, L. (John Wiley, New York), 1962.
49. Roy, S.R., Singh, J.P.: Aust. J. Phys. **38**, 763 1985.
50. Banerjee, A., Sanyal, A.K.: Gen. Relativ. Grav. **20**, 103 1988.
51. Coley, A.A.: Gen. Relativ. Grav. **22**, 3 1990.
52. Bali, R., Meena, B.L.: Proc. Nat. Acad. Sci. India **75**, 273 2005.
53. Chakraborty , N.C., Chakraborty S.: Int. J. Mod. Phys. D **10**, 723 2001.
54. Bali, R., Singh, D.K.: Astrophys. Space Sci. **300**, 387 2005.

55. Bali, R.: Eur. J. Thoer. Phys. **5**, 105 2008.
56. Singh, C.P., Zeyauddin, M., ShriRam: Astrophys. Space Sci. **315**, 181 2008.
57. Singh, C.P., Zeyauddin, M., ShriRam: Int. J. Mod. Phys.A **23**, 2719 2008.
58. Singh, C.P., Zeyauddin, M., ShriRam: Int. J. Theor. Phys. **47**, 3162 2008.
59. Singh, C.P., Beesham, A.: Int. J. Mod. Phys.A **25**, 3825 2010.
60. Singh, C.P.: Braz. J. Phys. **41**, 323 2011.
61. Linchnerowicz, A.: Relativistic Hydrodynamics and Magneto Hydrodynamics, Benjamin, New York, p.13 (1967).
62. Maartens, R.: Pramana J. phys. **55**, 575 (2000).